

**A NANORUBY-BASED
PHOTOLUMINESCENT PROBE
TOWARDS BIOIMAGING APPLICATIONS**

By

Wan Aizuddin W. Razali

A THESIS SUBMITTED

FOR THE DEGREE OF DOCTOR OF PHILOSOPHY

DEPARTMENT OF PHYSICS AND ASTRONOMY

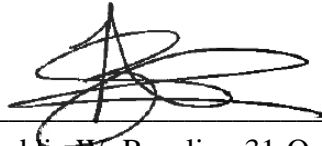
MARCH 2016



MACQUARIE
University

Except where acknowledged in the customary manner, the material presented in this thesis is, to the best of my knowledge, original and has not been submitted in whole or part for a degree in any university.

Several parts of this thesis materialized as a result of collaborative efforts with my supervisors and researchers at other institutions. Their contributions are recognised and have been duly acknowledged at the respective sections.

A handwritten signature in black ink, consisting of several loops and a central vertical stroke, positioned above a horizontal line.

Wan Aizuddin W. Razali 31-October-2016

Acknowledgments

All praise is to God, the Lord of the Worlds. By His grace, this work came to completion. My gratitude goes to my parents for their support, encouragement and faith in my ability. I thank them for their unflinching prayers. My special thanks go to my beloved wife, Maisarah Sulaman for her endless patience, encouragement, and always being there when I needed her.

I would like to convey my deepest gratitude to my main supervisor A/Prof. Andrei Zvyagin for his patience, dedicated support and inspirational motivation. My heartfelt gratitude is equally extended for his valuable inputs on my thesis. I would also like to acknowledge my associate supervisor, Prof. Ewa Goldys who provided the opportunity for me to join this wonderful group and supported my research effort. I would like to thank my co-supervisor Dr. Varun Sreenivasan, for sharing his knowledge, guidance and his kind help in my research. My gratitude also goes to the contributing authors of this work, and my collaborators for their useful contributions.

I am also thankful to my colleagues, Katya, Annie, Olivia, Anna, Sandhya, Deming, Saabah, Kashif, Tom, Zahra, Aziz, and my other wonderful friends, who have contributed directly or indirectly to this success, and who have shared their time and their thoughts with me.

I am deeply grateful to the Malaysia Ministry of Education and Universiti Teknologi MARA for providing me the scholarship to undertake this doctoral study at Macquarie University. I am also grateful to Macquarie University, which provided the financial support to conduct this research.

Finally, I would like to express my deep appreciation and respect for the staff in Macquarie University, including Physics and Astronomy Department, Microscopy Unit and Higher Degree Research for assisting my study.

List of Publications

Papers

1. **W. A. W. Razali**, V. K. A. Sreenivasan, E. M. Goldys, and A. V. Zvyagin. "Large-scale production and characterization of biocompatible colloidal nanoalumina." *Langmuir*, vol. 30, no. 50 (2014): 15091-15101.
2. **W. A. W. Razali**, V. K. A. Sreenivasan, K. Zhang, R. Heintzmann, E. M. Goldys and A. V. Zvyagin. Mass production of nanorubies photoluminescent probe for bioimaging. Prepared for submission to RSC Advances journal.
3. **W. A. W. Razali**, V. K. A. Sreenivasan, C. Bradac, M. Connor, E. M. Goldys, and A. V. Zvyagin. "Wide-field time-gated photoluminescence microscopy for fast ultrahigh-sensitivity imaging of photoluminescent probes". *Journal of Biophotonics*, vol. 9, no. 8 (2016): 848-858.

Conference Presentations and Posters

1. **W. A. W. Razali**, A. M. Edmonds, M. A. Sobhan, V. K. A. Sreenivasan, E. A. Grebenik, E. M. Goldys, and A. V. Zvyagin. "Nano-ruby: A promising fluorescent probe for background-free cellular imaging", 9th Asia-Pacific Conference on Near-field Optics (APNFO), 2013
2. **W. A. W. Razali**, V. K. A. Sreenivasan, E. M. Goldys and A. V. Zvyagin. "Mass-production, characterization and functionalization of nano-alumina", 21st biennial Australian Institute of Physics Congress "The Art of Physics" (AIP), 2014
3. V. K. A. Sreenivasan, **W. A. W. Razali**, C. Bradac, E. A. Grebenik, M. Santiago, E. M. Goldys, M. Connor, A. V. Zvyagin. "Mass-production,

characterization, functionalization and imaging of nanoruby photoluminescent probes towards imaging GPCR-signalling with single-particle precision”, 5th International NanoMedicine Conference, 2014.

4. **W. A. W. Razali**, V. K. A. Sreenivasan, E. M. Goldys and A. V. Zvyagin. “Ultrasensitive nanoruby imaging using time gated luminescence microscopy”, 10th Asia-Pacific Conference On Near-Field Optics (APNFO), 2015.
5. **W. A. W. Razali**, V. K. A. Sreenivasan, E. M. Goldys and A. V. Zvyagin. “Large scale production, characterisation and functionalisation of nanoruby”, 6th International NanoMedicine Conference, 2015.
6. **W. A. W. Razali**, V. K. A. Sreenivasan, E. M. Goldys and A. V. Zvyagin. “Nanoruby: a promising photoluminescent probe for biomolecular imaging”, Applied Nanotechnology and Nanoscience International Conference (ANNIC), 2015.

Abstract

In the past decades, fluorescent organic dyes have been used extensively as molecular probes in bioimaging. However, their irreversible transition to the dark-state, termed photobleaching, photoinduced cytotoxicity, and biodegradability limit their application scope. Photoluminescent nanomaterials provide a lucrative alternative to the fluorescent organic dyes due to their virtually unlimited photostability, inert core, controllable surface chemistry, biocompatibility, etc. In this study, I report on the development of a new-generation molecular probe based on a photoluminescent nanomaterial, termed as “nanorubies”, which represents ruby nanocrystals of the composition alpha-alumina (α -Al₂O₃) doped with chromium (Cr³⁺). In addition to the photoluminescent nanomaterial merits, nanoruby emission takes place in a remarkably narrow spectral band in the far-red spectral range (692 nm), and characterised by long photoluminescent lifetime (3.7 ms).

The first reported advance of this study addresses development of a top-down, large-scale production of photoluminescent nanomaterials. Top-down methods take advantage of the existing variety of bulk and thin-film solid-state materials for improved prediction and control of the resultant nanomaterial properties. The power of this approach is demonstrated by using high-energy ball milling (HEBM) of alumina (Al₂O₃) and nanoruby. Nanoalumina and nanoruby particles with a mean size less 100 nm in their most stable α -crystallographic phase were produced in gram quantities suitable for biological and biomedical applications. Nanomaterial contamination from zirconia balls used in HEBM was reduced from 19% to 2% using a selective acid etching procedure.

The biocompatibility of the milled nanomaterial was demonstrated by forming stable colloids in water and physiological buffers corroborated by the corresponding measured zeta potentials of +40 mV and -40 mV and characterised by *in vitro* cytotoxicity assays. The feasibility of anchoring a host of functional groups and biomolecules to milled nanoalumina and nanoruby surfaces was demonstrated by functionalisation of their

surface which resulted in decoration of the nanoparticle surface with amino, carboxyl and polyethylene glycol groups suitable for further conjugation with functional biomolecules.

Photoluminescence probes in combination with fast and sensitive imaging systems are much in demand. I describe a wide-field, time-gated photoluminescence microscopy system customised for ultrasensitive imaging of probes with long photoluminescence lifetime and exemplified by the use of nanorubies as a probe. The detection sensitivity relied on the long photoluminescence lifetime of nanoruby, which allowed its discrimination from the autofluorescence background and laser backscatter by employing a time-gated imaging acquisition mode. This mode enabled several-fold improvement of the photoluminescence imaging contrast of discrete ruby nanoparticles dispersed on a coverslip, and clearly visualised discrete nanorubies submerged in a layer of organic fluorescent dye, which would obscure the presence of most other photoluminescent nanoparticles. The ultrahigh-sensitivity imaging of photoluminescent molecular probes offers new opportunities, such as visualisation of intracellular molecular trafficking and detection of rare biomolecular events in an optically crowded background.

In partnership with my group members, I have demonstrated specific labelling of hemagglutinin-tagged μ -opioid receptors by using biohybrid nanoruby complexes in conjunction with anti-hemagglutinin antibody, which has demonstrated the power of this new-generation photoluminescence nanotechnology not only for molecular-specific visualisation, but also for targeted delivery and therapy applications. Further, the real-time video-microscopy of nanoruby-based binding assay in serum has been demonstrated. This result shows the potential for pathogen detection in biological fluids, prospectively leading to early diagnosis applications.

Content

Acknowledgements	v
List of Publications	vii
Abstract	ix
CHAPTER 1: General Introduction and Outline	1
1.1 Thesis Outline	4
1.2 References	5
CHAPTER 2: Photoluminescent Nanoparticles for Bioimaging	7
2.1 Introduction	7
2.2 Fundamentals of Photoluminescence	7
2.2.1 Absorption and Emission	8
2.2.2 Photoluminescence Lifetime	10
2.2.3 Quantum Efficiency	10
2.3 Photoluminescent nanoparticles	11
2.2.1 Quantum Dots	12
Synthesis of Quantum Dots	13
Functionalisation and Conjugation of Quantum Dots	14
Bioimaging Applications of Quantum Dots	14
2.2.2 Fluorescent Nanodiamonds	15
Synthesis of Fluorescent Nanodiamonds	17
Functionalisation and Conjugation of Fluorescent Nanodiamonds	18
Bioimaging Application of Fluorescent Nanodiamonds	18
2.2.3 Upconversion Nanoparticles	19

	Synthesis of Upconversion Nanoparticles	22
	Functionalisation of Upconversion Nanoparticles	22
	Bioimaging Applications of Upconversion Nanoparticles	23
2.4	Limitation of the Existing Photoluminescent Nanoparticle Probes	25
2.4.1	Limitations of Quantum Dots	25
2.4.2	Limitations of Fluorescent Nanodiamonds	26
2.4.3	Limitations of Upconversion Nanoparticles	27
2.5	Nanoruby	28
2.5.1	Composition and Structure	29
2.5.2	Nanoruby Production Method	30
	Chemical Methods	30
	Laser Ablation	33
	Milling Method	35
2.5.3	Nanoruby Properties	37
	Optical Property	37
	Colloidal Stability	39
	Cytotoxicity	40
2.5.4	Nanoruby Functionalisation	41
2.5.5	Bioimaging Applications of Nanoruby	43
2.5	Conclusion	45
2.6	References	46
	CHAPTER 3: Ball-Milling Method and Characterisation of Nanocrystals	59
3.1	Nanoparticles Production Method	59
3.1.1	Milling Method	62
3.1.2	High-Energy Ball Milling Method	62
3.1.3	Milling Ball Motion and Energy Transfer Model	64

3.1.4	Milling Parameters	68
	Materials of Milling Ball	68
	Size Selection of Milling Ball	71
	Milling Speed	73
	Milling Duration	74
	Charge Ratio	76
	Milling Aid	77
3.1.5	Milling Procedure and Related Apparatus	79
3.2	Characterisation Techniques	82
3.2.1	Dynamic Light Scattering	82
3.2.2	Transmission Electron Microscopy	85
3.2.3	Scanning Electron Microscopy	86
3.2.4	Energy-Dispersive X-Ray Spectroscopy	87
3.2.5	X-Ray Diffraction	88
3.2.6	Fourier Transform Infrared Spectroscopy	91
3.2.7	Thermogravimetric Analysis	92
3.2.8	Spectrofluorometer	93
3.2.9	Epi-Luminescence Microscopy	94
3.3	References	97
CHAPTER 4: Large-Scale Production and Characterisation of Biocompatible Colloidal Nanoalumina		105
4.1	Introduction to paper	105
4.2	Authors' contribution	106
4.3	Full paper	107
4.6	References	120

CHAPTER 5: Mass Production of Nanorubies Photoluminescent Probe for Bioimaging	121
5.1 Background	121
5.2 Introduction to paper	122
5.3 Author's contribution	122
5.4 Full paper	124
5.5 References	161
CHAPTER 6: Wide-Field Time-Gated Photoluminescence Microscopy for Fast Ultrahigh-Sensitivity Imaging of Photoluminescent Probes	163
6.1 Introduction to the paper	163
6.2 Authors' contribution	164
6.3 Full paper	165
6.4 Time-gated photoluminescence microscopy	179
6.5 Avidin-biotin interaction and its application.	183
6.6 References	185
CHAPTER 7: Summary and Future Scope	187
7.1 Summary	187
7.2 Future Scope	189
7.3 References	191
APPENDIX A	193
APPENDIX B	197

1

General Introduction and Outline

Fluorescence microscopy potentiated by labelling biological structures of interest with photoluminescent (PL) nanoparticles (NPs) is an important tool in the life sciences. This imaging modality provides a direct, less invasive and very sensitive access to observation of cellular morphology and processes in cells and tissues [1, 2]. Single-molecule imaging represents a more specialised modality of the fluorescence microscopy, where the detection sensitivity is pushed to its limits, allowing observation of single fluorescent molecules and hence single labelled biomolecules. This ultrahigh-sensitivity modality was introduced by Moerner and Orritt [3], and Willian Moerner was awarded by a Nobel prize in 2014 for this pioneering work. Imaging and tracking single biomolecules allow the abrogation of the ensemble averaging, which was and is commonly used in biomedical research, but can mask rare (albeit important) biological events behind the scene of the mainstream processes. The following are three examples in the life sciences allow to appreciate the scale and importance of this imaging modality.

Seisenberger *et al.* have demonstrated real-time single-molecule imaging of the infection pathway of an adeno-associated virus [4]. It was the single-molecule imaging, which allowed uncovering anomalous diffusion of the endosome and the virus in the cytoplasm and the nucleus in addition to the expected free diffusion. In addition, the real-time visualisation of the infection pathway of a single virus revealed a much faster infection than was generally observed.

The second example relates to the neuronal signaling reflected in the behaviour of AMPA receptors on the cell membranes (AMPA= α -amino-3-hydroxy-5-methyl-4-isoxazolepropionic acid). The mobility and localisation of AMPA receptors at the neuronal junctions controls the level of electrical signals in neurons. This, in turn, is pivotal for long-term memory and learning [5]. Imaging of discrete AMPA membrane receptor trafficking in synaptically connected immunostained neurons during neuronal activity uncovers intricate mechanisms at the onset of receptor activations in the living brain. AMPA receptors alternate abruptly between periods of rapid diffusion on the cellular membrane and periods of restricted motion within a sub-micron area termed confinement. This confinement occurs mostly when the receptors are near synapses. Read out of the averaged diffusion of the AMPA receptors would provide a distorted and misleading picture of neuron functionality, whereas the single-nanoparticle tracking technique captures intricate functionality of the neurons versus various physiological and therapeutic factors, and is routinely used in the field of neuroscience [6].

The third example relates to the uncovering of pathways in the cell of G-protein coupled receptors (GPCRs), which are the largest family of cell-surface proteins that mediate signalling related to physiological and sensory functions. Imaging and tracking the molecular pathways of discrete GPCR opioid receptors unveil the dynamics of drug-receptor binding, internalisation, dissociation, and recycling, which play a pivotal role in regulation of motivation, anxiety, breathing, and metabolism.

These single-molecule studies place high demands on labelling fluorophore, which are often constrained by undesirable photophysical properties. These include transient (photoblinking) and irreversible (photobleaching) photon-induced transitions to dark states. Fluorescent organic dye molecules, such as green fluorescent protein (GFP), and fluorescent organic dyes, such as fluorescein, are widely used as fluorescent probes [7, 8]. However, their emission can survive for about 10^6 cycles of the excitations and emissions, followed by irreversible photobleaching [9]. In terms of the single-molecule tracking duration, the fluorescence persists only for ≈ 3 ms under the saturation excitation by assuming the fluorescence lifetime 3 ns, and can be extended to second-long observation time by optimising signal-to-noise ratio [10]. In the context of biomedical imaging, which favours the longer-wavelength excitation/emission (falling into the so-called biological tissue transparency window, ranging from 700 nm to 1300

nm), such fluorophores as Alexa Fluor 750, Cy5 and Cy7 dyes are typically prone to photobleaching. Fluorescence dye also suffer from potential cytotoxicity, poor resistance to aggressive chemical and biological environment, and limited ability to penetrate cells [11]. Although the design of improved quality organic fluorophores is in continuous progress, there is a strong demand for alternative solutions.

Nanotechnology provides the solution by ushering into the single-molecular fluorescence imaging field with new types of molecular probes based on PL NPs. Nanodiamonds [12] and upconversion nanoparticles (UCNPs) [13] are able to counter the photobleaching problem by producing unfading emission. These nanomaterials exhibited reduced cytotoxicity [14]. NPs offer a lucrative opportunity to achieve high-contrast detection by means of time-gated imaging, which has been reported using lanthanide-based NPs [15, 16]. NP surface modification displaying specific functional groups is now under active development towards targeted imaging and drug delivery [17]. At the same time, the existing NP-based molecular probes are not ideal. For example, owing to their nonlinear excitation pathway, UCNPs require high power densities to reach the optimal brightness [18] and are susceptible to environmental photoluminescence quenching. Some NPs are cytotoxic, and influence of carbon nanotubes, metal oxide (e.g., ZnO) and semiconductor Quantum Dots (QDs) to biological systems is still debated [19, 20]. Despite of the emerging promise PL NPs for single-molecule imaging and tracking, there is a need to populate the existing arsenal of PL NPs.

Ruby nanocrystals known as “nanorubies” is one of the newly discovered PL nanomaterial [21]. Nanorubies have attractive properties, including virtually unlimited photostability, a narrow photoluminescence line at 692 nm, exceptionally long emission lifetime (≈ 3.7 ms), high quantum yield reaching 90% in bulk, and reported biocompatibility. This material is worthwhile to explore for biological applications due to its remarkable properties, combined with ease of obtaining synthetic ruby crystal at low cost. This project focuses on the high-scale production of nanoruby by using milling method. It will be also demonstrated how nanorubies can be employed in several bioimaging applications, where single-molecule tracking is the central application.

1.1 Thesis Outline

This thesis comprises seven chapters. Chapter 1 introduces the background, main objectives and thesis outline. Chapter 2 reviews the fundamentals of the existing PL NPs, including quantum dots, nanodiamonds and upconversion NPs, their synthesis methods and applications in biological imaging. The limitations of these PL nanomaterials in the context of single-molecule imaging modality are also discussed. Finally, nanoruby properties, production methods, functionalisation approaches and applications will be overviewed.

Chapter 3 reviews the existing NP production methods, with the main emphasis on milling methods. Discussion of the key parameters affecting the size, crystal quality and yield of as-produced NPs will represent an essential part of this chapter. The overview of the characterisation methods used in this project is also provided.

Chapter 4 (Publication I) W. A. W. Razali, V. K. A. Sreenivasan, E. M. Goldys and A. V. Zvyagin. "Large-Scale Production and Characterization of Biocompatible Colloidal Nanoalumina" (Langmuir 30, no. 50 (2014): 15091-15101) reports the large-scale production of nanoalumina using a high-energy ball-milling (HEBM) method. Abstract: The rapid uptake of nanomaterials in life sciences calls for the development of universal, high-yield techniques for their production and interfacing with biomolecules. Top-down methods take advantage of the existing variety of bulk and thin-film solid-state materials for improved prediction and control of the resultant nanomaterial properties. We demonstrate the power of this approach using high-energy ball milling (HEBM) of alumina (Al_2O_3).

Chapter 5 (Publication II) W. A. W. Razali, V. K. A. Sreenivasan, K. Zhang, E. M. Goldys and A. V. Zvyagin. "Mass Production of Nanorubies Photoluminescent Probe for Bioimaging" (Prepared for submission to RSC Advances journal) presents the mass-production of nanoruby by using a HEBM method. The as-produced nanorubies were investigated in terms of their size, structure, optical properties and cytotoxicity. The applications of as-produced, surface-modified and antibody-coupled nanorubies for cell labelling and μ -opioid receptor labelling were demonstrated.

Chapter 6 (Publication III) W. A. W. Razali, V. K. A. Sreenivasan, C. Bradac, M. Connor, E. M. Goldys, and A. V. Zvyagin. "Wide-field time-gated photoluminescence microscopy for fast ultrahigh-sensitivity imaging of

photoluminescent probes” (Journal of Biophotonic 9, no. 8 (2016): 15091-15101) is devoted to the demonstration of the time-gated imaging modality potentiated by nanoruby towards single-molecule imaging. The long-photoluminescence lifetime characteristic of nanoruby has been exploited in achieving ultrahigh-sensitive imaging system. The live cell labelling and real time kinetic binding of nanoruby in biological fluid also been demonstrated.

The final chapter, Chapter 7 provides a summary of this work and discusses the future scope on this work.

1.2 References

- [1] "Introduction to Fluorescence," in *Principles of Fluorescence Spectroscopy*, J. Lakowicz, Ed., ed: Springer US, 2006, pp. 1-26.
- [2] R. Weissleder, "A clearer vision for in vivo imaging," *Nature biotechnology*, vol. 19, pp. 316-317, 2001.
- [3] W. Moerner, "New directions in single-molecule imaging and analysis," *Proceedings of the National Academy of Sciences*, vol. 104, pp. 12596-12602, 2007.
- [4] G. Seisenberger, M. U. Ried, T. Endress, H. Buning, M. Hallek, and C. Brauchle, "Real-time single-molecule imaging of the infection pathway of an adeno-associated virus," *Science*, vol. 294, pp. 1929-1932, Nov 2001.
- [5] M. Heine, L. Groc, R. Frischknecht, J.-C. Béïque, B. Lounis, G. Rumbaugh, *et al.*, "Surface mobility of postsynaptic AMPARs tunes synaptic transmission," *Science*, vol. 320, pp. 201-205, 2008.
- [6] R. Frischknecht, M. Heine, D. Perrais, C. I. Seidenbecher, D. Choquet, and E. D. Gundelfinger, "Brain extracellular matrix affects AMPA receptor lateral mobility and short-term synaptic plasticity," *Nature neuroscience*, vol. 12, pp. 897-904, 2009.
- [7] R. Y. Tsien, "The green fluorescent protein," *Annual review of biochemistry*, vol. 67, pp. 509-544, 1998.
- [8] X. Fei and Y. Gu, "Progress in modifications and applications of fluorescent dye probe," *Progress in Natural Science*, vol. 19, pp. 1-7, 2009.
- [9] R. Zondervan, F. Kulzer, M. A. Kol'chenk, and M. Orrit, "Photobleaching of rhodamine 6G in poly (vinyl alcohol) at the ensemble and single-molecule levels," *The Journal of Physical Chemistry A*, vol. 108, pp. 1657-1665, 2004.
- [10] U. Resch-Genger, M. Grabolle, S. Cavaliere-Jaricot, R. Nitschke, and T. Nann, "Quantum dots versus organic dyes as fluorescent labels," *Nature methods*, vol. 5, pp. 763-775, 2008.
- [11] R. Alford, H. M. Simpson, J. Duberman, G. C. Hill, M. Ogawa, C. Regino, *et al.*, "Toxicity of organic fluorophores used in molecular imaging: literature review," *Molecular imaging*, vol. 8, p. 341, 2009.
- [12] J. M. Say, C. van Vreden, D. J. Reilly, L. J. Brown, J. R. Rabeau, and N. J. King, "Luminescent nanodiamonds for biomedical applications," *Biophysical Reviews*, vol. 3, pp. 171-184, 2011.

- [13] D. K. Chatterjee, A. J. Rufaihah, and Y. Zhang, "Upconversion fluorescence imaging of cells and small animals using lanthanide doped nanocrystals," *Biomaterials*, vol. 29, pp. 937-943, 2008.
- [14] T. Cao, Y. Yang, Y. Gao, J. Zhou, Z. Li, and F. Li, "High-quality water-soluble and surface-functionalized upconversion nanocrystals as luminescent probes for bioimaging," *Biomaterials*, vol. 32, pp. 2959-2968, 2011.
- [15] J. Yuan and G. Wang, "Lanthanide-based luminescence probes and time-resolved luminescence bioassays," *TrAC Trends in Analytical Chemistry*, vol. 25, pp. 490-500, 2006.
- [16] I. Hemmilä and V. Laitala, "Progress in Lanthanides as Luminescent Probes," *Journal of Fluorescence*, vol. 15, pp. 529-542.
- [17] S. Osswald, G. Yushin, V. Mochalin, S. O. Kucheyev, and Y. Gogotsi, "Control of sp^2/sp^3 carbon ratio and surface chemistry of nanodiamond powders by selective oxidation in air," *Journal of the American Chemical Society*, vol. 128, pp. 11635-11642, 2006.
- [18] J.-C. Boyer and F. C. Van Veggel, "Absolute quantum yield measurements of colloidal $NaYF_4: Er^{3+}, Yb^{3+}$ upconverting nanoparticles," *Nanoscale*, vol. 2, pp. 1417-1419, 2010.
- [19] C. E. Bradburne, J. B. Delehanty, K. Boeneman Gemmill, B. C. Mei, H. Mattoussi, K. Susumu, *et al.*, "Cytotoxicity of quantum dots used for in vitro cellular labeling: role of QD surface ligand, delivery modality, cell type, and direct comparison to organic fluorophores," *Bioconjugate chemistry*, vol. 24, pp. 1570-1583, 2013.
- [20] N. Chen, Y. He, Y. Su, X. Li, Q. Huang, H. Wang, *et al.*, "The cytotoxicity of cadmium-based quantum dots," *Biomaterials*, vol. 33, pp. 1238-1244, 2012.
- [21] A. M. Edmonds, M. A. Sobhan, V. K. A. Sreenivasan, E. A. Grebenik, J. R. Rabeau, E. M. Goldys, *et al.*, "Nano-Ruby: A Promising Fluorescent Probe for Background-Free Cellular Imaging," *Particle & Particle Systems Characterization*, vol. 30, pp. 1-8, 2013.

Photoluminescent Nanoparticles for Bioimaging

2.1 Introduction

In this chapter, basic concepts and terminology of photoluminescence are introduced, followed by examples of the most widespread photoluminescent (PL) nanoparticles (NPs), quantum dots, which represent the state-of-the-art mature nanotechnology material. An overview of fluorescent nanodiamonds and upconversion nanoparticles will be presented to demonstrate the modern trends in the development of prospective PL nanomaterials. The advantages and limitations of these NPs in the context of biological imaging will be discussed. In the final section, I will introduce nanoruby, which is portrayed as an alternative PL nanomaterial to the existing PL NPs. Photoluminescence mechanism, production methods, optical properties, chemical stability, and biocompatibility of nanorubies will be reviewed.

2.2 Fundamentals of Photoluminescence

Luminescence is an emission of light from any substance, which occurs from electronically excited states [1]. Types of luminescence are categorised depending on the excitation pathway, and include physical (absorption of light), mechanical (friction), or chemical (chemical reactions), as listed in Table 2.1. Photoluminescence is one type of luminescence, where light emission is produced by the absorption of photons from an external source. In this process, a molecule absorbs photon at a wavelength in the

ultraviolet, visible or infrared spectral range, making a transition to the excited state, with concomitant emission of a photon, when the molecule undergoes transition to the ground state. Note that the photon emission is one of the possible pathways of the excited state transition to the ground state. In the great majority of cases, the process of photon absorption and emission incurs an energy penalty, so that the emitted photon is “red-wavelength-shifted” – the effect known as a Stokes shift. For example, ultraviolet (UV) light absorbed by a quinine molecule is red-wavelength-shifted to emitted light to blue light, causing the blue glow, as observed by Stokes [2] and Herschel [3]. The photoluminescence can be further categorised into fluorescence or phosphorescence, depending on the electronic configuration of the excited state and the emission pathway, as it will be discussed in the next subsection.

Table 2.1: Types of luminescence. Reproduced from Ref. [4].

Luminescence types	Excitation method
Photoluminescence	Absorption of light
Radioluminescence	Ionizing radiation
Cathodoluminescence	Cathode rays
Electroluminescence	Electric field
Thermoluminescence	Heating
Chemiluminescence	Chemical process
Bioluminescence	Biochemical process
Triboluminescence	Frictional and electrostatic forces
Sonoluminescence	Ultrasounds

2.2.1 Absorption and Emission

The energy levels of a molecule are customarily represented by using a Jablonski energy diagram (shown in Figure 2.1), which is used to explain processes that occur between the absorption and emission of light by the molecule [5]. Figure 2.1 shows the energy levels typical for an organic fluorescent molecule, including ground state (S_0), excited singlet states (S_1 and S_2), and excited triplet state. At room temperature, a molecule stays in the ground state. By absorbing light, the molecule makes a transition from the ground state to the excited state of either S_1 or S_2 , as shown by upward arrows

in Figure 2.1. The molecule is then rapidly relaxed (characteristic time $\approx 10^{-12}$ s) to the lowest vibrational state of S_1 non-radiatively, bearing an energy penalty. This process is known as internal conversion. The molecule returns to the ground state from the excited singlet state, emitting light with the energy equal to the energy difference between the two levels. This process is known as fluorescence, and generally occurs in aromatic molecules, such as rhodamine, fluorescein and acridine, termed fluorochromes or fluorophores [6]. The molecule in the S_1 state can also make an alternative transition to the triplet state T_1 (Figure 2.1, dotted downward arrow). The conversion from S_1 to T_1 is called intersystem crossing. Emission produced when the molecule returns to the ground state from T_1 is known as phosphorescence which was first observed by a French physicist Edmond Becquerel, before Stokes observed fluorescence [7].

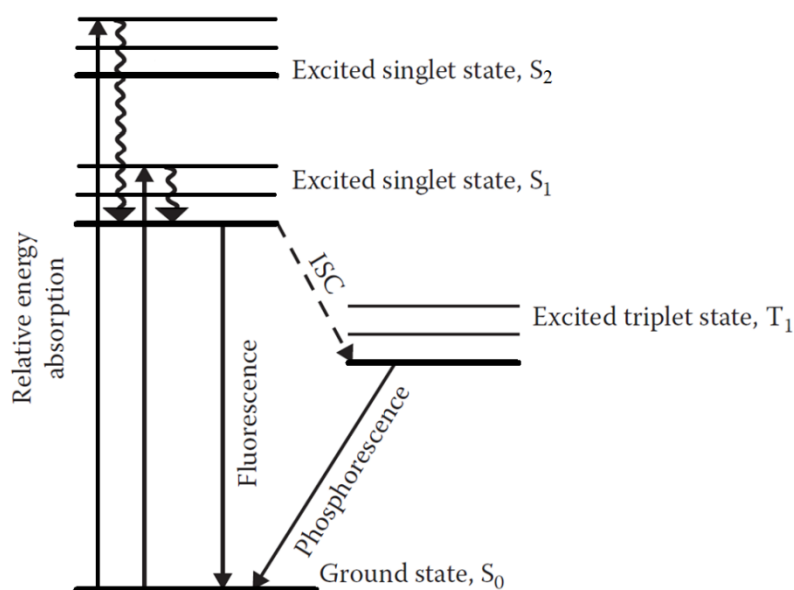


Figure 2.1: A Jablonski energy diagram showing the ground state, excited singlet state, and excited triplet state of a material. The thicker lines represent electronic energy levels, while the thinner lines denote the vibrational energy states. The wavy lines denote non-radiative relaxation process. The dotted arrow shows intersystem crossing (ISC). Straight arrows show transitions between the states associated with absorption or emission of a photon. Adapted from Ref. [8].

2.2.2 Photoluminescence Lifetime

Generally, photoluminescent lifetime (τ) is defined as the mean time taken for a molecule to decay from the excited state to the ground state, either via fluorescence or phosphorescence, including nonradiative processes [9]. It can be specifically defined as the inverse of the sum of the rate constants that deplete the excited state. Thus, the relative contributions of the internal conversion, intersystem crossing and the radiative process will determine the lifetime value. The magnitude of the rate constants that deplete S_1 are typically around 10^8 s^{-1} , implicating the photoluminescence lifetime of the order of $<10 \text{ ns}$ [6]. Most organic fluorophores are characterised by lifetimes, ranging from tens picoseconds to tens of nanoseconds. In the case of phosphorescence emission, the rate at which the triplet state is depleted, generally, slower (between 10^4 s^{-1} and 1 s^{-1}), leading to lifetimes ranging from sub-milliseconds to seconds. Since the effect of autofluorescence will be alluded frequently in this thesis, its emission properties stem from organic fluorophore constituents present in biological systems referred to as endogenous fluorophores. Therefore, τ of the autofluorescence [10] ranges from hundreds of picoseconds [11] to several nanoseconds [9].

2.2.3 Quantum Efficiency

Quantum efficiency (η) of the fluorophore is an important property of a fluorophore. The fluorescence power P [W] emitted by a fluorophores is determined by its absorption cross-section σ_a and the quantum efficiency according to the following relation: $P = \eta \sigma_a I_{ex}$, where I_{ex} stands for the excitation intensity [W/cm^2], often referred to as “power density”. Quantum efficiency can be defined as a ratio of the number of photons emitted to the number of molecules in the excited state [12]. This can be interpreted as a ratio of the number of emitted to the number of absorbed photons in a simple case of the perfectly efficient absorption process resulting in the molecule transition to the excited energy level. We note that in several particular cases, including energy upconversion transfer, this definition breaks down and requires more general definition, which is introduced in my colleagues’ paper [13] and termed “conversion efficiency”.

2.3 Photoluminescent Nanoparticles

PL NPs have been ushered into the life sciences heralded by new discoveries in single-molecule imaging, whole-animal imaging, and diagnostic imaging. The emerging discipline of theranostics demonstrates an explosive growth, as evidenced by the journal impact-factor of Theranostics journal reaching 8 within two years. We will consider several types of PL NPs, which vary in their photophysical and chemical properties, and make us an almost complete suite of PL nanomaterials suitable for biomedical applications. These NPs include the well-established quantum dots, reasonably well-explored fluorescent nanodiamonds, and upconversion NPs introduced almost two decades ago [14, 15]. Fluorescent carbon dots [16], metal nanoclusters [17, 18], plasmonic nanoparticles, upconversion nanoparticles [19] and nanorubies [20] are some of the newly developed PL probes. None of the PL NPs is ideal: some of them exhibit unwanted fluorescence intermittency (known as “photoblinking”), some are notoriously cytotoxic and chemical stability is often an issue in biomedical applications. These shortfalls drive the nanoscience research towards PL nanomaterials with improved properties. As an overview, Table 2.2 shows the comparisons of organic dye and other PL NPs including quantum dots (QDs), upconversion NPs (UCNP), fluorescent nanodiamonds (FNDs, implying nitrogen-vacancy centre ND), and nanorubies.

Table 2.2: Comparison of fluorescent probe properties.

	Typical Organic Dye	QDs	UCNPs	FNDs	Nanorubies
Excitation	UV/Visible	UV/Visible	Near IR	Visible	Visible
Emission (nm)	405-805[21]	400-1400 [22]	300-900 [23, 24]	560-800 [25, 26]	692, 694 [20]
Lifetime	<10 ns	10 – 20 ns	100 – 10 ms	10 – 20 ns	>3 ms
Photostability	×	√	√	√	√
Non-blinking	×	×	√	√	√
Non-toxicity	×	×	√	√	√
High conversion efficiency	√	√	×	√	√

In the following section, photoluminescence mechanisms, optical and chemical properties, and bioimaging application of three types of PL NPs: QDs, FNDs, and

UCNPs will be discussed, followed by discussion of their limitations in the context of biomedical optical imaging.

2.2.1 Quantum Dots

QDs are semiconductor nanocrystals whose size ranges from 2 to 10 nm. The typical composition of QDs is cadmium selenide (CdSe), cadmium sulphide (CdS), indium phosphide (InP) and indium arsenide (InAs) [22]. The fluorescence emission of QDs is tunable by changing their size, which relates to the quantum confinement effect [27]. For example, the bandgap of CdS QDs is tunable from 4.5 to 2.5 eV [28]. The smaller the QD, the larger the bandgap, which means that the more energy is required to excite the electron from the valence band to the conduction band, followed by emission of the higher-energy (shorter wavelength) photon. The size reduction is manifested by the emission “colour” shift from red to blue, as shown in Figure 2.2. Figure 2.3a shows the QDs fluorescence emission dependency on the composition and size. QDs have exceptionally broad excitation spectrum ranging from UV and exhibiting a local size-tunable peak. QDs typically emit in a narrow fluorescence band, as shown in Figure 2.3b.

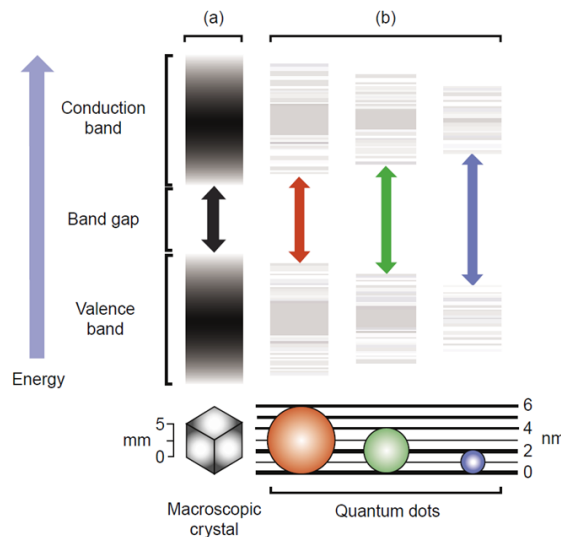


Figure 2.2: (a) Schematic diagram explain the origin of the size-dependent fluorescence of quantum dots. (b) The larger the QD, the narrower its bandgap: red large-size QD in comparison with blue small-size QD. Reproduced from Ref. [29].

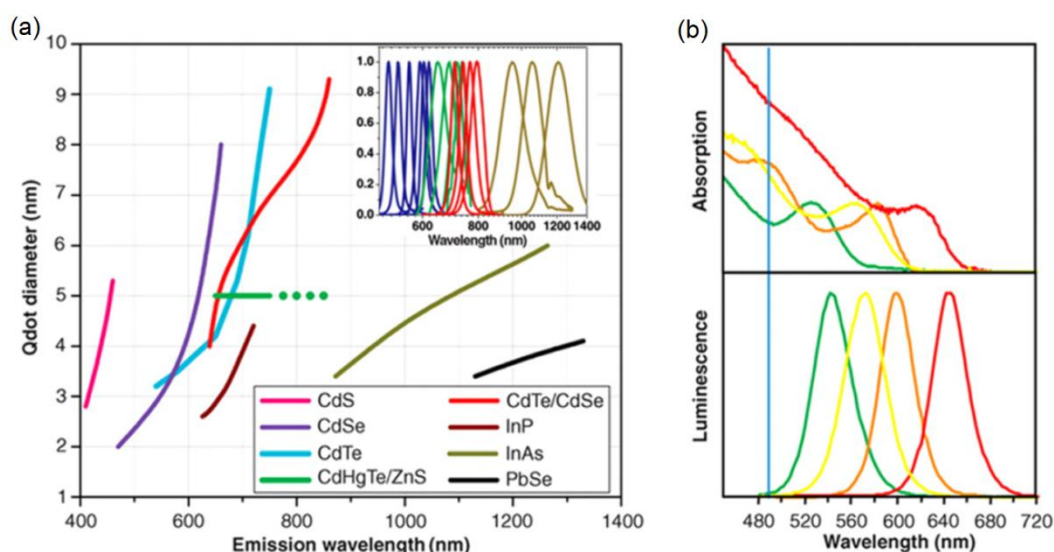


Figure 2.3: (a) Fluorescence emission characteristics of QDs with different compositions and sizes. (b) Absorption (top) and emission (bottom) spectra of four different sizes CdSe/ZnS QD samples. The blue vertical line indicates the 488-nm line of an argon-ion laser, which can be used to efficiently excite all four types of QDs simultaneously. Reproduced from Ref. [22].

Synthesis of Quantum Dots

QDs are typically synthesised by employing wet chemistry protocols, including less common aqueous synthesis [30, 31] and widespread high-temperature organic solvent methods [32]. Murray *et al.* have pioneered a high-temperature ($\approx 300^\circ\text{C}$) organic solvent method for the synthesis of high crystal quality CdX (X = S, Se, Te) quantum dots [33]. The organic solvent was needed to disperse nanocrystals, control the reaction speed and adjust the reaction temperature in a wide range [34]. The size of as-produced nanocrystals are controllable by the precursor concentration and reaction time [35]. The recognition of QDs came when the core/shell architecture of these nanoparticles was introduced. As a result, the quantum efficiency was improved by confining the excitation to the core and eliminating the surface defects, with the increase from several percent to 80%. The shell is typically designed by selecting the high bandgap materials such as CdS and ZnS, with the condition that the bandgap width exceeds that of the core material, in the case considered here CdSe. The as-produced shell is generally hydrophobic, requiring further functionalisation, which is discussed in the next subsection.

Functionalisation and Conjugation of Quantum Dots

QD surface needs to be modified with biocompatible moieties or coated with a polymer layer to hydrophilise this nanomaterial and form an interface with biological environment. This provides anchoring points to enable conjugation with biological molecules, such as peptides [36, 37], antibodies [38, 39], aptamers [40, 41], and DNAs [42, 43]. A schematic diagram of the QD architecture, with the functionalisation and conjugation layers is shown in Figure 2.4. The functionalisation is carried out by a cap exchange, where TOPO surface molecules are replaced with hydrophilic functional groups, such as carboxyl and amine groups. Poly(ethylene glycol) (abbreviated as PEG), poly(acrylic acid) and polyanhydride polymers are used to modify QDs surface [44, 45]. PEG is now very common in biochemical procedures, allowing improvement of aqueous stability and reduction of aggregation and non-specific binding of QDs to cells and surfaces [46].

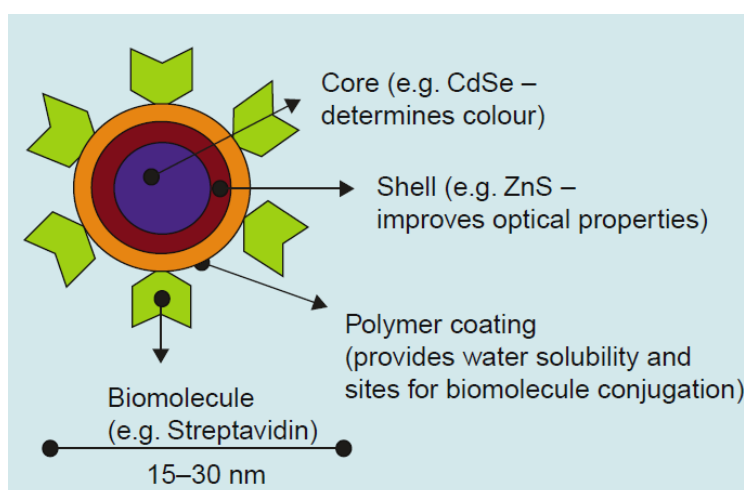


Figure 2.4: Schematic representation of a QDs structure, functionalisation and conjugation. Reproduced from Ref. [29].

Bioimaging Applications of Quantum Dots

It has been long recognised that QDs were suitable for bioimaging applications due to the following properties: good photostability, large Stokes shift, spectrally broad absorption cross-section (see Figure 2.3b), and narrow photoluminescence spectra. The large absorption cross-section enables simultaneous excitation of several types of QDs by one excitation source. QDs have relatively long-photoluminescence lifetime (> 10 ns) in comparison with endogenous organic molecules [47]. In addition, it has been

found that the QD two-photon cross-section is exceptionally high ($>10\,000$ GM) in comparison with that of organic fluorophores (1–300 GM). The QD technology is now mature and various types of QDs with choices of surface coating and surfaces functional groups are available commercially, with the industry leaders of the QD production being Evident Technologies (www.evidenttech.com) and Invitrogen Corporation (www.invitrogen.com).

QDs have been applied for imaging in live cells, biological tissues, live animals, biosensing and diagnostics [48]. Their applications as a molecular-specific probe in cancer imaging have been reported [49, 50]. Recently, Tang *et al.* [51] have developed ultrasmall water-soluble Ag_2S QDs for cancer cell targeting. Ag_2S QDs were conjugated with a cyclic peptide, arginine-glycine-aspartic acid-(D)phenylalanine-lysine (cRGDfk) for targeting the $\alpha_v\beta_3$ integrin receptor, which enabled successfully targeting and imaging of tumour, as shown in Figure 2.5. QDs are utilised as multicolour fluorescent labels for both *in vitro* and *in vivo* imaging [8,9]. Applications of QDs for ultrahigh-sensitivity imaging and tracking of neurotransmitters are worthy to note [10–12].

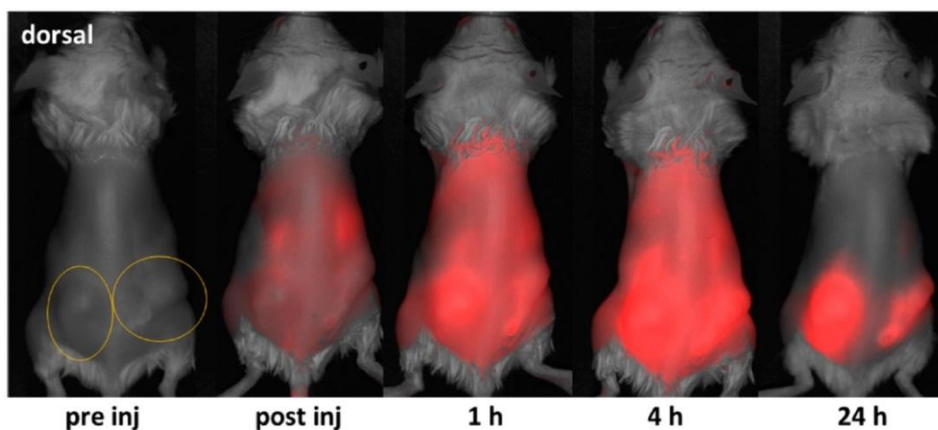


Figure 2.5: *In vivo* fluorescence imaging of cRGDfK- Ag_2S in 4T1luc tumor-bearing Balb/c mouse at different time points after the intravenous administration. Circles indicate bilateral subcutaneous tumor locations. Reproduced from Ref. [51].

2.2.2 Fluorescent Nanodiamonds

Nano-sized diamond particles known as single-digit nanodiamonds (NDs) were discovered accidentally in the USSR in 1963, but they were not publicised until late 1982 [52]. The inner core of detonation NDs comprises carbon atoms in the sp^3 -hybrid state,

with the size ranging from 1 to 10 nm and the outer layer containing carbon atoms in the sp^2 -hybrid state [53]. This hybrid layer is situated between the core and the outer layers, containing carbon atoms in both sp^3 and sp^2 hybridisations (see Figure 2.6a). The NDs structure is distorted owing to defects formed during the synthesis and purification. These defects can be impurities or intrinsic point defects, such as lattice vacancies. As an example, a nitrogen vacancy (N-V) point defect is formed by a vacancy stabilising near the nitrogen substitutional defect [54], as shown in Figure 2.6b. This centre is a colour centre, which render NDs fluorescent [55]. The negatively charged nitrogen-vacancy (NV^-) is most common defect and characterised by fluorescence featuring a narrow zero-phonon line at 637 nm [25, 56]. The neutral N-V centre (NV^0) is characterised by a zero-phonon line at 575 nm, as shown in Figure 2.6c. ND fluorescence is very photostable, with virtually unlimited emission upon continuous excitation, which is usually accomplished with a 532-nm laser [57]. In most cases NDs are non-cytotoxic, which has sparked a great deal of interest in the biological community [58, 59].

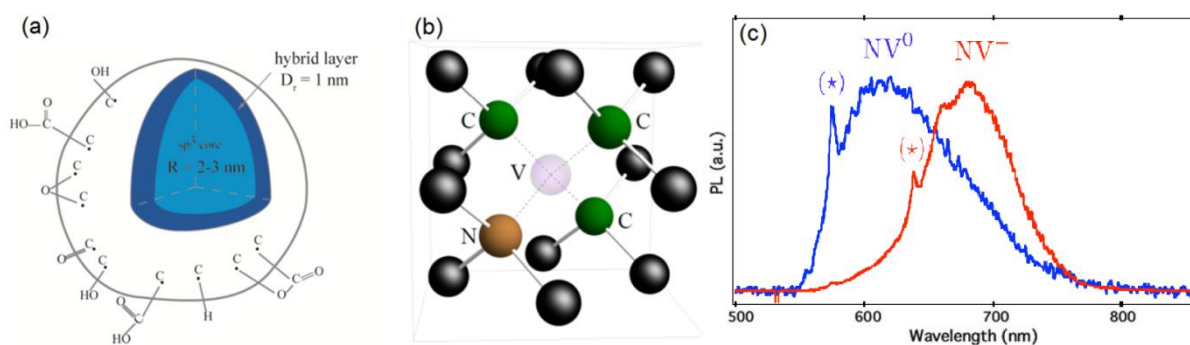


Figure 2.6: (a) Schematic representation of the nanodiamond structure. (b) Schematic of the nitrogen-vacancy centre and diamond lattice depicting the vacancy (transparent), the nearest neighbour carbon atoms to the vacancy (green), the substitutional nitrogen atom (brown), and the next-to-nearest carbon neighbours to the vacancy (black). (c) Photoluminescence spectra normalized to their respective maximum value of single NV^- [red (grey) curve] and NV^0 [blue (dark grey) curve] colour centres in nanodiamonds. The zero-phonon line (★symbols) of NV^- (respectively, NV^0) emission is located at 637 nm (respectively, 575 nm). Reproduced from Refs. [60] (a), [25] (b) and [26] (c).

Synthesis of Fluorescent Nanodiamonds

NDs are synthesised using high-pressure high-temperature (HPHT), detonation, chemical vapour deposition and high-energy ball milling [61, 62]. HPHT method usually yields diamond crystals of the size range from micrometres to millimetres, and these can be milled using a ball milling machine resulting in NDs with size as small as several nanometres [63]. The detonation method (Figure 2.7) is implemented by exploding trinitrotoluene (TNT) with hexogen ($C_3H_6N_6O_6$) in a closed metallic chamber in an inert atmosphere followed by disintegration of as-produced NDs [61]. The detonation method yields NDs as small as 5 nm. Fluorescence of detonation NDs is faint due to the profound surface effects on the colour-centres and largely distorted crystal lattice. In order to create colour-centre in synthetic nanodiamonds, which are usually non- or mildly-fluorescent, NDs are exposed to high-energy electron or light ion beams, and then annealed at temperature of $>750^{\circ}C$, activating the thermal diffusion of vacancies. As a result of the annealing, a vacancy is stabilised in an adjacent crystal node of the substitutional nitrogen defect, forming an N-V centre. Substitutional nitrogen defects can be converted to N-V centres by means of mild intensity electron exposure, the unconverted nitrogen defects can donate electrons to N-Vs producing negatively-charged NV^{-} [64].

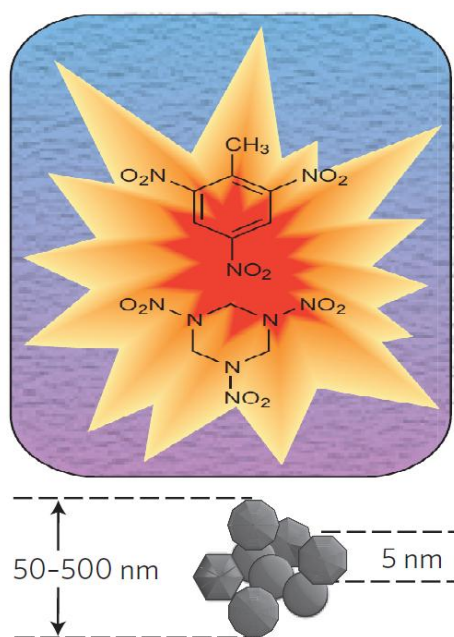


Figure 2.7: Detonation synthesis of nanodiamonds. Explosives with a negative oxygen balance are detonated in a closed metallic chamber in an atmosphere of N_2 , CO_2 and liquid or solid H_2O . Diamond-containing soot is collected from the bottom and the walls of the chamber at the completions of the process. Reproduced from Ref. [61].

Functionalisation and Conjugation of Fluorescent Nanodiamonds

As-produced NDs are poorly dispersible in water, since their surface is populated with a sp^2 hybridised carbon, graphite, which is especially profound in detonation NDs. Further processing is needed, aiming to remove the graphitic layer displaying a sp^3 hybridised surface [65]. This makes NDs water-mixable and stable due to the electrostatic surface charge repulsion. The zeta potential being a measure of the surface charge has been reported to have a high value of -45 mV in water [66]. However, even a small concentration of salt (10 mM NaCl) can cause aggregation of NDs [67]. This is explained by charge screening due to high-mobility positive ions of the salt, neutralising the ND surface and diminishing the repulsion force leading to aggregation [67]. Forming steric hindrance on the surface represents one approach to counter this problem, and this is typically realised by macromolecule functionalisation, such as proteins and polymers, making them also suitable for biomolecule targeting [68]. This functionalisation is realised by means of the following approaches: (i) adsorption, (ii) polymer coating, and (iii) covalent or high-bond linking. The use of a high-affinity linker, such as a streptavidin:biotin molecular pair, represents an example of (iii) approach. It was realised for example by binding biotin molecules to the polycrystalline diamond layers using anchoring hydroxyl groups by a popular EDC/NHS reaction. The success of this reaction was confirmed by binding fluorescent streptavidin to the biotinylated surface of nanodiamonds and fluorescence microscopy observation [69].

Bioimaging Application of Fluorescent Nanodiamonds

FND probes seemed attractive for biomedical applications owing to: (i) non-cytotoxicity, (ii) physical and chemical stability, (iii) small-size ranging from several nm to 100 nm, and (iv) surface moieties amiable for biofunctionalisation. It is known that carboxyl groups represent about 7% of the other surface moieties, as a result of the acid surface etching, and this makes NDs suitable for biofunctionalisation via covalent binding. The core inertness, large effective surface and large surface charge make them suitable protein purification, whereas the high quantum efficiency and absorption cross-section of N-V centres were attractive for fluorescent molecular probes.

Fu *et al.* [70] have demonstrated incubation of 35-nm FNDs together with HeLa cells cultured in Dulbecco's Modified Eagle's Medium at 37°C on a chamber slide. Most of the FNDs were found to form aggregates in the cell, while some of them were

detectable in the cytoplasm. Single FNDs were still observable. Mohan *et al.* [71] reported the long-term *in vivo* imaging of FNDs in worms *C. elegans*, investigating the FNDs interactions with living organisms. FNDs conjugated with biomolecules were observed entering intestinal cells, and was likely to occur via endocytosis, as shown in Figure 2.8. This observation was carried out by using a hybrid of epi-luminescence and differential interference contrast microscope. FNDs appeared stable, nontoxic, causing no detectable stress to the worms. This application showed the feasibility of applying FNDs for imaging in translucent biological systems.

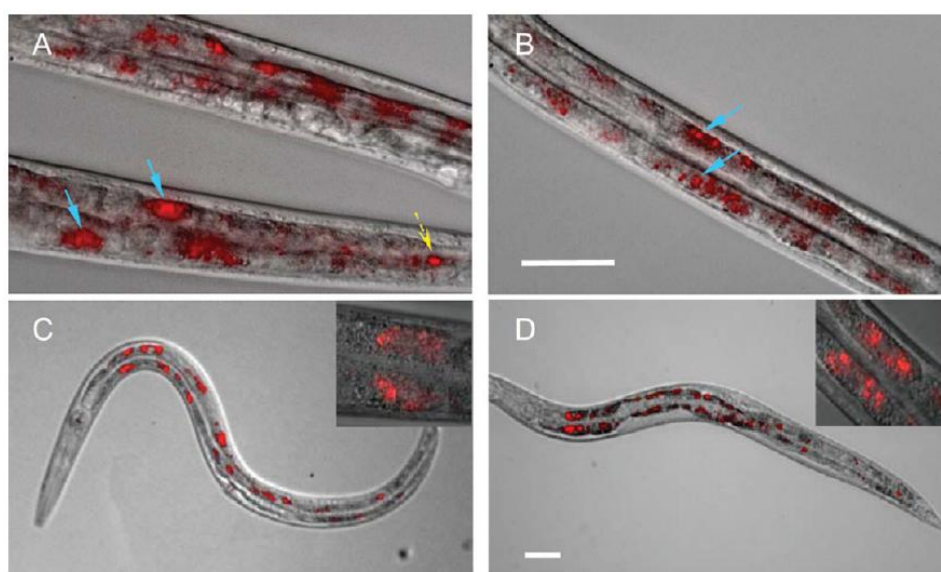


Figure 2.8: Epi-luminescence/differential interference contrast-merged images of *C. Elegans* worm fed with bioconjugated FNDs. (A, B) Worms fed with dextran-coated FNDs (A) and BSA-coated FNDs (B) for 3 h. FNDs can be seen to be localised within the intestinal cells (blue solid arrows) and a few stay in the lumen (yellow dash arrow). (C, D) The worms fed with dextran-coated (C) and BSA-coated (D) FNDs for 3 h were recovered to *E. coli* bacterial lawns for 1 h. In both cases, the FNDs staying in the lumen were excreted out, whereas the ones localized in the cells retained in organism. Insets: 100× magnified images of the FNDs within the intestinal cells. Anterior is left and dorsal is up in all the figures. Scale bars, 50 μm. Reproduced from Ref. [71].

2.2.3 Upconversion Nanoparticles

Upconversion nanoparticles (UCNPs) are relative new PL nanomaterials, which attract a great deal of interest of the scientific community with over six thousand papers

published over the last three years. They exhibit advantages crucial for biomedical imaging, especially, for single nanoparticle detection technique, including the exceptional upconversion properties and excellent photostability [72]. The mechanism of the UCNP photoexcitation is based on the absorption of two or more low-energy, infrared photons at wavelength 980 nm, which occurs as a result of the illumination with the low-intensity ($1 \times 10^3 \text{ W/cm}^2$) laser, relatively low in comparison with $I_{ex} \approx 10^6 \text{ W/cm}^2$ used in multiphoton microscopy [73]. UCNPs are characterised by long-photoluminescence lifetime ranging from 100 μs to several ms [74]. The mechanism of the UCNP photoexcitation involves several absorption and non-radiative energy-transfer steps. UCNPs represent an inorganic crystal matrix (fluoride or oxide) doped with two types of lanthanide ions, termed sensitizer and activator ions. Lanthanide ions feature the energy level structure of 4f and 5d shell electrons that have more than one metastable level and are able for upconversion, except for essentially two-level Yb^{3+} ion, which functions as a sensitizer. Yb^{3+} absorbs an IR photon undergoing a $^2\text{F}_{7/2} \rightarrow ^2\text{F}_{5/2}$ transition (see Figure 2.9a). The absorbed energy is transferred to the nearest ion Er^{3+} (or Tm^{3+}) ion via a non-radiative process. Er^{3+} ion functions as an activator. The network of the excited Yb-ions is formed over the lifetime of metastable Yb upon the continuous excitation with 980-nm photons, and this energy is stored and spread over the entire nanocrystal. There is a probability of the energy transfer from a sensitizer to an activator Er^{3+} (or Tm^{3+}) occurring non-radiatively at the rate of $\approx 1000 \text{ s}^{-1}$ for the case of $\text{Cs}_3\text{Lu}_2\text{Br}_9$ [75]. The activator, such as Er^{3+} in the $^4\text{I}_{11/2}$ metastable state, can coalesce with the proximal metastable Yb^{3+} ($^2\text{F}_{5/2}$) via a collective process known as the energy transfer upconversion (Figure 2.9b). As a result, the Er^{3+} ($^4\text{I}_{11/2}$) ions make a transition to the next energy-level ($^4\text{F}_{7/2}$) at the expense of the Yb^{3+} ($^2\text{F}_{5/2}$) \rightarrow Yb^{3+} ($^2\text{F}_{7/2}$). Then, the activator non-radiatively relaxes to ($^4\text{S}_{3/2}$) (refer to Figure 2.9a,b) from where it radiates in a green and red spectral bands, where the non-radiative phonon-assisted transition Er^{3+} ($^4\text{S}_{3/2}$) \rightarrow Er^{3+} ($^4\text{F}_{9/2}$) is also involved.

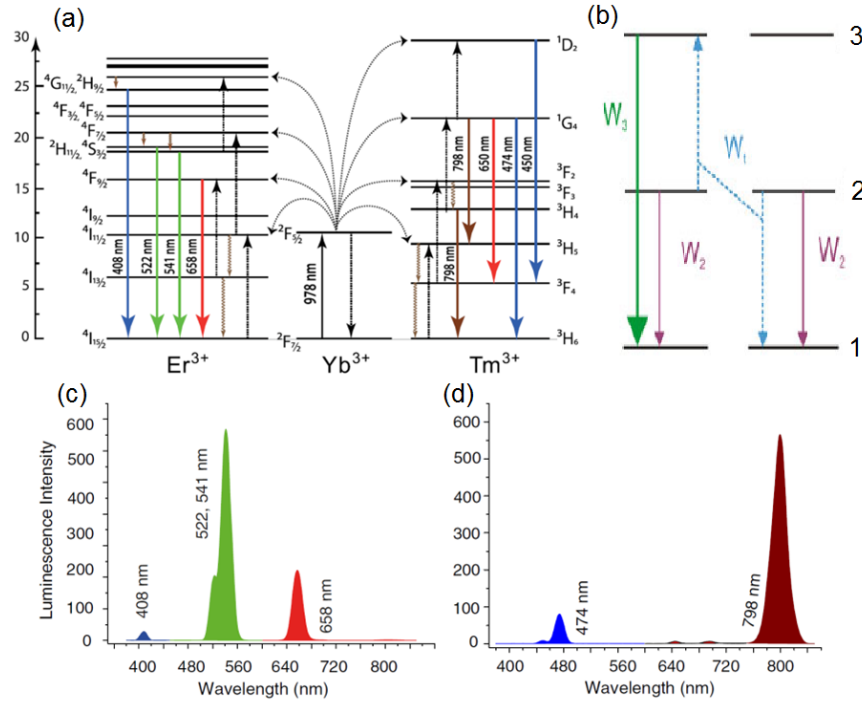


Figure 2.9: Two energy level diagrams: (a) detailed and (b) simplified of sensitiser Yb^{3+} ions with activator Er^{3+} or Tm^{3+} ions. Photoluminescence spectra of (c) $\text{NaYF}_4\text{:Yb:Er}$; and (d) $\text{NaYF}_4\text{:Yb:Tm}$ nanomaterials, with their corresponding transmission electron microscopy images Reproduced from Ref. [76].

The choice of the sensitiser in UCNP remains fixed to ytterbium, whereas the activators are varied in types of lanthanide ions and doping concentration. Tm^{3+} represents one of the most popular choices of the activator for animal imaging applications. It is excited at 980 nm and radiates at 800 nm and 474 nm, absorbing two or three sequential photons, respectively (Figure 2.9d). The conversion efficiency (η_{UP}) defined as power ratio of the emission/excitation [Watts/Watts] increases versus I_{ex} until it reaches the saturation at I_{ex} ranging from 10 to 1000 W/cm^2 [13, 77]. At the onset of the UCNP technology, η_{UP} was very small for the nanometre-sized nanoparticles, until a recent breakthrough in the synthesis procedures of UCNP [78, 79]. This synthesis has yielded much higher η_{UP} , which keeps growing and now reaching quite high values of $\eta_{UP} \approx 10\%$. My colleagues have recently demonstrated single UCNP visualisation by a naked eye by means of the grossly enhanced activator doping and $I_{ex} \approx 10^6 \text{ W/cm}^2$ [80].

Synthesis of Upconversion Nanoparticles

Several synthesis procedures for UCNPs have been developed, with the most successful reactions being thermal decomposition, co-precipitation and solvothermal reactions [81]. Thermal decomposition method involves two steps. In the first step, small-size cubic phase crystals are produced by mixing precursors and at 150°C these in oleic acid and octadecane. In the second step, the mixture was sealed and quickly heated to 320°C under argon condition to convert the sample to hexagonal phase characterised by the higher quantum efficiency. Nanocrystal powders in the granule size range of 10 – 300 nm were synthesised [82]. η_{UP} of UCNPs is measured by using an integrating sphere. The results of measurements of η_{UP} carried out at the home laboratory are shown in Figure 2.10a, b. They demonstrate the remarkable progress achieved in the photophysical properties of UCNP over several years. $\eta_{UP} = 0.03\%$ for 10-nm α -phase UCNPs, which were produced at the inception of this technology; $\eta_{UP} = 2\%$ for 60-nm β -phase UCNPs [83].

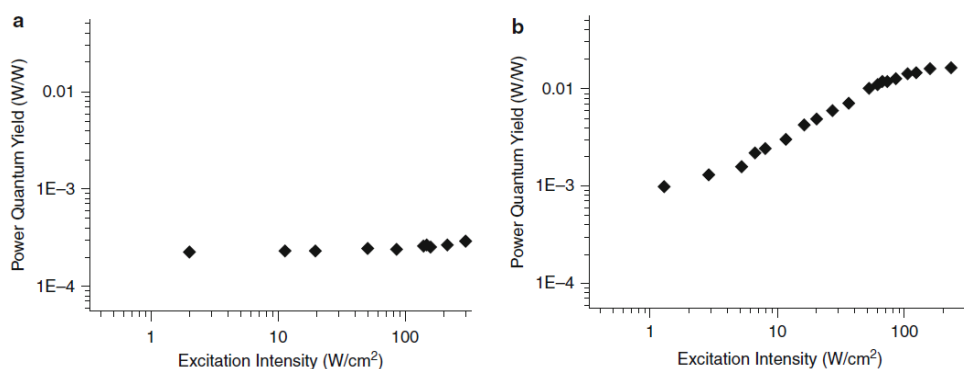


Figure 2.10: Log-log plots of the conversion efficiency η_{UP} of (a) α - and (b) β - phase UCNPs of the respective mean diameters, 10 nm and 60 nm. Reproduced from Ref. [83].

Functionalisation of Upconversion Nanoparticles

UCNPs produced by thermal decomposition are hydrophobic due to the oleic acid remaining on the surface. Surface-modification is required to render UCNPs hydrophilic. The displacement of oleic groups with the other functional groups such as citric [73] and mercaptopropionic [84] has been demonstrated, but this resulted in the NP limited colloidal stability near pH 7. Coating UCNPs with silica represents a proven universal approach to counter the poor hydrophobicity [85, 86]. Capping the UCNP

surface with amphiphilic polymer followed by this polymer functionalisation and covalent binding of biomolecules was promising and remains to be used in reported procedures [87].

Bioimaging Applications of Upconversion Nanoparticles

UCNPs are very attractive as PL molecular probes, because of the following reasons: (i) their characteristic excitation at 980 nm, ‘anti-Stokes’ large-spectral-shift emission mode allows effective suppression of the background signal due to biological tissue autofluorescence, since the autofluorescence is considerably diminished in this spectral range, and spectral filtering is efficient. Imaging of UCNPs on the background of human skin tissue autofluorescence has been demonstrated, exhibiting high contrast, with signal background level only twice exceeding the noise level of EMCCD camera [76]. (ii) Excitation and emission of UCNP doped with Tm are at 978 and 800 nm, respectively, falling into the biological tissue transparency window (see Figure 2.11). The absorption and scattering of haemoglobin and water are low in this window, which allow centimetre-deep penetration of near-infrared excitation and emission light. (iii) The photoluminescence lifetime of UCNP τ_{UP} is long, measured in terms of sub-milliseconds, which enables complete suppression of the light scatter and autofluorescence by employing the time-gated detection mode, and will be described in Chapter 6 [88].

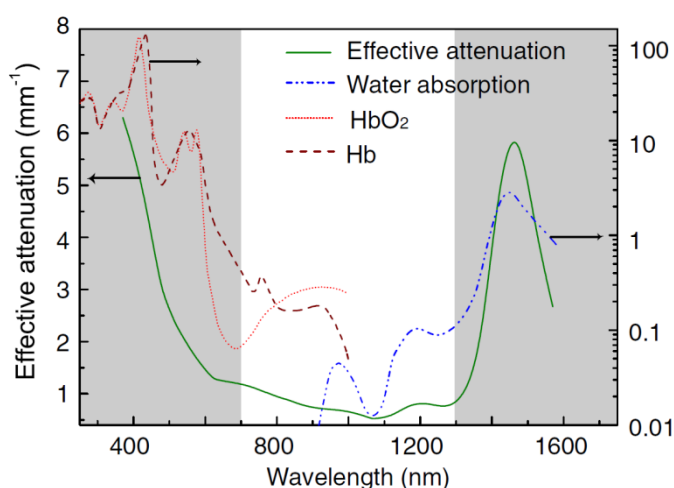


Figure 2.11: (a) Effective attenuation of human skin (solid green line) predominantly determined by water (H₂O, blue “- - -” line), haemoglobin (Hb, brown “- -” line), oxy-hemoglobin (HbO₂, red solid “-” line), in addition to the scattering effects. The

definition of the biological tissue transparency window varies with the most common wavelength boundaries 700 – 1300 nm (clear window among the gray-shaded area). Reproduced from [76].

UCNPs have been applied for optical imaging in tissues [83], skin [76], cells [89-91] and small-animals [89, 92, 93]. Grebenik *et al.* have demonstrated UCNP-assisted targeting breast cancer lesions, which could be useful for the detection of early-stage breast cancer. Antibodies raised against the human epidermal growth factor (HER2/neu) receptors overexpressed in the targeted type of cancer were coupled to the UCNPs by using a high-affinity protein pair barnase:barstar. This enabled binding to the HER2/neu receptors in human breast adenocarcinoma cells SK-BR-3 (See Figure 2.12a,b). Photoluminescence imaging under 978-nm excitation showed the immobilisation of UCNP-Bs:Bn-antibody biohybrid nanostructures on the SK-BR-3 cells with a 10-fold higher signal compared to the control CHO-K1 cells, as shown in Figure 2.12c,d. For imaging UCNPs in small animals, Nyk *et al.* [89] have reported the use of UCNP for *in vitro* and *in vivo* imaging. This study involved the injection of UCNPs into Balb-c mice. From the imaging, UCNPs signals in the liver and the spleen can be clearly visualised in the photoluminescence images of animals (Figure 2.13), which indicates a high uptake of UCNPs by these organs.

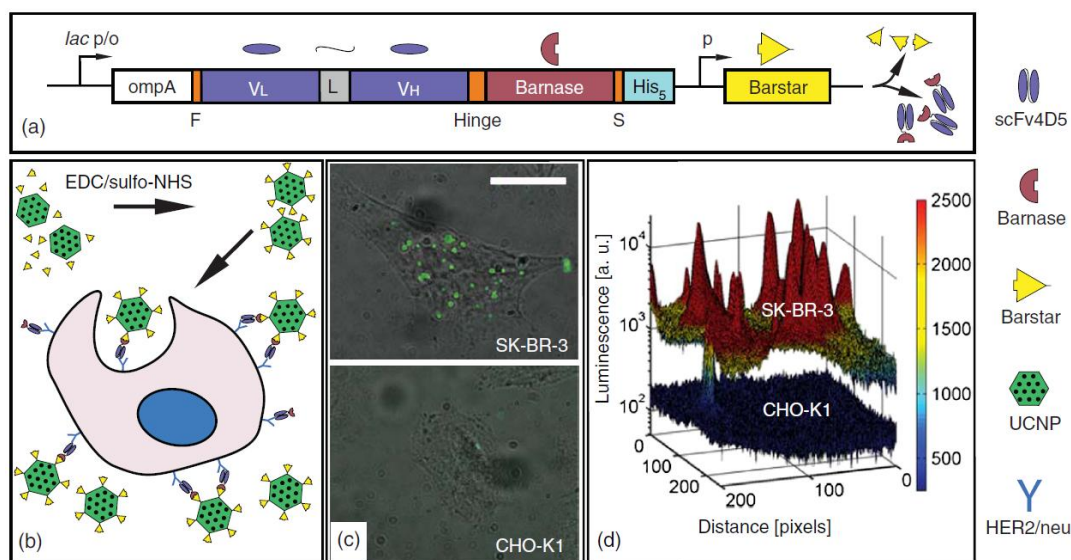


Figure 2.12: (a) Cell labeling with UCNP-Bs:Bn- antibody biohybrid nanostructures. (a) Targeting vector, Bn-scFv4D5 gene construction. (b) The concept of the cell labelling with self-assembled UCNP biohybrid nanostructures UCNPBs:Bn-antibody.

(c) Epi-luminescence imaging of the HER2/neu overexpressing SK-BR-3 cells labeled with UCNPBs:Bn-antibody. Scale bar, 20 μm . (d) Three-dimensional surface plot of the photoluminescence signal acquired from the CHO-K1 and SK-BR-3 cells incubated with UCNPBs:Bn-antibody. Reproduced from Ref. [94].

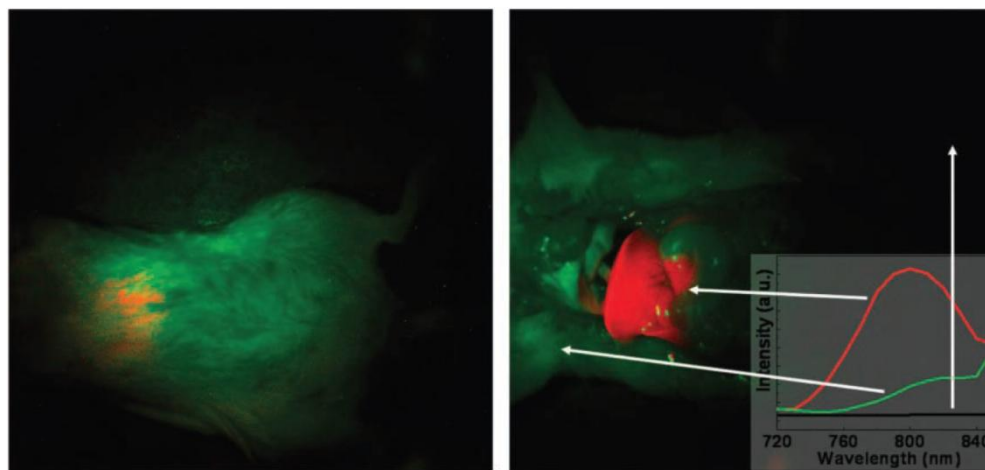


Figure 2.13: Whole body images of a mouse injected with UCNPs; intact mouse (left), same mouse after dissection (right). The red colour indicates the emission from UCNPs, green and black colours show the background, as indicated by arrows. The inset presents the photoluminescence spectra corresponding to the spectrally unmixed components of the multispectral image. Reproduced from Ref. [89].

2.4 Limitation of the Existing Photoluminescent Nanoparticle Probes

2.4.1 Limitations of Quantum Dots

The key shortfalls of QDs in the context of biomedical imaging applications are photoblinking and cytotoxicity. The phenomenon of fluorescence intermittency, also known as photoblinking, is manifested by random switching between “on” (emitting) and “off” (quiescent) states of the single two-level quantum system under continuous excitation. Photoblinking remains of the unresolved mystery of modern physics. The mechanisms of photoblinking fall beyond the scope of this chapter and this thesis, and we resort to discuss this phenomenon only from a utilitarian point of view. It therefore suffices to state that photoblinking relates to the competition between the radiative and

non-radiative relaxation pathways [22]. Photoblinking is random, and in most cases cannot be easily described in terms of the meantime of the statistical probability. In one measurement run, the emitter blinks often, while in another measurement run, the emitter state is either “on”, or “off” for the entire duration of the experiment. In relation to QDs, a naïve observer can state that QDs photobleach, which in fact indicates their trapping in the dark “off”, which is still reversible. Photoblinking is disruptive in the course of a fluorescence imaging session, and unwanted in, for example, single molecule tracking experiments. This problem is ameliorated by creating a thick shell on the QDs surface [95], attaching functional groups on the QDs surface [96, 97].

The cytotoxicity of QDs presents another major issue, which will almost certainly preclude approval of this nanomaterial in clinical applications. The cytotoxicity of QDs is caused by the presence of cadmium (Cd) and Tellurium (Te) elements in the core composition of the most common commercially-available quantum dots. These toxic heavy metal ions could be released in the cell or biological tissue, exerting toxic stress to the living biological system. In cell experiments, the leaching out of the toxic atoms in the intracellular space induced the cell apoptosis [98, 99]. Recently, Bradburne *et al.* [100] conducted a comprehensive comparative study of *in vitro* cellular cytotoxicity of CdSe/ZnS core/shell materials. They found that the cytotoxicity was due to several factors including QD ligand structure, QD dose (concentration and time of incubation during delivery), and the method of the facilitated QD delivery. Several approaches have been developed to overcome this problem. These include (i) employing surface capping [101], and (ii) replacing the core from toxic element to non-toxic element [102]. The other studies pointed to the toxicity mechanisms related to the cell internalisation pathways. The toxicity was reduced by using surface functionalisation, which slowed down the cellular uptake [103].

2.4.2 Limitations of Fluorescent Nanodiamonds

The main limitation of FNDs relates to the optical contrast achievable on the background of cell and tissue autofluorescence. Referring to our earlier discussion of the nitrogen-vacancy colour centre (N-V), FNDs are characterised by the broad excitation spectral band situated in visible spectral range (see Figure 2.6) and broad emission in the far-red extending to near-infrared. The most efficient excitation of FNDs takes place in the green spectral band, typically realised by 532-nm laser. This

excitation elicits significant autofluorescence response in the biological sample under study, which leads to the reduction of the optical contrast measured as a ratio S_{FND}/B_{af} , S_{FND} – fluorescence signal from the FND, B_{af} – background signal due to the autofluorescence. S_{FND} depends on the number of N-V centres that exist in the particle, which in turn depend on the nanocrystal size. The numbers of N-V centres are roughly estimated to be $N \approx 100$ in the 140-nm ND crystal. This leads to the emission cross-section per one fluorescent ND: $N\eta\sigma_a$, and is evaluated to be $100 \times 0.7 \times (3 \times 10^{-17}) \text{ cm}^2 \approx 2 \times 10^{-15} \text{ cm}^2$ [104], which is favourably compared with the golden standard of QD (10^{-15} cm^2). In case of the smaller-size fluorescent ND, this value is diminished drastically, because of the much reduced implantable number of the colour-centres N , and diminished $\eta < 0.2$, as evaluated recently [105, 106]. This results in the rather dim appearance of fluorescent NDs in cells and tissues, which limits their application scope to imaging of >100 -nm fluorescent NDs in cells or translucent organisms, such as *C. elegans* worms. It is important to point to the high cost of the fluorescent ND production, which requires high-energy electron or light-ion irradiation, implying the use of expensive specialised equipment. Also, it is challenging to produce NDs in large scale, despite several promising developments in this direction [107].

2.4.3 Limitations of Upconversion Nanoparticles

The main consideration of the UCNP feasibility of optical biomedical imaging applications relates to its dependence of the conversion efficiency measured in terms of η_{UP} on the excitation intensity I_{ex} . This dependence is constant in most quantum emitters under the unsaturated condition. In contrast $\eta_{UP} \propto I_{ex}^n$ in UCNP, where n varies from 1 in the unsaturated regime, and drops to ≤ 1 , when I_{ex} reaches the saturation value, which is measured in the range of $10 - 100 \text{ W/cm}^2$. This reads that the optimal photoluminescence properties of UCNP are attained only when I_{ex} reaches and exceeds the saturation value, i.e. $I_{ex} > 10 - 100 \text{ W/cm}^2$. [108]. These values are readily achievable at the tight focal volume in e.g. confocal microscopy configuration, and achievable under loose focussing conditions. Indeed, the first spectacular demonstrations of UCNP imaging in cells were performed in the laser-scanning microscopy. Although wide-field imaging and microscopy is still possible and employed in a number of applications [13], one needs to be mindful about the laser

safety limitations. According to the US laser safety standards, the maximum permissible laser intensity at 980 nm is 730 W/cm². Simple calculations show that it is not easy to achieve in wide-field microscopy, which makes this imaging modality suboptimal. At the same time, laser-scanning microscopy imposes another limitation related to the necessity to dwell on each pixel in access of $\approx 5\tau_{UP}$, which makes the image acquisition slow. This I_{ex} constrain imposes severe limitation of animal imaging, where focussing at depth in highly scattering biological tissue is impossible over the depth > 1 mm [109]. The latest studies demonstrated an approach to increase the UCNP action cross-section by forming fluorescent dye antennas on the surface of UCNP, allowing harvesting infrared light efficiently and non-radiatively passing the energy to UCNP. η_{UP} was demonstrated to be increased by 3300 times [110]. This approach, however, has to demonstrate its feasibility and its principle excitation mechanism has to be understood before it can be used in small animal imaging.

Above discussion explain the limitations of QD, FND and UCNP which constrain their application. Large-scale production of the considered PL NPs remains challenging due to the NP production high cost and complexity. In the next section, we will introduce alternative PL NPs nanorubies, which present a lucrative alternative to the existing PL nanomaterials in several practical and photophysical aspects.

2.5 Nanoruby

Ruby crystal has been employed as a laser medium by T. H. Maiman, who invented the first laser in 1960 [111]. Reduction of the ruby dimensionality to the nanometre-size range confers several interesting and useful properties of the resultant nanoparticles, which are termed nanorubies. As it can be inferred from the ruby bulk properties, nanorubies possess excellent photostability, long-photoluminescence lifetime, and biocompatibility, which make them suitable for bioimaging applications [20]. Large-scale inexpensive production of nanorubies appears possible and will be addressed in this thesis. As a result of this work, several useful chemical and colloidal properties of nanorubies are also identified, explored and demonstrated in imaging applications.

2.5.1 Composition and Structure

Ruby is alpha-alumina ($\alpha\text{-Al}_2\text{O}_3$) crystal doped with Cr^{3+} of the low molar concentration. The amount of Cr_2O_3 doping varies from 0.1 to 1 wt %. Cr^{3+} ions are excited in broad UV/blue and green spectral bands, which corresponds to the Cr^{3+} ion transition from the $^4\text{A}_2$ ground state to $^4\text{F}_1$ and $^4\text{F}_2$ states, respectively. The ion makes a rapid transition to the ^2E metastable state, which consists of two sublevels, $2\bar{\text{A}}$ and $\bar{\text{E}}$. The transition from these sublevels to the ground state is accompanied by emission of photoluminescence comprising two sharp zero-phonon emission lines at 694.3 and 692.9 nm known as R_1 and R_2 lines. The energy diagram of the emission process is shown in Figure 2.14. The photoluminescence lifetime at room-temperature is in the order of 4 ms for a ruby crystal with the Cr^{3+} doping <1%, and the quantum efficiency being of the order of 0.9 [112].

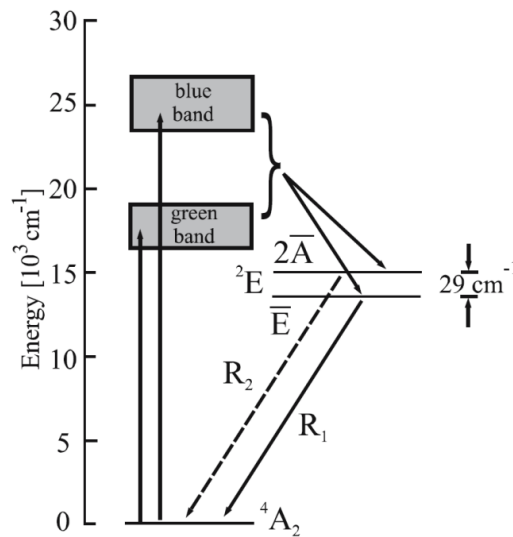


Figure 2.14: A simplified energy level diagram of a ruby crystal. Reproduced from Ref. [113].

The ruby crystal host is Al_2O_3 crystal in its alpha phase (corundum phase) formed by Al^{3+} and O^{2-} ions in a rhombohedral (trigonal) system as shown in Figure 2.15 [114]. Aluminum atoms occupy two-thirds of the octahedral interstices in the hexagonal close packed array of oxygen atoms [115]. Each aluminum ion is surrounded by six oxygens in a distorted octahedron [116]. The Cr^{3+} site is displaced 0.03 Angstroms from the Al^{3+} site [117]. The displacement is along the c-axis towards the

nearest cation (see Figure 2.15). The ruby crystal has excellent physical properties, such as high melting temperature, chemical stability, high refractive index and high hardness. Therefore, it can be used in many applications, such as high-temperature components, catalyst substrates, biomedical implants, abrasive materials, and bearings [115].

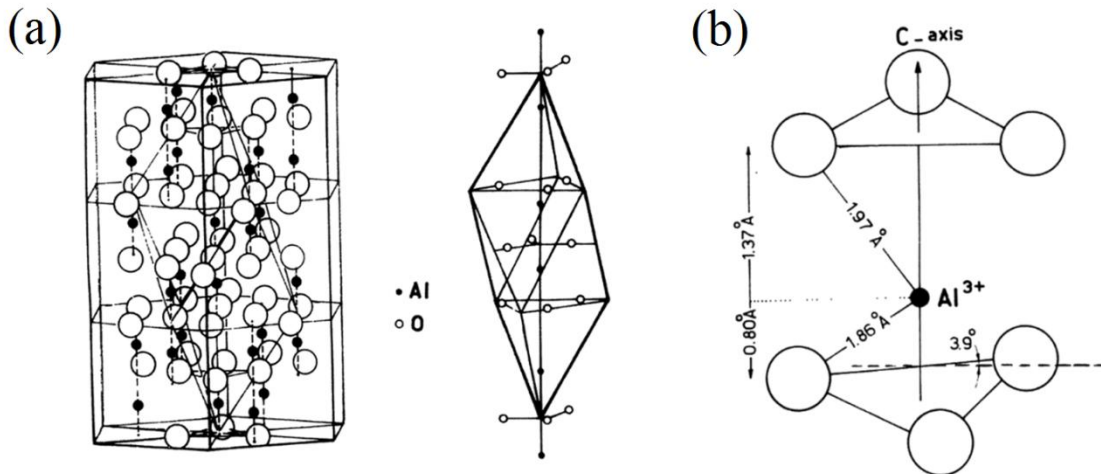


Figure 2.15: (a) The structure of a ruby crystal. Open circle mark oxygen ions, whereas solid circles mark aluminum ions. (b) Coordinations of the Al atoms in the ruby crystal structure. Reproduced from Ref. [114].

2.5.2 Nanoruby Production Method

A number of methods have been introduced for production nanorubies or its host nanomaterial (nanoalumina) [118-123], including chemical, ball-milling, and laser ablation methods. In this section, these methods will be explained in relation to their experimental procedures and results.

Chemical Methods

This production approach commonly makes use transformation of various alumina phases poorly controlled in the chemistry synthesis processes to the required alpha-phase via temperature treatment. Alumina has more than 15 crystallographic phases with the most stable structure being alpha-phase alumina (α -Al₂O₃) [124]. Gamma-phase alumina (γ -Al₂O₃) is formed at low temperatures, and is transform to the alpha-phase in the sequence of gamma→delta→theta→alpha alumina with increasing temperatures. α -Al₂O₃ can be obtained at the temperature above 1200°C. Figure 2.16

shows the transformation of aluminium hydroxides and oxohydroxides, such as diaspore, gibbsite, boehmite and bayerite to α -phase through the temperature treatment.

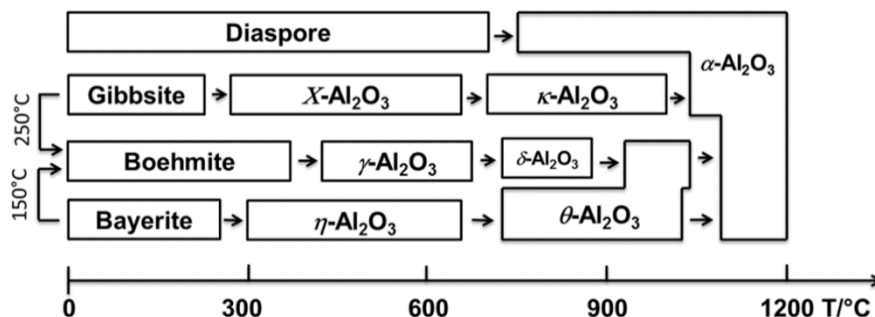


Figure 2.16: A schematic diagram of the temperature transformation of hydroxides or oxyhydroxides to α - Al_2O_3 via the formation of transitional alumina phase. Reproduced from Ref. [125].

Patra *et al.* [126] have introduced a sol-emulsion-gel method to produce $\text{Al}_2\text{O}_3:\text{Cr}^{3+}$, which has a good control over the particle nucleation, growth and agglomeration. In their method, $\text{Al}(\text{NO}_3)_3 \cdot 9\text{H}_2\text{O}$ was precipitated by adding ammonia solution. The sol obtained by using acetic acid was heated at 70–80°C, followed by an addition of chromium acetate. Cyclohexane and sorbitan monooleate was used as a solvent to obtain emulsified sol droplets. Sol droplets were converted to gel particles by adding organic amine. The obtained washed and dried products were calcinated at 900°C and 1025°C to yield α - Al_2O_3 . However, the resultant sample was found agglomerated, as shown in Figure 2.17, with particles size was estimated as 15–30 nm, as found from the XRD spectra. Zeng *et al.* [127] have reported the production of alumina nano-powder using a sol-gel method. Boehmite (γ - AlOOH) sol was prepared from $\text{AlCl}_3 \cdot 6\text{H}_2\text{O}$ raw material through a hydrolysis process. The reaction between AlCl_3 and ammonia solution was carefully controlled to get high quality boehmite sol. The prepared boehmite calcinated at 500°C to form γ - Al_2O_3 nano-powder, with the granule average diameter of 6 nm, followed by calcination at 1100°C to get α - Al_2O_3 nano-powder, with the mean diameter of 30 nm. In 2011, Loan *et al.* [128] have demonstrated the use of a sol-gel method to produce $\text{Al}_2\text{O}_3:\text{Cr}^{3+}$ powders without emulsion. The samples were prepared from aluminium nitrate $\text{Al}(\text{NO}_3)_3 \cdot 9\text{H}_2\text{O}$, chrome nitrate $\text{Cr}(\text{NO}_3)_3 \cdot 9\text{H}_2\text{O}$. The gel was obtained by an addition of citric acid. Then xerogel was formed by heating the gel at 120°C, followed by annealing at 650–1300°C for 5 hours.

Exclusively α -phase sample was obtained after a heat-treatment at 1300°C. The size of γ - Al_2O_3 phase sample after annealed at 900°C was measured as 6–7 nm, although the size of as-produced α - Al_2O_3 particles was not reported.

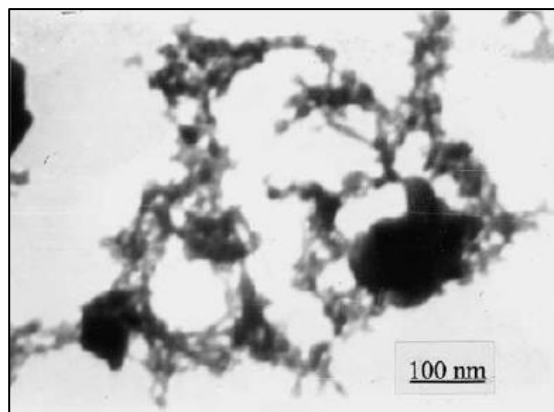


Figure 2.17: TEM image of the 0.2 mol% Cr sample sintered at 1025°C. Reproduced from Ref. [126].

A low-temperature combustion method is simpler compared to the sol-gel method. Mi *et al.* [129] have employed this method to prepare $\text{Cr}^{3+}:\text{Al}_2\text{O}_3$ nano-powders. Precursor materials $\text{Al}(\text{NO}_3)_3 \cdot 9\text{H}_2\text{O}$, $\text{Cr}(\text{NO}_3)_3 \cdot 9\text{H}_2\text{O}$, and urea were thoroughly milled until a cream-like paste formed. Glucose was added as a dispersive agent to avoid agglomeration. Then the sample was fired at 600°C until turned into brown powders. Finally, the powder was fired by muffle furnace at 700°C, 800°C, 900°C, 1000°C, 1100°C and 1200°C to get α -phase crystallites. This method produced well-dispersed spherical particles, with the average size of 20 – 35 nm. The comparison between the sample with and without using glucose is shown in Figure 2.18. The glucose is proven to reduce the agglomeration. Kakooei *et al.* [130] have employed the same method to synthesise chromium-doped alumina using sucrose instead of glucose. They obtained particles, with the average crystalline size of 35 nm. Janez *et al.* [131] have reported the similar method without adding glucose/sucrose to produce chromium-doped aluminate nano-powder. After a sintering process to transform the sample from γ - Al_2O_3 to α - Al_2O_3 , the particle size increased from 20–50 nm to 500 nm. It can be therefore inferred that the adding glucose/sucrose gives a significant effect on the agglomeration prevention.

Tok *et al.* [132] have employed a flame spray pyrolysis method to synthesise agglomerate-free nano-sized Al_2O_3 particles, with the size range of 5 – 30 nm. Anhydrous AlCl_3 powders were injected into a flame gun using a heating chamber at 300°C by means of nitrogen gas and it was directly sprayed into the collection chamber. Al_2O_3 NPs calcinated at 1100°C for 2 h using a heating rate of $10^\circ\text{C}.\text{min}^{-1}$. The produced sample is shown in Figure 2.19.

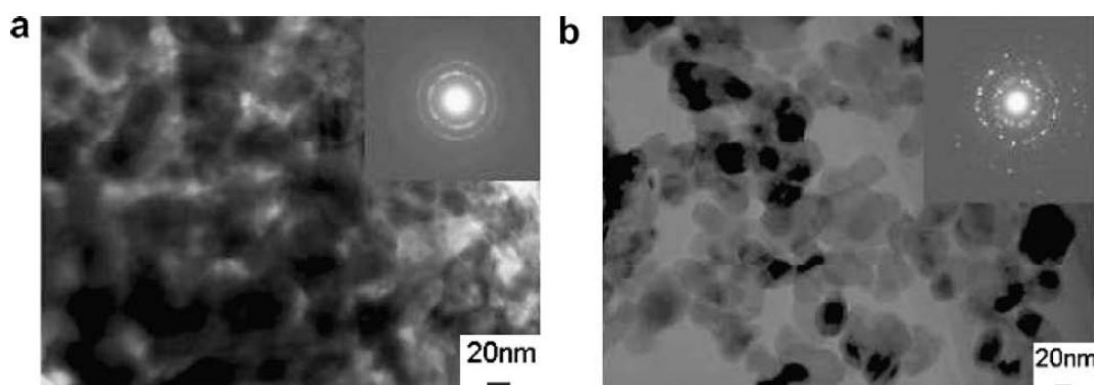


Figure 2.18: TEM images of the sample without (a) and with (b) using glucose. Insets are electron diffraction pattern of the sample. Reproduced from Ref. [129].

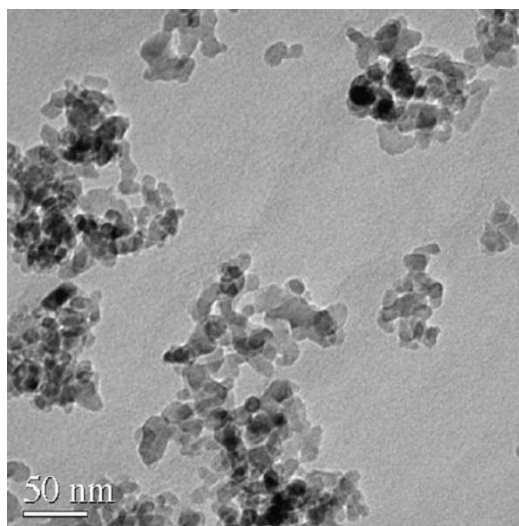


Figure 2.19: TEM image of as-sprayed alumina NPs. Reproduced from Ref. [132].

Laser Ablation

Laser ablation is a method capable to produced nanoparticles, with outstanding purity compared to the other manufacturing routes [133]. There have been numerous works on

the fabrication of metal NPs using laser ablation, such as gold, silver and platinum [134-136]. Laser ablation of crystalline materials require the higher laser intensity around $5 \times 10^{20} \text{ W/m}^2$ due to the transparent properties of the crystals, which leads to the lower laser absorption by the crystal [137, 138]. Our group pioneered the nanoruby production by using femtosecond laser ablation [20]. In this work, the sample was held above a quartz cuvette, which was filled with ultra-pure deionised water. The ablated sample was collected straight away after the ablation in the water. The experimental setup is shown in Figure 2.20a. The ablation was performed in the air due to the higher efficiency in terms of the mass of NPs generated per hour. Using this method, highly stable nanorubies, with the mean size 17 nm were produced (Figure 2.20b).

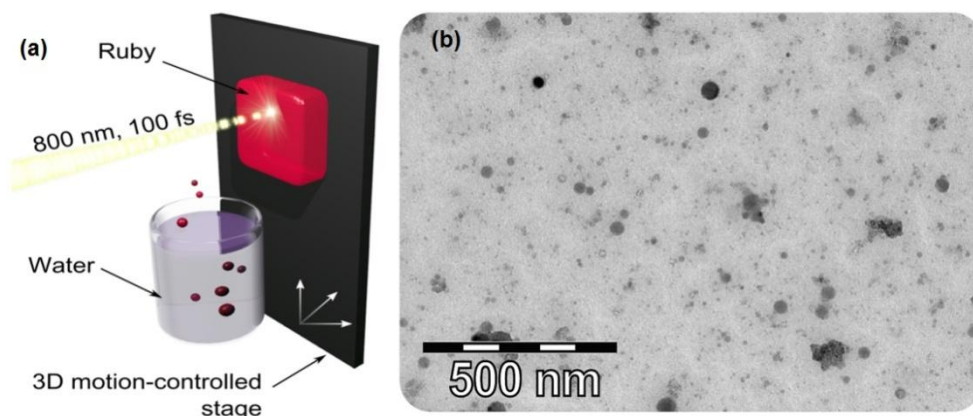


Figure 2.20: (a) Experimental setup used to perform the femtosecond laser ablation of a bulk ruby sample. The ablated material was collected in water (b) TEM image of nanorubies produced by the femtosecond laser ablation. Reproduced from Ref. [20].

Laser ablation of alumina crystals had been reported prior to the demonstration of the laser ablation production of nanorubies [139]. A bulk $\alpha\text{-Al}_2\text{O}_3$ target was immersed in distilled water, and a 1064-nm nanosecond laser was employed to ablate the target. Ablated NPs were spherical in shape, and the average particle size was ranged from 12 to 18 nm depending on the laser power and water levels. Yatsui *et al.* [140] have demonstrate the production of ultrafine alumina powders with the mean diameter of 11.8 nm by using laser ablation technique. Nd :YAG laser (1064 nm, 7 ns) was used with filter-target distance of 6 cm. The ablation was carried out in oxygen flow at the rate 11min^{-1} with pressure 200 Torr. The laser fluence at the target was 16 J/cm^2 . Piriya Wong *et al.* [141] have demonstrated the production of alumina NPs using

laser ablation at the energies of 1, 3 and 5 J, where the target was immersed in deionised water. The particle mean size was increased with the increasing of the laser energy. Most of the as-produced NPs had spherical shape with the size less than 100 nm. Sajti *et al.* [133] have reported the ablation efficiency and influence of the laser parameters on the material removal rate by a nanosecond laser irradiation of α -Al₂O₃, which was studied in gas and liquid phases. The material removal rate of the laser ablation in the air was 12 ng/pulse, using 4.6-mJ pulse energy at a 4-kHz repetition rate, whereas 88 ng/pulse in the water flow. Khan *et al.* [142] have demonstrated continuous-wave laser ablation by using a 1070-nm fibre laser source with corundum (α -Al₂O₃) target submerged in deionised water. It was found that the average size of spherical Al₂O₃ NPs was in the range of 17 to 29 nm (Figure 2.21), and this size was increased with the increase of the laser power and laser exposure time. The ablated NPs were dominated by γ -Al₂O₃ with a small amount of α -Al₂O₃. It can be concluded that the laser ablation is able to produce alumina/ruby NPs of spherical shape and good purity. However, this method produces Al₂O₃ NPs in α - and γ -phase. The production is expensive, as it requires the use of high-cost powerful nanosecond or femtosecond laser source, and the yield is typically low.

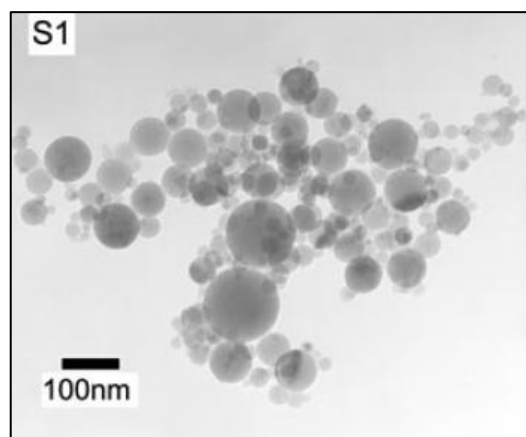


Figure 2.21: A TEM micrograph of alumina NPs generated by the continuous-wave laser ablation. Reproduced from [142].

Milling Method

Milling method is classified as the top-down approach, which can be applied for large-scale nanomaterial production [143-145]. From the best of our knowledge, no work has been reported on the usage of this method to produce nanorubies. However, milling

method has been widely used to mill coarse alumina, which has similar physical property to ruby crystals [146-152]. Karagedov *et al.* have demonstrated alpha alumina milling using planetary ball milling with steel bowls/milling balls [146]. “Grinding catalyst” also been used, but no specific detail of this material has been given. After the milling process, the milled powder was boiled in 3 – 5% HCl to remove “grinding catalyst” and to purify the sample from contaminations caused by the steel milling balls/bowl wear. Nanoalumina with the mean size ranging from 18 nm to 40 nm was obtained by using this technique (see Figure 2.22). Tonejc *et al.* [153] have employed tungsten carbide-lined ball mill filled with a 10-mm tungsten carbide balls to mill boehmite (aluminium oxide hydroxide) powder. It was reported that the milling process induced the transformation from boehmite to corundum (α -Al₂O₃) phase similar to temperature treatment. It was also mentioned that the milling process yielded the smaller α -Al₂O₃ grain size compared to that of the temperature treatment. We demonstrate the application of the milling approach to produce nanorubies, which will be reported in the next chapter.

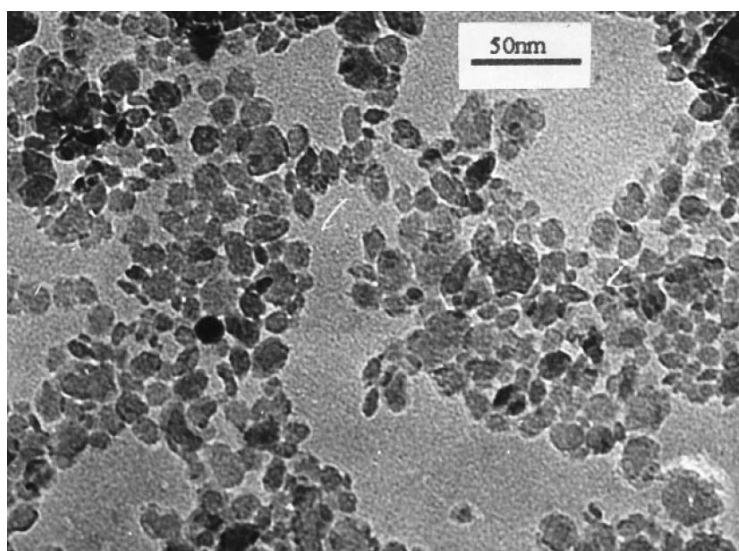


Figure 2.22: A TEM image of the sample milled for 20 min at 40×g, followed by a deaggregation process. Reproduced from Ref. [154].

2.5.3 Nanoruby Properties

Optical Property

The optical properties of nanoruby depend on the crystal phase and Cr^{3+} content. Mi *et al.* [129] have examined $\text{Al}_2\text{O}_3:\text{Cr}^{3+}$ nano-powders versus temperature and Cr^{3+} doping. The highest photoluminescence intensity was obtained after the sample was treated at 1200°C , as shown in Figure 2.23a. The optimum Cr^{3+} doping for the sample was at the level of 1.0 wt%. The photoluminescence intensity was decreased, when the Cr^{3+} ion concentration was increased to > 1.0 wt %, as shown in Figure 2.23b. This occurred due to Cr^{3+} ions getting too close at the high Cr^{3+} concentration, resulting in the concentration quenching [129]. The distance between Cr^{3+} ions should be larger than the critical distance, R_c to avoid the concentration quenching. R_c can be calculated based on Dexter's theory:

$$R_c = 2[3V/4\pi x_c Z]^{1/3}, \quad (2.1)$$

where V is the volume of the unit cell, X_c is a theoretical concentration of the doping ions, and Z is the number of host cation in the unit cell [155].

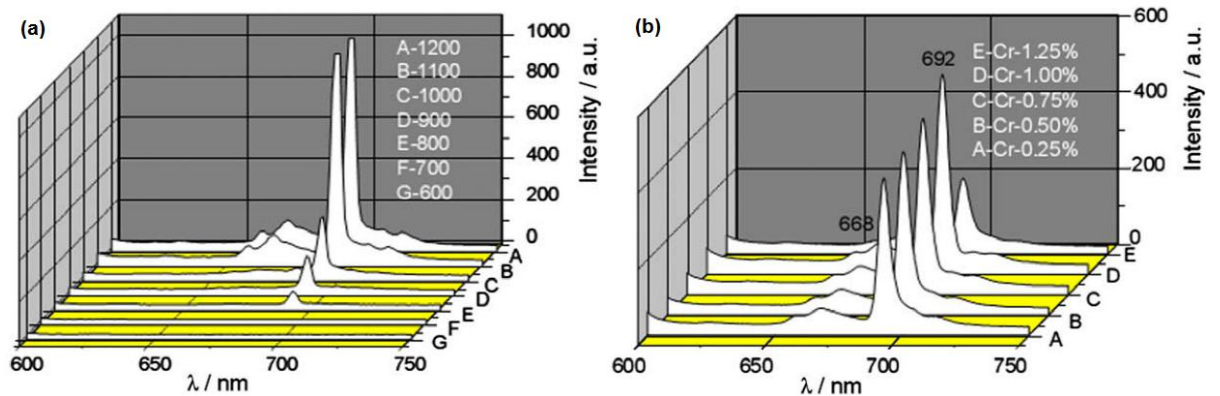


Figure 2.23: The effect of (a) temperature (A to G different annealing temperature in $^\circ\text{C}$), and (b) Cr^{3+} concentration (A to E different Cr^{3+} concentration) on the photoluminescence properties. Reproduced from Ref. [124].

Cheng *et al.* [124] have reported the effect of the annealing temperature to the $\text{Al}_2\text{O}_3:\text{Cr}^{3+}$ nanotubes. The sample annealed at the temperature less than 1000°C had broad and low photoluminescence intensity, as shown in Figure 2.24a. The sample annealed at 1200°C exhibited high photoluminescence intensity, with two clearly resolvable sharp peaks centred at 694.3 (R_1) and 692.9 (R_2). This result indicates that the characteristic R_1 , R_2 doublet line transitions of ruby can only be observed at the high crystalline phase $\alpha\text{-Al}_2\text{O}_3$ nanotubes calcinated at the temperatures higher than 1200°C . The same effect was also found in nanorubies produced by the laser ablation, as shown in Figure 2.24b. Two different photoluminescence profiles are observed, the first profile shows narrow ruby emission with R_1 and R_2 , while the second profile shows broad spectrum spread from 685 nm to 900 nm [20].

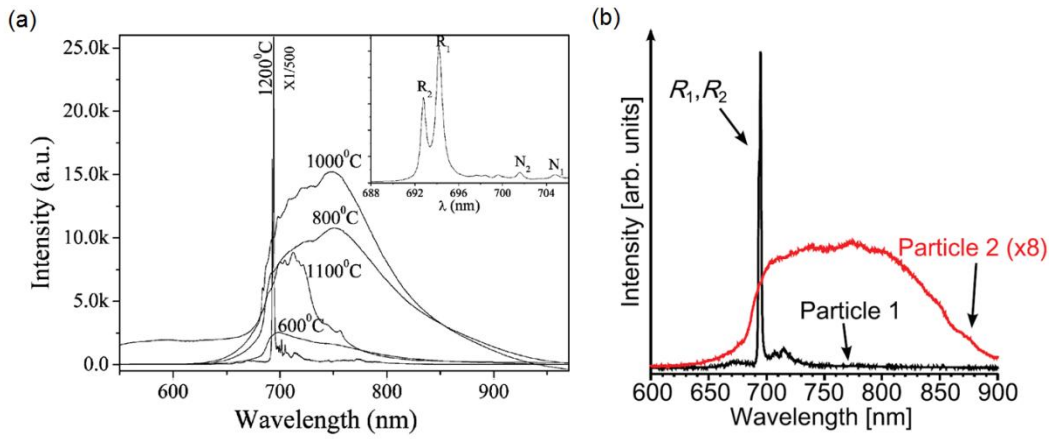


Figure 2.24: (a) Photoluminescence spectra of ruby nanotubes at the different annealing temperatures. (inset) Zoomed spectrum of the sample annealed at 1200°C showing the R_1 and R_2 peak. (b) Two photoluminescence spectra of the nanorubies sample produced by the femtosecond laser ablation. Reproduced from Ref. [124] (a) and [20] (b).

As we demonstrate in this work, long-photoluminescence lifetime τ_r of nanoruby can be used to increase its optical contrast on the background of biological systems, if it is implemented in combination with the time-gated imaging system, which will be discussed later in Chapter 6. Pflitsch *et al.* [156] have measured τ_r of bulk ruby crystal and found that the ruby crystal lifetime was 2.7 ms and 4 μs at the temperature of 294 K and 833 K respectively. Chandler *et al.* [116] used two experimental setups to measure $\tau_r \approx 3.7$ ms. Liu *et al.* [155] have reported employing ruby microspheres to

measure τ_r and found it dependent on the Cr^{3+} concentration: $\tau_r = 4.40, 3.88, 3.24, 2.39, 2.11$ ms, corresponding to 0.1, 0.3, 0.5, 0.7, and 0.9 mol% of the Cr^{3+} concentration, respectively. Edmond *et al.* have measured τ_r of two types of nanorubies particles, α - and γ -phase, which appeared equal to 3.71 ms and 3.87 ms, respectively [20].

Measurements of the quantum efficiency of nanorubies produced by the laser ablation provided the lower boundary estimate of 25 % [20]. This measurement and analysis was based on the measurement τ_r of discrete nanoparticles, and their modified radiative rate benchmarked against that of bulk ruby crystal [157]. The nanoruby emission properties were not affected by environmental conditions, showing no quenching effects [158].

Colloidal Stability

Colloidal stability of NPs can be assessed by measuring the zeta potential. Zeta potential (ζ) [mV] is a measure of the electrostatic potential at the electrical double layer surrounding a nanoparticle in solution [159]. A high magnitude of the zeta potential ($|\zeta| > 30$ mV) points to the colloid stability [160]. Edmonds *et al.* [20] have assessed the colloidal stability of laser-ablation-produced nanorubies by measuring ζ ranging from 30 mV to 40 mV, suggesting excellent colloidal stability. The stability of nanorubies in aqueous solutions can be explained by the amphoteric property of Al_2O_3 . The surface charge produces ion complexation reaction, which depends on pH of the solvent. At pH lower than an isoelectric point, positive (AlOH_2^+) dominates, whereas at pH higher than the isoelectric point, negative (AlO^-) dominate. These mechanisms contribute to the good hydrophilic property caused by the electrostatic double layer repulsion force, as explained by Derjaguin, Landau, Vervy, and Overbeek (DLVO) theory.

Colloidal nanorubies were found stable in buffer solutions, as evidenced by the high zeta potential value in buffers, including PBS (12 mM, pH 7.4), borate (50 mM, pH 9.1) buffers, as shown in Figure 2.25. It was found that $\zeta < 0$ at pH 4.6 – 9 due to the chemisorption of buffer anions, such as PO_4^{3-} in PBS. Nanorubies possess high negative ζ , making them stable in buffer solutions [20].

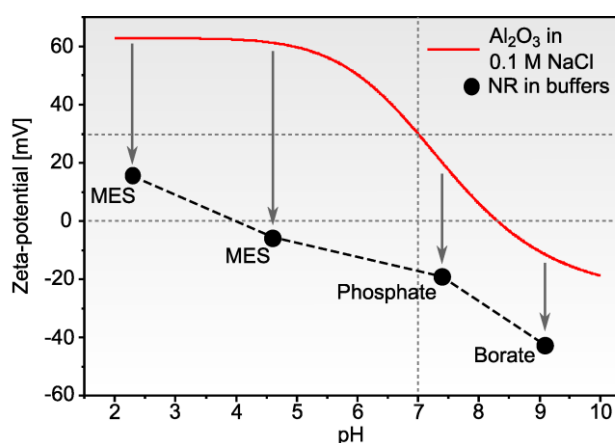


Figure 2.25: Zeta-potential of nanorubies, as a function of pH in buffers (labelled), in comparison with that of Al₂O₃ in a saline solutions (0.1 M NaCl). Reproduced from Ref. [20].

Cytotoxicity

Metal oxide based NPs such as TiO₂, ZnO, ZrO₂, and Al₂O₃ are generally expected to exhibit low toxicity stemming from their low toxicity property of the corresponding bulk material [161]. The most common cytotoxicity assaying method, metabolic activity test (MTT) was used to evaluate cytotoxicity of these NPs in human fetal lung fibroblasts. Al₂O₃ has demonstrated least cytotoxicity in comparison with ZnO, TiO₂, and SiO₂ NPs [145]. The toxicity is dose-dependent dropping down to 80% of the control value after 48-h exposure to 1.5-mg/mL Al₂O₃ colloidal particles mean-sized 190 nm. The size of the tested particles was a concern, derating these published results. The size increase was, probably, due to the aggregation in the cell growth medium during the incubation. Our results demonstrated that Al₂O₃ NPs were non-cytotoxic (Figure 2.26). MTT tests of as-produced and amine-functionalised nanoalumina colloids were carried out in the concentration range up to 100 µg/mL, demonstrating the cell viability unchanged. This test indicated that nanoalumina particles produced in this work demonstrated propensity towards biocompatibility. An additional test of the cytotoxicity by means of a trypan blue-based assay corroborated the very low cell loss during the incubation of nanorubies [20].

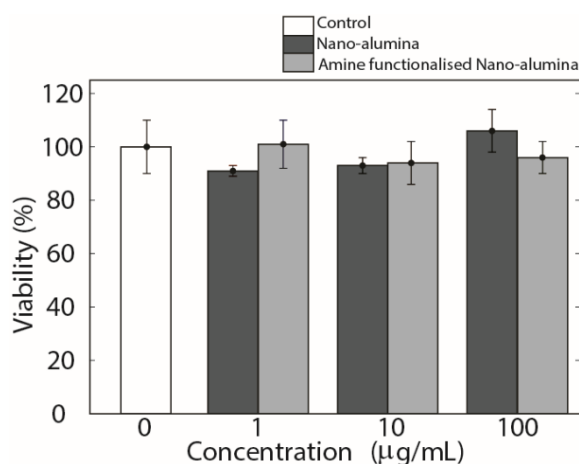


Figure 2.26: A bar chart of the cell viability treated with nanoalumina (black) and amine-functionalised nanoalumina (grey) samples benchmarked against the untreated control cells (white). Reproduced from Ref. [145].

2.5.4 Nanoruby Functionalisation

Nanoruby surface functionalisation is required to improve their colloidal stability and prepare this surface for bioconjugation by grafting anchoring moieties. To the best of my knowledge, no surface-functionalisation process of this nanomaterial has been reported. At the same time, surface-functionalisation of nanoalumina and metal oxide nanoparticles can be used as guidance for nanoruby functionalisation. A number of functional groups can be grafted on alumina surface, as it has been demonstrated for amine, carboxyl, sulfonate, phosphate, phenyl [162-166], methacrylate [167], polyethylene glycol (PEG) [168], and polyelectrolyte groups [169].

The surface-functionalisation is carried out by either physisorption or covalent attachment of target moieties. Polyelectrolyte compounds, such as poly(acrylic acid)(PAA) and ammonium salt of polymethacrylic acid, are used to for the physisorption approach on the alumina surface [169]. The physisorbed compounds display carboxyl groups to aqueous environment, increasing the dispersibility of alumina [170]. Wiśniewska *et al.* [171] have investigated the effect of the PAA addition to alumina suspensions at pH 3, 6 and 9. The addition of PAA with the high molecular weight (100000 and 240000) stabilised the alumina suspension at all tested pH values. Shin *et al.* [169] studied the adsorption of polydiallyldimethylammonium chloride (PDADMAC) on the alumina surface, reporting the high adsorption of PDADMAC at

alkaline pH. Alumina suspension with 1.0 wt% PDADMAC showed high stability in broad pH range. Yang *et al.* [172] examined the colloidal stability of alumina functionalised with 1,2-dihydroxy-3,5-benzenedisulfonic acid disodium salt (Tiron) at different pHs. The adsorption of Tiron shifted the isoelectric point (IEP) from 8.2 to 4.5, and increased the absolute zeta-potential value. The optimum pH value and the optimum dosage of Tiron were evaluated as 8.5 and 0.8 dB% respectively, enabling the most stable alumina suspension. Greenwood *et al.* [173] studied the adsorption of polyamide and PDADMAC onto alumina particles using electro-acoustics, and found the critical dependence of the adsorption on the ionic strength of the suspension [173].

The surface-functionalisation using the covalent attachment is achieved by using a silane coupling agent, which is known as a silanisation process. The silane coupling agent has hydrolysable group (OR) and organo-functional group (F) reactive groups coordinated to a silicon atom, as shown in Figure 2.27a. Figure 2.27b shows that the common silane-coupling agents have been used to functionalise metal oxide surface. Figure 2.28 displays the schematic diagram of the silanisation process. In this process, the Si–OR bonds are hydrolysed in water to form silanol Si–OH groups. These OH groups cross-link with OH groups on the oxide surface to form hydrogen bondings through a condensation process (see Figure 2.28). Covalent bonds are formed after the drying process, which also release water. This method has been applied to attach amine groups on the nanoalumina surface by using aminopropyltriethoxysilane [145, 163, 164] and aminopropyltrimethoxysilane [162], as the coupling agents. The other silane coupling agents, such as 3-(triethoxysilyl) propylsuccinicanhydride, 3-(trihydroxysilyl)-1-propanesulfonic acid, phenyltriethoxysilane and 3-methacryloxypropyl trimethoxysilane (MPS), were used for attachment of carboxyl, sulfonate, phenyl, and methacrylate groups, respectively.

Silane chemistry method can be used to graft PEG covalently, as demonstrated by Popat *et al.* [174]. In their work, PEG reacted with silicon tetrachloride, which resulted in PEG-OSiCl₃. Then the silanisation process was performed to attach PEG to the oxide surface. Commercial silane PEG reagents are available commercially, and their applications are reported elsewhere [175]. Isocyanate [i.e. diphenylmethane-4,4'-di-isocyanate (MDI)] reactive with –OH, –COOH moieties represents an alternative coupling agent, which is suitable for modification of the alumina surface. Li *et al.* [176]

have successfully grafted MDI on the nanoalumina and showed the improvement of the nanoalumina dispersion in ethanol.

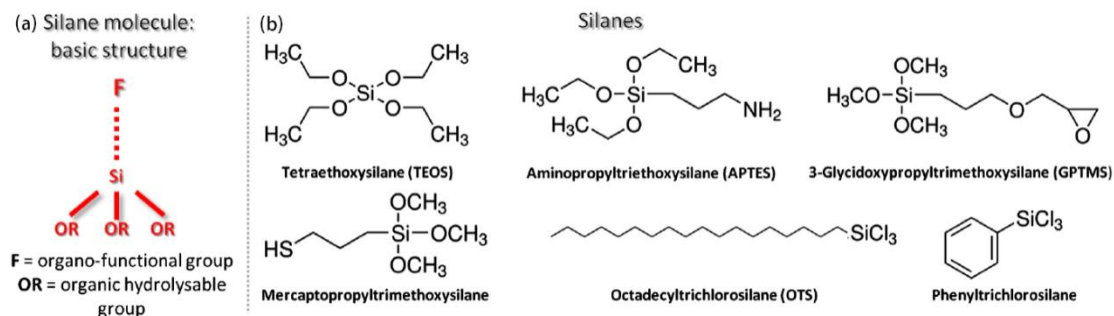


Figure 2.27: (a) A structure diagram of a silane molecule. (b) Chemical structures of the mostly used silane precursors for the surface functionalisation of ceramic materials. (c) Schematic diagram of the silanisation process. Reproduced from [177].

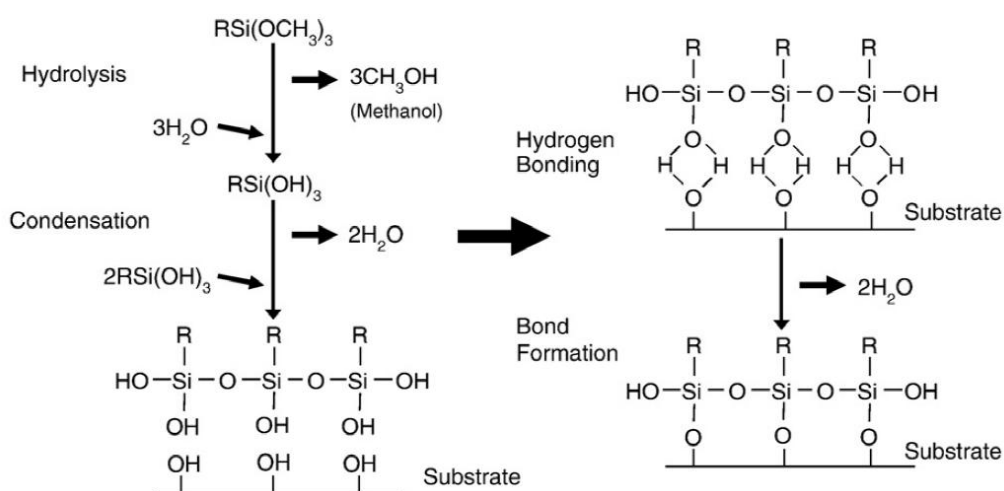


Figure 2.28: A schematic diagram of the silanisation process, which shows a four-steps reaction: hydrolysis, condensation, hydrogen bonding and bond formation. Reproduced from Ref. [178].

2.5.5 Bioimaging Applications of Nanoruby

Nanoruby is photostable, reasonably efficient nano-emitter, characterised by the high absorption cross-section of Cr^{3+} ion = $9 \times 10^{-20} \text{ cm}^2$. Its action cross-section is evaluated as $\approx 10^{-16} \text{ cm}^2$ for a 50-nm ruby nanoparticle of the doping molar ratio of 0.8%, which is comparable with many organic fluorescent dye molecules. It also has a high quantum yield conservatively estimated as $\geq 25\%$ [20]. This makes it attractive for molecular-specific labelling. Its exceptionally long photoluminescence lifetime of 3.7 ms,

however, that what makes it useful to fluorescent optical imaging on the background of autofluorescence, as detailed in the following chapters.

The promising imaging performance has been demonstrated by my colleagues prior to this work [20]. The short-lifetime autofluorescent background was completely suppressed in case of the nanoruby submersion in a solution of conventional organic dye Rhodamine 6G characterised by $\tau \approx 4$ ns, and emission spectral band at 551 nm. Nanorubies were internalised non-specifically in CHO-K1 cells via endocytosis. It was demonstrated that nanorubies were clearly visualised on the cellular environment by means of spectral filtration of the nanoruby photoluminescence signals, as shown in Figure 2.29a. The signal from cells autofluorescence was eliminated completely, when the time-gated detection mode was switched on (Figure 2.29b).

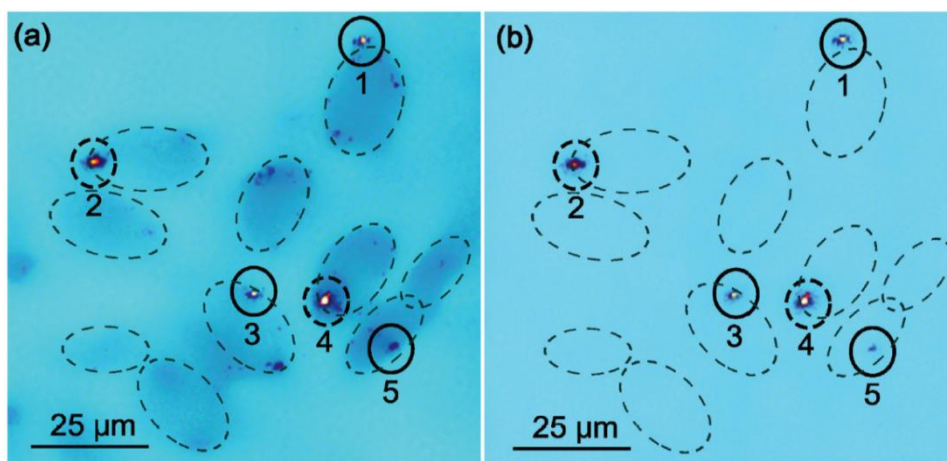


Figure 2.29: Fluorescence confocal microscopy of nanorubies internalised in CHO-K1 cells captured using (a) spectral filtration and (b) time-gating detection. The dashed lines mark the cell membranes. Reproduced from Ref. [20].

Nanorubies were coupled to antibodies by performing a simplified bioconjugation protocol based on the physisorption, and deployed in a rabbit-anti rabbit IgG immunoassay, as shown in Figure 2.30. The strong nanoruby photoluminescence signal indicated the binding of nanorubies to anti-rabbit IgG and immobilisation on the glass surface coated with rabbit IgGs, as shown in Figure 2.30b. This demonstrates the utility of nanoruby-based molecular probe for bioimaging and biosensing.

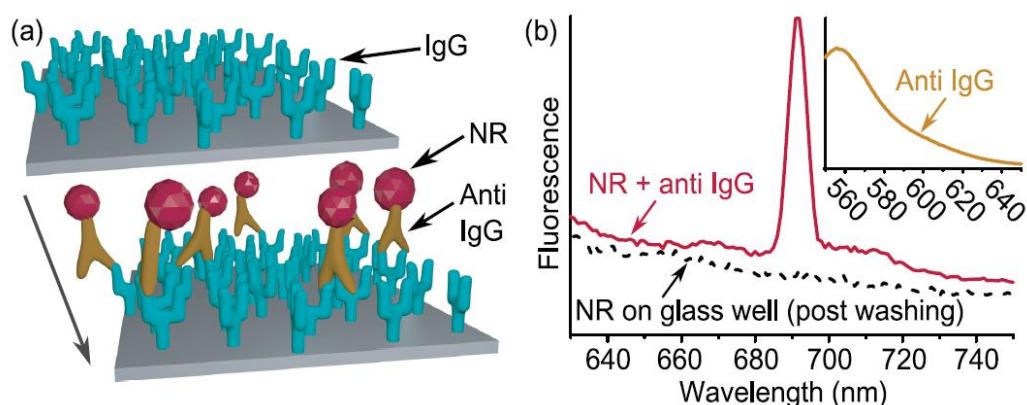


Figure 2.30: An immunoassay of Alexa Fluor532 stained anti-rabbit IgG coupled to nanoruby particles immobilised on a glass plate coated with rabbit IgGs. (a) An artistic rendering of the experimental method. (b) Emission spectra of Alexa Fluor 532 anti-rabbit IgG (inset), together with nanoruby photoluminescence on a glass slide (dashed line) and nano-ruby coupled with dye-stained antibody (solid line). Reproduced from Ref. [20].

2.5 Conclusion

The selection of PL nanomaterials for bioimaging application is governed by a combination of their physical, chemical and optical properties. The core chemical inertness, simple surface functionalisation and minimum cytotoxicity are the important components to be considered. The optical properties are the main factor to determine the utility of these nanomaterials. As it was discussed in this chapter, the existing PL NPs have several limitations, such as photoblinking, cytotoxicity, and low chemical stability, which constrained their application scope. Nanoruby provides an interesting alternative to the existing PL NPs due to its unique properties including excellent photostability, narrow emission spectrum, long-photoluminescence lifetime, and biocompatibility. The easiness in obtaining synthetic ruby crystal at low cost motivates us to use a milling method. Large-scale, simple and low-cost nanoruby production can be realised using this method. Furthermore, as-produced nanorubies are readily dispersible in water. The next chapter will detail the state-of-the-art production methods, following by the relevant suite of characterisation methods and instrumentation relevant to this work.

2.6 References

- [1] "Introduction to Fluorescence," in *Principles of Fluorescence Spectroscopy*, J. Lakowicz, Ed., ed: Springer US, 2006, pp. 1-26.
- [2] G. G. Stokes, "On the change of refrangibility of light," *Philosophical Transactions of the Royal Society of London*, pp. 463-562, 1852.
- [3] J. Herschel, "On the Epipolic Dispersion of Light, Being a Supplement to a Paper Entitled," On a Case of Superficial Colour Presented by a Homogeneous Liquid Internally Colourless", *Philosophical Transactions of the Royal Society of London*, pp. 147-153, 1845.
- [4] B. Valeur and M. N. Berberan-Santos, *Molecular fluorescence: principles and applications*: John Wiley & Sons, 2012.
- [5] J. C. Croney, D. M. Jameson, and R. P. Learmonth, "Fluorescence spectroscopy in biochemistry: teaching basic principles with visual demonstrations," *Biochemistry and Molecular Biology Education*, vol. 29, pp. 60-65, 2001.
- [6] E. M. Goldys, *Fluorescence applications in biotechnology and life sciences*: John Wiley & Sons, 2009.
- [7] B. Valeur and M. N. Berberan-Santos, "A brief history of fluorescence and phosphorescence before the emergence of quantum theory," *Journal of Chemical Education*, vol. 88, pp. 731-738, 2011.
- [8] J. W. Robinson, E. S. Frame, and G. M. Frame II, *Undergraduate instrumental analysis*: CRC Press, 2014.
- [9] M. Y. Berezin and S. Achilefu, "Fluorescence lifetime measurements and biological imaging," *Chemical reviews*, vol. 110, pp. 2641-2684, 2010.
- [10] M. Monici, "Cell and tissue autofluorescence research and diagnostic applications," *Biotechnology annual review*, vol. 11, pp. 227-256, 2005.
- [11] E. Dimitrow, I. Riemann, A. Ehlers, M. J. Koehler, J. Norgauer, P. Elsner, *et al.*, "Spectral fluorescence lifetime detection and selective melanin imaging by multiphoton laser tomography for melanoma diagnosis," *Experimental dermatology*, vol. 18, pp. 509-515, 2009.
- [12] W. Melhuish, "Nomenclature, symbols, units and their usage in spectrochemical analysis-Part VI: molecular luminescence spectroscopy," *Pure and Applied Chemistry*, vol. 56, pp. 231-245, 1984.
- [13] A. Nadort, V. K. A. Sreenivasan, Z. Song, A. V. Nechaev, V. A. Semchishen, V. Y. Panchenko, *et al.*, "Quantitative Imaging of Single Upconversion Nanoparticles in Biological Tissue," *PLOS ONE*, vol. 8, p. e63292, 2013.
- [14] S. Santra, J. Xu, K. Wang, and W. Tand, "Luminescent nanoparticle probes for bioimaging," *Journal of nanoscience and nanotechnology*, vol. 4, pp. 590-599, 2004.
- [15] M. Chen and M. Yin, "Design and development of fluorescent nanostructures for bioimaging," *Progress in Polymer Science*, vol. 39, pp. 365-395, 2014.
- [16] W. Kong, R. Liu, H. Li, J. Liu, H. Huang, Y. Liu, *et al.*, "High-bright fluorescent carbon dots and their application in selective nucleoli staining," *J. Mater. Chem. B*, vol. 2, pp. 5077-5082, 2014.
- [17] L. Zhang and E. Wang, "Metal nanoclusters: new fluorescent probes for sensors and bioimaging," *Nano Today*, vol. 9, pp. 132-157, 2014.

- [18] P. Zhang, X. X. Yang, Y. Wang, N. W. Zhao, and C. Z. Huang, "Rapid synthesis of highly luminescent and stable Au 20 nanoclusters for active tumor-targeted imaging in vitro and in vivo," *Nanoscale*, vol. 6, pp. 2261-2269, 2014.
- [19] S. W. Wu, G. Han, D. J. Milliron, S. Aloni, V. Altoe, D. V. Talapin, *et al.*, "Non-blinking and photostable upconverted luminescence from single lanthanide-doped nanocrystals," *Proceedings of the National Academy of Sciences of the United States of America*, vol. 106, pp. 10917-10921, 2009.
- [20] A. M. Edmonds, M. A. Sobhan, V. K. A. Sreenivasan, E. A. Grebenik, J. R. Rabeau, E. M. Goldys, *et al.*, "Nano-Ruby: A Promising Fluorescent Probe for Background-Free Cellular Imaging," *Particle & Particle Systems Characterization*, vol. 30, pp. 1-8, 2013.
- [21] I. Johnson and M. T. Spence, "Molecular Probes Handbook, A Guide to Fluorescent Probes and Labeling Technologies (Invitrogen) Life Technologies," NY, USA, 2011.
- [22] X. Michalet, F. F. Pinaud, L. A. Bentolila, J. M. Tsay, S. Doose, J. J. Li, *et al.*, "Quantum dots for live cells, in vivo imaging, and diagnostics," *Science*, vol. 307, pp. 538-544, 2005.
- [23] B. Zhou, B. Shi, D. Jin, and X. Liu, "Controlling upconversion nanocrystals for emerging applications," *Nature nanotechnology*, vol. 10, pp. 924-936, 2015.
- [24] D. K. Chatterjee, M. K. Gnanasammandhan, and Y. Zhang, "Small upconverting fluorescent nanoparticles for biomedical applications," *Small*, vol. 6, pp. 2781-2795, 2010.
- [25] M. W. Doherty, N. B. Manson, P. Delaney, F. Jelezko, J. Wrachtrup, and L. C. Hollenberg, "The nitrogen-vacancy colour centre in diamond," *Physics Reports*, vol. 528, pp. 1-45, 2013.
- [26] L. Rondin, G. Dantelle, A. Slablab, F. Grosshans, F. Treussart, P. Bergonzo, *et al.*, "Surface-induced charge state conversion of nitrogen-vacancy defects in nanodiamonds," *Physical Review B*, vol. 82, p. 115449, 2010.
- [27] V. I. Klimov, *Nanocrystal quantum dots*: CRC Press, 2010.
- [28] W. K. Leutwyler, S. L. Bürgi, and H. Burgl, "Semiconductor clusters, nanocrystals, and quantum dots," *Science*, vol. 271, pp. 933-937, 1996.
- [29] D. Ioannou and D. K. Griffin, "Nanotechnology and molecular cytogenetics: the future has not yet arrived," *Nano reviews*, vol. 1, 2010.
- [30] A. L. Rogach, T. Franzl, T. A. Klar, J. Feldmann, N. Gaponik, V. Lesnyak, *et al.*, "Aqueous Synthesis of Thiol-Capped CdTe Nanocrystals: State-of-the-Art," *The Journal of Physical Chemistry C*, vol. 111, pp. 14628-14637, 2007.
- [31] N. Gaponik, D. V. Talapin, A. L. Rogach, K. Hoppe, E. V. Shevchenko, A. Kornowski, *et al.*, "Thiol-capping of CdTe nanocrystals: an alternative to organometallic synthetic routes," *The Journal of Physical Chemistry B*, vol. 106, pp. 7177-7185, 2002.
- [32] B. Dabbousi, J. Rodriguez-Viejo, F. V. Mikulec, J. Heine, H. Mattoussi, R. Ober, *et al.*, "(CdSe) ZnS core-shell quantum dots: synthesis and characterization of a size series of highly luminescent nanocrystallites," *The Journal of Physical Chemistry B*, vol. 101, pp. 9463-9475, 1997.
- [33] C. B. Murray, D. J. Norris, and M. G. Bawendi, "Synthesis and characterization of nearly monodisperse CdE (E = sulfur, selenium, tellurium) semiconductor nanocrystallites," *Journal of the American Chemical Society*, vol. 115, pp. 8706-8715, 1993.

- [34] S. Kudera, L. Carbone, L. Manna, and W. Parak, "Growth mechanism, shape and composition control of semiconductor nanocrystals," in *Semiconductor Nanocrystal Quantum Dots*, A. Rogach, Ed., ed: Springer Vienna, 2008, pp. 1-34.
- [35] X. Michalet, F. Pinaud, T. D. Lacoste, M. Dahan, M. P. Bruchez, A. P. Alivisatos, *et al.*, "Properties of fluorescent semiconductor nanocrystals and their application to biological labeling," *Single Molecules*, vol. 2, pp. 261-276, 2001.
- [36] W. Cai, D.-W. Shin, K. Chen, O. Gheysens, Q. Cao, S. X. Wang, *et al.*, "Peptide-labeled near-infrared quantum dots for imaging tumor vasculature in living subjects," *Nano letters*, vol. 6, pp. 669-676, 2006.
- [37] J.-J. Li and K.-D. Zhu, "Coherent optical spectroscopy in a biological semiconductor quantum dot-DNA hybrid system," *Nanoscale research letters*, vol. 7, pp. 1-7, 2012.
- [38] X. Wu, H. Liu, J. Liu, K. N. Haley, J. A. Treadway, J. P. Larson, *et al.*, "Immunofluorescent labeling of cancer marker Her2 and other cellular targets with semiconductor quantum dots," *Nature biotechnology*, vol. 21, pp. 41-46, 2003.
- [39] W. B. Tan, S. Jiang, and Y. Zhang, "Quantum-dot based nanoparticles for targeted silencing of HER2/neu gene via RNA interference," *Biomaterials*, vol. 28, pp. 1565-1571, 2007.
- [40] V. Bagalkot, L. Zhang, E. Levy-Nissenbaum, S. Jon, P. W. Kantoff, R. Langer, *et al.*, "Quantum dot-aptamer conjugates for synchronous cancer imaging, therapy, and sensing of drug delivery based on bi-fluorescence resonance energy transfer," *Nano letters*, vol. 7, pp. 3065-3070, 2007.
- [41] Z.-Q. Cui, Q. Ren, H.-P. Wei, Z. Chen, J.-Y. Deng, Z.-P. Zhang, *et al.*, "Quantum dot-aptamer nanoprobe for recognizing and labeling influenza A virus particles," *Nanoscale*, vol. 3, pp. 2454-2457, 2011.
- [42] K. Du, S. H. Ko, G. M. Gallatin, H. P. Yoon, J. A. Liddle, and A. J. Berglund, "Quantum dot-DNA origami binding: a single particle, 3D, real-time tracking study," *Chemical Communications*, vol. 49, pp. 907-909, 2013.
- [43] M. Li, N. Wang, W. Zang, Y. Ma, H. Mao, and G. Zhao, "Sensitive SNP Detection of KIF6 Gene by Quantum Dot-DNA Conjugate Probe-Based Assay," *Analytical Letters*, vol. 46, pp. 508-517, 2013.
- [44] B. Dubertret, P. Skourides, D. J. Norris, V. Noireaux, A. H. Brivanlou, and A. Libchaber, "In vivo imaging of quantum dots encapsulated in phospholipid micelles," *Science*, vol. 298, pp. 1759-1762, 2002.
- [45] X. Gao, Y. Cui, R. M. Levenson, L. W. Chung, and S. Nie, "In vivo cancer targeting and imaging with semiconductor quantum dots," *Nature biotechnology*, vol. 22, pp. 969-976, 2004.
- [46] J. V. Jokerst, T. Lobovkina, R. N. Zare, and S. S. Gambhir, "Nanoparticle PEGylation for imaging and therapy," *Nanomedicine*, vol. 6, pp. 715-728, 2011.
- [47] W. J. Jin, J. M. Costa-Fernández, R. Pereiro, and A. Sanz-Medel, "Surface-modified CdSe quantum dots as luminescent probes for cyanide determination," *Analytica chimica acta*, vol. 522, pp. 1-8, 2004.
- [48] J.-J. Zhu, J.-J. Li, H.-P. Huang, and F.-F. Cheng, *Quantum Dots for DNA Biosensing*: Springer, 2013.

- [49] L.-W. Wang, C.-W. Peng, C. Chen, and Y. Li, "Quantum dots-based tissue and in vivo imaging in breast cancer researches: current status and future perspectives," *Breast cancer research and treatment*, vol. 151, pp. 7-17, 2015.
- [50] S. Santra, D. Dutta, G. A. Walter, and B. M. Moudgil, "Fluorescent nanoparticle probes for cancer imaging," *Technology in cancer research & treatment*, vol. 4, pp. 593-602, 2005.
- [51] R. Tang, J. Xue, B. Xu, D. Shen, G. P. Sudlow, and S. Achilefu, "Tunable ultrasmall visible-to-extended near-infrared emitting silver sulfide quantum dots for integrin-targeted cancer imaging," *ACS nano*, vol. 9, pp. 220-230, 2015.
- [52] V. Danilenko, "On the history of the discovery of nanodiamond synthesis," *Physics of the Solid State*, vol. 46, pp. 595-599, 2004.
- [53] D. Ho, *Nanodiamonds: applications in biology and nanoscale medicine*: Springer Science & Business Media, 2009.
- [54] R. Mildren and J. Rabeau, *Optical engineering of diamond*: John Wiley & Sons, 2013.
- [55] O. Williams, *Nanodiamonds* vol. 31: Royal Society of Chemistry, 2013.
- [56] A. Gruber, A. Dräbenstedt, C. Tietz, L. Fleury, J. Wrachtrup, and C. Von Borczyskowski, "Scanning confocal optical microscopy and magnetic resonance on single defect centers," *Science*, vol. 276, pp. 2012-2014, 1997.
- [57] R. Igarashi, Y. Yoshinari, H. Yokota, T. Sugi, F. Sugihara, K. Ikeda, *et al.*, "Real-time background-free selective imaging of fluorescent nanodiamonds in vivo," *Nano letters*, vol. 12, pp. 5726-5732, 2012.
- [58] S.-J. Yu, M.-W. Kang, H.-C. Chang, K.-M. Chen, and Y.-C. Yu, "Bright Fluorescent Nanodiamonds: No Photobleaching and Low Cytotoxicity," *Journal of the American Chemical Society*, vol. 127, pp. 17604-17605, 2005.
- [59] A. M. Schrand, H. Huang, C. Carlson, J. J. Schlager, E. Omacr Sawa, S. M. Hussain, *et al.*, "Are diamond nanoparticles cytotoxic?," *J Phys Chem B*, vol. 111, pp. 2-7, 2007.
- [60] A. Y. Vul, A. Aleksenskiy, and A. Dideykin, "Detonation nanodiamonds: technology, properties and applications," *Nanosciences and Nanotechnologies, Encyclopedia of Life Support Systems (EOLSS), Developed under the Auspices of the UNESCO, EOLSS Publishers, Oxford, UK, ISBN*, pp. 978-92, 2009.
- [61] V. N. Mochalin, O. Shenderova, D. Ho, and Y. Gogotsi, "The properties and applications of nanodiamonds," *Nature nanotechnology*, vol. 7, pp. 11-23, 2012.
- [62] J. M. Say, C. van Vreden, D. J. Reilly, L. J. Brown, J. R. Rabeau, and N. J. King, "Luminescent nanodiamonds for biomedical applications," *Biophysical Reviews*, vol. 3, pp. 171-184, 2011.
- [63] B. Jean-Paul, A. C. Patrick, J. Fedor, W. Joerg, A. Pascal, S. Mohamed, *et al.*, "High yield fabrication of fluorescent nanodiamonds," *Nanotechnology*, vol. 20, p. 235602, 2009.
- [64] N. Manson, J. Harrison, and M. Sellars, "Nitrogen-vacancy center in diamond: Model of the electronic structure and associated dynamics," *Physical Review B*, vol. 74, p. 104303, 2006.
- [65] K. B. Holt, "Diamond at the nanoscale: applications of diamond nanoparticles from cellular biomarkers to quantum computing," *Philosophical Transactions of the Royal Society of London A: Mathematical, Physical and Engineering Sciences*, vol. 365, pp. 2845-2861, 2007.

- [66] A. Zhukov, F. Gareeva, A. Aleksenskii, and A. Y. Vul, "Surface charge of detonation nanodiamond particles in aqueous solutions of simple 1: 1 Electrolytes," *Colloid journal*, vol. 72, pp. 640-646, 2010.
- [67] V. K. Sreenivasan, E. A. Ivukina, W. Deng, T. A. Kelf, T. A. Zdobnova, S. V. Lukash, *et al.*, "Barstar: barnase—a versatile platform for colloidal diamond bioconjugation," *Journal of Materials Chemistry*, vol. 21, pp. 65-68, 2011.
- [68] S. V. Kuchibhatla, A. Karakoti, and S. Seal, "Colloidal stability by surface modification," *Jom*, vol. 57, pp. 52-56, 2005.
- [69] D. Delabouglise, B. Marcus, M. Mermoux, P. Bouvier, J. Chane-Tune, J.-P. Petit, *et al.*, "Biotin grafting on boron-doped diamond," *Chemical Communications*, pp. 2698-2699, 2003.
- [70] C.-C. Fu, H.-Y. Lee, K. Chen, T.-S. Lim, H.-Y. Wu, P.-K. Lin, *et al.*, "Characterization and application of single fluorescent nanodiamonds as cellular biomarkers," *Proceedings of the National Academy of Sciences*, vol. 104, pp. 727-732, 2007.
- [71] N. Mohan, C.-S. Chen, H.-H. Hsieh, Y.-C. Wu, and H.-C. Chang, "In vivo imaging and toxicity assessments of fluorescent nanodiamonds in *Caenorhabditis elegans*," *Nano letters*, vol. 10, pp. 3692-3699, 2010.
- [72] L. Y. Ang, M. E. Lim, L. C. Ong, and Y. Zhang, "Applications of upconversion nanoparticles in imaging, detection and therapy," *Nanomedicine*, vol. 6, pp. 1273-1288, 2011.
- [73] S. Wu, G. Han, D. J. Milliron, S. Aloni, V. Altoe, D. V. Talapin, *et al.*, "Non-blinking and photostable upconverted luminescence from single lanthanide-doped nanocrystals," *Proceedings of the National Academy of Sciences*, vol. 106, pp. 10917-10921, 2009.
- [74] M. V. DaCosta, S. Doughan, Y. Han, and U. J. Krull, "Lanthanide upconversion nanoparticles and applications in bioassays and bioimaging: A review," *Analytica chimica acta*, vol. 832, pp. 1-33, 2014.
- [75] M. P. Hehlen, G. Frei, and H. U. Güdel, "Dynamics of infrared-to-visible upconversion in $\text{Cs}_3\text{Lu}_2\text{Br}_9:1\% \text{Er}^{3+}$," *Physical Review B*, vol. 50, p. 16264, 1994.
- [76] Z. Song, Y. G. Anissimov, J. Zhao, A. V. Nechaev, A. Nadort, D. Jin, *et al.*, "Background free imaging of upconversion nanoparticle distribution in human skin," *Journal of biomedical optics*, vol. 18, pp. 061215-061215, 2013.
- [77] R. H. Page, K. I. Schaffers, P. A. Waide, J. B. Tassano, S. A. Payne, W. F. Krupke, *et al.*, "Upconversion-pumped luminescence efficiency of rare-earth-doped hosts sensitized with trivalent ytterbium," *Journal of the Optical Society of America B-Optical Physics*, vol. 15, pp. 996-1008, 1998.
- [78] F. Wang, R. Deng, J. Wang, Q. Wang, Y. Han, H. Zhu, *et al.*, "Tuning upconversion through energy migration in core-shell nanoparticles," *Nat Mater*, vol. 10, pp. 968-973, 2011.
- [79] H. X. Mai, Y. W. Zhang, R. Si, Z. G. Yan, L. D. Sun, L. P. You, *et al.*, "High-quality sodium rare-earth fluoride nanocrystals: Controlled synthesis and optical properties," *Journal of the American Chemical Society*, vol. 128, pp. 6426-6436, 2006.
- [80] J. Zhao, D. Jin, E. P. Schartner, Y. Lu, Y. Liu, A. V. Zvyagin, *et al.*, "Single-nanocrystal sensitivity achieved by enhanced upconversion luminescence," *Nat Nano*, vol. 8, pp. 729-734, 2013.

- [81] C. F. Gainer and M. Romanowski, "A review of synthetic methods for the production of upconverting lanthanide nanoparticles," *Journal of Innovative Optical Health Sciences*, vol. 7, p. 1330007, 2014.
- [82] F. Wang, J. Wang, and X. Liu, "Direct Evidence of a Surface Quenching Effect on Size - Dependent Luminescence of Upconversion Nanoparticles," *Angewandte Chemie*, vol. 122, pp. 7618-7622, 2010.
- [83] A. Nadort, V. K. Sreenivasan, Z. Song, E. A. Grebenik, A. V. Nechaev, V. A. Semchishen, *et al.*, "Quantitative imaging of single upconversion nanoparticles in biological tissue," *PloS one*, vol. 8, p. e63292, 2013.
- [84] D. Li, B. Dong, X. Bai, Y. Wang, and H. Song, "Influence of the TGA modification on upconversion luminescence of hexagonal-phase NaYF₄: Yb³⁺, Er³⁺ nanoparticles," *The Journal of Physical Chemistry C*, vol. 114, pp. 8219-8226, 2010.
- [85] R. S. Niedbala, H. Feindt, K. Kardos, T. Vail, J. Burton, B. Bielska, *et al.*, "Detection of analytes by immunoassay using up-converting phosphor technology," *Analytical Biochemistry*, vol. 293, pp. 22-30, 2001.
- [86] Z. Li and Y. Zhang, "Monodisperse Silica - Coated Polyvinylpyrrolidone/NaYF₄ Nanocrystals with Multicolor Upconversion Fluorescence Emission," *Angewandte Chemie*, vol. 118, pp. 7896-7899, 2006.
- [87] T. Pellegrino, L. Manna, S. Kudera, T. Liedl, D. Koktysh, A. L. Rogach, *et al.*, "Hydrophobic nanocrystals coated with an amphiphilic polymer shell: a general route to water soluble nanocrystals," *Nano letters*, vol. 4, pp. 703-707, 2004.
- [88] R. Connally and J. Piper, "Solid-state time-gated luminescence microscope with ultraviolet light-emitting diode excitation and electron-multiplying charge-coupled device detection," *Journal of biomedical optics*, vol. 13, pp. 034022-034022-6, 2008.
- [89] M. Nyk, R. Kumar, T. Y. Ohulchanskyy, E. J. Bergey, and P. N. Prasad, "High contrast in vitro and in vivo photoluminescence bioimaging using near infrared to near infrared up-conversion in Tm³⁺ and Yb³⁺ doped fluoride nanophosphors," *Nano letters*, vol. 8, pp. 3834-3838, 2008.
- [90] M. Wang, C.-C. Mi, W.-X. Wang, C.-H. Liu, Y.-F. Wu, Z.-R. Xu, *et al.*, "Immunolabeling and NIR-excited fluorescent imaging of HeLa cells by using NaYF₄: Yb, Er upconversion nanoparticles," *Acs Nano*, vol. 3, pp. 1580-1586, 2009.
- [91] H. Hu, L. Xiong, J. Zhou, F. Li, T. Cao, and C. Huang, "Multimodal - Luminescence Core - Shell Nanocomposites for Targeted Imaging of Tumor Cells," *Chemistry-A European Journal*, vol. 15, pp. 3577-3584, 2009.
- [92] L. Cheng, K. Yang, S. Zhang, M. Shao, S. Lee, and Z. Liu, "Highly-sensitive multiplexed in vivo imaging using PEGylated upconversion nanoparticles," *Nano research*, vol. 3, pp. 722-732, 2010.
- [93] J. Zhou, Z. Liu, and F. Li, "Upconversion nanophosphors for small-animal imaging," *Chemical Society Reviews*, vol. 41, pp. 1323-1349, 2012.
- [94] E. A. Grebenik, A. Nadort, A. N. Generalova, A. V. Nechaev, V. K. Sreenivasan, E. V. Khaydukov, *et al.*, "Feasibility study of the optical imaging of a breast cancer lesion labeled with upconversion nanoparticle biocomplexes," *Journal of biomedical optics*, vol. 18, pp. 076004-076004, 2013.

- [95] B. Mahler, P. Spinicelli, S. Buil, X. Quelin, J.-P. Hermier, and B. Dubertret, "Towards non-blinking colloidal quantum dots," *Nature materials*, vol. 7, pp. 659-664, 2008.
- [96] V. Fomenko and D. J. Nesbitt, "Solution control of radiative and nonradiative lifetimes: A novel contribution to quantum dot blinking suppression," *Nano letters*, vol. 8, pp. 287-293, 2008.
- [97] S. Hohng and T. Ha, "Near-complete suppression of quantum dot blinking in ambient conditions," *Journal of the American Chemical Society*, vol. 126, pp. 1324-1325, 2004.
- [98] S.-J. Yu, M.-W. Kang, H.-C. Chang, K.-M. Chen, and Y.-C. Yu, "Bright fluorescent nanodiamonds: no photobleaching and low cytotoxicity," *Journal of the American Chemical Society*, vol. 127, pp. 17604-17605, 2005.
- [99] N. h. SHIAO, "Cytotoxic effect of CdSe quantum dots on mouse embryonic development," *Acta Pharmacologica Sinica*, vol. 29, pp. 259-266, 2008.
- [100] C. E. Bradburne, J. B. Delehanty, K. Boeneman Gemmill, B. C. Mei, H. Mattoussi, K. Susumu, *et al.*, "Cytotoxicity of quantum dots used for in vitro cellular labeling: role of QD surface ligand, delivery modality, cell type, and direct comparison to organic fluorophores," *Bioconjugate chemistry*, vol. 24, pp. 1570-1583, 2013.
- [101] L. Ye, K.-T. Yong, L. Liu, I. Roy, R. Hu, J. Zhu, *et al.*, "A pilot study in non-human primates shows no adverse response to intravenous injection of quantum dots," *Nature nanotechnology*, vol. 7, pp. 453-458, 2012.
- [102] G. Mandal, M. Darragh, Y. A. Wang, and C. D. Heyes, "Cadmium-free quantum dots as time-gated bioimaging probes in highly-autofluorescent human breast cancer cells," *Chemical Communications*, vol. 49, pp. 624-626, 2013.
- [103] E. Chang, N. Thekkek, W. W. Yu, V. L. Colvin, and R. Drezek, "Evaluation of quantum dot cytotoxicity based on intracellular uptake," *Small*, vol. 2, pp. 1412-1417, 2006.
- [104] R. Schirhagl, K. Chang, M. Loretz, and C. L. Degen, "Nitrogen-vacancy centers in diamond: nanoscale sensors for physics and biology," *Annual review of physical chemistry*, vol. 65, pp. 83-105, 2014.
- [105] F. A. Inam, M. D. Grogan, M. Rollings, T. Gaebel, J. M. Say, C. Bradac, *et al.*, "Emission and nonradiative decay of nanodiamond NV centers in a low refractive index environment," *ACS nano*, vol. 7, pp. 3833-3843, 2013.
- [106] B. R. Smith, D. W. Inglis, B. Sandnes, J. R. Rabeau, A. V. Zvyagin, D. Gruber, *et al.*, "Five - Nanometer Diamond with Luminescent Nitrogen - Vacancy Defect Centers," *Small*, vol. 5, pp. 1649-1653, 2009.
- [107] Y.-R. Chang, H.-Y. Lee, K. Chen, C.-C. Chang, D.-S. Tsai, C.-C. Fu, *et al.*, "Mass production and dynamic imaging of fluorescent nanodiamonds," *Nature nanotechnology*, vol. 3, pp. 284-288, 2008.
- [108] J.-C. Boyer and F. C. Van Veggel, "Absolute quantum yield measurements of colloidal NaYF₄: Er³⁺, Yb³⁺ upconverting nanoparticles," *Nanoscale*, vol. 2, pp. 1417-1419, 2010.
- [109] C. Vinegoni, D. Razansky, S. A. Hilderbrand, F. Shao, V. Ntziachristos, and R. Weissleder, "Transillumination fluorescence imaging in mice using biocompatible upconverting nanoparticles," *Optics letters*, vol. 34, pp. 2566-2568, 2009.

- [110] W. Zou, C. Visser, J. A. Maduro, M. S. Pshenichnikov, and J. C. Hummelen, "Broadband dye-sensitized upconversion of near-infrared light," *Nature Photonics*, vol. 6, pp. 560-564, 2012.
- [111] T. H. Maiman, "Stimulated Optical Radiation in Ruby," *Nature*, vol. 187, pp. 493-494, 1960.
- [112] A. Mandelis, M. Munidasa, and A. Othonos, "Single-ended infrared photothermal radiometric measurement of quantum efficiency and metastable lifetime in solid-state laser materials: The case of ruby ($\text{Cr}^{3+}:\text{Al}_2\text{O}_3$)," *Quantum Electronics, IEEE Journal of*, vol. 29, pp. 1498-1504, 1993.
- [113] M. B. Walter Koechner, *Solid-State Lasers: A Graduate Text*. New York Berlin Heidelberg: Springer, 2002.
- [114] A. Bishay, *Recent advances in science and technology of materials* vol. 2: Springer Science & Business Media, 2012.
- [115] R. H. D. James F. Shackelford, *Ceramic and Glass Materials Structure, Properties and Processing*. New York: Springer Science, 2007.
- [116] D. E. Chandler, Z. K. Majumdar, G. J. Heiss, and R. M. Clegg, "Ruby crystal for demonstrating time-and frequency-domain methods of fluorescence lifetime measurements," *Journal of fluorescence*, vol. 16, pp. 793-807, 2006.
- [117] J. A. Burt, "Spectroscopic Studies of Ruby during Shock Loading," 1989.
- [118] I. A. Rahman and V. Padavettan, "Synthesis of Silica Nanoparticles by Sol-Gel: Size-Dependent Properties, Surface Modification, and Applications in Silica-Polymer Nanocomposites: A Review," *Journal of Nanomaterials*, vol. 2012, pp. 1-15, 2012.
- [119] A. Jaworek, "Micro- and nanoparticle production by electrospraying," *Powder Technology*, vol. 176, pp. 18-35, 2007.
- [120] R. Mueller, L. Mädler, and S. E. Pratsinis, "Nanoparticle synthesis at high production rates by flame spray pyrolysis," *Chemical Engineering Science*, vol. 58, pp. 1969-1976, 2003.
- [121] M. Iwamoto, K. Kuroda, V. Zaporozhchenko, S. Hayashi, and F. Faupel, "Production of gold nanoparticles-polymer composite by quite simple method," *The European Physical Journal D - Atomic, Molecular, Optical and Plasma Physics*, vol. 24, pp. 365-367, 2003.
- [122] K. Nakaso, B. Han, K. H. Ahn, M. Choi, and K. Okuyama, "Synthesis of non-agglomerated nanoparticles by an electrospray assisted chemical vapor deposition (ES-CVD) method," *Journal of Aerosol Science*, vol. 34, pp. 869-881, 2003.
- [123] C. Lam, Y. F. Zhang, Y. H. Tang, C. S. Lee, I. Bello, and S. T. Lee, "Large-scale synthesis of ultrafine Si nanoparticles by ball milling," *Journal of Crystal Growth*, vol. 220, pp. 466-470, 2000.
- [124] B. Cheng, S. Qu, H. Zhou, and Z. Wang, " $\text{Al}_2\text{O}_3:\text{Cr}^{3+}$ Nanotubes Synthesized via Homogenization Precipitation Followed by Heat Treatment," *The Journal of Physical Chemistry B*, vol. 110, pp. 15749-15754, 2006.
- [125] P. Ptacek, "Strontium Aluminate-Cement Fundamentals, Manufacturing, Hydration, Setting Behaviour and Applications," 2014.
- [126] A. Patra, R. E. Tallman, and B. A. Weinstein, "Effect of crystal structure and dopant concentration on the luminescence of Cr^{3+} in Al_2O_3 nanocrystals," *Optical Materials*, vol. 27, pp. 1396-1401, 2005.

- [127] W. M. Zeng, L. Gao, and J. K. Guo, "A new sol-gel route using inorganic salt for synthesizing Al_2O_3 nanopowders," *Nanostructured Materials*, vol. 10, pp. 543-550, 1998.
- [128] T. T. Loan, N. N. Long, and L. H. Ha, "Synthesis and Optical Properties of Al_2O_3 : Cr^{3+} Powders," *e-Journal of Surface Science and Nanotechnology*, vol. 9, pp. 531-535, 2011.
- [129] X. Mi, X. Zhang, X. Ba, Z. Bai, L. Lu, X. Wang, *et al.*, "Preparation and luminescent properties of $\text{Cr}^{3+}:\text{Al}_2\text{O}_3$ nano-powders by low-temperature combustion synthesis," *Advanced Powder Technology*, vol. 20, pp. 164-168, 2009.
- [130] S. Kakooei, J. Rouhi, E. Mohammadpour, M. Alimanesh, and A. Dehzangi, "Synthesis and Characterization of Cr-Doped Al_2O_3 Nanoparticles Prepared Via Aqueous Combustion Method," *Caspian Journal of Applied Sciences Research*;2012, Vol. 1 Issue 13, p16, vol. 1, pp. 16-22, 2012.
- [131] J. Križan, J. Možina, I. Bajsić, and M. Matjaž, "Synthesis and fluorescent properties of chromium-doped aluminate nanopowders," *Acta chimica Slovenica*, vol. 59, pp. 163-168, 2012.
- [132] A. I. Y. Tok, F. Y. C. Boey, and X. L. Zhao, "Novel synthesis of Al_2O_3 nanoparticles by flame spray pyrolysis," *Journal of Materials Processing Technology*, vol. 178, pp. 270-273, 2006.
- [133] C. Sajti, R. Sattari, B. Chichkov, and S. Barcikowski, "Ablation efficiency of α - Al_2O_3 in liquid phase and ambient air by nanosecond laser irradiation," *Applied Physics A*, vol. 100, pp. 203-206, 2010.
- [134] D. Oseguera-Galindo, A. Martinez-Benitez, A. Chávez-Chávez, G. Gómez-Rosas, A. Pérez-Centeno, and M. Santana-Aranda, "Effects of the confining solvent on the size distribution of silver NPs by laser ablation," *Journal of Nanoparticle Research*, vol. 14, pp. 1-6, 2012.
- [135] E. Giorgetti, M. Muniz-Miranda, P. Marsili, D. Scarpellini, and F. Giammanco, "Stable gold nanoparticles obtained in pure acetone by laser ablation with different wavelengths," *Journal of Nanoparticle Research*, vol. 14, pp. 1-13, 2012.
- [136] T. D. Nguyen, Q. D. Nguyen, and T. T. Nguyen, "Preparation of platinum nanoparticles in liquids by laser ablation method," *Advances in Natural Sciences: Nanoscience and Nanotechnology*, vol. 5, p. 035011, 2014.
- [137] R. R. Gattass and E. Mazur, "Femtosecond laser micromachining in transparent materials," *Nature photonics*, vol. 2, pp. 219-225, 2008.
- [138] E. Gamaly, A. Rode, B. Luther-Davies, and V. Tikhonchuk, "Ablation of solids by femtosecond lasers: Ablation mechanism and ablation thresholds for metals and dielectrics," *Physics of Plasmas*, vol. 9, pp. 949-957, 2002.
- [139] S. A. Al-Mamun, R. Nakajima, and T. Ishigaki, "Effect of liquid level and laser power on the formation of spherical alumina nanoparticles by nanosecond laser ablation of alumina target," *Thin Solid Films*, vol. 523, pp. 46-51, 2012.
- [140] K. Yatsui, T. Yukawa, C. Grigoriu, M. Hirai, and W. Jiang, "Synthesis of ultrafine γ - Al_2O_3 powders by pulsed laser ablation," *Journal of Nanoparticle Research*, vol. 2, pp. 75-83, 2000.
- [141] V. Piriawong, V. Thongpool, P. Asanithi, and P. Limsuwan, "Preparation and Characterization of Alumina Nanoparticles in Deionized Water Using Laser Ablation Technique," *Journal of Nanomaterials*, vol. 2012, p. 6, 2012.

- [142] S. Z. Khan, Z. Liu, and L. Li, "Characteristics of γ - Al_2O_3 nanoparticles generated by continuous-wave laser ablation in liquid," *Applied Physics A*, vol. 101, pp. 781-787, 2010.
- [143] I.-Y. Jeon, H.-J. Choi, S.-M. Jung, J.-M. Seo, M.-J. Kim, L. Dai, *et al.*, "Large-scale production of edge-selectively functionalized graphene nanoplatelets via ball milling and their use as metal-free electrocatalysts for oxygen reduction reaction," *Journal of the American Chemical Society*, vol. 135, pp. 1386-1393, 2012.
- [144] C. Lam, Y. Zhang, Y. Tang, C. Lee, I. Bello, and S. Lee, "Large-scale synthesis of ultrafine Si nanoparticles by ball milling," *Journal of crystal growth*, vol. 220, pp. 466-470, 2000.
- [145] W. A. W. Razali, V. K. A. Sreenivasan, E. M. Goldys, and A. V. Zvyagin, "Large-Scale Production and Characterization of Biocompatible Colloidal Nanoalumina," *Langmuir*, vol. 30, pp. 15091-15101, 2014.
- [146] G. R. Karagedov and N. Z. Lyakhov, "Preparation and sintering of nanosized α - Al_2O_3 powder," *Nanostructured Materials*, vol. 11, pp. 559-572, 1999.
- [147] J. S. Forrester, H. J. Goodshaw, E. H. Kisi, G. J. Suaning, and J. S. Zobec, "Effect of Mechanical Milling on the Sintering Behaviour of Alumina," *J. Aust. Ceram. Soc.*, vol. 44, pp. 47-52, 2008.
- [148] C. B. Reid, J. S. Forrester, H. J. Goodshaw, E. H. Kisi, and G. J. Suaning, "A study in the mechanical milling of alumina powder," *Ceramics International*, vol. 34, pp. 1551-1556, 2008.
- [149] M. Muslimin and M. Yusoff, "The Effect of High-Energy Milling on the Crystallite Size of Alumina," 2009.
- [150] R. Tomasi, A. A. Rabelo, A. S. Chinelatto, L. Reis, B. Fo, and J. Walter, "Characterization of high-energy milled alumina powders," *Cerâmica*, vol. 44, pp. 166-170, 1998.
- [151] W. Peukert, H.-C. Schwarzer, and F. Stenger, "Control of aggregation in production and handling of nanoparticles," *Chemical Engineering and Processing: Process Intensification*, vol. 44, pp. 245-252, 2005.
- [152] F. Stenger, S. Mende, J. Schwedes, and W. Peukert, "The influence of suspension properties on the grinding behavior of alumina particles in the submicron size range in stirred media mills," *Powder Technology*, vol. 156, pp. 103-110, 2005.
- [153] A. Tonejc, A. M. Tonejc, D. Bagović, and C. Kosanović, "Comparison of the transformation sequence from γ - AlOOH (boehmite) to α - Al_2O_3 (corundum) induced by heating and by ball milling," *Materials Science and Engineering: A*, vol. 181, pp. 1227-1231, 1994.
- [154] G. Karagedov, "Synthesis, Processing and Sintering of Nanosized Alpha Alumina Powder," *Ceramics-Processing, Reliability, Tribology and Wear, Volume 12*, pp. 63-68.
- [155] D. G. Liu, "Effects of Cr content and morphology on the luminescence properties of the Cr-doped alpha- Al_2O_3 powders," *Ceramics International*, vol. 39, pp. 4765-4769, 2013.
- [156] C. Pflitsch, R. Siddiqui, and B. Atakan, "Phosphorescence properties of sol-gel derived ruby measured as functions of temperature and Cr^{3+} content," *Applied Physics A*, vol. 90, pp. 527-532, 2008.

- [157] H. Chew, "Radiation and lifetimes of atoms inside dielectric particles," *Physical Review A*, vol. 38, p. 3410, 1988.
- [158] W. Q. Zhang, W. Razali, V. Sreenivasan, T. M. Monro, and D. Taylor, "Universal optical fibre fluorescence sensing platform for wine monitoring," in *40th Australian Conference on Optical Fibre Technology (In submission)* Adelaide, Australia, 2015.
- [159] J. Clogston and A. Patri, "Zeta Potential Measurement," in *Characterization of Nanoparticles Intended for Drug Delivery*. vol. 697, S. E. McNeil, Ed., ed: Humana Press, 2011, pp. 63-70.
- [160] R. C. Murdock, L. Braydich-Stolle, A. M. Schrand, J. J. Schlager, and S. M. Hussain, "Characterization of nanomaterial dispersion in solution prior to in vitro exposure using dynamic light scattering technique," *Toxicological Sciences*, vol. 101, pp. 239-253, 2008.
- [161] A. B. Djurišić, Y. H. Leung, A. Ng, X. Y. Xu, P. K. Lee, and N. Degger, "Toxicity of Metal Oxide Nanoparticles: Mechanisms, Characterization, and Avoiding Experimental Artefacts," *Small*, vol. 11, pp. 26-44, 2015.
- [162] S. Gupta, P. C. Ramamurthy, and G. Madras, "Synthesis and characterization of flexible epoxy nanocomposites reinforced with amine functionalized alumina nanoparticles: a potential encapsulant for organic devices," *Polymer Chemistry*, vol. 2, pp. 221-228, 2011.
- [163] F. Meder, T. Daberkow, L. Treccani, M. Wilhelm, M. Schowalter, A. Rosenauer, *et al.*, "Protein adsorption on colloidal alumina particles functionalized with amino, carboxyl, sulfonate and phosphate groups," *Acta Biomaterialia*, vol. 8, pp. 1221-1229, 2012.
- [164] Z. Ghezelbash, D. Ashouri, S. Mousavian, A. Ghandi, and Y. Rahnama, "Surface modified Al_2O_3 in fluorinated polyimide/ Al_2O_3 nanocomposites: Synthesis and characterization," *Bulletin of Materials Science*, vol. 35, pp. 925-931, 2012.
- [165] L. A. S. A. Prado, M. Sriyai, M. Ghislandi, A. Barros-Timmons, and K. Schulte, "Surface modification of alumina nanoparticles with silane coupling agents," *Journal of the Brazilian Chemical Society*, vol. 21, pp. 2238-2245, 2010.
- [166] S. H. Hyun, S. Y. Jo, and B. S. Kang, "Surface modification of γ -alumina membranes by silane coupling for CO_2 separation," *Journal of membrane science*, vol. 120, pp. 197-206, 1996.
- [167] Z. Guo, T. Pereira, O. Choi, Y. Wang, and H. T. Hahn, "Surface functionalized alumina nanoparticle filled polymeric nanocomposites with enhanced mechanical properties," *Journal of Materials Chemistry*, vol. 16, pp. 2800-2808, 2006.
- [168] A. Y. El-Naggar, "Characterization of Modified and Polymer Coated Alumina Surfaces by Infrared Spectroscopy," *Journal of Spectroscopy*, vol. 2013, p. 5, 2013.
- [169] Y.-J. Shin, C.-C. Su, and Y.-H. Shen, "Dispersion of aqueous nano-sized alumina suspensions using cationic polyelectrolyte," *Materials research bulletin*, vol. 41, pp. 1964-1971, 2006.
- [170] P. C. Hidber, T. J. Graule, and L. J. Gauckler, "Influence of the dispersant structure on properties of electrostatically stabilized aqueous alumina suspensions," *Journal of the European Ceramic Society*, vol. 17, pp. 239-249, 1997.

- [171] M. Wiśniewska, K. Terpiłowski, S. Chibowski, T. Urban, V. Zarko, and V. Gun'ko, "Investigation of stabilization and destabilization possibilities of water alumina suspension in polyelectrolyte presence," *International Journal of Mineral Processing*, vol. 132, pp. 34-42, 2014.
- [172] L. Jiang and L. Gao, "Effect of Tiron adsorption on the colloidal stability of nano-sized alumina suspension," *Materials chemistry and physics*, vol. 80, pp. 157-161, 2003.
- [173] R. Greenwood and K. Kendall, "Effect of ionic strength on the adsorption of cationic polyelectrolytes onto alumina studied using electroacoustic measurements," *Powder technology*, vol. 113, pp. 148-157, 2000.
- [174] K. C. Popat, G. Mor, C. A. Grimes, and T. A. Desai, "Surface modification of nanoporous alumina surfaces with poly (ethylene glycol)," *Langmuir*, vol. 20, pp. 8035-8041, 2004.
- [175] L. Gu, D. J. Hall, Z. Qin, E. Anglin, J. Joo, D. J. Mooney, *et al.*, "In vivo time-gated fluorescence imaging with biodegradable luminescent porous silicon nanoparticles," *Nature communications*, vol. 4, 2013.
- [176] H. Li, Y. Yan, B. Liu, W. Chen, and S. Chen, "Studies of surface functional modification of nanosized α -alumina," *Powder Technology*, vol. 178, pp. 203-207, 2007.
- [177] L. Treccani, T. Yvonne Klein, F. Meder, K. Pardun, and K. Rezwan, "Functionalized ceramics for biomedical, biotechnological and environmental applications," *Acta Biomaterialia*, vol. 9, pp. 7115-7150, 2013.
- [178] Y.-C. Yang, S.-B. Jeong, B.-G. Kim, and P.-R. Yoon, "Examination of dispersive properties of alumina treated with silane coupling agents, by using inverse gas chromatography," *Powder Technology*, vol. 191, pp. 117-121, 2009.

Ball-Milling Method and Characterisation of Nanocrystals

In this chapter, production of nanocrystals from crystal materials is reviewed, focusing on a ball-milling approach, which is central to this thesis. Although the presented ball-milling approach is applicable to a broad range of crystals and solid-state material, I predominantly overview the most relevant two types of crystals, alumina (Al_2O_3) and ruby ($\text{Al}_2\text{O}_3\text{:Cr}$), used in the ball-milling processes. The chapter consists of two main parts: The first part introduces the milling approach, including its fundamentals, practical considerations and presents several examples. The second part addresses the instrumental implementation of the ball-milling technology, paying particular attention to instruments employed in this doctoral research project.

3.1 Nanoparticles Production Method

Recently, the nanotechnology field has progressed rapidly heralded by the production of new nanomaterials, pushing the nanoparticle production methods towards facile, inexpensive and large-scale end. The existing production schemes can be broadly classified into bottom-up and top-down approaches illustrated in Figure 3.1. The bottom-up approach implies synthetic production of nanomaterials from atomic and molecular precursors. The bottom-up approaches include hydrothermal, sol gel, electro-spraying, spray pyrolysis, reduction, chemical vapour deposition methods [1-5]. The

advantage of this approach is it produces small and uniform nanoparticles, shape and composition control, and immediate surface-chemistry reactions for surface functionalisation [6-9]. However, in most cases this approach involves in fine control of several reaction parameters, aggregation problem, high temperature treatment, high cost associated with chemicals of high purity, hazardous chemistry procedures, and low production yield [10, 11]. The top-down approaches rely on diminishing the existing bulk materials to nanoscale sizes. The examples of the top-down methods include milling, laser ablation and detonation [12-14]. These methods are usually straightforward and offer high-yield production [12, 15, 16]. At the same time, wide-size distribution of the as-produced nanomaterial, and poor control over the nanomaterial shape and surface properties remain challenges of this approach.

Since the focus of this thesis is on nanoruby and related nanoalumina, it is worthwhile to compare bottom-up and top-down approaches of these nanomaterials production. Most of the bottom-up approaches yielded nanoruby in its less stable crystallographic gamma-phase, which needs further annealing at high temperatures up to 1000°C to transform it to the stable alpha-phase to reinstate its advantageous photoluminescent properties [17, 18]. It is also challenging to realise large-scale production of nanoalumina [19]. Milling method is suitable for large-scale nanoparticle production. However, this method is subject to the contamination from the milling material and defect in the nanocrystalline structure [20, 21]. The contamination mainly due to the wear from milling media including balls and bowl [22]. The contamination can be reduced by choosing suitable milling parameters, which will be discussed in following section.

Laser ablation of ruby crystal has been reported as the top-down production of nanorubies. It yielded high-purity nanorubies, although the operating cost was expensive, and low production yield [23]. The comparison between bottom-up and top-down approach is presented in Table 3.1. The analysis of pro-s and con-s of each method led my colleagues and me to opt for ball-milling as the most suitable method. The versatility of this method was attractive, since it allowed exploration of the whole range of the existing active laser media crystals as potential PL nanomaterials. In the following subsection, I will introduce the ball-milling method.

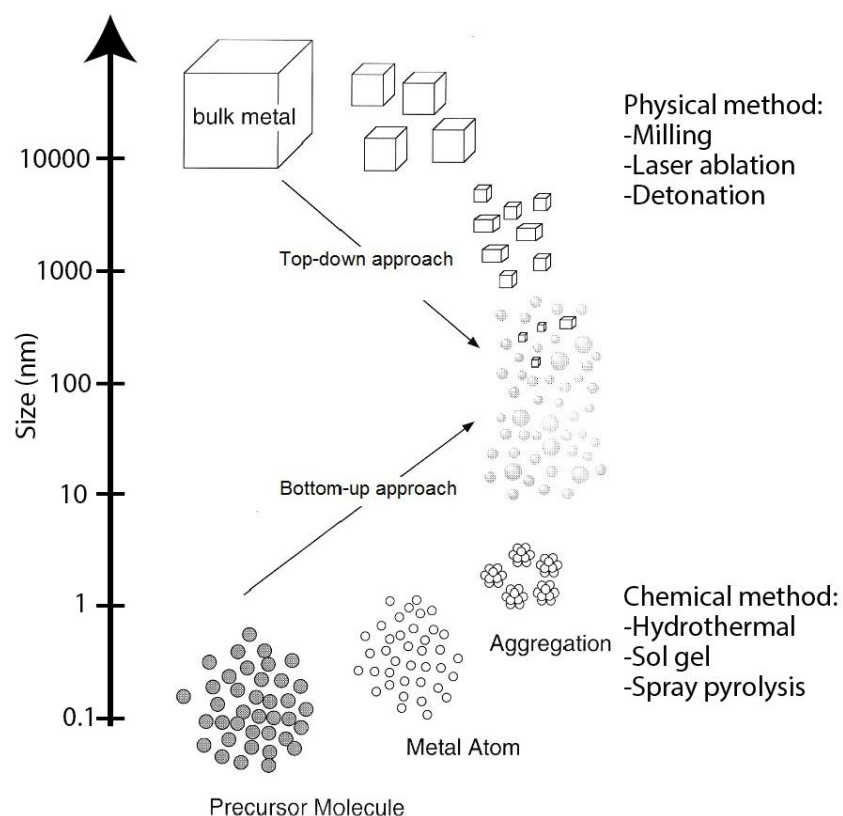


Figure 3.1: Top-down and bottom-up approaches for producing nanomaterials. Adapted from Ref. [24].

Table 3.1: The comparison between bottom-up and top-down approach.

APPROACH	BOTTOM-UP	TOP-DOWN	
METHOD	Hydrothermal, sol-gel, etc.	Laser Ablation	Ball Milling
High production yield	×	×	√
Ease of production	×	√	√
Non hazardous	×	√	√
Low cost	×	×	√
Temperature annealing	×	×	√
Size control	√	×	√
Shape control	√	√	×
Purity	√	√	×

3.1.1 Milling Method

Particle size reduction can be achieved by a crushing and milling process. The crushing process refers to the reduction of large chunks of material to size of several centimetres in diameter or smaller, while milling refers to the reduction of material to sizes in sub-micron or even in the nanometre range [25]. Milling has been used in industries to decrease the particle size, and increase the surface area of solid materials [26]. In the milling process, mechanical alloying (MA) and mechanical milling (MM) are two important terms, which refer to different processes and functions. MA is the process of mixing of two or more materials (metals or alloys) until a homogenous alloy is obtained. While, MM (also refers as mechanical grinding or comminution) is a process where reduction of the particle size and/or other transformations are induced mechanically [27]. In general, MM requires shorter processing times compared to MA, because MM only involves milling of one material, hence it does not require long time to homogenise the materials [27]. In this project, only one material is milled at one time, thus milling only refers to MM. Ruby crystal milling is a challenging task, because the ruby crystal (also known as corundum) is the second hardest material after the diamond [28]. Therefore, several parameters need to be carefully adjusted in order to obtain NPs with desired size, surface properties and monodispersity, while keeping contamination as low as possible [29]. These parameters will be explained in the following section.

3.1.2 High-Energy Ball Milling Method

Milling devices have been developed for different purposes which can be described based on their shape and size. The details of these milling devices are reviewed in Refs [27, 30, 31]. Generally, milling devices can be grouped into low-energy and high-energy ball milling devices (HEBM). The low-energy ball milling includes a tumble, jar and mill [29, 32], whereas HEBM includes attrition/stirred, shaker and planetary ball mills [27, 33]. The HEBM term is frequently used in mechanochemistry to describe the character of applied milling equipment [30]. In order to achieve quick and efficient particle size reduction, HEBM is preferable due to its higher impact on the milling material (also known as feed material), as compared to the low-energy ball milling. My colleagues and I employed HEBM method, which had several advantages, such as a simple set up, requiring small amount of the feed material, good cleanability and

moderate cost of the device [34]. The basic mechanism of HEBM process is that the feed material experiences high-energy impact at a small contact area through compressive shear forces, which are produced by head-on and shearing collision, respectively. The head-on and shearing collision between milling balls as well as between milling balls and inner wall of milling bowl are shown in Figure 3.2. The impact from these collisions, contributes to the formation of cracks, which leads to the breakage of particles, resulting in particle size reduction.

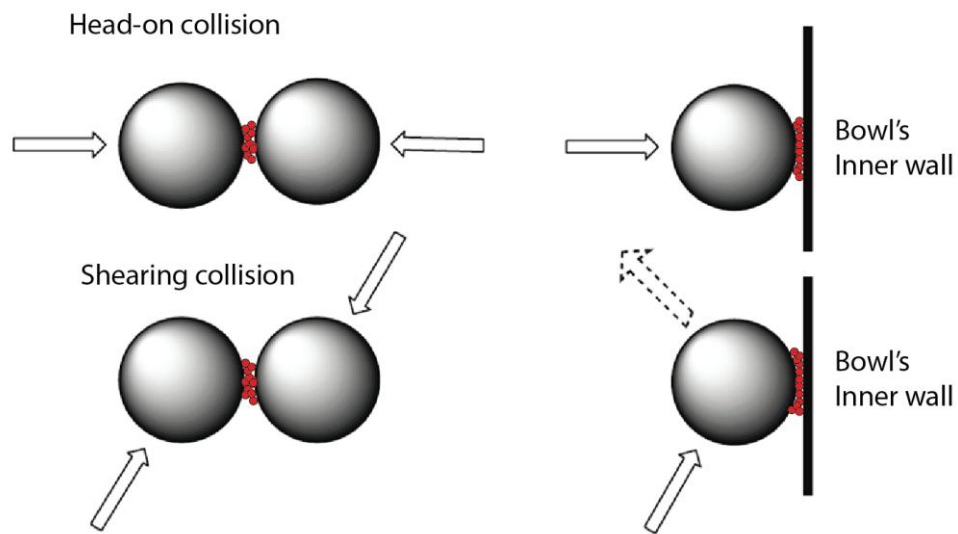


Figure 3.2: The impact energy on feed material (small red circle) at a small contact area between milling balls (large grey balls) in a head-on (top) and shearing collision (bottom) at high speed. Adapted from Ref. [35].

A planetary ball mill consists of a main rotating disk known as a turn-table, which supports two or four bowls. The bowls are placed symmetrically for the mass balance during rotation of the turn-table. The milling bowls rotate with respect to the center of the turn table, and also rotate along their own axis in the different direction, as shown in Figure 3.3a [36]. The milling bowl and the rotating disk rotate in the opposite directions, so that the centrifugal forces alternately act in the same and opposite directions [30, 37, 38]. The milling balls inside the bowl experiences the centrifugal force that leads to large impact energies and effective milling performance. In this milling process, the force acting on balls is amplified and centrifugal force of 50 times gravitational force ($m \times g$) can easily be obtained [29]. As a result, the milling balls move at high speeds along the wall of the milling bowl, and at a certain position, collide

with the opposite wall of the milling bowl, resulting in high-energy collisions impacting the milling material inside the bowl. This motion of the milling balls inside a bowl is depicted in Figure 3.3b. The sample is effectively comminuted through the beating, crushing and milling action.

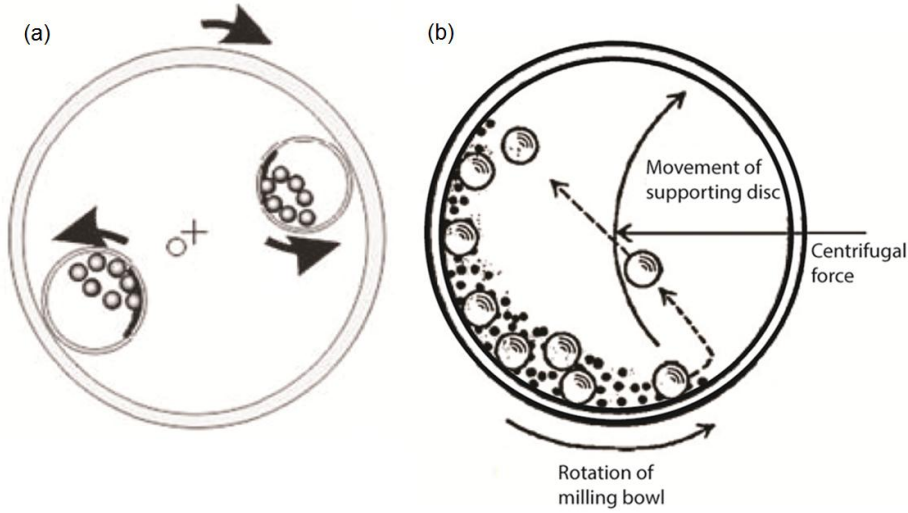


Figure 3.3: (a) The motion of the supporting disk and milling bowl in planetary ball milling (b) The motion of the milling balls inside the bowl. Reproduced from Ref. [29].

3.1.3 Milling Ball Motion and Energy Transfer Model

The milling ball motion in the planetary ball milling has been investigated in detail and reported in literature [36, 39, 40]. The detailed motion of the milling ball in the planetary ball milling is shown in Figure 3.4a. It is shown that the milling bowl rotates around its center C as well as around the origin O , which is the center of the rotating disk in the opposite direction. ω and Ω are the angular velocities of the bowl and rotating disk, respectively. The distance between O and C is r_d and the radius of the bowl is r_c . The rotation of the bowl drives the milling ball to move along the inner wall of the bowl. The different speeds between the bowl's inner wall and milling ball create strong friction, which then acts on the feed material. At a certain point, the centrifugal force from the rotating disk movement forces the milling ball to leave its position from the bowl's inner wall (detachment). The forces involved in this process and the point, where the milling ball detaches from the bowl's inner wall are shown in Figure 3.4b. F_v

and F_d are the centrifugal forces produced by the rotation of the bowl and rotating disk, respectively.

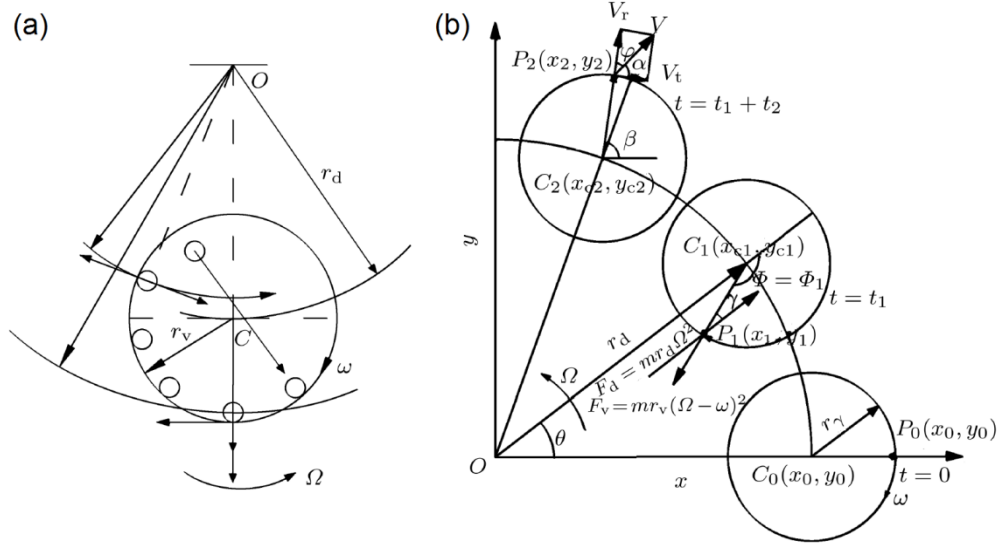


Figure 3.4: (a) Schematic diagram of the milling ball and bowl motion in planetary ball milling. (b) The motion trajectory of a ball, showing the positions of the ball on the bowl's inner wall. P_0 is the initial point ($t=0$), P_1 is the detachment point ($t=t_1$) and P_2 is the collision point ($t=t_1+t_2$). Reproduced from Ref. [39].

The position vectors x and y of the ball at any instant t during this period, can be expressed as:

$$x = r_d \cos \Omega t + r_v \cos (\Omega - \omega) t, \quad (1)$$

$$y = r_d \sin \Omega t + r_v \sin (\Omega - \omega) t. \quad (2)$$

The velocity components in the x and y directions given by:

$$\begin{aligned} \frac{dx}{dt} &= -\Omega r_d \sin \Omega t - (\Omega - \omega) r_v \sin (\Omega - \omega) t, \end{aligned} \quad (3)$$

$$\begin{aligned} \frac{dy}{dt} &= \Omega r_d \cos \Omega t - (\Omega - \omega) r_v \cos (\Omega - \omega) t. \end{aligned} \quad (4)$$

Centrifugal force (F_c) acting on the ball originates from the rotation of the vial and disk (F_v and F_d) and points to the axis of the vial can be obtained,

$$F_c = F_v - \cos \gamma F_d, \quad (5)$$

$$F_d = mr_d \Omega^2, \quad (6)$$

$$F_v = mr_v \omega^2, \quad (7)$$

$$\gamma = \pi - \phi. \quad (8)$$

$$F_c = mr_v \omega^2 + \cos \phi mr_d \Omega^2 \quad (9)$$

the take-off rotation angle

$$\cos \phi_1 = \frac{r_v (\Omega - \omega)^2}{r_d \Omega^2} \quad (10)$$

$$t_1 = \frac{\phi_1}{\omega} \quad (11)$$

The take-off speed (v) of the milling ball at the position P_1 :

$$v = \sqrt{\Omega^2 r_d^2 + (\Omega - \omega)^2 r_v^2 + 2\Omega(\Omega - \omega)r_v r_d \cos \phi_1} \quad (12)$$

Chattopadhyay *et al.* [41] and Yong *et al.* [39] studied the effect of the ω/Ω ratio to the milling balls motion. It was reported that the suitable ω/Ω ratio should be between 0.7 to 3.7. If the ratio is outside this range, the milling ball adheres to the bowl's wall without rolling or sliding on the inner wall [39]. In our experiment, the ω/Ω ratio of our milling instrument was 1, which is in the suitable parameter range.

In order to examine the impact energy generated during the milling process, simulations based on Discrete Element Method (DEM) have been carried out [33, 34, 36, 42, 43], aiming to estimate the grinding rate of the milling process. The numerical results were in good agreement with the experimental result [36]. In this method, Mio *et al.* [36] applied the Voigt model to simulate the force action during the milling balls collision, as shown in Figure 3.5. In this model, two types of forces were considered: a compressive force, F_n and shear force, F_t . These forces can be calculated using the following equation:

$$F_n = K_n \Delta u_n + \eta_n \frac{\Delta U_n}{\Delta t}, \quad (13)$$

$$F_t = \min \left\{ \mu F_n, K_t \Delta(u_t + r_B \phi) + \eta_t \frac{\Delta(u_t + r_B \phi)}{\Delta t} \right\}, \quad (14)$$

where, K and η are spring coefficient and dumping coefficient, respectively, the subscripts n and t denote normal and tangential components. u and φ are relative displacement and relative angular displacement, respectively. μ is the coefficient of friction, and r_B is the ball radius. The detailed parameters used in this simulation can be found in Ref. [36].

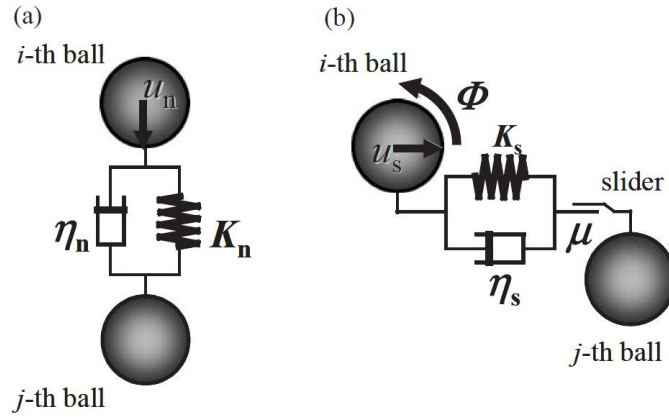


Figure 3.5: Voigt model. (a) Compressive force, (b) shear force.

The impact energy can be calculated from the velocity, v between two colliding balls or a ball colliding against the inner wall of milling bowl. The v can be calculated from Eq. (12) by assuming that the velocity of the ball does not change following the detachment [41]. The equation for the impact energy can be derived from the kinetics energy equation as given by Eq. (15) [36]:

$$E_i = \sum_{j=1}^n \frac{1}{2} m v_j^2, \quad (15)$$

where m is mass of a milling ball, n denotes the number of collisions occurring within a second. The specific impact energy of milling balls, E_w (J/(kg.s)) can be expressed by Eq. (16) and W (in kilogram) is the amount of feed material in the bowl.

$$E_w = \sum_{j=1}^n \frac{1}{2W} m v_j^2 \quad (16)$$

The specific impact energy, E_w can be used to estimate the size of the milled sample and the grinding rate. The K_P can be calculated by the following equation:

$$K_P = k E_w \quad (17)$$

where k denotes as grindability of the sample, which depend on the material properties and/or the initial particle size [43]. This equation shows that the grinding rate can be increased by increasing the revolution speed. The particle size of the sample can be calculated using empirical equation [36]:

$$\frac{D_t}{D_0} = \left(1 - \frac{D_l}{D_0}\right) \exp(-K_p t) + \frac{D_l}{D_0}, \quad (18)$$

where, D_l denotes the median size at grinding limit and K_p is the grinding rate.

3.1.4 Milling Parameters

There are several factors that affect the milling rate, as illustrated in Figure 3.6. However, in this study we only focus on seven main parameters, as given below:

- i. Material of milling ball
- ii. Size of milling ball
- iii. Milling speed
- iv. Milling duration
- v. Charge ratio
- vi. Milling aid

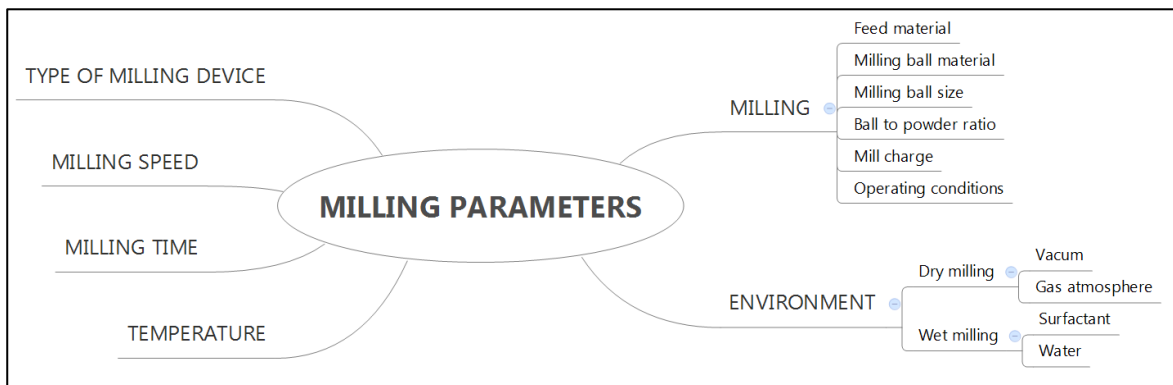


Figure 3.6: An overview of the main factors to be considered in the milling process.

Adapted from Ref. [30].

Materials of Milling Ball

Milling ball selection is based on the properties of powder to be ground. To ensure effective milling, it is important to have milling ball denser than the feed material [30,

44]. Table 3.2 shows the list of the common milling ball, including their properties and specific usage. It is shown that tungsten carbide (WC) milling balls have the highest density, which make them an attractive milling media to achieve the high impact energies and fast size reduction [45]. However, several reasons prevented us from using these to mill alumina and ruby: 1. Our planetary ball mill (Pulverisette 7) is incompatible with WC ball mills in aqueous conditions for prolonged durations (≈ 20 minutes), because of the high internal pressures. 2. Decrease of the milling time to ≈ 5 min on and 8 min off cycles resulted in the blackening of the sample due to contamination. The demonstrated toxicity of the as-produced material to astrocytes and colon epithelial cells [46], especially cobalt-stabilised tungsten carbide NPs, is a concern, contributing to disadvantages of WC milling material.

Table 3.2: Milling ball types with their properties and function. Reproduced from Ref. [45].

Milling ball type	Density g/cm ³	Abrasion resistance	Used for milling material
Agate (SiO ₂)	2.65	good	soft to medium-hard samples
Corundum (Al ₂ O ₃)	3.8	fairly good	medium-hard, fibrous samples
Tungsten carbide (WC)	14.3	very good	hard, abrasive samples
Zirconia (ZrO ₂)	5.9	very good	fibrous, abrasive samples
Stainless steel (Fe, Cr, Ni)	7.8	fairly good	medium-hard, brittle samples
Tempered steel (Fe, Cr)	7.9	good	hard, brittle samples

Figure 3.7 shows the hardness of different types of milling balls and minerals in different scales. The Mohs scale is the scratch hardness of minerals on the basis of 10-step scale. It can be determined by scratching the particular material with the substance of known hardness [47]. While, Brinell (HB), Rockwell (HRA/HRB/HRC) and Vickers (HV) are the scale used for metallurgical industrial sector [48]. Based on Figure 3.7, yttria stabilised zirconia (YSZ) can be used, as an alternative to WC milling balls due to its comparable hardness. Moreover, zirconia milling balls show very good abrasion resistance, indicating low corrosion rate and minimal contamination (see Table 3.2).

Reid *et al.* [49] have reported that zirconia milling ball produced the lowest contamination compared to alumina, steel and WC milling ball suggesting its superior properties. The result is shown in Figure 3.8. In addition, based on zirconia milling balls wear experiment proved that YSZ ball was better than MgO-stabilised zirconia. It was found that yttria-stabilised zirconia ball mass only lost 0.14% , while MgO-stabilised zirconia lost 0.6% after 200-h milling time [50]. Due to these excellent properties, we opted for YSZ milling balls. Although the price of YSZ milling ball is expensive, it can be considered reasonable to be used due to the advanced milling performance and exceptionally long lifetime [50].

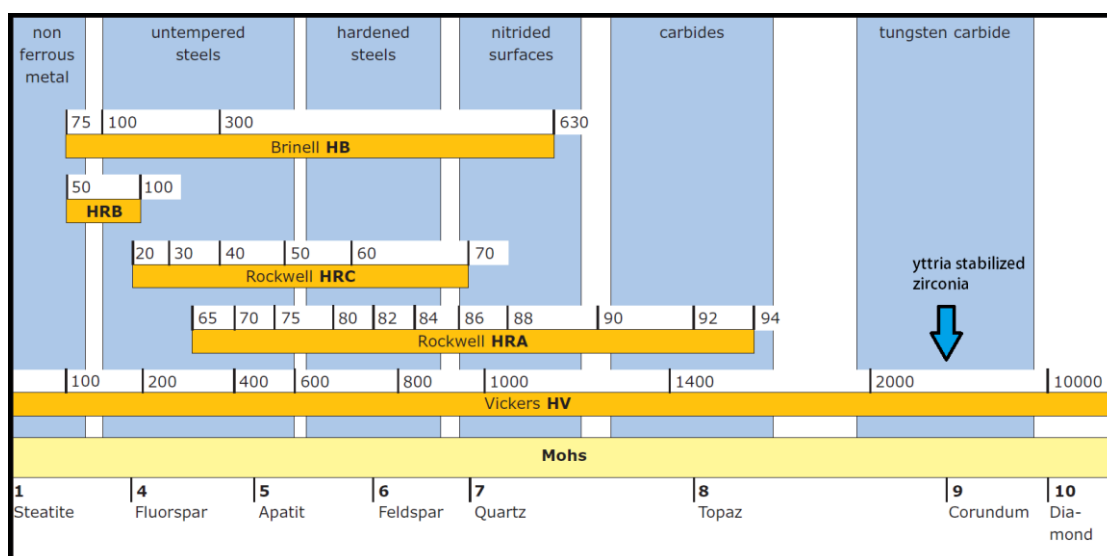


Figure 3.7: Hardness of milling balls and minerals in different scale. Reproduced from Ref. [48]. The arrow shows the hardness of yttria-stabilised zirconia cited from <http://www.noboran.com/>.

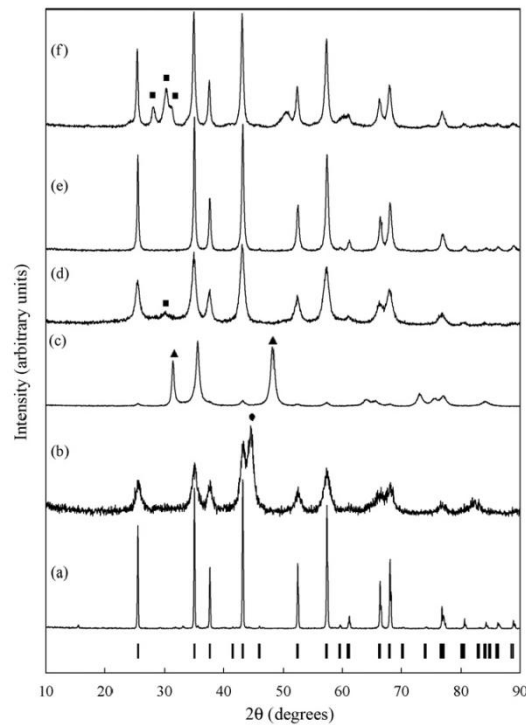


Figure 3.8: XRD patterns from Al_2O_3 powders using selected milling media. (a) unmilled, (b) hardened Fe balls and bowl (● Fe contamination), (c) WC balls and vial (▲ WC contamination) (d) ZrO_2 balls in an ZrO_2 bowl (■ ZrO_2 contamination), (e) Al_2O_3 balls and Al_2O_3 bowl, and (f) Al_2O_3 bowl and Al_2O_3 and ZrO_2 balls. Reproduced from Ref. [49].

Size Selection of Milling Ball

The milling ball size selection is closely related to the type and size of the feed material. An appropriate size of the milling ball is the size that can break the largest feed particles [51]. If the milling ball size is too small, the impact is too weak to break the particle. On the other hand, oversized milling balls reduce the contact frequency and worsen the grinding capacity [51]. Larger balls can deliver larger impact, which is suitable to be applied for breaking large and hard material. From the other reference, the milling ball size is recommended to be between 4 to 10 times the maximum size of agglomerated milling material [52]. This ratio is reported to produce the most effective crushing effect. While based on practical experience, Bond *et al.* [51] suggested that 1-inch milling balls break a 1-mm feed particles, 2-inch milling balls break 4-mm feed particles and 3-inch milling balls break 9-mm feed material particles. In order to

determine the optimal milling ball diameter, Magdalinovic *et al.* [53] have carried out theoretical and experimental study of the effect of milling ball size, and suggested the following universal formula:

$$d_b = Kd^n \quad (19)$$

where d_b is the ball diameter, d is the diameter of the grain size of the feed material, K and n are the parameters, which depend on the mill characteristics, grinding conditions and feed material. This relationship shows that the milling ball and feed material sizes play an important role in the effective milling process. From their calculation, the K and n values for quartz milling was found to be 19.69 and 0.67. Considering the d value is 0.8 mm, the d_b is 17 mm. The proper milling ball size for types of the feed material as suggested by ball milling company is explained in the Table 3.3. The variation of the findings is likely due to different milling methods and types of milling balls.

Table 3.3: Feed material types with respect to the proper milling ball size. Reproduced from Ref. [45].

Types of feed material	Proper ball size
Hard samples with maximum input size of 5 mm	15 mm - 20 mm
Medium input size of 0.5 – 1 mm	10 mm - 15 mm
Fine material 0.1 – 0.5 mm	5 mm - 10 mm
Very fine material < 0.1 mm	3 mm or smaller
Homogenizing of dry or liquid samples	10 mm - 5 mm

For NPs production, small-size milling balls are required, since the smaller milling balls generate more contact per mill revolution due to the smaller spaces created between the balls during the collision, thus they can produce smaller particle [45, 54]. The milling ball companies recommend the milling balls with the diameter between 0.1 mm and 0.3 mm for nanoparticle production [55]. In addition, they claim that the final particle size that can be obtained is $1/1000^{\text{th}}$ of the milling balls size. According to this recommendation, particle size of 100 nm requires 0.1 mm milling ball. Stenger *et al.* [56] have investigated the influence of the milling ball diameter (varied from 1.3 mm size to 0.2 mm) to the resultant particle size. They concluded that 0.2-mm ball produced the smallest particle size below 10 nm (see Figure 3.9). In contrast, Boudou *et al.* [57] have reported the production of nanodiamonds, with the resultant size ≈ 10 nm using 10-

mm tungsten carbide milling balls. In their work, diamond powder with 2- μm size was milled for 24 hours to achieve the nanoscale range. However, the large size of milling balls is likely to produce serious contaminations due to the corrosion of the ball milling surface, as a result of the high collision impact between milling balls. By considering these findings, the ball size of 0.2 mm seemed the most reasonable to produced ruby nanoparticles.

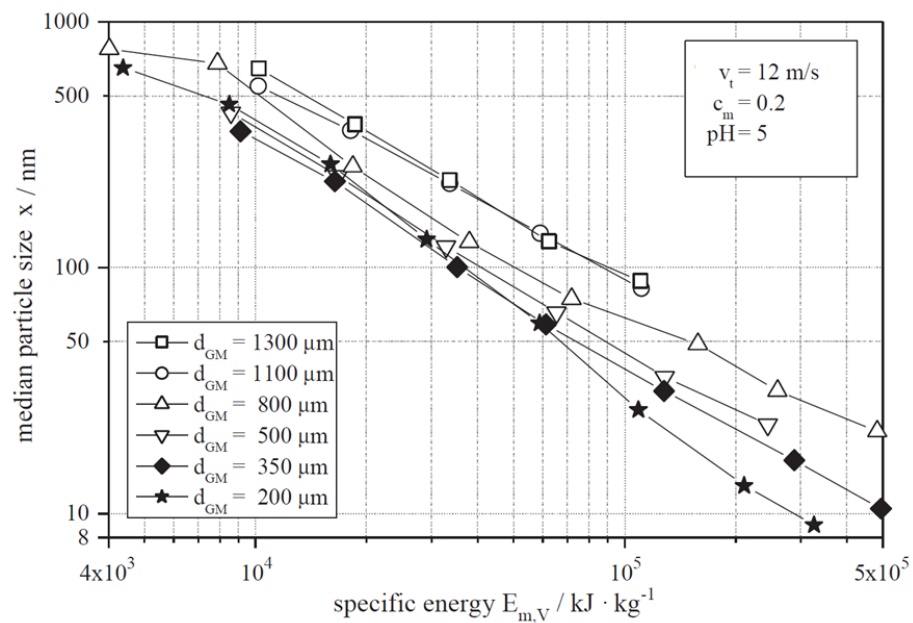


Figure 3.9: Influence of zirconia milling ball diameter (d_{GM}) on the milling result. V_t is milling speed and c_m is mass concentration. Reproduced from Ref. [56].

Milling Speed

Generally, higher milling speed gives faster size reduction. Based on Mio *et al.* [42] experimental and simulation analysis of particle size at different speeds, the smaller particle size can be obtained faster with higher milling speed. Their result is shown in Figure 3.10. Ahamed *et al.* [58] have demonstrated the higher milling speed produced crystallites of the smaller sizes. In their study, 6063-alloy milled for 20 hours with 300 rpm and 700 rpm milling speed. 32-nm and 55.46-nm crystallite sizes were achieved after 20 h at 700 rpm and 40 h at 300 rpm milling, respectively. Rochman *et al.* [59] have reported that the processes of amorphisation, super-saturated solid solution and particle refinement were faster with the increase of the milling speed. Also, at the high milling speed, the temperature can increase drastically, which may affect the sample

properties. However, the temperature can be controlled by introducing a pause time after a certain time range and using a fan installed in the milling machine. 8 min pause time following 5 min of the milling was chosen for the experimental conditions used in our experiment, ensuring the outside bowl's temperature less than 70 °C.

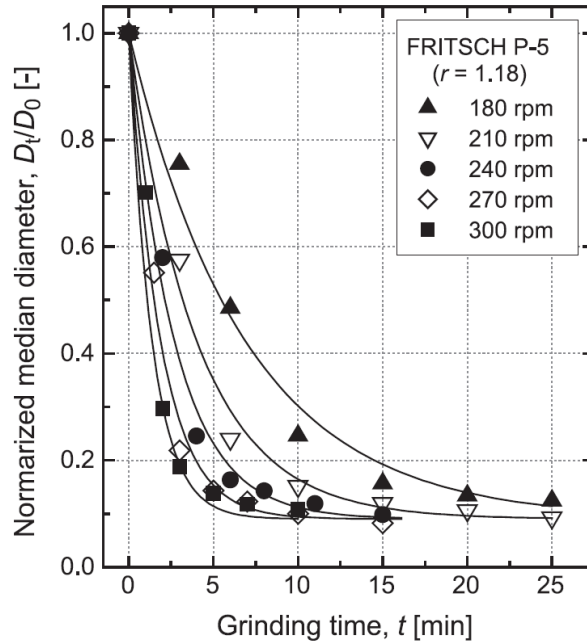


Figure 3.10: Normalised median diameter of the sample ground by the planetary ball milling (Pulverisette-5) as a function of milling time at different speeds. r is the speed ratio between bowl and disk. The marked values are the experimental data while the solid lines are the simulation results. Reproduced from Ref. [42].

Milling Duration

The longer milling duration can provide the finer particles, and could lead to structural changes in the sample [60, 61]. Heitjans *et al.* [62] have demonstrated milling LiNbO_3 , Li_2O , $\alpha\text{-Al}_2\text{O}_3$ and TiO_2 micron-sized powders using a shaker mill (SPEX 8000), with alumina bowl/balls. The study showed that the average grain diameter of nanocrystallite ceramics was reduced with the longer milling duration. It was found that the sample size decreased in the first 5 hours of the milling. However, no further size reduction was observed after 5 hours, with the resultant average grain size of about 20 nm, as shown in Figure 3.11. This observation was explained as the saturation effect, and can be minimised under liquid nitrogen environment [63]. Similar trend was observed by Zahrani *et al.* [64], who showed that the size of the fluorapatite nanocrystalline

stabilised after 4 hours of milling. They also found that the crystallite size increased with decreasing the milling speed or by decreasing the powder-to-ball weight ratio. Li *et al.* [65] have produced the nanometre-sized grains of Cu using HEBM method and found that the grain sizes decreased, as the milling time increased, approaching a steady value of about 27.5 nm after 9 hours. On the other hand, Lee *et al.* [61] reported that the longer milling led to the phase evolution of Fe_2O_3 NPs during the milling process. Besides, the longer milling duration also lead to the increase of contamination, which was corroborated by Castro *et al.* [66]. In the reported case, aluminum particles of the purity 99.9%, with the size range of 50-100 μm were milled by using a SPEX 800 ball mill. In their work, stainless steel and WC milling ball/bowl were employed. From the X-ray fluorescence (XRF) analysis, the contamination was found to increase with the longer milling time. The result is shown in Figure 3.12.

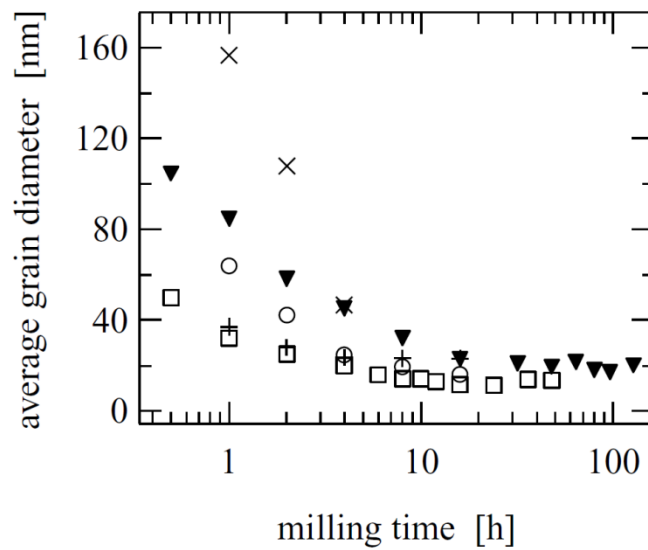


Figure 3.11: Average grain sizes versus milling time for some oxide ceramics: LiBO_2 (□), LiNbO_3 (▼), Li_2O (+), $\alpha\text{-Al}_2\text{O}_3$ (○) and TiO_2 rutile (×). Reproduced from Ref. [62].

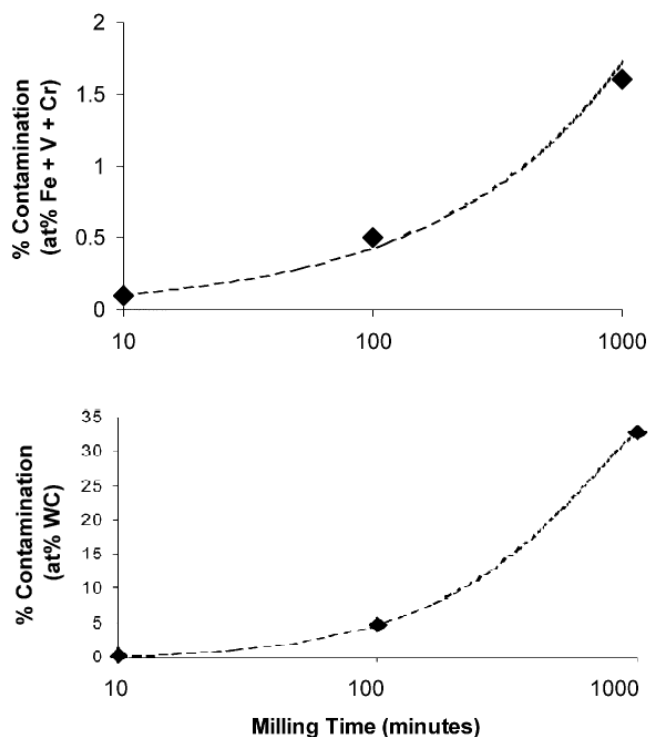


Figure 3.12: A plot of the contamination level in aluminum powder milled with stainless steel (top) and WC (bottom) milling balls/bowl, as a function of the milling time. Reproduced from Ref. [66].

Charge Ratio

Charge ratio (CR) is defined as the ratio of the mass of balls to the powder, which also known as a ball-to-powder ratio (BPR). CR values have been reported in the literature [37, 60, 67, 68]. Normally, the CR ratio is chosen between 5:1 to 20:1. The CR value has a significant effect on the milling time to achieve small particle size within the shortest time frame. However, the CR value needs to be carefully selected, it represents a trade-off between the milling time and contamination level of a sample. Also, the filling needs to be considered. It is also suggested that, 50% of the space should be left empty in order to give enough space for balls to accelerate [69].

The effect of the CR on the milling sample has been reported in literature. Sneed *et al.* [37] have investigated the variation of the CR from 10:1 to 30:1 to prepare aluminum-nanodiamond composite. They found that 30:1 CR produced the smallest and most uniform particle sizes with good dispersion. Othman *et al.* [68] have demonstrated milling of hydroxyapatite material, using several types of milling balls (stainless steel, agate, alumina and zirconia), with CRs of 5:1, 10:1, 15:1 and 20:1. They found that only

agate and stainless steel milling balls led to the formation of single-phase hydroxyapatite nanocrystals. Stainless steel milling balls with the CR of 10:1 were found to produce the finer powder compared with the 20:1 CR [68]. In the report most relevant to the topic of this dissertation, Reid *et al.* [49] have demonstrated milling alumina powders, using the CR ratio of 10:1, whereas Forrester *et al.* [67] used 3:1 ratio for the same material to reduce the contamination. While Salah *et al.* [60] demonstrated the production of ZnO NPs using the CR 15:1 ratio and successfully obtained nanoparticles mean-sized 30 nm.

From the information above, the reasonable CR value is estimated to be $\approx 10:1$. This ratio can be increased in order to get a shorter milling time. However, contamination is also increases versus the high CR value. If the contamination level is high, one should reduce the CR value and at the same time increase the milling time. In the case of milling balls with the higher abrasion resistance, the CR value can be set higher.

Milling Aid

Wet milling is an important approach to obtain small-size NPs. This approach provides the faster size reduction and smaller-size particles compared to the dry milling, as illustrated in Figure 3.13. The material packing effect taking place in the dry milling precludes the production of the smaller size particles [52], and can be reduced by using dispersing agents, underpinning a rationale behind the wet milling. The major challenge of the size reduction in the submicron particle size range is an attraction force between small particles, which result in their agglomeration and mutual adherence. These small particles, especially in the nanometre range, have a strong tendency to agglomerate, owing to their relatively large specific surface area, which increases Van der Waals attraction between these particles.

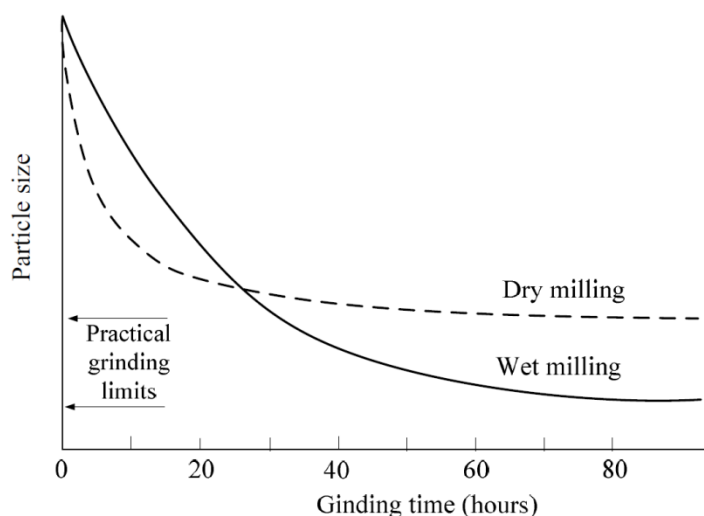


Figure 3.13: Schematic diagram of the effect of wet milling on the particle size. Reproduced from Ref. [70].

The agglomeration reduces the milling efficiency by counteracting the milling forces. Figure 3.14 shows how the agglomeration affects the efficiency of the milling process [71]. Milling in liquid reduces this effect by creating the higher shear force of the feed material and makes the transport of additives to the particle surfaces easier. Therefore, in case of the nanoparticle production, milling aid (also referred as processing control agent or lubricant) is important. Also, the milling aid helps the milling process by adsorbing on the surface of the particles to minimise cold welding between powder particles [72]. Cold welding effect results in bonding smaller nanoparticles to one another [73]. Peukert *et al.* [74] have modelled this process and demonstrated that oxide particles as small as 10 nm can be produced by using suitable milling aid.

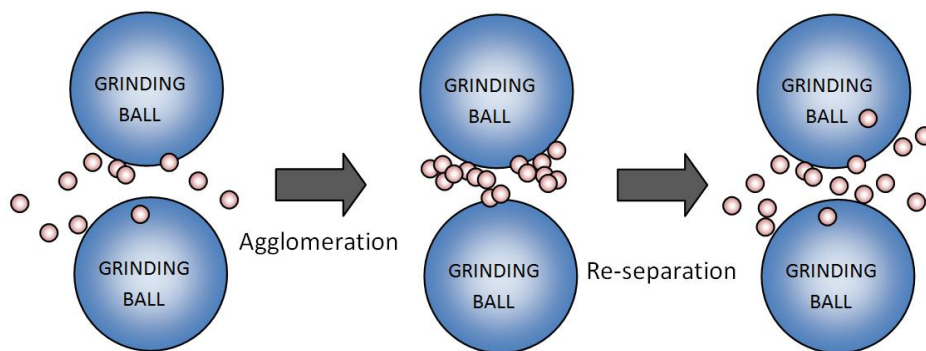


Figure 3.14: The effect of agglomeration on the efficiency of the milling process.

Distilled water was used as a milling aid for alumina [75] and iron [15, 76] powder milling. Lee *et al.* [61] have applied methyl alcohol to produce iron-oxide NPs. After 100-h milling, the sample crystallite size was found significantly reduced to 11.5 nm. Sack *et al.* [77] used methanol and methyl isobutyl ketone, as a milling suspension in order to study the milling behaviour of alumina powder. Akdogan *et al.* used a wet milling method to produce anisotropic $\text{Nd}_2\text{Fe}_{14}\text{B}$ NPs. Heptane (99.8%) mixed with oleic acid (OA) (90%) was applied as a milling aid and it strongly influenced the evolution of the particle shape [78].

The suspension stability of the milling sample can affect the size and stability of as-produced NPs [56, 79]. Sakthivel *et al.* [79] have investigated the effect of pH suspension on the stability and particle size of silica NPs. NaOH was used to change the pH of the sample suspension. Their result showed that pH 12 gave the highest zeta-potential of -51.2 mV, indicating a stable suspension was produced. This pH value also enabled the improved size reduction compared to pH 10 and 8 with the resultant size of 29 nm. Stenger *et al.* have reported that the low suspension pH value produced smaller alumina particle and suggested that the suspension stability did not influence the milling behavior, but influenced the dispersed state of particles [56].

3.1.5 Milling Procedure and Related Apparatus

The feed material needs to be prepared before commencing the milling process, except for micron-sized particles, such as commercially-available alumina micronised powder, which is suitable for straightforward milling. The main material of this project, synthetic ruby crystal sized $7\text{ cm} \times 2\text{ cm} \times 1\text{ cm}$ (Figure 3.15) had to be crushed prior to milling. This process can be carried out by using a hydraulic press (Enerpac, US), as shown in Figure 3.16, by crushing the ruby crystal repeatedly, until it breaks into small pieces. Then the crushed ruby crystals are sieved using a $63\text{-}\mu\text{m}$ metal sieve to collect only small size ruby crystal particles. The remaining particles, which do not pass sieve holes, undergo repeated crushing, until a desired amount of the powder is collected.

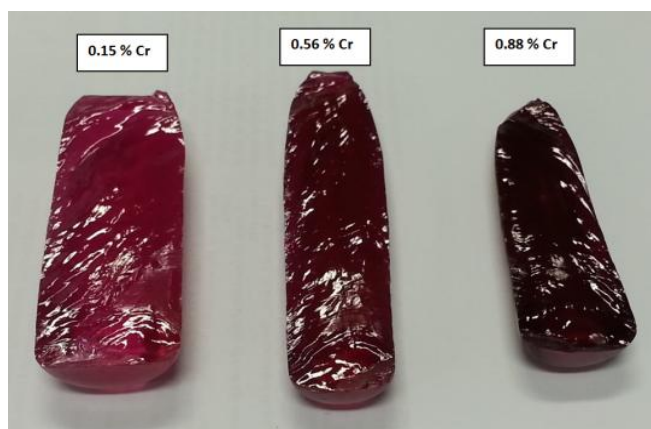


Figure 3.15: Synthetic ruby crystals of the three doping ratios of Cr^{3+} .



Figure 3.16: Hydraulic press.

A Pulverisette-7 (Fritsch, Germany) high-energy planetary ball mill (Figure 3.17) can be used to mill micrometre-sized alumina/ruby powder. 30 g of 0.2 mm YSZ milling balls (Glenmill, USA) are filled into a 20-mL zirconia bowl (Figure 3.18). 3 g of alumina/ruby powder is placed on the top of a YSZ milling ball layer, followed by an addition of 9-mL milliQ water, as the milling aid. The bowl is closed tightly with a lid. A rubber seal is also placed in between the bowl's rim to ensure the bowl is sealed tightly. This rubber seal also has a semi-circle notch with a diameter of 2 mm (see dashed circle in Figure 3.18b), which functions to release the pressure during

overpressure condition. The maximum speed of 1100 rpm is typically chosen in order to get the fastest size reduction. The milling process is carried out by 3-min milling time, followed by 8-min pause time, in order to maintain the external bowl temperature below 70°C. The milling process is done for 100 cycles, which is equivalent to 5-h milling time.

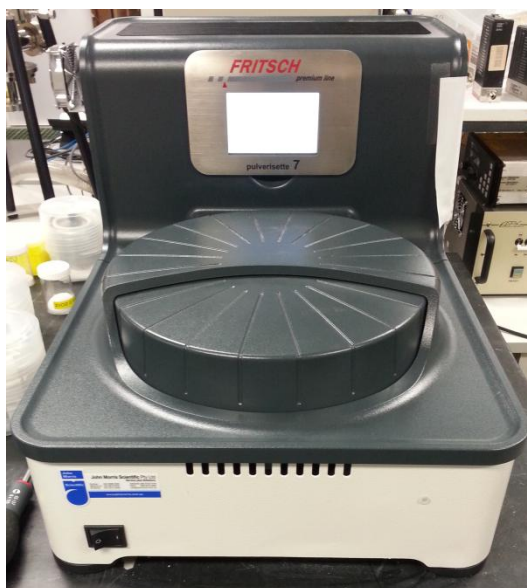


Figure 3.17: Pulverisette-7 machine.

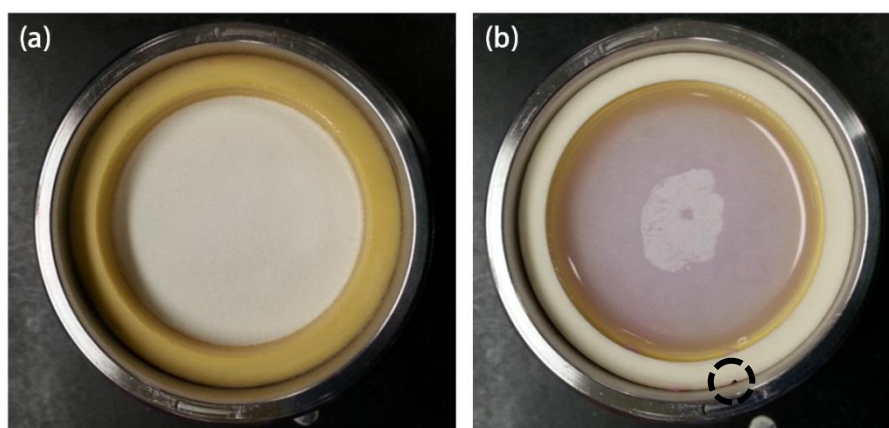


Figure 3.18: (a) 0.2-mm Yttria-stabilised Zirconia (YSZ) milling balls inside zirconia bowl. (b) The bowl filled with ruby powder and water. A rubber seal placed on the bowl's rim. A semi-circle notch marked by the dashed circle.

For the extraction process, the lid is removed and replaced with a discharge device, which consists of a 0.08-mm metal sieve, as shown in Figure 3.19a. Then, 50 mL syringe is attached to the discharge device and 10-mL MilliQ water is pumped into the bowl. In the upside down position, the suspension is shaken several times until the sample and water are mixed properly (Figure 3.19b). The sample is then transferred into a syringe by pumping the syringe several times. Then the extracted sample is transferred into a bigger container. This process is repeated several times until the extracted suspension becomes clear.

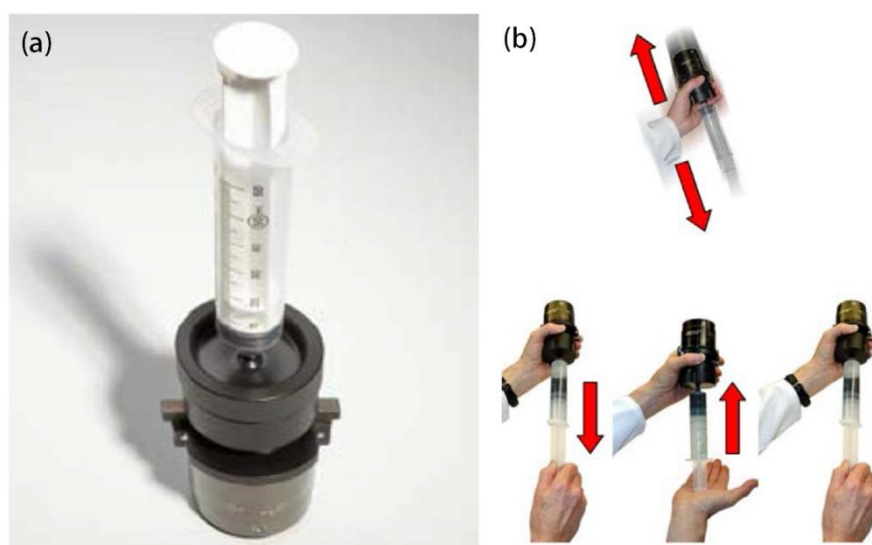


Figure 3.19: (a) The bowl with a discharge device and syringe. (b) Shaking (top) and pumping (bottom) process.

3.2 Characterisation Techniques

Techniques that are conventionally used for characterisation of as-produced nanoparticles are described in this second part of the chapter. Brief explanation of the basic principles of these instruments and sample preparations are also provided. A particular attention is paid to the characterisation techniques and methods, which are directly applicable to the procedures used in this project.

3.2.1 Dynamic Light Scattering

Dynamic light scattering (DLS) is a technique for measuring particle size based on the dynamic changes of the scattered light intensity [80]. Zetasizer Nano-ZS (Malvern, UK) is the most common commercially-available DLS instrument for measuring the size

distribution and zeta potential of NPs in a colloidal form (as shown in Figure 3.20a). For the sample preparation, the NPs (nanoalumina or nanorubies) are diluted in either water or buffer and transferred to a capillary cell (DTS1070, Malvern, U.K.) for measurement. A typical set-up for the DLS instrument is shown in Figure 3.20b. The main components of this instrument are a diode laser source operating at wavelength of 630 nm, sample chamber and detector. The laser light beam is focused into the sample, which is then scattered by particles undergoing a Brownian motion in a liquid. The scattered light is collected by the detector for further analysis. The intensity of the scattered light is measured at a given angle as a function of time. The Brownian motion of the dispersed particles determines the rate of the change of the scattered light intensity. Small particles diffuse more quickly in a liquid compared to the larger particles. Therefore, the particle root-mean-squared velocity is used to determine the size of the particle [81]. For the measurement, the mean translational diffusion coefficient is obtained from the temporal intensity changes. The fast intensity changes are related to a rapid decay of the correlation function and a large diffusion coefficient. The diffusion coefficient is then used to calculate the particle size by using Stokes–Einstein equation [82].

$$D = \frac{\kappa T}{6\pi\eta R} \quad (20)$$

where D is the diffusion coefficient of the particle, κ is the Boltzman's constant, T is the temperature, η is the viscosity of the solvent and R is the radius of the particle.

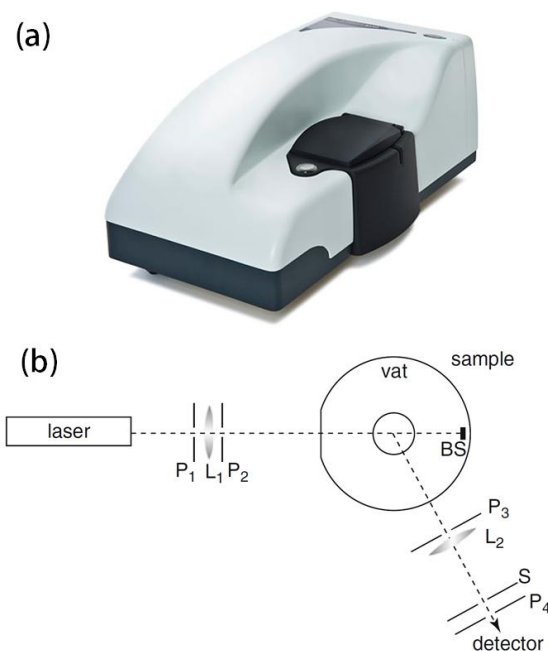


Figure 3.20: (a) Zetasizer Nano-ZS system. (b) Typical set-up of a DLS instrument. P, L, BS, and S are pinholes, lens, beam stop, and slits respectively. Image (a) taken from <http://www.malvern.com/> and (b) Reproduced from Ref. [80].

Also, DLS is capable to measure the zeta potential, which is a physical property related to the electrostatic charge associated with the solid/liquid interface. Zeta potential is a useful parameter for the quantitation of the surface charge of NPs. The surface charge value can determine the degree of the stability of the sample. Stable colloids are characterised by a high magnitude of the zeta potential ($|\zeta| > 30$ mV) [83]. Specifically, the zeta potential is the electrostatic potential measured at the fluid slippage plane. The slippage plane is a virtual boundary that separates the ions that move with the nanoparticle and the ions that stay with the stationary bulk solvent, as shown in Figure 3.21. Zeta potential can be determined by measuring the velocity of a particle moving in a liquid, when an electrical field is applied, which is referred as electrophoretic mobility. The Henry's equation is used to calculate the zeta potential [84].

$$U_E = \frac{2\varepsilon \zeta f(ka)}{3\eta} \quad (21)$$

where U_E is the electrophoretic mobility, ε is the dielectric constant, ζ is the zeta potential, η is the viscosity of the dispersant, and $f(ka)$ is the Henry function. The $f(ka)$ value is 1.5 and 1 for high ionic strength and low dielectric media, respectively.

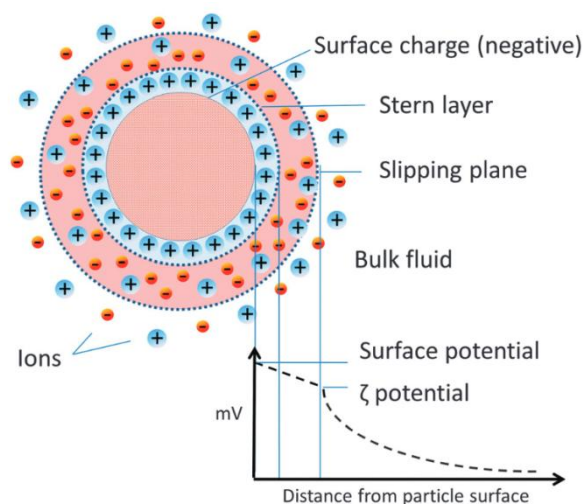


Figure 3.21: Schematic representation of the zeta potential: ionic concentration and potential differences as a function of the distance from the charged surface of a particle suspended in a medium. Reproduced from Ref. [85].

3.2.2 Transmission Electron Microscopy

Transmission electron microscopy (TEM, Philips CM10, Netherlands) operates at an acceleration voltage of 100 kV (Figure 3.22) is used to determine the size and morphology of as-produced NPs, in our case, nanoalumina/nanoruby. Several drops of the sample under investigation are deposited on a 300-mesh copper grid and allowed to dry in a desiccator. In the TEM imaging system, a beam of electrons is focused onto a sample and their absorption is detected in transmission providing details on internal composition of the sample. The transmitted electrons are detected on a cathodoluminescent screen, photographic film layer or intensified CCD camera. TEM providing the atomic-scale resolution (≈ 0.1 nm), is useful for imaging micro-particles and NPs, whose morphological features are on the nanometre-scale [86]. A limitation of TEM relates to the required vacuum conditions and time-consuming involved sample preparation procedures [87]. The obtained TEM image are usually digitally analysed to obtain the particle size distributions.

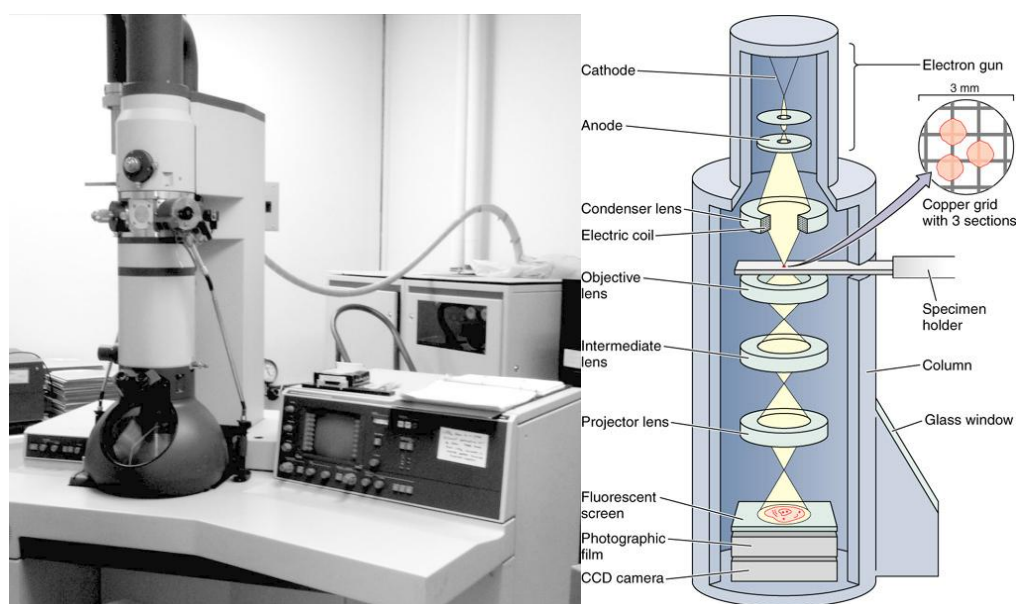


Figure 3.22: (a) Philips CM10 Transmission electron microscope (TEM) (b) Schematic diagram of a TEM. Image (a) taken from <https://www.utoledo.edu/and> (b) <http://intranet.tdmu.edu.ua>

3.2.3 Scanning Electron Microscopy

Scanning electron microscope (SEM; JEOL 6480LV, JEOL Ltd, Japan) (Figure 3.23a) is used to measure the size of micro-alumina powders. The sample is prepared by drop-casting a 20- μ L alumina suspension on a glass coverslip and letting it dry, using a hot plate and sputter-coated with a gold layer prior to imaging. Scanning electron microscopy (SEM) imaging is mostly used, as a surface imaging tool that provides morphological (3D) and topographical characteristics of the specimen surface with the resolution attainable at the scale of ≈ 10 nm. An electron column is the main component of SEM instrument, where an electron beam is generated under vacuum focused to a small diameter, and scanned across the surface of a specimen by electromagnetic deflection coils. An electronic console provides control over the instrument adjustments, such as the filament current, accelerating voltage, focus, magnification, brightness and contrast. In this technique, a tightly focused beam of electrons is raster-scanned over a specimen, while secondary or backscattered electrons are detected, as shown in Figure 3.23b [88]. Relatively large field-of-view and reasonably high magnification attributed to SEM modality are useful for searching small structures, such as single NPs and investigating biological objects [89]. The advantage of this method is

the sample preparation at the nano-scale thickness is not required. Hence, SEM is considerably simpler compared to TEM due to facile sample preparation procedure.

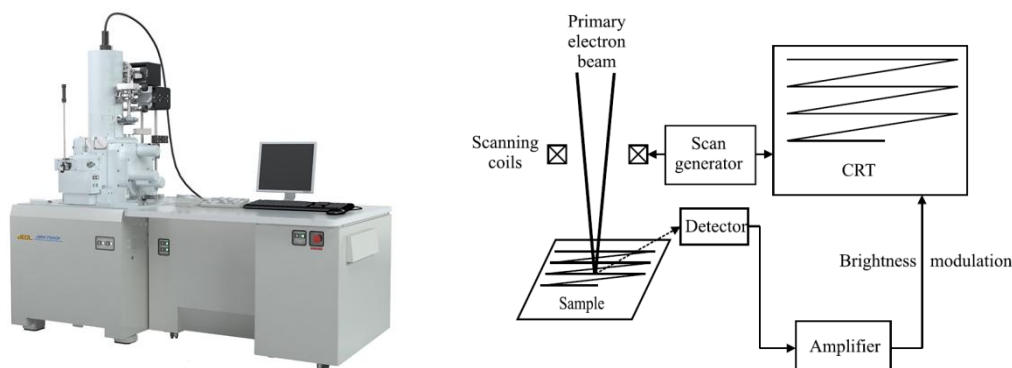


Figure 3.23: (a) JEOL Scanning electron microscope (SEM) (b) Schematic diagram of a SEM principle. Image (a) taken from <http://www.jeol.co.jp/en/products/> and (b) Reproduced from Ref. [90].

3.2.4 Energy-Dispersive X-Ray Spectroscopy

Energy-dispersive X-ray spectroscopy (EDX) detector JED-2300 (JEOL Ltd, Japan) is used for the elemental analysis (Figure 3.24a). A few drops of the nanoalumina/nanoruby sample under investigation are dried on a clean glass coverslip, transferred onto a sticky carbon stub, and pressed gently using a spatula to ensure sample preservation. Loosely adhered sample grains are removed from the carbon stub with a blower to avoid contamination of the EDX vacuum chamber during measurements. EDX analysis is an energy dispersive spectroscopy of the X-rays emitted from a sample during electron irradiation [90]. The detection technique resembles that of a backscattered-electrons solid-state detector. X-rays penetrating the semiconductor detector are absorbed and it generates electron–hole pairs. The formation of such a pair in a silicon semiconductor requires energy of approximately 3.8 eV. The number of electron–hole corresponding to a current pulse is measured by using an n-doped silicon detector crystal (Figure 3.24b), which generates charge carriers. The charges are amplified in a field effect transistor (FET). To suppress the thermal noise of the amplifier, the detector is usually cooled with liquid nitrogen. The charges produced are integrated and processed to determine the energy of an individual detected X-ray photon [90]. EDX spectrum is generated and represented as a plot of X-ray counts versus

energy (in keV) (see Figure 3.25). Each chemical element has characteristic peak positions corresponding to the allowed transitions in its electron shell. Therefore, the element of the analysed sample can be identified based on the peak present in the EDX spectrum. The example of EDX spectrum with identified peak is shown in Figure 3.25.

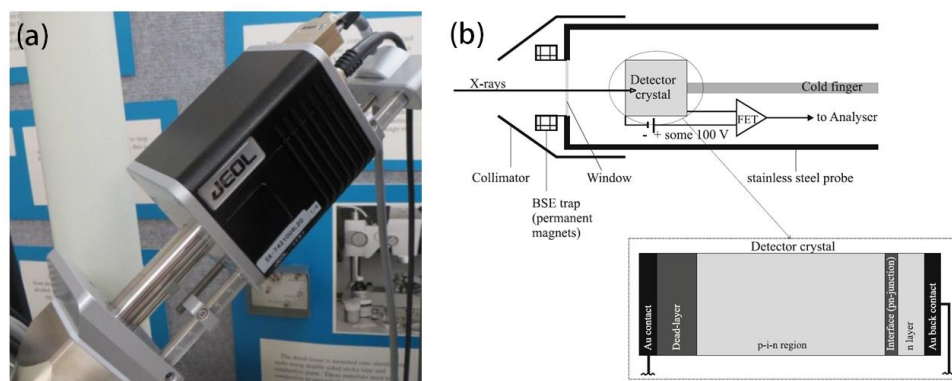


Figure 3.24: (a) JEOL EDX detector (b) Schematic diagram of EDX detector. Image (b) Reproduced from Ref. [90].

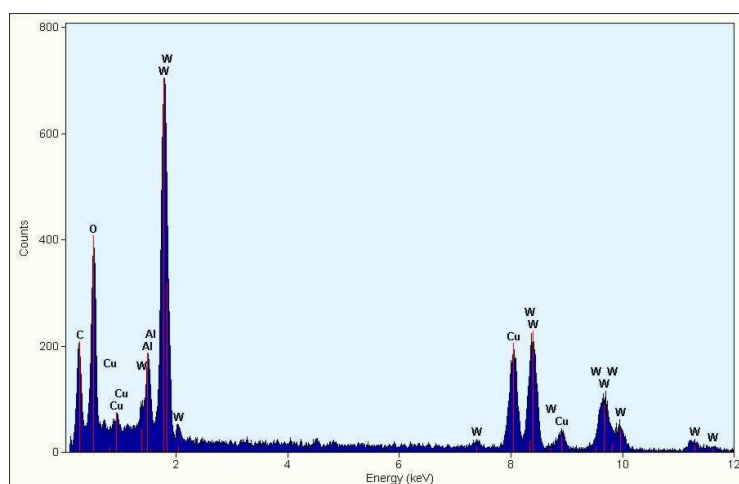


Figure 3.25: A typical EDX spectrum of aluminum tungsten oxide. Image taken from Ref. [91].

3.2.5 X-Ray Diffraction

The crystal structure of nanoalumina/nanoruby sample can be determined by X-ray diffraction spectroscopy (XRD) using an X'Pert PRO analytical diffractometer (PANalytical, Netherlands) (Figure 3.26a) acquired in the diffraction angle (2θ) range from 5 to 90° . The diffractometer is operated at a tube voltage and current of 45 kV and

40 mA, respectively. Several drops of the sample are deposited on a low-background silica mount and dried in an oven prior to the measurements.

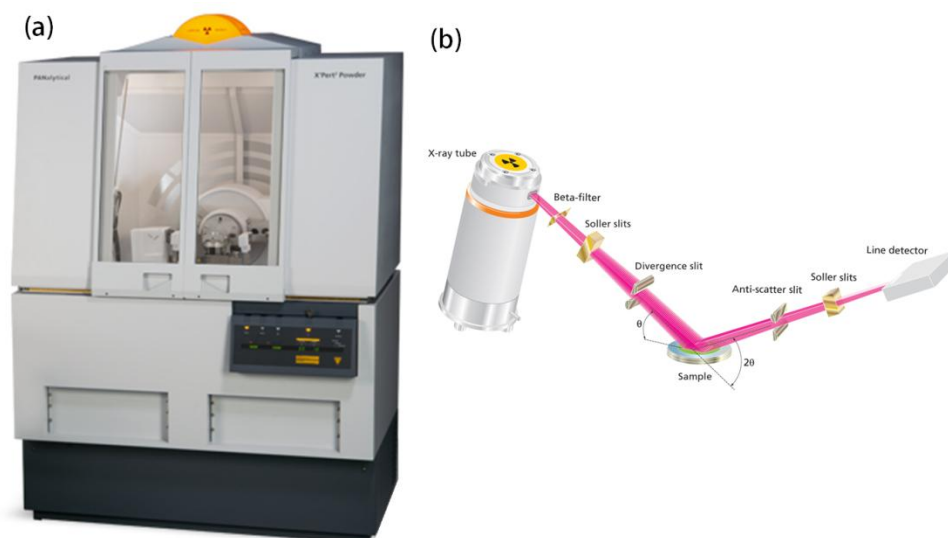


Figure 3.26: (a) PANalytical X'Pert Pro X-ray diffraction (XRD) system. (b) A schematic diagram of XRD system. Images taken from <http://www.panalytical.com/>

X-ray diffraction (XRD) technique is based on constructive interference of monochromatic X-rays and a crystalline sample [67]. These X-rays are generated by a cathode ray tube and fired onto the sample. The interaction of the incident rays with the sample produces constructive interference (and a diffracted ray), when the conditions satisfy Bragg's law ($n\lambda=2d \sin\theta$) (Figure 3.27). This law relates the wavelength, λ of the X-ray radiation to the diffraction angle, θ and the lattice spacing, d in the crystalline sample (n is an integer number). These diffracted X-rays are then detected, processed and counted. By scanning the sample through a range of 2θ angles, all possible diffraction directions of the lattice are attained due to the random orientation of the material. X-rays are used to produce diffraction patterns, because their wavelength is typically the same order of magnitude (1–100 Angstroms) as the spacing d between the planes in the crystal. Conversion of the diffraction peaks to d -spacings allows identification of the mineral since each sample has a characteristic set of the d -spacings, or crystallographic planes. Typically, this is achieved by comparison of the d -spacings with standard reference patterns.

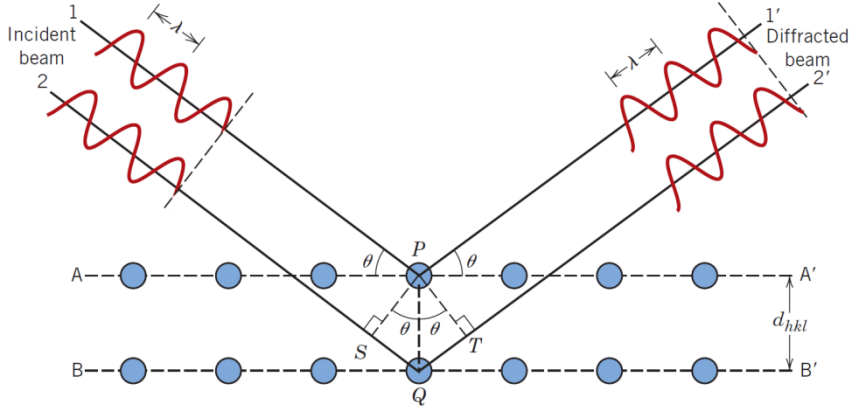


Figure 3.27: Diffraction of X-rays by the planes of an atom. Reproduced from Ref. [92].

XRD system consists of three main components: an X-ray tube, a sample holder, and an X-ray detector, as shown in Figure 3.26b. A cathode ray tube generates characteristic X-ray spectra. These spectra consist of several characteristic lines, commonly, K_α and K_β . By filtering these spectra by using foils or crystal monochrometers, monochromatic X-rays can be obtained which are needed for diffraction. These X-rays are collimated and directed onto the sample. The intensity of the reflected X-rays is recorded, as the sample and detector are rotated. When the geometry of the incident X-rays impinging the sample satisfies the Bragg equation, constructive interference occurs and an intensity peak is detected [67]. A detector records and processes this X-ray signal, while the electronics is used to convert the signal to a count rate. For typical powder patterns, data is collected at 2θ from $\approx 5^\circ$ to 70° , angles that are present in the X-ray scan. The scan generates a set of peaks at certain positions, which occur where the X-ray beam has been diffracted by the crystal lattice. The unique set of d -spacings derived from this pattern can be used to identify the mineral. Also, from this peak, the crystallite size and strain can be measured by using Williamson–Hall approximation, as shown in the following equation [93]:

$$\beta \cos \theta = \frac{K\lambda}{D} + 4\varepsilon \sin \theta \quad (22)$$

where β is the line full width at half maximum intensity (FWHM) in radians, D is the crystallite size, K is the shape factor 0.9, λ is the wavelength of Cu K_α radiation, and ε is the crystal strain.

3.2.6 Fourier Transform Infrared Spectroscopy

Fourier transform infrared (FTIR) spectrometer (Nicolet iS10, Thermo Fisher Scientific Inc., USA) is commonly used to identify the chemical groups in samples (Figure 3.28a). The measurements are carried out at room temperature in the spectral range of 600–4000 cm^{-1} . Air-dried samples are placed directly on an attenuated total reflectance (ATR) crystal window. FTIR spectroscopy is a technique, which is used to identify organic molecules or the presence of certain functional groups in the molecule. The infrared spectroscopy works in the IR region of the electromagnetic spectrum. When IR radiation is passed through a sample, the molecules absorb of this radiation at a certain frequency that is characteristic of their structure. The obtained spectrum displays the molecular absorption and transmission, and provides a molecular fingerprint of the sample. FTIR spectra give information about the chemical bonding of the atoms, which is usually represented by the absorption bands caused by the vibration between the atomic bonds of the sample. Each material is composed of different combination of atoms, so different compounds produce different infrared spectra. Therefore, FTIR spectroscopy provides qualitative analysis of different materials. In addition, the size of the peaks in the spectrum is a direct indication of the amount of material present [94]. An ATR method allows to obtain FTIR spectra easily. Figure 3.28b shows a diagram of a typical ATR in FTIR instrument. An ATR cell consists of a high-refractive index material, such as ZnSe or diamond sandwiched between a low-refractive index substrate and a lower-refractive index sample. IR radiation from the source enters the ATR crystal, where it undergoes a series of total internal reflections before exciting the crystal. During each reflection the radiation penetrates into the sample to the depth of a few microns. The result is a selective attenuation of the radiation at those wavelengths, which the sample absorbs. The powder samples need to be placed on the sample slot, and a force using compression tip is applied to ensure that it is in contact with the ATR crystal [95].

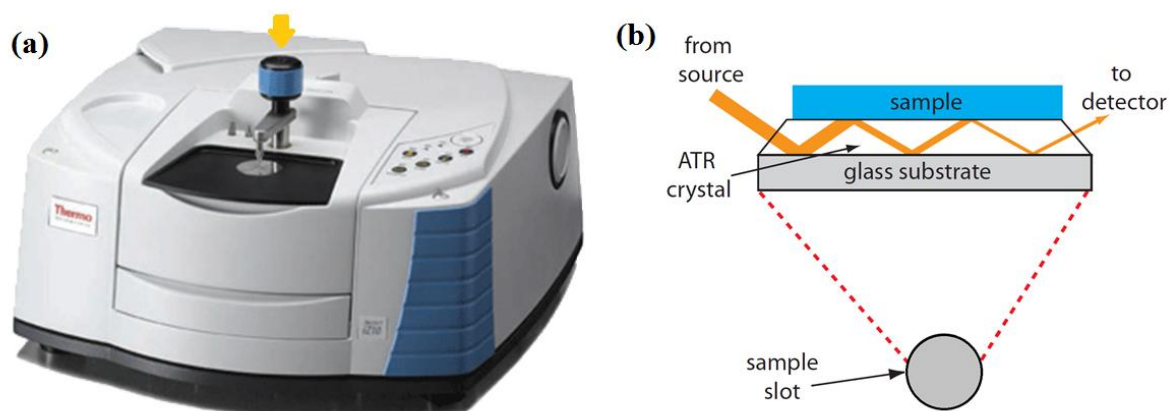


Figure 3.28: (a) Nicolet iS10 FTIR spectrometer. (b) A schematic of the ATR's sample slot, showing how the source's radiation interacts with the sample. The pressure tower (orange arrow) is used to ensure the contact of solid samples with the ATR crystal. Images (a) taken from <http://www.azom.com/> and (b) Reproduced from Ref. [95].

3.2.7 Thermogravimetric Analysis

To identify functional groups on the nanoalumina/nanoruby surface, thermogravimetric analysis (TGA) is performed using a Mettler Toledo TGA/DSC instrument at a heating rate of $10^{\circ}\text{C}/\text{min}$ from 25°C to 1000°C in a nitrogen atmosphere (Figure 3.29a). About 10 mg of nanoalumina samples are placed in an alumina crucible for each measurement. TGA is one of the technique modalities. The schematic diagram of a commercial TGA is presented in Figure 3.29a, showing a balance, purge gas inlet and outlet and thermocouple position beneath the sample pan. In this method, the mass (weight) of a sample is measured in a specified atmosphere as the temperature of the sample is programmed [96, 97]. Commonly, the temperature is increased linearly over a time period and the mass of the sample is constantly recorded. The output from TGA is a plot of mass (or mass percentage) versus temperature. The TGA plot is called a thermal curve. TGA can be used to investigate the suitable weighing form of material. It is also used to determine the range of the drying temperature. The data from TGA also can be used to evaluate kinetic parameter of weight change in the reaction [97].

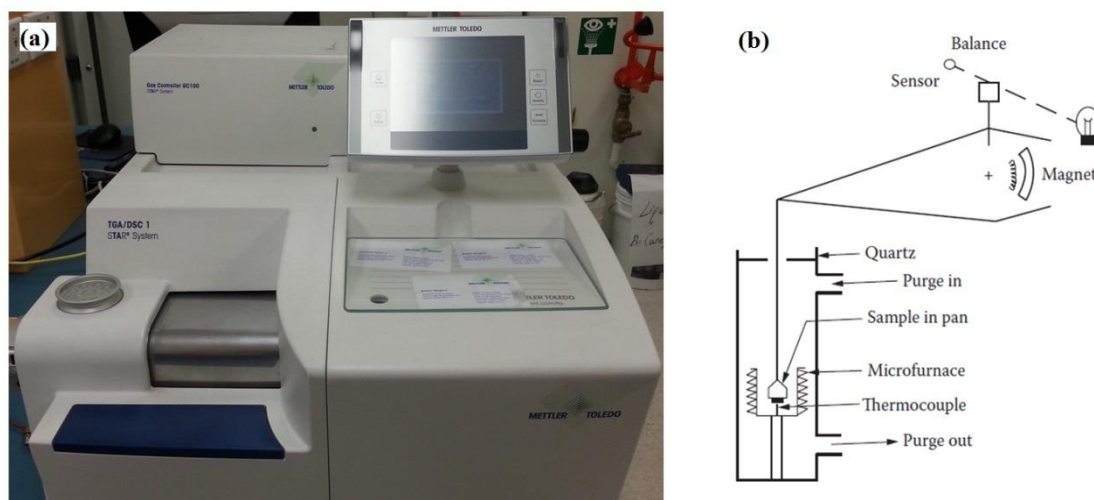


Figure 3.29: (a) Mettler Toledo thermogravimetric analysis (TGA) instrument (b) A schematic diagram of a commercial TGA, showing a purge gas inlet and outlet and the thermocouple position beneath the sample pan. Image (b) is reproduced from Ref. [96].

3.2.8 Spectrofluorometer

A Fluorolog Tau3 system (JY Horiba) spectrofluorometer is used to measure the photoluminescence excitation and emission spectra. It consists of three main components: an excitation source, sample compartment, and a detection unit (Figure 3.30). The excitation source is represented either by a xenon lamp or laser diode. In order to create a narrow and tunable excitation wavelength required for the purpose of measuring particular material, a single-grating excitation monochromator is placed after the xenon lamp. There is a chamber that holds liquid or solid sample in the sample compartment. The emission light from the sample compartment enters the detection unit equipped with a monochromator and high-sensitivity detector photomultiplier tube. For our measurement, the colloidal sample is transferred into a quartz cuvette and placed in the sample chamber. The Fluorolog was programmed to acquire excitation/emission spectra within a particular wavelength range. The data are exported and the reference baseline is subtracted.

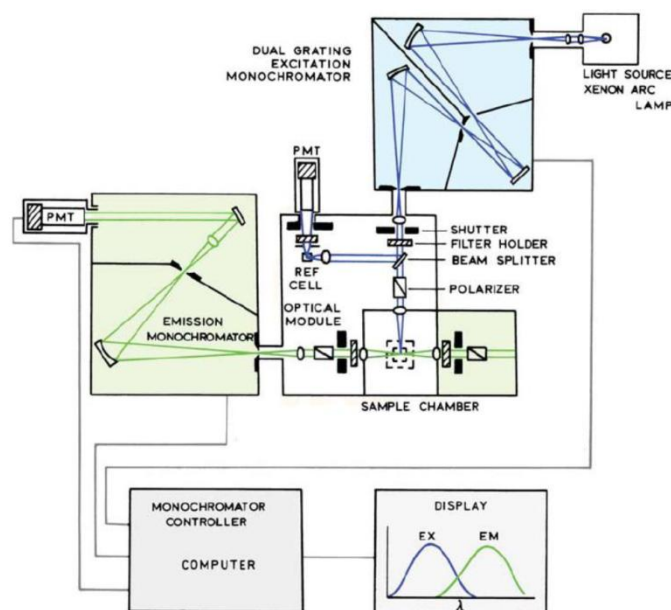


Figure 3.30: Schematic diagram of a PL unit, a spectrofluorometer Fluorolog-3 (HORIBA Jobin Yvon, NJ, USA).

3.2.9 Epi-Luminescence Microscopy

Epi-luminescence microscopy aided by specific labelling is a widespread microscopy modality to image stained morphology of biological systems and macromolecules at the tissue, cellular and sub-cellular levels. It relies on the specific binding of a PL molecular probe to a targeted biomolecule, followed by detection of the photoluminescence signal. The principle of epi-luminescence imaging is based on the excitation of a PL probe with relatively bright incident light of specific wavelength, followed by its spectral separation and detection of the photoluminescence emitted from the sample. This technique provides high-resolution microscopic imaging and high signal-to-noise ratio. A typical epi-luminescence microscope structure is presented in Figure 3.31a. The incident light is produced by a tungsten-halogen lamp, which is focused through a collector lens system. The collector system (see Figure 3.31b) may include neutral density filters that uniformly attenuate most visible light, reduce the incident lamp power minimising photobleaching of fluorescent biological specimens. A heat filter is also installed in order to reduce the specimen overheating due to the optical excitation. Since the field and aperture diaphragms are larger than the field-of-view, a shutter is used to block incident light, when the sample is not being viewed to reduce photobleaching and phototoxicity. A PL filter cube containing an excitation filter,

dichroic mirror and emission filter is a critical component of the epi-luminescence microscope. It discriminates the excitation emission beams based on the spectral filtering, steering the excitation beam towards the specimen, while blocking this beam on its return path to avoid unwanted parasitic exposure in the detection module. At the same time, the filter cube is configured to pass wavelength-shifted light beam from the specimen. The excitation filter is typically a band pass filter, which selects a specific spectral band of light required to excite the PL-stained specimen. The filter cube contains a dichroic mirror, which represents a filter plate mounted at 45° with respect to the incoming beam, and is designed to reflect the excitation light off towards the specimen, passing the remaining light through the filter. The excitation light travels upwards through the objective lens and focuses onto the sample in the configuration of an inverted microscope. The emission light collected and collimated by the objective lens propagates downwards through the microscope, passes through the dichroic mirror and an emission filter, which is purpose-designed to pass the photoluminescence emission and block the excitation beam produced by spurious reflections from the specimen and optics. The filtered photoluminescence light is then either directed to the eyepieces or sent through a microscope port to a CCD camera (Figure 3.31c) [98].

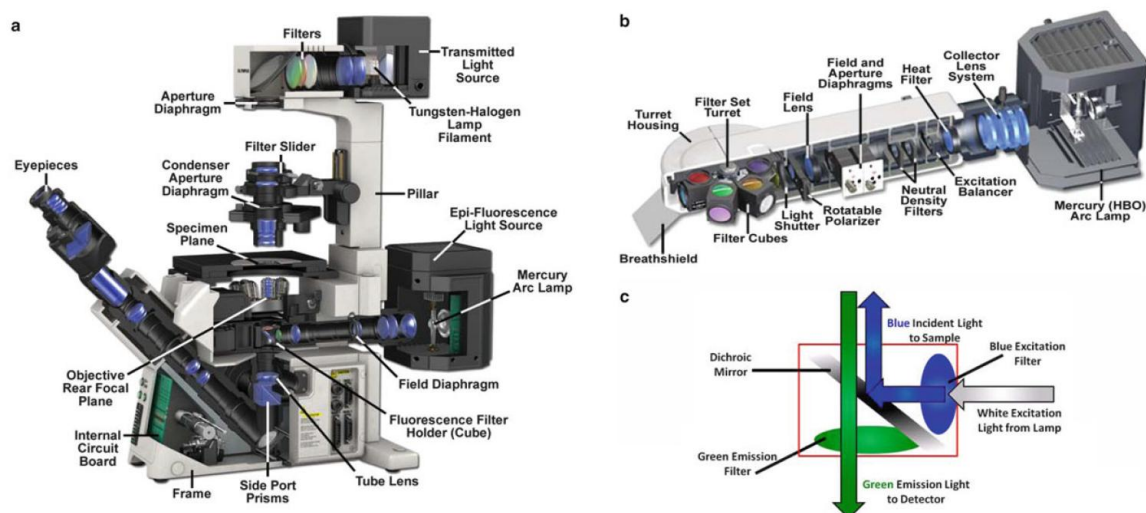


Figure 3.31: (a) Cut through of an epi-luminescence microscope (Olympus IX81, Olympus, Japan) showing details of the excitation and PL emission light paths. (b) Detailed view of the epi-illumination arm for the IX81 microscope showing components of the photoluminescence light path. (c) Schematic of a PL filter cube. Blue light is

selected from the white incident light from the lamp using a blue band pass excitation filter built for green fluorescent protein (GFP) detection. The blue light reflects off the dichroic mirror and is directed upwards to the objective lens then focused on the sample. Green emission light from the sample passes through the dichroic mirror and through a green band pass emission filter to the detector. The emission filter also reduces image background by rejecting any reflected blue incident light. Reproduced from Ref. [98].

In our optical microscopy system built in-house, an inverted microscope (Olympus IX70, Japan) platform is used, as shown schematically in Figure 3.32. An electron-multiplied CCD camera (EMCCD, iXon 885 DU, Andor Technology Ltd., UK) is attached to the detection port of the microscope. External 405-nm laser source (TG_405_1.1, Quantitative Ltd., Australia) and 405-nm laser (FB-532-1000-FS-FS-1-1-ST, RGB Lase) are coupled to an illumination port of the microscope using Köhler-type optical configuration, produce uniform illumination at the specimen plane, as described elsewhere [28]. An oil-immersion objective lens (100 \times , NA 1.3, Olympus, Japan) is commonly used for capturing of high-resolution images in bright-field, epifluorescence and time-gated modes. A filter-set designed for nanoruby signal detection contains an excitation filter (650-nm short pass), dichroic mirror (660-nm long pass) and emission filter (664-nm long pass).

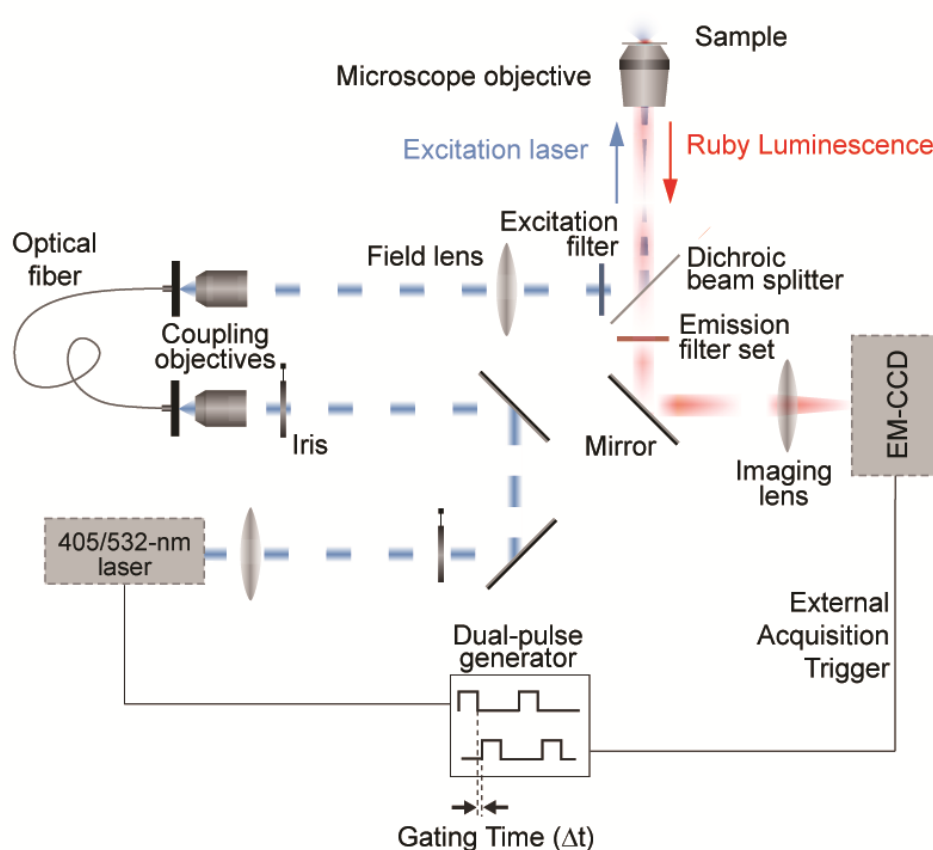


Figure 3.32: A schematic diagram of the optical microscopy system configured for the high-sensitivity imaging of nanoruby samples. 405-nm and 532-nm laser beams are coupled to the microscope using Köhler-type optical configuration to provide a uniform illumination at the specimen plane. The photoluminescence emission from the sample is collected through optical filters by using an EMCCD. The laser output and camera exposure are synchronised by using a dual-pulse generator for time-gated imaging.

3.3 References

- [1] I. A. Rahman and V. Padavettan, "Synthesis of Silica Nanoparticles by Sol-Gel: Size-Dependent Properties, Surface Modification, and Applications in Silica-Polymer Nanocomposites: A Review," *Journal of Nanomaterials*, vol. 2012, pp. 1-15, 2012.
- [2] A. Jaworek, "Micro- and nanoparticle production by electrospraying," *Powder Technology*, vol. 176, pp. 18-35, 2007.
- [3] R. Mueller, L. Mädler, and S. E. Pratsinis, "Nanoparticle synthesis at high production rates by flame spray pyrolysis," *Chemical Engineering Science*, vol. 58, pp. 1969-1976, 2003.
- [4] M. Iwamoto, K. Kuroda, V. Zaporozhchenko, S. Hayashi, and F. Faupel, "Production of gold nanoparticles-polymer composite by quite simple method,"

The European Physical Journal D - Atomic, Molecular, Optical and Plasma Physics, vol. 24, pp. 365-367, 2003.

- [5] K. Nakaso, B. Han, K. H. Ahn, M. Choi, and K. Okuyama, "Synthesis of non-agglomerated nanoparticles by an electrospray assisted chemical vapor deposition (ES-CVD) method," *Journal of Aerosol Science*, vol. 34, pp. 869-881, 2003.
- [6] E. Wetterskog, M. Agthe, A. Mayence, J. Grins, D. Wang, S. Rana, *et al.*, "Precise control over shape and size of iron oxide nanocrystals suitable for assembly into ordered particle arrays," *Science and Technology of Advanced Materials*, vol. 15, p. 055010, 2014.
- [7] N. Toshima and T. Yonezawa, "Bimetallic nanoparticles—novel materials for chemical and physical applications," *New Journal of Chemistry*, vol. 22, pp. 1179-1201, 1998.
- [8] AZoNano. (2004). *Bottom-up Methods for Making Nanotechnology Products*. Available: <http://www.azonano.com/article.aspx?ArticleID=1079>
- [9] X. Du, S. Zhao, Y. Liu, J. Li, W. Chen, and Y. Cui, "Facile synthesis of monodisperse α -alumina nanoparticles via an isolation-medium-assisted calcination method," *Applied Physics A*, vol. 116, pp. 1963-1969, 2014.
- [10] F. Mirjalili, M. Hasmaliza, and L. C. Abdullah, "Size-controlled synthesis of nano α -alumina particles through the sol–gel method," *Ceramics International*, vol. 36, pp. 1253-1257, 2010.
- [11] P. T. Anastas and J. C. Warner, *Green Chemistry: Theory and Practice*: Oxford University Press New York, 1998.
- [12] T. P. Yadav, R. M. Yadav, and D. P. Singh, "Mechanical Milling: a Top Down Approach for the Synthesis of Nanomaterials and Nanocomposites," *Nanoscience and Nanotechnology*, vol. 2, pp. 22-48, 2012.
- [13] H. Zeng, X.-W. Du, S. C. Singh, S. A. Kulinich, S. Yang, J. He, *et al.*, "Nanomaterials via Laser Ablation/Irradiation in Liquid: A Review," *Advanced Functional Materials*, vol. 22, pp. 1333-1353, 2012.
- [14] N. E. Lyamkina, G. A. Chiganova, V. V. Slabko, A. M. Vorotynov, and M. A. Taranova, "Ultrafine Cr-Doped Al_2O_3 Prepared by Detonation Synthesis," *Inorganic Materials*, vol. 41, pp. 830-835, 2005.
- [15] M. M. Can, S. Ozcan, A. Ceylan, and T. Firat, "Effect of milling time on the synthesis of magnetite nanoparticles by wet milling," *Materials Science and Engineering: B*, vol. 172, pp. 72-75, 2010.
- [16] M. A. Meitl, T. M. Dellinger, and P. V. Braun, "Bismuth–Ceramic Nanocomposites with Unusual Thermal Stability via High-Energy Ball Milling," *Advanced Functional Materials*, vol. 13, pp. 795-799, 2003.
- [17] V. D. Zhuravlev, V. G. Bamburov, A. R. Beketov, L. A. Perelyaeva, I. V. Baklanova, O. V. Sivtsova, *et al.*, "Solution combustion synthesis of α - Al_2O_3 using urea," *Ceramics International*, vol. 39, pp. 1379-1384, 2013.
- [18] A. Patra, R. Tallman, and B. Weinstein, "Effect of crystal structure and dopant concentration on the luminescence of Cr^{3+} in Al_2O_3 nanocrystals," *Optical Materials*, vol. 27, pp. 1396-1401, 2005.
- [19] O. D. Veleev and S. Gupta, "Materials fabricated by micro-and nanoparticle assembly—the challenging path from science to engineering," *Adv. Mater*, vol. 21, pp. 1897-1905, 2009.

- [20] P. Sharma, K. Biswas, A. K. Mondal, and K. Chattopadhyay, "Size effect on the lattice parameter of KCl during mechanical milling," *Scripta Materialia*, vol. 61, pp. 600-603, 2009.
- [21] H. J. Fecht, "Nanostructured Materials and Composites Prepared by Solid State Processing," in *Nanostructured Materials Processing, Properties And Potential Applications*, C. C. Koch, Ed., ed New York USA: William Andrew Publishing, 2002, p. 73.
- [22] C. C. Koch, "Synthesis of nanostructured materials by mechanical milling: problems and opportunities," *Nanostructured Materials*, vol. 9, pp. 13-22, 1997.
- [23] A. M. Edmonds, M. A. Sobhan, V. K. A. Sreenivasan, E. A. Grebenik, J. R. Rabeau, E. M. Goldys, *et al.*, "Nano-Ruby: A Promising Fluorescent Probe for Background-Free Cellular Imaging," *Particle & Particle Systems Characterization*, vol. 30, pp. 1-8, 2013.
- [24] Y. Ju-Nam and J. R. Lead, "Manufactured nanoparticles: An overview of their chemistry, interactions and potential environmental implications," *Science of The Total Environment*, vol. 400, pp. 396-414, 2008.
- [25] R. E. Schilling. (2010, Choose the Right Grinding Mill.
- [26] E. Leonel, E. Nassar, K. Ciuffi, M. dos Reis, and P. Calefi, "Effect of high-energy ball milling in the structural and textural properties of kaolinite," *Cerâmica*, vol. 60, pp. 267-272, 2014.
- [27] C. Suryanarayana, *Mechanical alloying and milling*: CRC Press, 2004.
- [28] H. Atkinson, "Hardness tests for rock characterization," *Comprehensive rock engineering. Principles, practice & projects*, vol. 3, pp. 105-117, 2014.
- [29] R. A. Varin, T. Czujko, and Z. S. Wronski, *Nanomaterials for Solid State Hydrogen Storage*. New York USA: Springer Science, 2009.
- [30] P. Balaz, "High-Energy Milling," in *Mechanochemistry in Nanoscience and Minerals Engineering*, ed: Springer Berlin Heidelberg, 2008, pp. 103-132.
- [31] DeCastro, C. L, and B. S. Mitchell, "Nanoparticles from mechanical attrition," in *Synthesis, functionalization and surface treatment of nanoparticles.*, M.-I. Baraton, Ed., ed Carlifonia, USA: American Scientific Publisher, 2003, pp. 1-15.
- [32] S. Gour, "Manufacturing nano-sized powders using salt-and sugar-assisted milling," Drexel University, 2010.
- [33] Y. Feng, K. Han, and D. Owen, "Discrete element simulation of the dynamics of high energy planetary ball milling processes," *Materials Science and Engineering: A*, vol. 375, pp. 815-819, 2004.
- [34] C. F. Burmeister and A. Kwade, "Process engineering with planetary ball mills," *Chemical Society Reviews*, vol. 42, pp. 7660-7667, 2013.
- [35] D. Ho, *Nanodiamonds: applications in biology and nanoscale medicine*: Springer Science & Business Media, 2009.
- [36] H. Mio, J. Kano, and F. Saito, "Scale-up method of planetary ball mill," *Chemical Engineering Science*, vol. 59, pp. 5909-5916, 2004.
- [37] B. D. Sneed, "Synthesis and Characterization Of Aluminum-Nanodiamond Composite Powders by High Energy Ball Milling," Master's Thesis, Naval Postgraduate School, 2011.
- [38] W. Cao, "Synthesis of Nanomaterials by High Energy Ball Milling," I. Skyspring Nanomaterial, Ed., ed.

- [39] L. Sheng-Yong, M. Qiong-Jing, P. Zheng, L. Xiao-Dong, and Y. Jian-Hua, "Simulation of ball motion and energy transfer in a planetary ball mill," *Chinese Physics B*, vol. 21, p. 078201, 2012.
- [40] G. Kakuk, I. Zsoldos, Á. Csanády, and I. Oldal, "Contributions to the modelling of the milling process in a planetary ball mill," *Rev. Adv. Mater. Sci.*, vol. 22, pp. 21-38, 2009.
- [41] P. P. Chattopadhyay, I. Manna, S. Talapatra, and S. K. Pabi, "A mathematical analysis of milling mechanics in a planetary ball mill," *Materials Chemistry and Physics*, vol. 68, pp. 85-94, 2001.
- [42] H. Mio, J. Kano, F. Saito, and K. Kaneko, "Optimum revolution and rotational directions and their speeds in planetary ball milling," *International Journal of Mineral Processing*, vol. 74, Supplement, pp. S85-S92, 2004.
- [43] J. Kano, H. Mio, and F. Saito, "Correlation of Size Reduction Rate of Inorganic Materials with Impact Energy of Balls in Planetary Ball Milling," *Journal of chemical engineering of Japan*, vol. 32, pp. 445-448, 1999.
- [44] V. Y. Prokof'ev and N. E. Gordina, "Comminution and mechanochemical activation in oxide ceramics technology (review)," *Glass and Ceramics*, vol. 69, pp. 65-70, 2012.
- [45] "pulverisette 7 Operating Manual," F. Germany, Ed., 06/07 ed.
- [46] S. Bastian, W. Busch, D. Kühnel, A. Springer, T. Meißner, R. Holke, *et al.*, "Toxicity of tungsten carbide and cobalt-doped tungsten carbide nanoparticles in mammalian cells in vitro," *Environ Health Perspect*, vol. 117, pp. 530-536, 2009.
- [47] *Mohs Hardness Scale*. Available: <http://geology.com/minerals/mohs-hardness-scale.shtml>
- [48] "The art of milling," R. G. Haan, Ed., ed. Germany, 2008.
- [49] C. B. Reid, J. S. Forrester, H. J. Goodshaw, E. H. Kisi, and G. J. Suaning, "A study in the mechanical milling of alumina powder," *Ceramics International*, vol. 34, pp. 1551-1556, 2008.
- [50] A. G. King, *Ceramic Technology and Processing: A Practical Working Guide*. United State: Noyas Publication/William Andrew Publishing, 2002.
- [51] F. C. Bond, "Grinding ball size selection," *Mining Engineering*, vol. 10, pp. 592-595, 1958.
- [52] "Jar, Ball and Pebble Milling Theory and Practice," I. Operating Division of ER Advanced Ceramics, Ed., ed.
- [53] N. Magdalinovic, M. Trumic, M. Trumic, and L. Andric, "The Optimal Ball Diameter in a Mill," *Physicochem. Probl. Miner.Process.*, vol. 48, pp. 329-339, 2012.
- [54] F. M. Katubilwa, M. H. Moys, D. Glasser, and D. Hildebrandt, "An attainable region analysis of the effect of ball size on milling," *Powder Technology*, vol. 210, pp. 36-46, 2011.
- [55] N. Ltd. *YSZ media*.
- [56] F. Stenger, S. Mende, J. Schwedes, and W. Peukert, "The influence of suspension properties on the grinding behavior of alumina particles in the submicron size range in stirred media mills," *Powder Technology*, vol. 156, pp. 103-110, 2005.

- [57] B. Jean-Paul, A. C. Patrick, J. Fedor, W. Joerg, A. Pascal, S. Mohamed, *et al.*, "High yield fabrication of fluorescent nanodiamonds," *Nanotechnology*, vol. 20, p. 235602, 2009.
- [58] H. Ahamed and V. S. Kumar, "A Comparative Study on the Milling Speed for the Synthesis of Nano- Structured Al 6063 Alloy Powder by Mechanical Alloying," *Journal of Minerals & Materials Characterization & Engineering*, vol. 10, pp. 507-515, 2011.
- [59] N. T. Rochman, S. Kuramoto, R. Fujimoto, and H. Sueyoshi, "Effect of milling speed on an Fe–C–Mn system alloy prepared by mechanical alloying," *Journal of materials processing technology*, vol. 138, pp. 41-46, 2003.
- [60] N. Salah, S. S. Habib, Z. H. Khan, A. Memic, A. Azam, E. Alarfaj, *et al.*, "High-energy ball milling technique for ZnO nanoparticles as antibacterial material," *International journal of nanomedicine*, vol. 6, p. 863, 2011.
- [61] J.-S. Lee, C.-S. Lee, S.-T. Oh, and J.-G. Kim, "Phase evolution of Fe₂O₃ nanoparticle during high energy ball milling," *Scripta Materialia*, vol. 44, pp. 2023-2026, 2001.
- [62] P. Heitjans and S. Indris, "Fast diffusion in nanocrystalline ceramics prepared by ball milling," *Journal of Materials Science*, vol. 39, pp. 5091-5096, 2004.
- [63] S. Indris, D. Bork, and P. Heitjans, "Nanocrystalline Oxide Ceramics Prepared by High-Energy Ball Milling," *Journal of Materials Synthesis and Processing*, vol. 8, pp. 245-250, 2000.
- [64] E. Mohammadi Zahrani and M. H. Fathi, "The effect of high-energy ball milling parameters on the preparation and characterization of fluorapatite nanocrystalline powder," *Ceramics International*, vol. 35, pp. 2311-2323, 2009.
- [65] C. J. Li, X. K. Zhu, J. M. Tao, H. L. Tang, and T. L. Chen, "Bulk Nanocrystalline Cu Produced by High-Energy Ball Milling," *Materials Science Forum*, vol. 682, pp. 25-32, 2011.
- [66] C. L. DeCastro and B. S. Mitchell, "Nanoparticles from mechanical attrition," *Synthesis, Functionalization, and Surface Treatment of Nanoparticles*, pp. 1-15, 2002.
- [67] J. S. Forrester, H. J. Goodshaw, E. H. Kisi, G. J. Suaning, and J. S. Zobec, "Effect of Mechanical Milling on the Sintering Behaviour of Alumina," *J. Aust. Ceram. Soc.*, vol. 44, pp. 47-52, 2008.
- [68] R. Othman and A. Zakaria, "Optimisation of milling parameters during mechanical activation for direct synthesis of hydroxyapatite," *ASEAN Engineering Journal*, vol. 1, pp. 5-11, 2011.
- [69] P. Balaz, *Mechanochemistry in Nanoscience and Minerals Engineering*. German: Springer, 2008.
- [70] B. Li and H. Wang, "Effect of Ball Milling on Powder Preparation by Mechanical Methods," *Applied Mechanics and Materials*, vol. 182-183, pp. 1541-1544, 2012.
- [71] J. Stein, "Ultrafine Dry Grinding with Media Mills," *Proc. Euroforum 2005*, vol. 17, pp. 1-6, 2005.
- [72] C. Suryanarayana, "Mechanical alloying and milling," *Progress in Materials Science*, vol. 46, pp. 1-184, 2001.
- [73] N. Eom, M. H. Bhuiyan, T.-S. Kim, and S.-J. Hong, "Synthesis and Characterization of Agglomerated Coarse Al Powders Comprising Nanoparticles

- by Low Energy Ball Milling Process," *Materials transactions*, vol. 52, pp. 1674-1678, 2011.
- [74] W. Peukert, H.-C. Schwarzer, and F. Stenger, "Control of aggregation in production and handling of nanoparticles," *Chemical Engineering and Processing: Process Intensification*, vol. 44, pp. 245-252, 2005.
- [75] G. Matijašić, K. Žižek, and A. Glasnović, "Suspension rheology during wet comminution in planetary ball mill," *Chemical Engineering Research and Design*, vol. 86, pp. 384-389, 2008.
- [76] Y. Hwang, J.-K. Lee, J.-K. Lee, Y.-M. Jeong, S.-i. Cheong, Y.-C. Ahn, *et al.*, "Production and dispersion stability of nanoparticles in nanofluids," *Powder Technology*, vol. 186, pp. 145-153, 2008.
- [77] M. D. Sacks and C. S. Khadilkar, "Milling and Suspension Behavior of Al₂O₃ in Methanol and Methyl Isobutyl Ketone," *Journal of the American Ceramic Society*, vol. 66, pp. 488-494, 1983.
- [78] N. G. Akdogan, W. Li, and G. C. Hadjipanayis, "Anisotropic Nd₂Fe₁₄B nanoparticles and nanoflakes by surfactant-assisted ball milling," *Journal of Applied Physics*, vol. 109, pp. 109-111, 2011.
- [79] S. Sakthivel, V. V. Krishnan, and B. Pitchumani, "Influence of suspension stability on wet grinding for production of mineral nanoparticles," *Particuology*, vol. 6, pp. 120-124, 2008.
- [80] H. Merkus, "Dynamic Light Scattering," in *Particle Size Measurements*. vol. 17, ed: Springer Netherlands, 2009, pp. 299-317.
- [81] M. Instrument, "Zetasizer Nano Series: User Manual," ed: Worcestershire, UK, 2013.
- [82] "Zetasizer Nano User Manual," in *Malvern Instruments Ltd*, ed. UK, 2013.
- [83] J. Clogston and A. Patri, "Zeta Potential Measurement," in *Characterization of Nanoparticles Intended for Drug Delivery*. vol. 697, S. E. McNeil, Ed., ed: Humana Press, 2011, pp. 63-70.
- [84] M. J. López-Robledo, J. Silva-Treviño, T. Molina, and R. Moreno, "Colloidal stability of gadolinium-doped ceria powder in aqueous and non-aqueous media," *Journal of the European Ceramic Society*, vol. 33, pp. 297-303, 2013.
- [85] A. Liese and L. Hilterhaus, "Evaluation of immobilized enzymes for industrial applications," *Chemical Society Reviews*, vol. 42, pp. 6236-6249, 2013.
- [86] B. N. Wang, R. D. Bennett, E. Verploegen, A. J. Hart, and R. E. Cohen, "Quantitative characterization of the morphology of multiwall carbon nanotube films by small-angle X-ray scattering," *The Journal of physical chemistry C*, vol. 111, pp. 5859-5865, 2007.
- [87] A. Nouailhat, *An Introduction to Nanosciences and Nanotechnology* vol. 10: John Wiley & Sons, 2010.
- [88] W. Denk and H. Horstmann, "Serial block-face scanning electron microscopy to reconstruct three-dimensional tissue nanostructure," *PLoS Biol*, vol. 2, p. e329, 2004.
- [89] S. F. Lim, R. Riehn, W. S. Ryu, N. Khanarian, C.-k. Tung, D. Tank, *et al.*, "In vivo and scanning electron microscopy imaging of upconverting nanophosphors in *Caenorhabditis elegans*," *Nano Letters*, vol. 6, pp. 169-174, 2006.
- [90] "Scanning Electron Microscopy (SEM)," in *Electron Microscopy of Polymers*, ed: Springer Berlin Heidelberg, 2008, pp. 87-120.

- [91] X-ray Spectroscopy. Available:
http://www.microscopy.ethz.ch/xray_spectrum.htm.
- [92] W. D. Callister and D. G. Rethwisch, *Materials science and engineering: an introduction*, 7 ed. US: Wiley New York, 2007.
- [93] V. D. Mote, Y. Purushotham, and B. N. Dole, "Williamson-Hall analysis in estimation of lattice strain in nanometer-sized ZnO particles," *Journal of Theoretical and Applied Physics*, vol. 6, pp. 1-8, 2012.
- [94] N. Joshi, "Gold Nanoparticles and Their Polymer Composites: Synthesis Characterization and Applications," 2010.
- [95] D. Harvey, "Analytical Chemistry 2.0," 2010.
- [96] J. W. Robinson, E. S. Frame, and G. M. Frame II, *Undergraduate instrumental analysis*: CRC Press, 2014.
- [97] S. M. Khopkar, *Basic concepts of analytical chemistry*: New Age International, 1998.
- [98] D. J. Taatjes and B. T. Mossman, *Cell Imaging Techniques*: Springer, 2013.

Large-Scale Production and Characterisation of Biocompatible Colloidal Nanoalumina

A paper published by the Ph.D. candidate, Razali, *et al.*, “Large-Scale Production and Characterization of Biocompatible Colloidal Nanoalumina” provides the content for this chapter. The main body of the chapter is prefaced first by a short introduction to this paper [1], and as well contains a statement describing the contribution of the Ph.D. candidate. This is followed by the paper itself. This chapter concludes with an overview of the application of nanoalumina in the area of life sciences and provides a discussion on its large-scale production methods. Supplementary results obtained in the course of this work can be found in Appendix A.

4.1 Introduction to paper

This paper reports on the large-scale production of colloidal nanoalumina by using high-energy ball milling (HEBM) method for use in the life sciences. To date, most of the reported nanoalumina HEBM production methods have focused on their industrial use, specifically for the production of high green-density ceramics for biomedical implants, and this material often has unknown colloidal properties. Here, we report on a systematic investigation of the production method and characterisation of nanoalumina material in the context of its applications for a broader range of biomedical research and practices. The paper includes a thorough analysis of nanoalumina properties such as

particle size, contamination level, production yield, stability and its biocompatibility, which ensures its suitability in biological applications. We suggest in this report that the HEBM method for large-scale production in particular has the potential to meet the life science demands for new and future biocompatible nanomaterials.

4.2 Authors' contribution

The Ph.D. candidate (Mr. Wan Aizuddin W. Razali) is the first author of this paper. He developed the HEBM protocol for the fabrication of nanoalumina sourced from micron-sized alumina powder. He carried out the sample purification by using a method of selective acid etching and performed the stability analysis of nanoparticles. In addition, he performed the functionalisation step that applied silane-based reagents. He carried out the characterisations, including particle size measurement, zirconia contamination analysis, and functionalisation analysis. Finally, he compiled the results, drew the figures and prepared a first draft of the manuscript.

The second author, Dr. Sreenivasan, contributed towards optimisation of the milling parameters. He designed the characterisation experiments, carried out the data analysis of the XRD spectra, and performed cytotoxicity analysis. Prof. Goldys planned this project and revised the manuscript. A/Prof. Zvyagin (the corresponding author) conceived the idea for this work, coordinated the project and finalised the manuscript. All authors were involved in authorship of the manuscript.

4.3 Full paper

Langmuir

Article

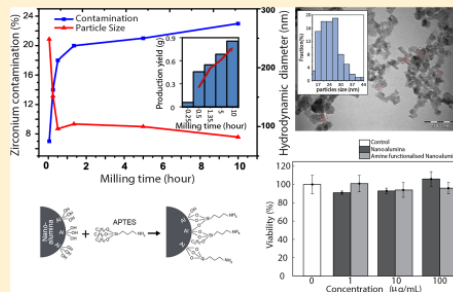
pubs.acs.org/Langmuir

Large-Scale Production and Characterization of Biocompatible Colloidal Nanoalumina

W. A. W. Razali,^{†,‡} V. K. A. Sreenivasan,[†] E. M. Goldys,[†] and A. V. Zvyagin^{*,†,§}[†]MQ Biofocus Research Centre, Faculty of Science, Macquarie University, Sydney, NSW 2109, Australia[‡]Department of Physics, Faculty of Applied Sciences, Universiti Teknologi MARA Pahang, 26400 Jengka, Pahang, Malaysia[§]N. I. Lobachevsky State University of Nizhny Novgorod, 603950 Nizhny Novgorod, Russia

Supporting Information

ABSTRACT: The rapid uptake of nanomaterials in life sciences calls for the development of universal, high-yield techniques for their production and interfacing with biomolecules. Top-down methods take advantage of the existing variety of bulk and thin-film solid-state materials for improved prediction and control of the resultant nanomaterial properties. We demonstrate the power of this approach using high-energy ball milling (HEBM) of alumina (Al_2O_3). Nanoalumina particles with a mean size of 25 nm in their most stable α -crystallographic phase were produced in gram quantities, suitable for biological and biomedical applications. Nanomaterial contamination from zirconia balls used in HEBM was reduced from 19 to 2% using a selective acid etching procedure. The biocompatibility of the milled nanomaterial was demonstrated by forming stable colloids in water and physiological buffers, corroborated by zeta potentials of +40 mV and −40 mV and characterized by *in vitro* cytotoxicity assays. Finally, the feasibility of a milled nanoalumina surface in anchoring a host of functional groups and biomolecules was demonstrated by the functionalization of their surface using facile silane chemistry, resulting in the decoration of the nanoparticle surface with amino groups suitable for further conjugation of biomolecules.



1. INTRODUCTION

Nanomaterials play an increasingly important role in the life sciences because of their unique properties. First, the nanoparticle (NP) core exhibits chemical and physical stability often accompanied by low (cyto)toxicity.¹ Second, their physical and chemical characteristics are highly controllable by means of their size, composition, and production methods. For example, silver NPs with an average size of 25 nm were found to have high antimicrobial and bactericidal activity against highly multiresistant strains.² Third, the abundance of reactive functional groups on the NP surface allows specific modification and tailoring of their chemical properties. A large and effective surface area can host a number of molecules and nanoparticle modules of various functionalities, including guiding/targeting, therapeutic, contrast-rendering, and so forth. Finally, the NP size matches critical physiological functions in a living organism, enabling new pharmacokinetics effects such as prolonged circulation in the bloodstream or preferential accumulation in tumor tissue (enhanced permeation and retention effect³). Because of these advanced properties, new-generation nanotechnology-based chemotherapies are expected to be more efficient and less toxic.⁴

To date, a vast variety of NP-derived multifunctional complexes have been reported, ranging from inorganic (iron oxide,⁵ gold,⁶ carbon,⁷ and silicon⁸) to organic (dendrimers,⁹ liposomes,¹⁰ and polymeric micelles¹¹) materials. Among these,

nanoalumina is widely used in various areas of biotechnology and theranostics, in addition to ubiquitous daily life and industrial applications. Nanoalumina is employed as additives,¹² dental formulations,¹³ biosensors, biocatalysts,¹⁴ and antigen carriers.¹⁵ Of particular note is its potential use for cancer treatment. Li et al.¹⁵ immobilized tumor-cell-derived antigens on α - Al_2O_3 nanoparticles to activate T-cells more efficiently, resulting in an improved tumor regression when compared to other metal oxide nanoparticles. Nanoalumina has also been used as an efficient protein physisorber, which can be utilized for drug delivery and protein purification. The interaction of nanomaterials with cells and tissues can be tailored by controlling the surface protein corona. The effect of hydrophobicity and surface charge on the protein adsorption and corona formation was studied by functionalizing nanoalumina with amino, carboxyl, sulfonate, and phosphate groups.¹⁶ The tunable propensity for the binding and repulsion of specific viruses to nanoalumina based on these functional groups also shows the immense potential of this nanomaterial.¹⁷ Liu et al.¹⁸ highlighted the potential of nanoalumina as a sensitive biosensor by the immobilization of horseradish peroxidase on the nanoalumina surface, presumably by physisorption. The

Received: August 14, 2014

Revised: November 24, 2014

Published: November 30, 2014



ACS Publications

© 2014 American Chemical Society

15091

dx.doi.org/10.1021/la5042629 | Langmuir 2014, 30, 15091–15101

wide use of nanoalumina in the life sciences demands its large-scale and affordable production.

To meet this emerging demand for new nanomaterials, a range of bottom-up approaches have been developed, including sol-gel, low-temperature combustion,¹⁹ homogenization precipitation,²⁰ microwave solvothermal,²¹ hydrothermal,²² and spray pyrolysis.²³ However, all of these methods are limited by the challenges in fine control of several reaction parameters and high cost associated with chemicals of high purity. Moreover, most of these procedures yield Al_2O_3 nanocrystals in the unstable γ phase, which needs further annealing at high temperatures up to 1000 °C to be transformed to a stable α phase to harness their superior surface and bulk properties.^{19,24} Similar problems also exist in some of the top-down approaches, including laser ablation, where a significant proportion of the generated nanocrystals are in the γ phase.²⁵

High-energy ball milling (HEBM) represents an alternative facile, low-cost NP production method that became increasingly popular as a result of the demand for the large-scale production of nanoscale particles, both alumina and other materials.^{26,27} Unlike the synthetic bottom-up approach, HEBM substrates are solid-state materials, such as crystals and glasses, with known physical and chemical properties. Ball milling is universally applicable, making a wealth of existing materials potentially available for nanobiotechnology applications. In addition, the top-down HEBM approach provides good control over nanomaterial properties, as derived from their substrates, which can be largely predicted. HEBM of nanoalumina- and alumina-containing composites, however, so far has been focused on industrial applications, specifically for producing high green-density ceramics for biomedical implants. Large-scale milling of alumina for these applications uses hardened steel milling media generating significant Fe contamination and reduced biocompatibility.^{28,29} A recent study has evaluated several milling media and identified ZrO_2 as most suitable in terms of reduced contamination and its known biocompatibility.³⁰ However, the characterization of the HEBM-generated nanoalumina in terms of its colloidal and surface physicochemical properties is lacking so far, preventing the rapid uptake of this scalable production method.

In this article, we demonstrate a large-scale production of colloidal nanoalumina using a HEBM method suitable for biomedical applications. The developed method is suitable for the reliable production of nanoalumina in gram quantities, with controllable colloidal properties. The as-produced particles were characterized in terms of size, crystal structure, contamination levels, and yield in relation to milling time. A selective acid-etching procedure is also demonstrated to reduce contamination from the milling media. Finally, the feasibility of HEBM-generated nanoalumina for bioapplications is demonstrated by characterizing the colloidal properties before and after surface functionalization and assessing their biocompatibility using *in vitro* toxicity tests. This work addresses most of the requirements of nanomaterial qualities, including purity, colloidal stability, biocompatibility, and controllable surface moieties needed for use in life sciences.

2. EXPERIMENTAL SECTION

2.1. Preparation and Milling. A Pulverisette-7 (Fritsch, Germany) high-energy planetary ball mill was used to produce nanoalumina from alumina powder in the corundum α phase (Sigma-Aldrich, Australia). Thirty grams of 0.2 mm (zirconia) ZrO_2 balls (Glenmill, USA) and 9 mL of a 0.33 g/mL microalumina suspension

prepared in Milli-Q water were added to a milling bowl. A similar sample was prepared for counter balance. The ball-to-powder mass ratio (charge ratio) was calculated to be 10. The mean size of the microalumina powder was around 1.5 μm on the basis of the SEM image analysis, as shown in Figure S1 (Supporting Information, SI). After milling, the nanoalumina sample was recovered from ZrO_2 microballs using a 0.08 mm metal sieve, i.e., a discharge device (Fritsch, Germany). Ten milliliters of Milli-Q water was added for each extraction until the extracted solution appeared clear to the eye. Normally, four to five extractions were performed, yielding 50 mL of the sample.

2.2. Milling Parameters. Milling parameters were chosen on the basis of our several preliminary experiments (data not shown) and literature. These include a milling aid, the bowl/ball type, the ball size, the charge ratio, the milling speed, and the duration of each milling cycle. The results reported in ref 31 provide evidence for obtaining smaller nanoparticles by using wet milling in comparison to dry milling conditions. Water was chosen as the wet milling aid to avoid potential cytotoxicity for biological applications from surfactants or other process control agents, although they have been shown to reduce agglomeration during milling.³² Milling bowl/balls made of ZrO_2 or tungsten carbide (WC) have been reported to be the most suitable for milling hard materials such as alumina and diamond. The higher density of WC balls and their susceptibility to acid etching (for postmilling purification) represent appealing properties of this material.²⁶ However, the use of 0.2 mm WC balls (Dynamic Media LLC, USA) in combination with water resulted in a positive gauge pressure build up during the milling process, as noted in the manual and observed by us. Significant contamination was also visible to the eye as dark coloration after extraction using the discharge device, as was observed by others.³⁰ ZrO_2 bowl/balls were found to be more compatible with wet milling. Reid et al. reported that ZrO_2 balls produced the lowest contamination while milling alumina, when compared to balls made of alumina, steel, and WC.³⁰ Balls of 0.2 mm diameter and a charge ratio of 10 were chosen on the basis of the trade-offs between the contamination, yield, size of initial milling material, and the size of desired NPs.³³ The ball/powder size ratio was calculated to be 133. The highest milling speed supported by our HEBM system (1100 rpm) was used to achieve faster size reduction.³⁴ The milling was carried out in alternating ON/OFF cycles of 3 and 8 min, respectively. The time periods of the cycles were chosen to maintain the temperature below 70 °C, as measured at the outer surface of the bowl. The total milling time (net ON time) was varied between 3 min and 10 h to characterize its effect on the NP size reduction, contamination, and nanoparticle yield (as detailed in Results and Discussions).

2.3. Characterization. Several parameters of the bulk, microalumina, and milled nanoalumina were characterized, including the size, surface charge, chemical composition, crystal structure, and surface functional groups. Methods used for these characterizations are briefly described below.

The size of the microalumina powder was measured and analyzed using a scanning electron microscope (SEM; JEOL 6480LV, JEOL Ltd, Japan). The sample was prepared by drop-casting a 20 μL alumina suspension on a glass coverslip and then dried using a hot plate and sputter-coated with a gold layer prior to imaging.

The size and morphology of as-produced nanoalumina were determined using a transmission electron microscope (TEM, Philips CM10, Netherlands) operated at an acceleration voltage of 100 kV. Several drops of the sample under investigation were deposited on a 300-mesh copper grid and allowed to dry in a desiccator. The particle-size distribution from the TEM image was digitally analyzed.

Dynamic light scattering (DLS; Zetasizer NS, Malvern, U.K.) was used to determine the hydrodynamic diameter and polydispersity index of the nanoalumina samples. These samples were diluted in either water or buffer and transferred to a capillary cell (DTS1061, Malvern, U.K.) for measurement. The surface charge of the nanoalumina colloids was measured in terms of the zeta potential based on the electrophoretic mobilities of the sample. The presented

data met the quality criteria set by the manufacturer, ensuring the data validity.

Elemental analysis was carried out using energy-dispersive X-ray spectroscopy (EDX) detector JED-2300 (JEOL Ltd, Japan). A few drops of the nanoalumina sample under investigation were dried on a clean glass coverslip, transferred onto a sticky carbon stub, and pressed gently using a spatula to ensure sample preservation. Loosely adhered sample grains were removed from the carbon stub with a blower to avoid contamination of the EDX vacuum chamber during measurements. Further elemental analysis was done using an inductively coupled plasma mass spectrometry (ICP-MS) Agilent 7500cs (Agilent Technologies, USA). The powdered samples were weighed, placed in Teflon beakers, and then digested with concentrated HNO_3 (nitric acid) and HF (hydrofluoric acid). Precisely measured spikes of an internal standard (containing 6 Li, 103 Rh, 115 In, and 209 Bi) were added to the samples to monitor the instrument drift. HNO_3 (nitric acid) was initially run three times as a rinse, followed by a method blank measurement to provide background counts. A series of external calibration standards (BCR-2a) and reference samples (BIR-1 and BHVO-2) were run at the start and end of all runs for accuracy evaluation.

The crystal structure of the milled nanoalumina sample was determined by X-ray diffraction spectroscopy (XRD, Cu $K\alpha$ X-ray characteristic line) using an X'Pert PRO analytical diffractometer (PANalytical, Netherlands) acquired in the diffraction angle (2θ) range from 5 to 90° . The diffractometer was operated at a tube voltage and current of 45 kV and 40 mA, respectively. Several drops of the sample were deposited on a low-background silica mount and dried in an oven prior to the measurements. The crystallite size and strain were measured using the Williamson–Hall approximation as shown in the following equation³⁵

$$\beta \cos \theta = \frac{K\lambda}{D} + 4\epsilon \sin \theta \quad (1)$$

where β is the line full width at half maximum intensity (fwhm) in radians, D is the crystallite size, K is the shape factor (0.9), λ is the wavelength of Cu $K\alpha$ radiation, and ϵ is the crystal strain.

A Fourier transform infrared (FTIR) spectrometer (Nicolet iS10, Thermo Fisher Scientific Inc., USA) was used to identify chemical groups on the as-produced and surface-functionalized nanoalumina samples. The measurements were carried out at room temperature in the spectral range of $600\text{--}4000\text{ cm}^{-1}$. Air-dried samples were placed directly on an attenuated total reflectance (ATR) crystal window illuminated by a collimated infrared light beam whose reflection was detected by a photodetector. The spectral peaks were benchmarked against the reference literature to identify the sample surface functional groups.

Thermogravimetric analysis (TGA) was performed using a Mettler Toledo TGA/DSC instrument at a heating rate of $10^\circ\text{C}/\text{min}$ from 25 to 1000°C in a nitrogen atmosphere. Around 10 mg of nanoalumina samples were placed in an alumina crucible for each measurement.

2.4. Selective Acid Etching to Reduce ZrO_2 Contamination. ZrO_2 contamination resulted from high-impact collisions of ZrO_2 balls with the other ZrO_2 balls, HEBM bowl walls, and alumina powder. We developed an acid-etching procedure to reduce the ZrO_2 contamination, largely preserving the alumina content, as confirmed by EDX and ICP-MS analysis. The etching procedure is detailed in the Results and Discussion. Briefly, 1 mL of the HEBM-extracted sample was mixed with 1 mL of 99.99% H_2SO_4 (sulfuric acid) (Sigma-Aldrich, Australia) and stirred gently. The mixture was centrifuged at 13 000g for 5 min, and the supernatant, containing predominantly H_2SO_4 and dissolved zirconium, was removed. The precipitated sample was resuspended in Milli-Q water and dispersed using a vortex mixer and an ultrasonic bath for 5 min. This washing procedure was repeated three times to ensure complete removal of the residual acid and dissolved contaminants.

2.5. Assessment of the Sample Colloidal Stability. The particle size and zeta potential were measured to study the colloidal stability of nanoalumina, titania NPs (Sigma-Aldrich, Australia), nanodiamonds (NanoAmando, NanoCarbon Research Institute, Ltd.,

Japan), and zinc oxide NPs (ZinClear, Antaria, Western Australia, Australia). The concentration of the test solutions was 0.25 mg/mL . The stability of the nanoalumina colloid in anionic buffers, including 2-(*N*-morpholino) ethanesulfonic acid (MES) (pH 2.77 and 5.5), phosphate-buffered saline (PBS) (pH 7.4), and borate (pH 9) were also investigated. The long-term stability of the nanoalumina colloid in PBS was evaluated by comparing its mean hydrodynamic diameters (measured by DLS) of the same colloidal sample at two time points: freshly dispersed and 6 h postdispersion. Prior to the DLS measurement, the sample was diluted 5-fold, followed by 5 min of sonication.

2.6. Nanoalumina Surface Amine-Functionalization. Thirty milligrams of dried as-produced nanoalumina was thoroughly washed three times with Milli-Q water by centrifugation and resuspended in 1 mL of 95% ethanol (5% Milli-Q water) in a clear vial, followed by sonication for 5 min to prepare a stable colloid. For surface-functionalization with amino groups, 100 μL of (3-aminopropyl) triethoxysilane (APTES) (Sigma-Aldrich, Australia) was added to the colloid, and the mixture was sonicated in a bath sonicator for 1 h. The sample was then washed five times with ethanol to ensure the complete removal of unreacted APTES and dried in an oven at 60°C for 1 h. A control sample was also prepared in parallel, following the same procedure, except that no APTES was added. This care in the preparation of the control sample was necessary to rule out an eclipsing effect resulting from the nanoalumina surface treatment with ethanol, which has been reported to yield aldehydes.³⁶

2.7. Cytotoxicity. Mouse pituitary tumor cells (AtT-20, passage no. <15) were grown in 96-well plates (Falcon) in culture media (100 $\mu\text{L}/\text{well}$) containing DMEM (Sigma) + 10% fetal bovine serum (Sigma) and penicillin/streptomycin (Life Technologies) to reach a confluence of 70–90% on the day of the toxicity assessment. Bare and amine-functionalized nanoalumina colloidal solutions were prepared in Milli-Q water and added to the culture plate wells in a 1:20 dilution in order to minimize changes in the osmolality and pH of the culture media. The final concentrations of nanoalumina colloid tested for cytotoxicity were 1, 10, and 100 $\mu\text{g/mL}$. An MTS assay (CellTiter 96 cell proliferation assay, Promega) was used to assess the toxicity to cells after 1 day of nanoalumina incubation. Twenty microliters of the MTS reagent was added per well, and the absorbance was measured at 490 nm after 3 to 4 h of incubation at 37°C using a plate reader (PHERAstar FS, BMG Labtech) as a measure of the cell proliferation. The background was evaluated by measuring the absorbance in wells devoid of cells but otherwise treated as above.

3. RESULTS AND DISCUSSION

3.1. Size, ZrO_2 Contamination, and Yield as a Function of Milling Time. We identified that the milling time was an important parameter in determining several characteristics of the nanoalumina sample, including its mean NP size, contamination, and production yield. The milling time was varied from 3 min to 10 h. EDX analysis was carried out in order to quantify the nanometer-sized contamination fraction of ZrO_2 in the produced sample batch, with the results presented in Figure 1a (inset). 4000 \times SEM magnification was used. The EDX spectra acquired from regions of approximately $160\text{ }\mu\text{m}^2$ are presented in Figure 1a. The data were normalized to the aluminum peak at 1.5 keV to avoid the read-out variations between samples and acquisition regions. Several peaks are notable in addition to those attributed to aluminum and oxygen. These include zirconium (Zr), silicon, carbon, and sodium. The sources of Zr contamination included collisional self-milling of the balls and corrosion of the milling bowl. The percentage contamination was calculated by measuring the area under the peaks of oxygen, aluminum, zirconium, silicon, and sodium. The carbon peaks originating from the carbon stubs used during sample preparation were ignored in the process of the normalization. The small sodium peak was likely due to the

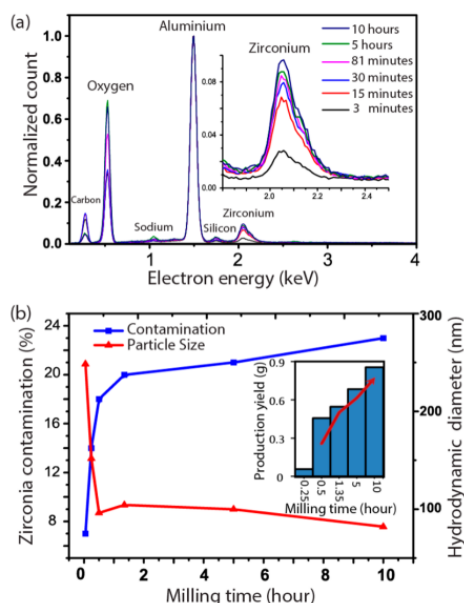


Figure 1. (a) EDX spectrum (counts normalized to the aluminum peak). An inset shows the close-up zirconium peaks. (b) Plot of the ZrO_2 contamination and hydrodynamic diameter of as-produced particles as a function of the milling time. The inset shows the production yield of nanoalumina vs milling time.

trace ions in the as-received microalumina or in Milli-Q water used for the milling and washing. The silicon peak originated from impurities in the as-received microalumina raw material. The Zr contamination presumably existed in the form of ZrO_2 . Therefore, on the basis of the stoichiometry of ZrO_2 and alumina, the percentage of ZrO_2 was calculated using the following formula

$$\text{wt \%}_{\text{ZrO}_2} = \frac{(\text{wt \%}_{\text{Zr}})M_{\text{ZrO}_2}}{M_{\text{Zr}}} \div \left(\frac{(\text{wt \%}_{\text{Zr}})M_{\text{ZrO}_2}}{M_{\text{Zr}}} + \frac{(\text{wt \%}_{\text{Al}})M_{\text{Al}_2\text{O}_3}}{2M_{\text{Al}}} \right) \quad (2)$$

where wt % is the weight percentage estimated from the EDX analysis and M_x is the molecular weight of x ($x = \text{ZrO}_2$, Zr, Al_2O_3 , or Al). The weight percentage of the ZrO_2 content of the samples were calculated to be 7, 14, 18, 20, 21, and 23% for 3, 15, 30, 81, 300, and 600 min of milling, respectively.

We also observed a clear relationship between the as-produced NP size and milling time, as illustrated in Figure 1b. The hydrodynamic diameter was determined by the DLS analysis. Two stages of the HEBM process are evident from Figure 1b: stage 1, commencement of the milling from the start to approximately 30 min; stage 2, from 30 min to 10 h. At the completion of stage 1, the particle mean diameter was drastically reduced from $1.5 \mu\text{m}$ (determined by SEM) to 96 nm (determined by DLS). This decrease correlated to a concomitant sharp increase in the ZrO_2 content to 80% of the maximum. We speculate that large, intact ZrO_2 grinding balls generated the most substantial impact on the initially loaded alumina micronized particles, fracturing them into nanoparticles, as clearly observable in Figure 1b (red triangles). At the same time, the collisions of ZrO_2 balls corroded the balls

and the bowl, increasing the ZrO_2 contamination. It was likely that this contamination resulted from the corrosion of both ZrO_2 balls and the ZrO_2 bowl; however, no bowl damage was visible to the eye. Our measurements were in contrast to the smaller levels (1 to 2%) of ZrO_2 contamination after much longer milling times (32 h), as observed previously;³⁰ however, these estimates are not directly comparable. The authors used dry milling conditions with the larger (10 mm) balls and a SPEX 8000 high-energy mixer/mill. It is generally accepted that the larger ball size and higher energy give rise to higher levels of contamination,³⁷ contrary to what they observed. This was likely to be due to the differences in the initial bulk alumina, exact ball/bowl composition, unspecified milling speed, and method of assessment. An increase in contamination with the milling time (measured in terms of the iron content using Rietveld refinement) has previously been reported during the milling of alumina using hardened steel balls.²⁹ However, no staged increase was noted by the authors.

During stage 2, the hydrodynamic diameter of nanoalumina changed at a much slower rate than in stage 1, reaching 96 nm after 10 h of milling. The observed slow milling rate was believed to be due to a saturation effect, which was reported elsewhere.^{34,38} Even though the saturation effect was reached in terms of the milled NP size at the completion of stage 1, further milling was required in stage 2 in order to increase the production yield of nanoalumina, as can be seen in Figure 1b (inset). The production yield can be estimated by means of DLS, which reported the as-produced NP hydrodynamic diameter distribution by volume. The volume of particles less than 100 nm in diameter determined by DLS (d_{DLS}) increased by 14% at the completion of stage 2. As a result of one HEBM 10 h session, 0.9 g of the nanoalumina sample was produced that contained particles with a (hydrodynamic) diameter of <100 nm. Further reduction in the size of NPs can be achieved if required for a particular application by minimizing the saturation effect either by purging the HEBM bowl with dry nitrogen during the milling process³⁹ or by reloading the bowl with the smaller-diameter grinding balls (e.g., ZrO_2), which offers greater contact with NPs produced in stage 1 per mill revolution and results in the further reduction of the NP size.³¹

3.2. Structure and Size. 3.2.1. Crystal-Phase Characterization. The crystal structure is an important factor that dictates the surface properties. It is therefore essential to characterize the crystal phase of as-produced nanoalumina. We carried out an XRD spectroscopic analysis of as-received microalumina powder and confirmed its α -crystal phase, as shown in Figure 2a. We anticipated that the milled sample would remain in this most stable phase of aluminum oxide because the outside temperature was maintained at a low value of <100 °C, thus minimizing the possibility of the crystal-phase transitions. Indeed, the XRD spectrum showed the unchanged crystallographic structure under these milling conditions (Figure 2b–e). In addition to the diffraction peaks from the α - Al_2O_3 crystal planes, two new peaks appeared at diffraction angles (2θ) of 18 and 20°, which were attributed to bayerite $[\text{Al}(\text{OH})_3]$ according to a crystallography database. The origin of these peaks might be either from individual bayerite nanocrystals or due to the formation of an $\text{Al}(\text{OH})_3$ layer on the nanoalumina particles. The formation of an $\text{Al}(\text{OH})_3$ layer on the surface of Al_2O_3 particles during the milling process has been reported by Stenger et al.⁴⁰

Peak broadening was also observed in the XRD plots (cf. Figure 2a–e), indicating a reduction in the crystal size and an

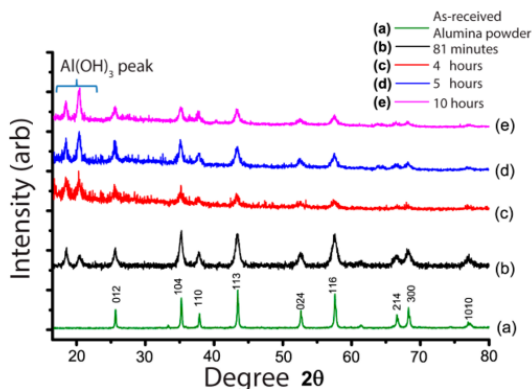


Figure 2. X-ray diffraction (XRD) spectra of alumina (a) as-received micrometer-size Al_2O_3 powder. HEBM processed for (b) 1.35, (c) 4, (d) 5, and (e) 10 h. The peaks above 22° confirmed the diffraction pattern of the α -alumina phase. The two new peaks at $2\theta < 22^\circ$ were attributed to the presence of bayerite.

increase in the lattice strain. The estimation of the size and strain using Williamson–Hall analysis,³⁵ as described in the Experimental Section, showed a reduction in the crystal size from ~ 200 to ~ 30 nm within the first data point at 81 min of milling (Figure S2, SI) and a 2-fold increase in the internal strain in comparison to the bulk material. We did not observe any further decrease in the crystal size or strain, although the significance of the linear fit for Williamson–Hall analysis was poor because of noise in the data. Similar trends have been reported elsewhere for alumina²⁹ and elemental ruthenium.⁴¹ Pooling the full width at half-maximum (fwhm) data of samples milled for 1.35, 4, and 5 h duration yielded a statistically significant fit (p value < 0.001), a crystal size of 40 ± 1 nm, and a strain value of 0.014 ± 0.002 . In comparison, the average Al_2O_3 granule diameter estimated by geometric TEM analysis was 25 nm. The difference in size was likely due to the effects of volume sampling and number sampling in these analyses and indicated that the produced nanoalumina were mostly single crystals.

It is worth noting that several bottom-up synthetic and top-down (femtosecond-laser ablation)²⁵ procedures produced metastable Al_2O_3 crystal phases (γ , δ , and θ) in addition to α - Al_2O_3 . Metastable-phase Al_2O_3 is usually unwanted because of the presence of crystalline defects.⁴² To mitigate this crystal-phase polydispersity, high-temperature treatment at $\sim 1000^\circ\text{C}$ is required to restore the stable α - Al_2O_3 phase.¹⁹ This additional technological procedure is cumbersome, accompanied by undesirable effects such as the sintering of crystallites and thus increasing size.^{20,43} The one-step production of α -nanoalumina, as demonstrated in this work, represents a significant simplification of the existing procedures.

3.2.2. Size Fractionation. The size distribution of as-produced nanoalumina in aqueous colloids was broad, as determined by the dynamic light scattering (DLS) method, with $\langle d_{\text{DLS}} \rangle = 70$ nm and fwhm = 46 nm (Figure 3). Centrifugation-based size separation was employed to reduce both $\langle d_{\text{DLS}} \rangle$ and the fwhm of the nanoalumina colloid, as reported elsewhere.²⁸ The colloid was centrifuged for 10 min at varying speeds, and the supernatant was collected and redispersed in water and its diameter distribution was measured

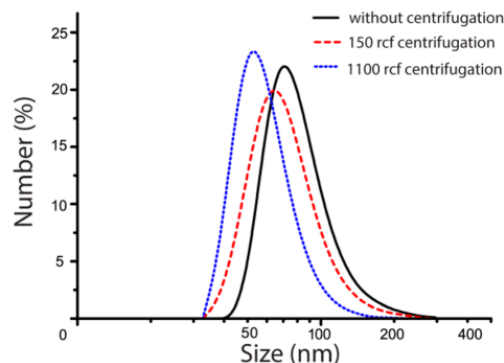


Figure 3. Plot of the hydrodynamic diameter distribution by number of as-produced nanoalumina samples measured by DLS. The size distributions of the nanoalumina obtained after 5 h of HEBM and subsequently centrifuged at 150 rcf and 1100 rcf for 10 min are shown by solid (black), dashed (red), and dotted (blue) lines, respectively.

by DLS, with the results presented in Figure 3. As expected, $\langle d_{\text{DLS}} \rangle$ was found to decrease to 64 and 52 nm at centrifugation speeds of 150g and 1100g, respectively. It was also found that after centrifugation at 1100g the fwhm was reduced to 31 nm. We note that DLS determines the hydrodynamic diameter of colloidal particles, which represents an overestimate of the physical diameter. Therefore, the mean physical diameter of the milled nanoalumina sample was independently determined by TEM and found to be much smaller than $\langle d_{\text{DLS}} \rangle$, which was likely due to the oligomerization of nanoalumina in aqueous suspensions.

TEM images of the milled samples are shown in Figure 4. Irregular shapes of the particles, displaying crystalline facets and sharp edges, are clearly observable. This architecture is common for milling procedures because of random breaking during collisions between grinding balls and the sample. Large, submicrometer-size particles were also present after milling (Figure 4a), which were removed during the centrifugation procedure (Figure 4b). The mean diameter of the nanoalumina sample particles postcentrifugation was $\langle d_{\text{TEM}} \rangle \cong 25$ nm.

3.3. Purification Process. After 5 h of milling, the nanoalumina contained $\sim 19\%$ ZrO_2 , as measured by EDX (Figure 5). Although most of the work on ball milling ignore contamination,⁴⁴ a few reports exist on the removal of the contamination by acid treatment. The corrosion of ceramics, including alumina and zirconia, has been investigated before.^{45,46} For example, Fe contamination (from hardened steel balls/bowls) was reduced from 10 to 2% on the basis of Reitveld refinement of XRD data by boiling the milled powder in HCl .^{28,29} However, a selective removal of ZrO_2 from milled nanoalumina has not been reported. Therefore, we developed a purification method using acid etching, as described in the Experimental Section. Etching using piranha solution (a 3:1 mixture of sulfuric acid and hydrogen peroxide (H_2O_2)) resulted in the dissolution of both ZrO_2 and Al_2O_3 components, but a preferential dissolution of ZrO_2 was desired. On the basis of the aforementioned reports and additional trial and error, sulfuric acid-based etching appeared most promising in differentially etching ZrO_2 and Al_2O_3 . Treatment with (50%) H_2SO_4 for several minutes reduced the ZrO_2 contamination significantly from 19 to 2%, with the almost unchanged hydrodynamic diameter of Al_2O_3 nanocrystals as shown in

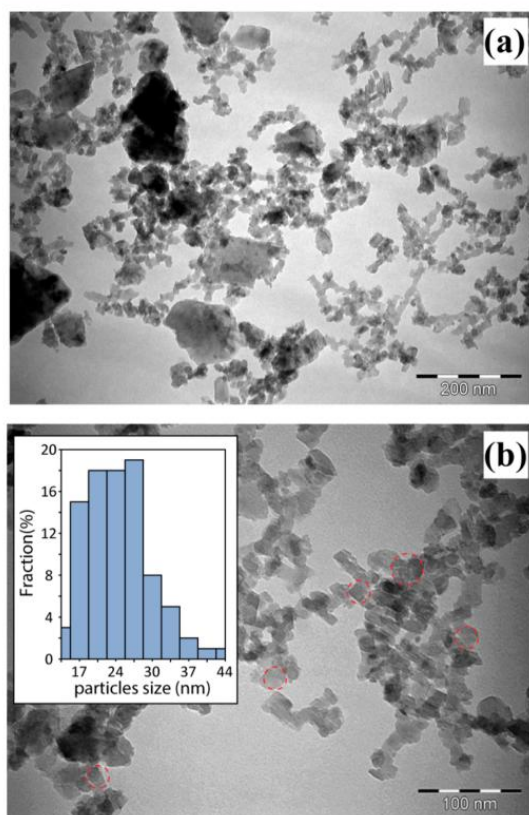


Figure 4. TEM images of the HEBM-processed nanoalumina samples: (a) as-produced, scale bar 200 nm; (b) centrifuged at 1100 rcf, scale bar 100 nm; (inset) size distribution histogram of sample in (b).

Figure 5c. The contamination was quantified using EDX spectra of as-produced and etched samples (Figure S3, SI). The significant reduction of the ZrO_2 percentage in the sample could be due to either the faster etching rate of ZrO_2 by sulfuric acid or the small crystal size and increased grain boundaries in the ZrO_2 particles generated by bowl/ball corruptions. The etching process duration was set to 10 min to avoid sulfur contamination that possibly occurred as a result of the surface adsorption of anions on the alumina surface. In comparison to the previously reported methods of contamination removal, this procedure was truly facile because it was carried out at room temperature. A modest temperature increase during etching was noted.

To evaluate the ZrO_2 content in the sample accurately, ICP-MS analysis was carried out. The amounts of ZrO_2 in the sample before and after purification were identified as 146 511 and 23 094 ppm, respectively. The percentage of ZrO_2 reduction after purification was calculated to be 84%. These measurements were in good agreement with the EDX analysis.

3.4. Colloidal Stability Analysis. Stable colloids are often characterized by a high magnitude of the zeta potential ($|\zeta| > 30$ mV).⁴⁷ The value of ζ of the as-produced alumina NP aqueous colloid was measured to be 39 mV (Figure 6a), confirming the origin of the observed stability for at least 1 month. (See the SI for a detailed explanation.)

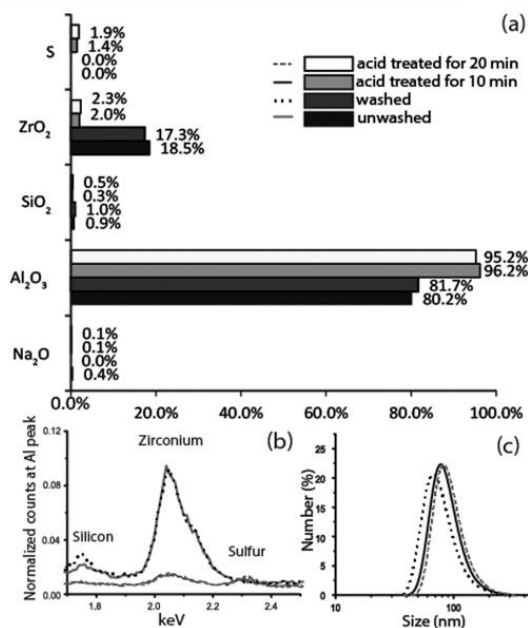


Figure 5. (a) Bar charts of the main contaminants in nanoalumina samples produced by HEBM before and after acid treatment based on EDX quantification analysis: unwashed nanoalumina, washed nanoalumina, acid treatment for 10 min, and acid treatment for 20 min. (b) EDX spectra normalized to Al peak displays peaks attributed to silicon, zirconium, and sulfur (marked on the graph). (c) DLS size analysis before and after purification.

To assess the mechanism of the observed colloidal stability, we carried out a comparative study using several types of NPs: titania (TiO_2), zinc oxide (ZnO), and nanodiamond (C sp^3). These NP types were chosen on the basis of the hypothesis that amphoterically induced electrical stabilization was possibly a common phenomenon for most metal oxide nanoparticles but not nanodiamonds. In water at pH 6.3, the zeta potentials of these NPs were measured to be 20, 31, and 58 mV, respectively, as shown in Figure 6. The NPs were stable in water for at least 1 month, showing no signs of aggregation. However, the NP stability in water alone is insufficient to ensure NP dispersibility in biological systems whose fluidic component is represented by physiological buffers containing salts. As an example, the NP incubation in cell cultures requires their dispersion in buffers. NP-assisted targeted delivery in a live organism is often realized by NP injection in the bloodstream, which requires the NP colloidal stability in blood plasma to prevent adverse effects, such as thrombosis, immune system response, and the engagement of the reticuloendothelial system measured in terms of the NP circulation half-lifetime.⁴⁸

In a buffer solution, the ionic strength is generally high, which causes a compression of the NP electrical double layer causing NP aggregation, as explained by Derjaguin–Landau–Verwey–Overbeek (DLVO) theory.⁴⁹ The ζ of alumina in water at different pH values is shown in Figure 6b, displaying a similar dependence as reported elsewhere⁵⁰ (where 0.01 M NaCl solution was used). The titration graph in Figure 6b displays a characteristic sigmoidal shape of positive and negative ζ at low and high pH values, respectively, where the

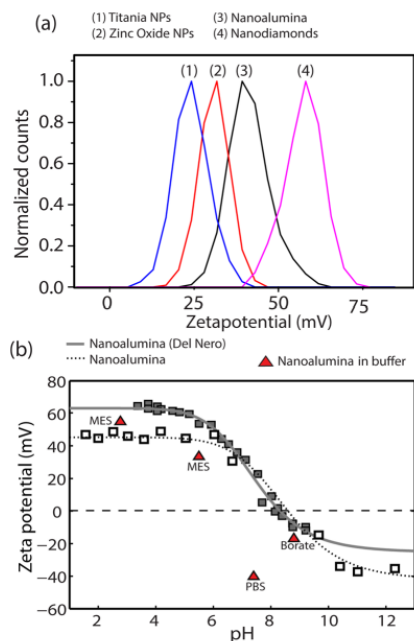


Figure 6. (a) Plots of the zeta potential of the tested samples. (b) Representative zeta potential values as a function of pH in 1 mM NaCl solution—a titration curve. Black open squares demarcate a titration curve of the washed nanoalumina colloidal sample fitted with a sigmoidal curve (gray dotted line). Gray closed squares demarcate a titration curve reproduced from the data set of Del Nero et al.⁵⁰ fitted with a sigmoidal curve (solid gray line). Red triangles demarcate the zeta potentials of washed nanoalumina colloidal sample in buffer solutions (labeled) of different pH values.

transition occurred at a pI of 8.1 ± 0.7 , i.e., the pH value at which $\zeta = 0$ mV, and hence the NP net surface charge was zero. The colloid was most prone to aggregation at pH values in the vicinity of the pI .

The characterization of NPs in biological solutions provides a stringent test of their colloidal stability, where PBS (potassium phosphate monobasic, sodium chloride, and sodium phosphate dibasic in molar concentrations of 1.54, 155.17, and 2.71 mM, respectively), was used as the most representative model of human bodily fluid in biological research.⁵¹ The ζ of nanoalumina in PBS was -40 mV, as shown in Figure 6b. The highly negative value of ζ was reported to be due to the adsorption of anionic phosphate ions on the surface, which determined the excellent stability of alumina in PBS. In addition, the percentage increase in the mean hydrodynamic diameter of NP was used as a measure of aggregation level $\zeta_{\text{PBS}/\text{H}_2\text{O}}$ of the tested NPs in PBS and was calculated as

$$\zeta_{\text{PBS}/\text{H}_2\text{O}} = \frac{\langle d_{\text{DLS}}^{(\text{PBS})} - d_{\text{DLS}}^{(\text{H}_2\text{O})} \rangle}{\langle d_{\text{DLS}}^{(\text{PBS})} \rangle} \times 100\% \quad (3)$$

where $\langle d_{\text{h}}^{(\text{H}_2\text{O})} \rangle$ and $\langle d_{\text{h}}^{(\text{H}_2\text{O})} \rangle$ are the mean hydrodynamic diameters of the NPs in aqueous and PBS colloids, respectively. $\zeta_{\text{PBS}/\text{H}_2\text{O}}$ was estimated by acquiring the $\langle d_{\text{DLS}} \rangle$ distributions in water and PBS using DLS (Figure 7) and substitution of their

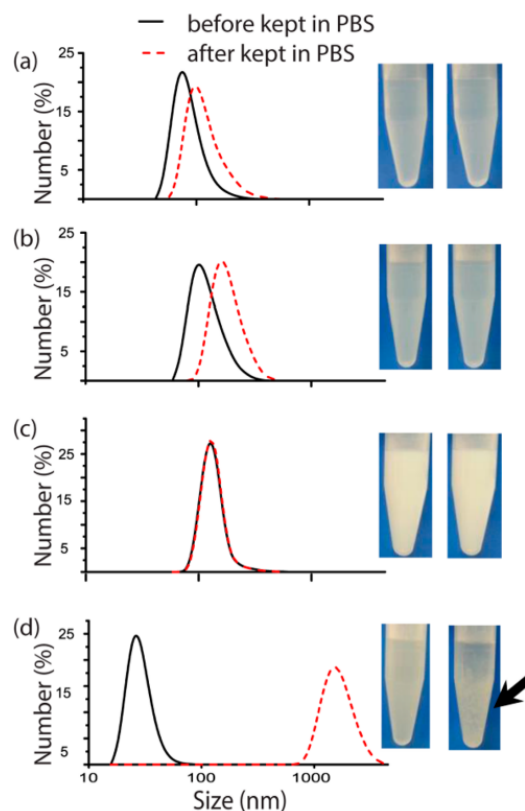


Figure 7. Plots of the hydrodynamic diameter distribution of colloidal NPs acquired by DLS in water (solid black) and PBS (dashed red lines, top to bottom): nanoalumina, zinc oxide NPs, titania NPs, and nanodiamonds. Two photographs besides each plot show the colloidal state: before (left) and 5 min (right) after dispersion in PBS.

$\langle d_{\text{DLS}} \rangle$ values into eq 3. Digital photographs of the samples dispersed in water and PBS were also taken and are presented in Figure 7 as insets. $\zeta_{\text{PBS}/\text{H}_2\text{O}}$ was determined to be 24, 37, 0.8, and 98% for nanoalumina, zinc oxide NPs, titania NPs, and nanodiamond samples, respectively. It was observed that only the nanodiamond buffer colloidal sample showed significant aggregation. The photograph of the nanodiamond colloidal sample clearly shows the onset of aggregation after 5 min in PBS to be visible as increased turbidity at the bottom of the vial (marked by an arrow). The other samples exhibited adequate colloidal stability in PBS solution, which can be interpreted to be due to the amphoteric nature of the tested metal oxide NPs, whereas nanodiamond is a nonamphoteric nanomaterial.

3.5. Surface Functionalization of Nanoalumina. The application of colloidal nanoalumina in the life sciences demands chemically accessible functional groups for conjugating biomolecules. To this end, we functionalized the OH-abundant alumina surface with amine groups using well-known silane chemistry. Aminopropyl trimethoxysilane (APTES) was chosen as a coupling agent because it is one of the most widely used agents for surface functionalization of materials with surface $-\text{OH}$ groups, such as silica and alumina.⁵² The $-\text{NH}_2$ moiety of APTES enables nanoalumina to anchor biomolecules

and drugs by forming strong covalent bonds. The procedure for the functionalization reaction of APTES with nanoalumina is schematically presented in Figure 8 (top inset).⁵³ The surface functional groups of the APTES-functionalized sample were analyzed and identified using FTIR spectroscopy, the zeta potential, and TGA. From the FTIR spectrum presented in Figure 8, five significant surface groups and their vibrational modes were identified and presented in Table 1. The band centered at 1029 cm^{-1} corresponded to the Al–O–Al bending vibration from the nanoalumina core,⁵⁴ and it was present in both as-produced and surface-functionalized samples. The broad band between $3213\text{--}3655$ and 1635 cm^{-1} originated from the stretching vibrational mode of O–H and the bending vibrational mode of O–H,⁵⁵ respectively. The O–H vibrational modes were due to the surface hydroxyl groups or adsorbed water molecules on the nanoparticle surface.⁵⁶ The OH group on alumina is an important functional group in the functionalization process. After the nanoalumina functionalization with APTES, two new bands appeared, providing strong evidence that the functionalization reaction was successful. The first band occurred at $1101\text{--}1166\text{ cm}^{-1}$ and was identified as C–N stretching, and the second band located at $2795\text{--}2991\text{ cm}^{-1}$ was assigned to C–H stretching.^{57,58} The expected characteristic Al–O–Si band was difficult to observe because it merged with the Al–O–Al band by virtue of the closely spaced vibrational frequencies resulting from the insignificant atomic mass difference of Al and Si.⁵⁹

We also carried out measurements of the zeta potential of as-produced and APTES surface-modified samples in solutions of different pH in order to validate the successful outcome of the functionalization reaction (Figure 8c). A significant positive shift of the nanoalumina pI point ($\Delta\text{pI} = 1.7$) from pH 8.81 to pH 10.51 was observed upon functionalization of the nanoalumina surface with APTES. The increment was in good agreement with that reported by Meder et al. pI of the functionalized nanoalumina was almost the same as that of pK_a of the APTES surface termina, propylamine, i.e., at pH 10.6.¹⁶ This result provided additional evidence that the nanoalumina surface was successfully modified as a result of the functionalization reaction. In this work, we added $464\text{ }\mu\text{mol m}^{-2}$ of APTES per μm^2 of alumina surface, which was greater than the saturating concentration of $26\text{ }\mu\text{mol m}^{-2}$ reported by Meder et al. to ensure complete surface functionalization. From the DLS size analysis, the hydrodynamic size of the nanoalumina before and after functionalization exhibited negligible changes, as shown in Figure 8d.

TGA analysis also confirmed the successful functionalization of amine groups on the nanoalumina surface. Figure 8d shows a weight loss in the temperature range of $400\text{--}800\text{ }^\circ\text{C}$ for the functionalized nanoalumina associated with the oxidation and decomposition of the aminopropyl group.⁶⁰ This result indicated the successful aminofunctionalization of nanoalumina surface using APTES to the alumina surface.

3.6. Cytotoxicity. The cytotoxicity of our nanoalumina sample before and after amine functionalization using APTES was tested using an in vitro cell-based MTS assay. The viability of AtT-20 cells treated with nanoalumina at concentrations of 1, 10, and $100\text{ }\mu\text{g/mL}$ for 1 day was measured on the basis of optical absorbance at a 490 nm spectral band induced by the bioreduction of the tetrazolium compound in the MTS reagent into a colored formazan product. As can be seen in Figure 9, the viability of the cells remained unaltered upon addition of the bare and amine-functionalized nanoalumina colloids up to

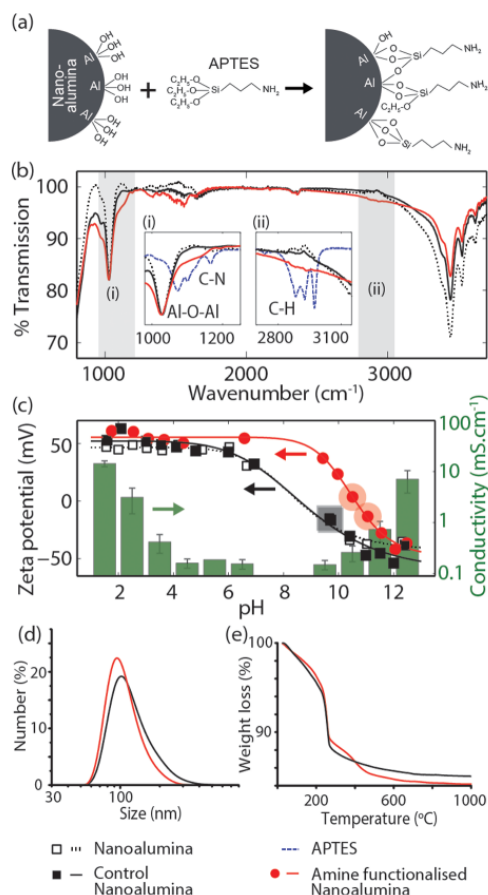
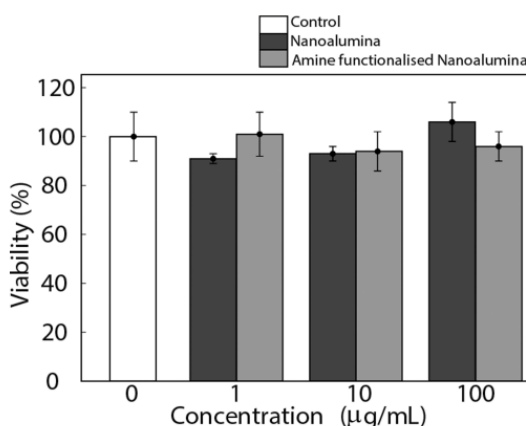


Figure 8. (a) Schematic diagram of aminofunctionalization of the nanoalumina surface using aminopropyl triethoxysilane (APTES). (b) Baseline-corrected and normalized (at the Al–O–Al peak) FTIR spectra of the nanoalumina samples washed with water (black dotted line), functionalized with amino groups (red solid line), and the nonfunctionalized control (black solid line). The control sample was treated with ethanol as for the functionalization reaction, without adding APTES. Insets: (i) close-up image of the spectral region between 980 and 1250 cm^{-1} showing peaks designated to belong to the Al–O–Al and C–N bonds; (ii) close-up image of the spectral region between 2695 and 3150 cm^{-1} showing a peak designated to belong to the C–H bond. The blue dotted line in the insets is the spectrum of APTES showing the C–N and C–H peaks before the reaction. (c) Representative zeta potentials (left y axis) of the three nanoalumina samples in aqueous solutions of varying pH. Closed black squares, closed red circles, and open black squares are the zeta potentials of washed, amino-functionalized, and control nanoalumina samples, respectively. The solid black, solid red, and dotted black lines represent sigmoidal fits to the respective data. Aggregation (diameter $>100\text{ nm}$) was observed in samples whose zeta potential fell between -30 and $+30\text{ mV}$. These data points are demarcated by large shaded circles. The mean conductivity values (right-hand ordinate) of the solutions within the pH range of $1\text{--}13$ are shown as green bars. Error bars represent standard deviations. (d, e) DLS size and TGA analysis of the control and aminofunctionalized nanoalumina, respectively.

Table 1. Assignment of the Infrared Absorption Bands of the APTES-Surface-Functionalized Nanoalumina Sample

characteristic band, cm^{-1}	assignment	ref
980–1095 (1029)	Al–O–Al	54
1101–1166	C–N stretching	57
2795–2991	CH stretching	58, 59
3213–3655	OH stretching	55, 56
1635	OH bending	55, 56

**Figure 9.** Bar chart of viability of cells treated with nanoalumina (black) and amine-functionalized nanoalumina (gray) samples benchmarked against the untreated control cells (white).

100 $\mu\text{g/mL}$, the highest concentration tested. This result demonstrated the excellent biocompatibility of the synthesized nanoalumina, despite the presence of zirconia impurities.

4. CONCLUSIONS

We demonstrated a high-yield, top-down approach to the production of nanoalumina using a high-energy ball milling method. As a result, nanoalumina (α -phase) powder with a mean diameter of 25 nm was produced per 10 h session, followed by a sulfuric acid treatment yielding 98% sample purity. The sample suspension in water and PBS solutions were stable for at least 1 month and were characterized by mean hydrodynamic diameters of 75 and 99 nm and zeta potentials of +40 and –40 mV, respectively. Notably, the other tested (amphoteric) metal oxide nanoparticles, TiO_2 and ZnO , exhibited comparable colloidal stability, whereas (nonamphoteric) nanodiamond colloid was unstable in buffers. Surface functionalization of the nanoalumina using facile silane chemistry was also demonstrated, which resulted in the decoration of the nanoparticle surface with amino groups suitable for further bioconjugation of tertiary biomolecules. The as-synthesized and amine-functionalized nanoalumina showed no measurable toxicity as reported by an in vitro MTS assay in cell cultures.

The demonstrated top-down method lends itself to a straightforward extension to the production of a variety of colloidal nanoparticles from solid-state bulk materials to meet the growing demands of the life sciences, where NPs of desired properties can be obtained by the selection of bulk material substrate properties.

■ ASSOCIATED CONTENT

Supporting Information

Stability mechanism of nanoalumina, SEM image of initial alumina powder, Williamson–Hall analysis to determine the crystallite size and strain, and EDX spectra of a purified nanoalumina sample using sulfuric acid. This material is available free of charge via the Internet at <http://pubs.acs.org>.

■ AUTHOR INFORMATION

Corresponding Author

*E-mail: andrei.zvyagin@mq.edu.au. Tel: +61-2-9850-7760. Fax: +61-2-9850-8115.

Notes

The authors declare no competing financial interest. All authors have given approval to the final version of the manuscript.

■ ACKNOWLEDGMENTS

We acknowledge financial support from Macquarie University, the Malaysian Government, Universiti Teknologi MARA, and the Targeted Federal Program of the Ministry of Education and Science of the Russian Federation (grant no. 14.578.21.0030). We thank Mr. Russel Field for his assistance with XRD measurements and ANFF for the ball milling machine. We acknowledge the assistance of Hamideh Shahheydari in carrying out cytotoxicity assays and the Australian School of Advanced Medicine for the cell culture facility. V.K.A.S. acknowledges Macquarie University for MQRF. We thank Assoc. Prof. Pearson and Mr. Wieland, Centre of Excellence Core to Crust Fluid Systems, Department of Earth and Planetary Sciences, Macquarie University for ICP-MS analysis. All the presented data were obtained using instrumentation funded by DEST Systemic Infrastructure grants, ARC LIEF, NCRIS, industry partners, and Macquarie University. We acknowledge the partial support of grant CE140100003.

■ REFERENCES

- (1) Zhu, Y.; Li, J.; Li, W.; Zhang, Y.; Yang, X.; Chen, N.; Sun, Y.; Zhao, Y.; Fan, C.; Huang, Q. The Biocompatibility of Nanodiamonds and Their Application in Drug Delivery Systems. *Theranostics* **2012**, *2*, 302–331.
- (2) Panáček, A.; Kvítek, L.; Prucek, R.; Kolář, M.; Večeřová, R.; Pizúrová, N.; Sharma, V. K.; Nevěčná, T. J.; Zbořil, R. Silver Colloid Nanoparticles: Synthesis, Characterization, and Their Antibacterial Activity. *J. Phys. Chem. B* **2006**, *110*, 16248–16253.
- (3) Maeda, H. Tumor-Selective Delivery of Macromolecular Drugs via the EPR Effect: Background and Future Prospects. *Bioconjugate Chem.* **2010**, *21*, 797–802.
- (4) Du, J.-Z.; Mao, C.-Q.; Yuan, Y.-Y.; Yang, X.-Z.; Wang, J. Tumor extracellular acidity-activated nanoparticles as drug delivery systems for enhanced cancer therapy. *Biotechnol. Adv.* **2010**, *21*, 789–803E.
- (5) Jun, Y.-w.; Lee, J.-H.; Cheon, J. Chemical Design of Nanoparticle Probes for High-Performance Magnetic Resonance Imaging. *Angew. Chem., Int. Ed.* **2008**, *47*, 5122–5135.
- (6) Sobhan, M. A.; Withford, M. J.; Goldys, E. M. Enhanced Stability of Gold Colloids Produced by Femtosecond Laser Synthesis in Aqueous Solution of CTAB. *Langmuir* **2009**, *26*, 3156–3159.
- (7) Ji, S.-r.; Liu, C.; Zhang, B.; Yang, F.; Xu, J.; Long, J.; Jin, C.; Fu, D.-l.; Ni, Q.-x.; Yu, X.-j. Carbon nanotubes in cancer diagnosis and therapy. *Biochim. Biophys. Acta, Rev. Cancer* **2010**, *1806*, 29–35.
- (8) Benezra, M.; Penate-Medina, O.; Zanzonico, P. B.; Schaer, D.; Ow, H.; Burns, A.; DeStanchina, E.; Longo, V.; Herz, E.; Iyer, S.; Wolchok, J.; Larson, S. M.; Wiesner, U.; Bradbury, M. S. Multimodal silica nanoparticles are effective cancer-targeted probes in a model of human melanoma. *J. Clin. Invest.* **2011**, *121*, 2768–2780.

- (9) Torchilin, V. P. Micellar Nanocarriers: Pharmaceutical Perspectives. *Pharm. Res.* **2007**, *24*, 1–16.
- (10) Peer, D.; Karp, J. M.; Hong, S.; Farokhzad, O. C.; Margalit, R.; Langer, R. Nanocarriers as an emerging platform for cancer therapy. *Nat. Nanotechnol.* **2007**, *2*, 751–760.
- (11) Koo, H.; Lee, H.; Lee, S.; Min, K. H.; Kim, M. S.; Lee, D. S.; Choi, Y.; Kwon, I. C.; Kim, K.; Jeong, S. Y. In vivo tumor diagnosis and photodynamic therapy via tumoral pH-responsive polymeric micelles. *Chem. Commun.* **2010**, *46*, 5668–5670.
- (12) Khalilpourazary, S.; Meshkat, S. S. Investigation of the effects of alumina nanoparticles on spur gear surface roughness and hob tool wear in hobbing process. *Int. J. Adv. Des. Manuf. Technol.* **2014**, *71*, 1599–1610.
- (13) Mendonça, G.; Mendonça, D. B. S.; Aragão, F. J. L.; Cooper, L. F. Advancing dental implant surface technology – From micron- to nanotopography. *Biomaterials* **2008**, *29*, 3822–3835.
- (14) Ge, J.; Lu, D.; Liu, Z.; Liu, Z. Recent advances in nanostructured biocatalysts. *Biochem. Eng. J.* **2009**, *44*, 53–59.
- (15) Li, H.; Li, Y.; Jiao, J.; Hu, H.-M. Alpha-alumina nanoparticles induce efficient autophagy-dependent cross-presentation and potent antitumor response. *Nat. Nanotechnol.* **2011**, *6*, 645–650.
- (16) Meder, F.; Daberkow, T.; Treccani, L.; Wilhelm, M.; Schowalter, M.; Rosenauer, A.; Mädler, L.; Rezwani, K. Protein adsorption on colloidal alumina particles functionalized with amino, carboxyl, sulfonate and phosphate groups. *Acta Biomater.* **2012**, *8*, 1221–1229.
- (17) Meder, F.; Wehling, J.; Fink, A.; Piel, B.; Li, K.; Frank, K.; Rosenauer, A.; Treccani, L.; Koeppen, S.; Dotzauer, A.; Rezwani, K. The role of surface functionalization of colloidal alumina particles on their controlled interactions with viruses. *Biomaterials* **2013**, *34*, 4203–4213.
- (18) Liu, X.; Luo, L.; Ding, Y.; Xu, Y. Amperometric biosensors based on alumina nanoparticles-chitosan-horseradish peroxidase nanobiocomposites for the determination of phenolic compounds. *Analyst* **2011**, *136*, 696–701.
- (19) Mi, X.; Zhang, X.; Ba, X.; Bai, Z.; Lu, L.; Wang, X.; Liu, Q. Preparation and luminescent properties of Cr³⁺:Al₂O₃ nano-powders by low-temperature combustion synthesis. *Adv. Powder Technol.* **2009**, *20*, 164–168.
- (20) Cheng, B.; Qu, S.; Zhou, H.; Wang, Z. Al₂O₃:Cr³⁺ Nanotubes Synthesized via Homogenization Precipitation Followed by Heat Treatment. *J. Phys. Chem. B* **2006**, *110*, 15749–15754.
- (21) Liu, D. Effects of Cr content and morphology on the luminescence properties of the Cr-doped alpha-Al₂O₃ powders. *Ceram. Int.* **2013**, *39*, 4765–4769.
- (22) Ghanizadeh, S.; Bao, X.; Vaidhyanathan, B.; Binner, J. Synthesis of nano α -alumina powders using hydrothermal and precipitation routes: a comparative study. *Ceram. Int.* **2014**, *40*, 1311–1319.
- (23) Manivasakan, P.; Karthik, A.; Rajendran, V. Mass production of Al₂O₃ and ZrO₂ nanoparticles by hot-air spray pyrolysis. *Powder Technol.* **2013**, *234*, 84–90.
- (24) Du, X.; Zhao, S.; Liu, Y.; Li, J.; Chen, W.; Cui, Y. Facile synthesis of monodisperse α -alumina nanoparticles via an isolation-medium-assisted calcination method. *Appl. Phys. A: Mater. Sci. Process.* **2014**, *116*, 1963–1969.
- (25) Edmonds, A. M.; Sobhan, M. A.; Sreenivasan, V. K. A.; Grebenik, E. A.; Rabeau, J. R.; Goldys, E. M.; Zvyagin, A. V. Nano-Ruby: A Promising Fluorescent Probe for Background-Free Cellular Imaging. *Part. Part. Syst. Charact.* **2013**, *1*–8.
- (26) Jean-Paul, B.; Patrick, A. C.; Fedor, J.; Joerg, W.; Pascal, A.; Mohamed, S.; Gopalakrishnan, B.; Rolf, R.; Alain, T.; Eric, G. High yield fabrication of fluorescent nanodiamonds. *Nanotechnology* **2009**, *20*, 235602.
- (27) Mohammadi Zahrani, E.; Fathi, M. H. The effect of high-energy ball milling parameters on the preparation and characterization of fluorapatite nanocrystalline powder. *Ceram. Int.* **2009**, *35*, 2311–2323.
- (28) Karagedov, G. R.; Lyakhov, N. Z. Preparation and sintering of nanosized α -Al₂O₃ powder. *Nanostruct. Mater.* **1999**, *11*, 559–572.
- (29) Goodshaw, H. J.; Forrester, J. S.; Suaning, G. J.; Kisi, E. H. Sintering temperature depression in Al₂O₃ by mechanical milling. *J. Mater. Sci.* **2007**, *42*, 337–345.
- (30) Reid, C. B.; Forrester, J. S.; Goodshaw, H. J.; Kisi, E. H.; Suaning, G. J. A study in the mechanical milling of alumina powder. *Ceram. Int.* **2008**, *34*, 1551–1556.
- (31) Li, B.; Wang, H. Effect of Ball Milling on Powder Preparation by Mechanical Methods. *Appl. Mech. Mater.* **2012**, *182-183*, 1541–1544.
- (32) Suryanarayana, C. Mechanical alloying and milling. *Prog. Mater. Sci.* **2001**, *46*, 1–184.
- (33) Forrester, J. S.; Goodshaw, H. J.; Kisi, E. H.; Suaning, G. J.; Zobec, J. S. Effect of mechanical milling on the sintering behaviour of alumina. *J. Aust. Ceram. Soc.* **2008**, *44*, 47–52.
- (34) Mio, H.; Kano, J.; Saito, F.; Kaneko, K. Optimum revolution and rotational directions and their speeds in planetary ball milling. *Int. J. Miner. Process.* **2004**, *74*, S85–S92.
- (35) Mote, V. D.; Purushotham, Y.; Dole, B. N. Williamson-Hall analysis in estimation of lattice strain in nanometer-sized ZnO particles. *J. Theor. Appl. Phys.* **2012**, *6*, 1–8.
- (36) Ivanova, A. S. Aluminum oxide and systems based on it: Properties and applications. *Kinet. Catal.* **2012**, *53*, 425–439.
- (37) Koch, C. C. Synthesis of nanostructured materials by mechanical milling: problems and opportunities. *Nanostruct. Mater.* **1997**, *9*, 13–22.
- (38) Heitjans, P.; Indris, S. Fast diffusion in nanocrystalline ceramics prepared by ball milling. *J. Mater. Sci.* **2004**, *39*, S091–S096.
- (39) Indris, S.; Bork, D.; Heitjans, P. Nanocrystalline Oxide Ceramics Prepared by High-Energy Ball Milling. *J. Mater. Synth. Process.* **2000**, *8* (3-4), 245–250.
- (40) Stenger, F.; Mende, S.; Schwedes, J.; Peukert, W. The influence of suspension properties on the grinding behavior of alumina particles in the submicron size range in stirred media mills. *Powder Technol.* **2005**, *156*, 103–110.
- (41) Hellstern, E.; Fecht, H. J.; Fu, Z.; Johnson, W. L. Structural and thermodynamic properties of heavily mechanically deformed Ru and AlRu. *J. Appl. Phys.* **1989**, *65*, 305–310.
- (42) Levin, I.; Brandon, D. Metastable Alumina Polymorphs: Crystal Structures and Transition Sequences. *J. Am. Ceram. Soc.* **1998**, *81*, 1995–2012.
- (43) Cava, S.; Tebcherani, S. M.; Souza, I. A.; Pianaro, S. A.; Paskocimas, C. A.; Longo, E.; Varela, J. A. Structural characterization of phase transition of Al₂O₃ nanopowders obtained by polymeric precursor method. *Mater. Chem. Phys.* **2007**, *103*, 394–399.
- (44) Wang, Y.; Suryanarayana, C.; An, L. Phase Transformation in Nanometer-Sized γ -Alumina by Mechanical Milling. *J. Am. Ceram. Soc.* **2005**, *88*, 780–783.
- (45) Schacht, M.; Boukis, N.; Dinjus, E. Corrosion of alumina ceramics in acidic aqueous solutions at high temperatures and pressures. *J. Mater. Sci.* **2000**, *35*, 6251–6258.
- (46) Ćurković, L.; Jelača, M. F. Dissolution of alumina ceramics in HCl aqueous solution. *Ceram. Int.* **2009**, *35*, 2041–2045.
- (47) Clogston, J.; Patri, A. Zeta Potential Measurement. In *Characterization of Nanoparticles Intended for Drug Delivery*; McNeil, S. E., Ed.; Humana Press: Totowa, NJ, 2011; Vol. 697, pp 63–70.
- (48) Arami, H.; Krishnan, K. M. Highly Stable Amine Functionalized Iron Oxide Nanoparticles Designed for Magnetic Particle Imaging (MPI). *IEEE Trans. Magn.* **2013**, *49*, 3500–3503.
- (49) Cao, G.; Wang, Y. *Nanostructures and Nanomaterials Synthesis: Properties and Applications*; World Scientific: Singapore, 2011.
- (50) Del Nero, M.; Galindo, C.; Barillon, R.; Halter, E.; Madé, B. Surface reactivity of α -Al₂O₃ and mechanisms of phosphate sorption: In situ ATR-FTIR spectroscopy and ζ potential studies. *J. Colloid Interface Sci.* **2010**, *342*, 437–444.
- (51) Du, S.; Kendall, K.; Toloueinia, P.; Mehrabadi, Y.; Gupta, G.; Newton, J. Aggregation and adhesion of gold nanoparticles in phosphate buffered saline. *J. Nanopart. Res.* **2012**, *14*, 1–14.
- (52) McCarthy, S. A.; Davies, G.-L.; Gun'ko, Y. K. Preparation of multifunctional nanoparticles and their assemblies. *Nat. Protoc.* **2012**, *7*, 1677–1693.

- (53) Ma, M.; Zhang, Y.; Yu, W.; Shen, H.-y.; Zhang, H.-q.; Gu, N. Preparation and characterization of magnetite nanoparticles coated by amino silane. *Colloids Surf, A* **2003**, *212*, 219–226.
- (54) Damayanti, N. P. Preparation of superhydrophobic PET fabric from Al_2O_3 - SiO_2 hybrid: geometrical approach to create high contact angle surface from low contact angle materials. *J. Sol-Gel Sci. Technol.* **2010**, *56*, 47–52.
- (55) Stuart, B. H. *Infrared Spectroscopy: Fundamentals and Applications*; John Wiley & Sons: New York, 2004.
- (56) Hass, K. C.; Schneider, W. F.; Curioni, A.; Andreoni, W. The Chemistry of Water on Alumina Surfaces: Reaction Dynamics from First Principles. *Science* **1998**, *282*, 265–268.
- (57) Kim, J.; Seidler, P.; Wan, L. S.; Fill, C. Formation, structure, and reactivity of amino-terminated organic films on silicon substrates. *J. Colloid Interface Sci.* **2009**, *329*, 114–119.
- (58) Ghezelbash, Z.; Ashouri, D.; Mousavian, S.; Ghandi, A.; Rahnama, Y. Surface modified Al_2O_3 in fluorinated polyimide/ Al_2O_3 nanocomposites: Synthesis and characterization. *Bull. Mater. Sci.* **2012**, *35*, 925–931.
- (59) Prado, L. A. S. A.; Sriyai, M.; Ghislandi, M.; Barros-Timmons, A.; Schulte, K. Surface modification of alumina nanoparticles with silane coupling agents. *J. Braz. Chem. Soc.* **2010**, *21*, 2238–2245.
- (60) Gupta, S.; Ramamurthy, P. C.; Madras, G. Synthesis and characterization of flexible epoxy nanocomposites reinforced with amine functionalized alumina nanoparticles: a potential encapsulant for organic devices. *Polym. Chem.* **2011**, *2*, 221–228.

Supporting Information

Large-Scale Production and Characterisation of Biocompatible Colloidal NanoAlumina

W. A. W. Razali, V. K. A. Sreenivasan, E. M. Goldys, A. V. Zvyagin

Supporting Information

Stability mechanism of nanoalumina

The high zeta potential is explained by the amphoteric nature of the alumina surface, which is typical for metal oxides. Because of the high isoelectric point (pI) of nano-alumina at 8.3, the hydroxyl groups on the surface of as-produced nano-alumina become positively charged in water forming an electrical double layer on the NP ²⁵. The reaction that renders charge to the alumina surface can be written as follows:

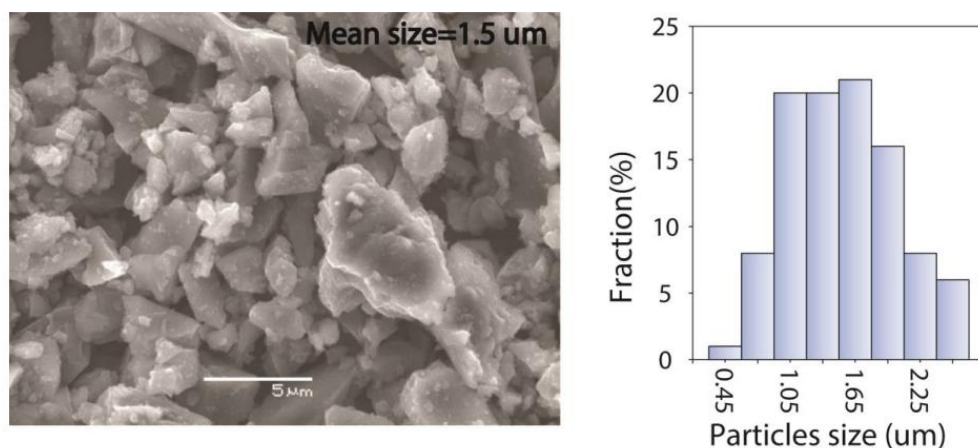
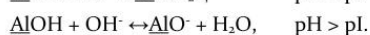
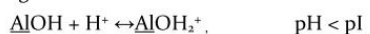


Fig. S1. SEM image of initial alumina powder.

This figure shows the mean size of unmilled alumina powder is 1.5 μm.

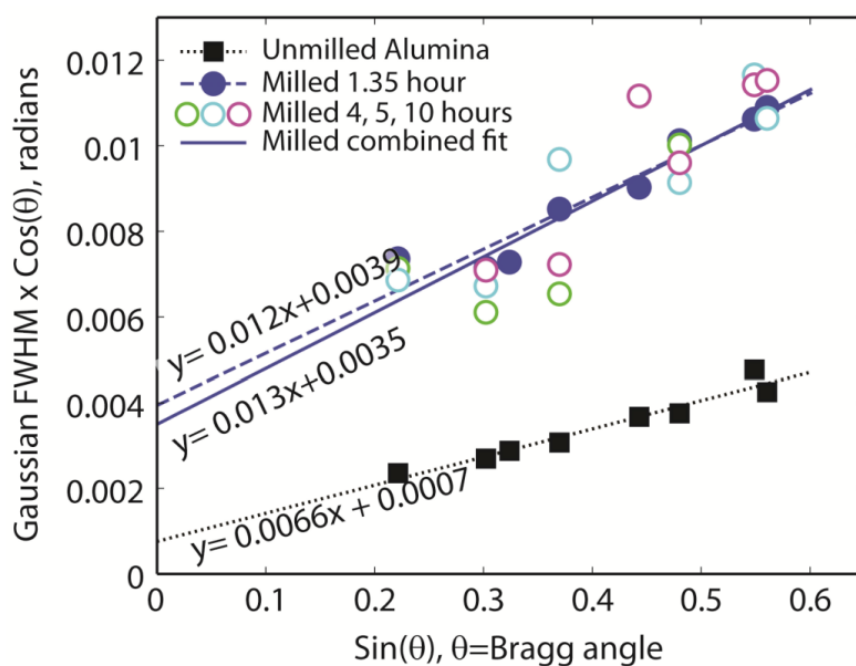


Fig. S2. Williamson-Hall analysis to determine crystallite size and strain.

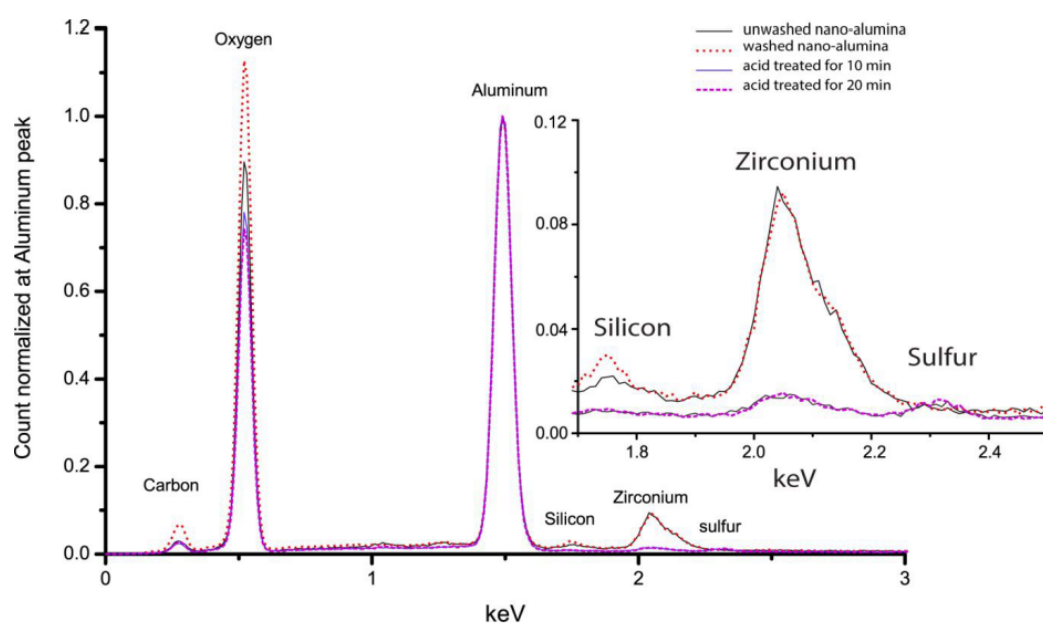


Fig. S3. EDX spectra of purified alumina sample using sulfuric acid.

The count of zirconium peak reduced after treatment with sulphuric acid.

4.6 References

- [1] W. A. W. Razali, V. K. A. Sreenivasan, E. M. Goldys, and A. V. Zvyagin, "Large-Scale Production and Characterization of Biocompatible Colloidal Nanoalumina," *Langmuir*, vol. 30, pp. 15091-15101, 2014.

Mass Production of Nanorubies

Photoluminescent Probe for

Bioimaging

This chapter is an adaptation of the report by Razali, *et al.*, “Mass Production of Nanorubies Photoluminescent Probe for Bioimaging”, which was under preparation for submission to the RSC Advances journal. This chapter is arranged as follows: The first section provides a brief introduction to the field of nanoruby science. The second section provides a short introduction to the paper, with a statement of the contribution of the PhD candidate. A full copy of the manuscript is appended to the last section of this chapter.

5.1 Background

The material ruby is a well-known precious gemstone, and its name is taken from its red-ruby-colouration. The colouration is a result of the presence of Cr^{3+} ions in the alumina crystal (α -phase, Al_2O_3 , or corundum) and this doping can be up to ≈ 1 wt %. Cr^{3+} ions in α - Al_2O_3 . This doping also provides ruby with photoluminescence properties and demonstrated by Maiman, who applied ruby crystal as a laser medium [1]. Ruby crystals are also commonly used for high temperature sensor [2-4], experimental study

[5, 6], shock pressure measurement [7], optical components [8, 9], and as abrasive materials [10]. The photoluminescence properties of ruby have also found application in biomedical optical imaging at the nano-scale. These small crystals, known as “nanorubies” have been shown to overcome some of the constraints seen with existing biomolecular probes which are based on organic fluorescent dyes and other photoluminescent nanomaterials. These advantages include excellent photostability, narrow photoluminescence emission, long photoluminescence lifetime, and high colloidal stability. These properties make nanorubies the choice for ultrahigh-sensitivity biomedical optical imaging, such as the imaging of discrete molecular trafficking in cells.

5.2 Introduction to paper

This paper reports on large-scale nanoruby production by using high-energy ball milling (HEBM), which has been applied for nanoalumina production as reported in previous chapter. This method produced grams of nanorubies per batch, with the size range of 10 – 200 nm. After acid etching purification process, the contamination level of the nanorubies reduced to 1% or less. This paper is different from the previous paper in several aspects. Firstly, it addresses the characterisation of nanoruby optical properties. Secondly, we report on new surface functionalisation (using silane-PEG) and bioconjugation (based on avidin-biotin interaction) approaches, which is demonstrated for μ -opioid receptors (MOR) labelling.

5.3 Author's contribution

The first author, Ph.D. candidate (Wan Aizuddin W. Razali) performed the production of the nanorubies using an HEBM method. The candidate has also developed a protocol of nanoruby milling. He carried out a purification method of the milled sample to reduce the contamination caused by zirconia milling balls/bowl. He performed a characterisation of the purified sample by means of size, contamination level, structural properties, and optical properties. He then also functionalised these nanorubies with amine, carboxyl and PEG groups using a silane chemistry method. Finally, he compiled the results, prepared the figures and wrote the manuscript attached to this chapter.

The second author, Dr. Sreenivasan assisted in the nanoruby functionalisation procedure, designed the PEG functionalisation protocol and performed the cytotoxicity analysis. He also carried out the cells and MOR labelling. The third author, Dr. Zhang carried out a silica coating of the nanoruby sample. Prof. Heintzmann carried out super-resolution imaging of the cells containing nanorubies. Prof. Goldys planned this project and provided the interpretation of results. A/Prof. Zvyagin (the corresponding author) suggested the main idea of this work, coordinated the project and finalised the manuscript. All authors were involved in the preparation of the manuscript.

5.4 Full paper

MASS PRODUCTION OF NANORUBIES PHOTOLUMINESCENT PROBE FOR BIOIMAGING

*Wan A. W. Razali,^{§,¶} Varun K. A Sreenivasan,^{§,¶,‡} Kai Zhang,[†] Rainer Heintzmann,[‡] Ewa M. Goldys,[‡] and Andrei V. Zvyagin.^{‡,‡, *}*

[§]MQ Photonics Research Centre, Faculty of Science, Macquarie University, Sydney, NSW 2109, Australia, [¶]Department of Physics, Faculty of Applied Sciences, Universiti Teknologi MARA Pahang, 26400 Jengka, Pahang, Malaysia, [‡]ARC Centre of Excellence for Nanoscale BioPhotonics (CNBP), Macquarie University, Sydney, NSW 2109, Australia, [‡]State Key Laboratory of Supramolecular Structure and Materials, College of Chemistry, Jilin University, Changchun 130012, PR China, [†]Department of Molecular Biology, Max Planck Institute for Biophysical Chemistry, Am Fassberg 11, 37077 Gottingen, Germany, and [‡]Laboratory of Optical Theranostics, N. I. Lobachevsky Nizhny Novgorod State University, 603950 Nizhny Novgorod, Russia.

KEYWORDS: nanoruby, photoluminescent, probe, high-energy ball milling, cell labelling, opioid receptor.

ABSTRACT Nanoruby is a promising photoluminescent probe for ultrahigh-sensitivity biological imaging characterised by excellent photostability, exceptionally long photoluminescent lifetime (≈ 4 ms) and low-level cytotoxicity. In this work, we demonstrate simple, affordable mass-production of nanorubies by using a high-energy ball milling method (HEBM). This method yielded grams of nanorubies per batch, with the size ranging from 10 to 200 nm. XRD analysis revealed α -crystal structure of the milled sample, which was 99% pure after an acid-based purification procedure. As-produced nanoparticles were surface-functionalised demonstrated by adapting a silanisation reaction, allowing flexible control of surface moieties, including amine, carboxyl and PEG groups. We examined the nanoruby performance of as a photoluminescent probe by performing labelling of cells and μ -opioid receptors.

INTRODUCTION

Fluorescence imaging is a non-invasive, sensitive optical imaging modality, which allows to highlight biomolecular species of interest. It is common to label these molecular species with fluorescent dyes, which suffer from several drawbacks, the most notable of these being photobleaching. Emission of a single fluorescent molecule lasts several seconds in average under continuous light excitation, which makes it unsuitable for long-term tracking of discrete molecules and events in the live cell¹. The excitation and emission spectra of fluorescent dyes are spectrally close and normally overlapped, which limits the efficiency of their spectral separation, especially in the scattering media². The cytotoxicity of some organic fluorescent dyes are poorly

controlled, and the fate of their phototoxicity degradation is always a concern in live cell and organism imaging³. Photoluminescent (PL) nanoparticles (NPs) have been introduced as alternative PL probes to enhance the sensitivity of the fluorescence imaging, ultimately achieving single molecule detection⁴.

These days, PL NPs are under research highlight due to almost unlimited photostability of selected PL NPs. They have a solid core and controllable surface moieties, which makes them interesting candidates for drug carriers. A subclass of PL NP is known to be biocompatible, exerting negligible cytotoxicity and characterised by rapid clearance from the organism with no systemic toxicity⁵. The examples of well-known PL NPs are Quantum Dots (QDs), gold NPs, upconversion NPs, and nanodiamonds⁶. QDs represent bright PL probes characterised by the high quantum yield up to 80%⁷. However, they have several limitations. For instance, the emission of single QDs is intermittent known as “photoblinking”^{8,9}. This phenomenon decreases the sensitivity of the fluorescence imaging, and has crucial bearing on the use of QDs for single-particle tracking. QDs are cytotoxic due to their material composition containing heavy toxic metals, such as cadmium in the core of the most widespread types of QDs^{10, 11}. Although, intense research towards overcoming these limitations is in progress, alternative nanomaterials are demanded.

In this paper, we report on large-scale production of newly-introduced PL NPs, known as “nanorubies”¹². Due to several useful properties of this material, nanorubies can populate an arsenal of the existing PL NPs for biomedical applications. Nanoruby is characterised by a narrow, almost zero-phonon line in the far-red spectral region (692 nm), where chromium ions embedded in an alumina host serve as active emission centres. Nanoruby is extremely photostable exhibiting no photoblinking, which makes these NP probes attractive for long-term

single particle tracking in living cells¹³. Nanoruby emission is characterised by a long photoluminescence lifetime ≈ 4 ms, which is enabling for discrimination of the fluorescence background characterised by short emission lifetime¹². It has been demonstrated that as-produced nanorubies were stable in water, and their cytotoxicity was found negligible¹². Therefore, an impact of this nanomaterial in the life sciences can be amplified, should be available in large amounts, hence its mass-production is needed. HEBM method represents an attractive approach towards achieving the aim of the mass-production of nanorubies. This method makes use of low-cost, readily available bulk materials whose properties are well-characterised, and hence the properties of derived nanomaterials can be to some extent predicted. This work demonstrates the broader prospects of using a HEBM method to produce PL nanomaterials in large scale.

MATERIALS AND METHODS

Milling process and preparation. Synthetic ruby crystals produced by Verneuil method were obtained from Henan Union Abrasive Corp, China. Firstly, these ruby crystals were crushed using a hydraulic press (Enerpac, US) to obtain micron-sized ruby powder. The obtained powder was sieved using a 63- μm metal sieve. The process was repeated until enough ruby powder was collected (3 g per milling batch). The mean size of the particle was evaluated as ≈ 40 μm based on dynamic light scattering (DLS, Mastersizer 2000, Malvern Instruments, UK) measurement.

A high-energy ball milling (Pulverisette 7, Fritsch, Germany) was used to convert micron-sized ruby powder to nanorubies. 30 grams of 0.2-mm zirconia balls were placed into a 20-mL zirconia bowl. 3 grams of ruby powders were placed onto zirconia balls, followed by an addition of 9-mL milliQ water, as a milling aid. The milling aid is known to minimise aggregation during the milling and further reduce the particle size^{14, 15}. Milling was performed at a maximum speed

of 1100 rpm in order to obtain the fastest possible size reduction¹⁶. The milling process was carried out in runs of 3 minutes per each run, followed by 8-min cooling time, in order to maintain the external bowl temperature below 70°C. This milling cycle was repeated 100 times, which was equivalent to 5 hours of milling.

In order to separate nanorubies from milling balls, the bowl was attached to a discharge device consisting of a 0.08-mm metal sieve. 50-mL syringe was attached to the discharge device and 10-mL MilliQ water was added into the bowl, followed by thorough shaking of the suspension. The sample was transferred into the syringe by pumping several times. Then the extracted sample was moved into a bigger container. This process was repeated until the extracted suspension became clear.

Characterisation. The structural properties of the micron-sized ruby and nanoruby were analysed by using x-ray diffraction spectroscopy (XRD, Cu K α X-ray characteristic line) with an X'Pert PRO analytical diffractometer (PANalytical, Netherlands). The spectra were acquired in the diffraction angle (2θ) ranging from 5° to 90°. The diffractometer was operated at a tube voltage and current of 45 kV and 40 mA, respectively. The nanoruby sample was washed with MilliQ water several times and centrifuged at 1000 \times g to remove large particles. Several drops of supernatant were deposited on a low-background silica mount and dried in an oven prior to the measurements.

Two devices were used for the size measurement. Firstly, a transmission electron microscope (TEM, Philips CM10, Netherlands) was operated to analyse the physical size and morphology of as-produced nanorubies. For the sample preparation, a 5- μ L sample was placed on a TEM copper grid and left overnight to dry. DLS (Zetasizer NS, Malvern, UK) was used to determine the hydrodynamics size of the produced nanorubies. DLS was also used to measure the surface

charge of the nanoruby particles in terms of its zeta potential. 0.8-mL sample was transferred to a capillary cell (DTS1070, Malvern, UK) to carry out the DLS measurements.

The elemental analysis was carried out by using an energy dispersive X-ray spectroscopy (EDX) detector JED-2300 (JEOL Ltd, Japan). A few drops of the nanoruby sample were dried on a clean glass coverslip, transferred onto a sticky carbon stub, and pressed gently using a spatula to ensure sample adhesion. Loosely bound sample grains were removed from the carbon stub with a blower to avoid contamination of the EDX vacuum chamber during measurements.

The excitation and emission spectra of the nanoruby was measured by using a spectrofluorometer (Fluorolog Tau3, JY Horiba, Japan). Colloidal nanoruby sample was transferred into a quartz cuvette for the measurement. To obtain a concentration curve, the emission spectra of these samples were measured versus concentration. The emission intensity was plotted against the concentration.

Colloidal refinement and fractionation. Micron-sized particles were still present in the milled nanoruby samples. Drying process was carried out to separate micron-sized particles. 20-mL of extracted-milled ruby was transferred into two 15-mL vials. Both vials were centrifuged at $2612\times g$ for 10 min. After discarding the clear supernatant, the tubes were placed in a hot water bath with temperature $\approx 100^{\circ}\text{C}$ to facilitate drying. Once dried, two layers of sample were observable – a white layer composed of nanorubies and a pink layer at the bottom comprising micro-rubies. The nanorubies were collected using a spatula.

To further refine the size distribution and chemical composition, 15 mg of the dried nanoruby powder was dispersed in MilliQ water for washing. The nanoruby colloid was centrifuged at $13000\times g$ for 5 min. The supernatant was replaced by fresh MilliQ, and the pellet was dispersed

by vortexing and sonicating. This washing process was repeated three times to obtain a colloidally stable suspension of nanorubies.

The granule size of the resultant nanorubies ranged from 10 nm to 200 nm, which needed further fractionation to obtain colloids with the improved polydispersity index. Firstly, the washed sample was centrifuged at $500\times g$ for 5 min to remove large particles. The supernatant was transferred into a new vial and further centrifuged at $1500\times g$ for 5 min, while the pellet was resuspended in MilliQ water and labelled, as a sample S1. The supernatant was further centrifuged at $5000\times g$ for 5 min, while the pellet was resuspended in MilliQ water and labelled as a sample S2. The supernatant was further centrifuged at $7000\times g$ for 5 min, while the pellet was resuspended in MilliQ water and labelled as a sample S3. The new supernatant was collected and labelled as a sample S4. The size distribution and morphology of the samples were analysed by using DLS and TEM.

Selective acid-etching to reduce the zirconia contamination. 1 mL of washed nanoruby (method mentioned previously) sample was mixed with 1 mL of 99.99% H_2SO_4 (sulfuric acid) (Sigma-Aldrich, Australia) and stirred gently. After 5 min, the mixture was centrifuged at $13000\times g$ for 5 min. The supernatant, which contains H_2SO_4 and dissolved metal oxides (mostly zirconia), was removed. The precipitated sample was resuspended in MilliQ water and dispersed using a vortex mixer and ultrasonic bath for 5 min. This washing procedure was repeated 3 times to ensure complete removal of the residual acid and dissolved contaminants.

Photostability and lifetime measurement. 50 μL of nanoruby was drop-cast on a coverslip for photostability and lifetime measurement. These measurements were carried out by time-lapse measurement of the photoluminescence intensity. The photoluminescence observation was carried out using a commercial inverted epi-luminescent microscope (Olympus IX70, Japan)

platform, with an oil-immersion objective lens (100×, NA 1.3, Olympus, Japan). An 532-nm laser (FB-532-1000-FS-FS-1-1-ST, RGB Lase, USA) was used as the excitation source. The photoluminescence was detected by an electron-multiplied CCD camera (EMCCD, iXon 885 DU, Andor Technology Ltd, UK). A schematic diagram of this microscopy system is included in **Figure S1 (Supporting information, SI)**. A filter set containing a laser-line filter, dichroic beam-splitter and long-pass (and band-pass) filters was mounted to separate the nanoruby photoluminescence from the excitation source light. In order to evaluate the sample photostability, it was illuminated at laser power densities of $0.6 \times 10^2 \text{ W/cm}^2$, $1.1 \times 10^2 \text{ W/cm}^2$, and $2.9 \times 10^2 \text{ W/cm}^2$. The photoluminescence signal was measured in every 30 s with 0.05 s camera exposure time. For the lifetime measurements, a field programmable gate array (FPGA, NI PCIe-7841R Virtex-5, National Instruments) was used to synchronise the laser pulse and image acquisition. The FPGA was programmed to generate two TTL pulse trains, one modulating the laser, while another triggering the EMCCD with flexible pulse durations, pulse separation and gating times (Δt). The laser “on” time was set to 10 ms (125 mW in continuous wave mode) and the camera exposure time was set at 1 ms. The Δt was varied from 0 to 40 ms with an 1-ms increment. The signal was captured using the EMCCD camera with 5 accumulations and the EM gain set to 10.

Cytotoxicity. Mouse pituitary tumour cells AtT20 cells (< 30 passages, gene-modified to express GPCRs) were plated at three concentrations 3000 cells per well, 10000 cells per well and 30,000 cells per well in a flat bottom 96-well plate, and cultured overnight in DMEM supplemented with 10% FBS and Penicillin/Streptomycin. The cells were grown for over 10 hours and treated with nanoruby at four concentrations: $0 \text{ }\mu\text{g.mL}^{-1}$ (control), $10 \text{ }\mu\text{g.mL}^{-1}$, $30 \text{ }\mu\text{g.mL}^{-1}$ and $100 \text{ }\mu\text{g.mL}^{-1}$ overnight in culture media. The next morning, the cell viability of the

nanoruby-treated cell cultures was measured by using an MTS assay (CellTiter 96 cell proliferation assay, Promega). To this aim, 20 μ L of MTS reagent was added to each well and the absorbance was measured at 490 nm after >2.5 hours of incubation. The measurements were carried out by using a PHERAstar FS (BMG Labtech) plate reader. The absorption background was measured by two methods. In the first method, the absorbance of the wells containing MTS reagent was measured, but without cells, as the background. In the second method, the absorbance was measured just after the addition of the reagents to cells was considered as an additional source of the signal offset. However, this method resulted in an increased uncertainty to the results and hence was not presented. We verified that the nanorubies did not measurably contribute to the 490-nm absorption, and thus introduced negligible artifacts.

Super-resolution imaging of the non-specific cells labelling (1) Mouse pituitary tumour cells expressing μ -opioid receptors (MOR-A₁T-20) were plated on a #1.5 coverslip placed inside sterile petridishes. The cells were grown in a humidified incubated containing 5% CO₂ in cell culture media, consisting of DMEM, 10% FBS, penicillin/streptomycin and 100 μ g/mL Hygromycin, the selection antibiotic for the expression of μ -opioid receptors (MOR). The expressed MORs were tagged with 3 repeats of hemagglutinin on the extracellular terminal to facilitate immunological targeting. On the next day, the cells were incubated with nanoruby colloids, which were devoid of aggregates (diluted 40 \times with supernatant after 1000 \times g centrifugation for 1 min) for 2 h at 37 °C. The cells were fixed with 37% paraformaldehyde prepared in phosphate buffered saline for 20 min. In order to visualise the cell membrane and nuclei, cells were treated by immunocytochemistry to label the membrane bound opioid receptors and the nuclei. To this aim, the cells were treated with 1% BSA in PBS for 1 hour to reduce non-specific labelling of antibodies used to label the receptors. A mouse-derived primary

antibody targeted against the hemagglutinin epitope on the receptors was diluted $500 \times$ in PBS containing 1% BSA and added to the cells, followed by incubation for 1 hour. An anti-mouse antibody labelled with AlexaFluor 594 was used as the secondary antibody, which was prepared by diluting the stock solution 1000 times in PBS containing 1% BSA. The cells were washed three times with PBS and incubated with 10 μ M Hoechst 33342 solution in PBS for 30 s and washed several times with PBS. The coverslip containing cells were mounted onto a glass slide using Dako fluorescence-free mounting medium, and the coverslip was secured in place using nail polish. The sample was imaged by using total internal reflection fluorescence microscopy (TIRF-M) combined with structured illumination microscopy (SIM). The TIRF-M technique in combination with a computer holographic illumination control was implemented on an in-house-made microscopy system. Three pairs of counter propagating evanescent waves (EWs) with angles of 60° to each other are generated by a computer hologram (spatial light modulator (SLM)) to form images with a sinusoidal structured illumination (grids 1–3). In total, 3×3 partial images are taken for each super-resolved image. Therefore, each grid is shifted twice over one grid period to illuminate every point of the object equally. The final image is reconstructed from all partial images using a custom MATLAB-based algorithm. Filter sets 1, 2, 3, and laser excitations were used to acquire cell membrane, nuclei and nanorubies, respectively, juxtaposed into one image. Filter set 1 contained a band-pass emission filters 570 nm - 620 nm, long-pass filter (wavelength cutoff, 750 nm); filter set 2 contained a band pass emission filter 420 nm - 480 nm, and a long-pass filter (wavelength cutoff, 750 nm); filter set 3 contained no excitation filters and a long-pass emission filter (wavelength cutoff, 655 nm). The corresponding laser excitations were 561-nm, 405-nm and 405-nm.

Amine and carboxyl functionalisation. 30 mg of nanoruby powder was thoroughly washed three times with MilliQ water by centrifugation and resuspended in 1 mL of 95% ethanol (5% MilliQ water) in a clear vial, followed by sonication for 5 min to prepare a stable colloid. For surface-functionalisation with amino-groups, 100 μL of (3-Aminopropyl) triethoxysilane (APTES) (Sigma-Aldrich, Australia) was added to the colloid, and the mixture was sonicated in a bath-sonicator for 1 hour. The sample was then washed five times with ethanol to ensure complete removal of unreacted APTES, and dried in an oven at 60 $^{\circ}\text{C}$ for 1 hour. For the carboxyl functionalisation, 20 mg of Succinic anhydride (SA) was dissolved in 120- μL Dimethyl sulfoxide (DMSO). 10 mg of amine-functionalised nanoruby was dispersed in 300- μL 100% ethanol. These two solutions were mixed together and left on a shaker overnight. The sample was then washed five times with ethanol and dried in an oven.

PEGylation and nanoruby silica-coating. (1) 1 mg.mL^{-1} nanoruby colloid was rinsed three times in water by centrifugation for 5 min at 5000 $\times g$, followed by replacing the supernatant with MilliQ water and redispersion by sonication and vortexing. These rinsing step were repeated once more, but ethanol was added to the pellet instead of water. 10-mM Silane-PEG ($M_w=2000$ Da; Laysan Bio, Inc, US) solutions were prepared in ethanol. This PEG-solution was used to replace the ethanol in the nanoruby colloid. The samples were vortexed thoroughly and sonicated for 1 hour. The samples were washed five times with ethanol at 10,000 $\times g$ for 5 min and dried overnight in a convection oven. (2) 5 mg of poly(vinylpyrrolidone) (Sigma-Aldrich, Australia), molecular weight, 360000 Da (PVP-360) was dissolved into 4-mL MilliQ water, followed by sonication for 5 mins. This solution was added into a 25-mL round-bottom flask containing 4 mL of nanoruby colloid. The mixture was stirred at 400 rpm for overnight. To remove an excess of PVP, the PVP-modified nanorubies were washed with MilliQ water, followed by washing with a

mixture of MilliQ water and ethanol (1:1 in volume). In order to perform silica-coating, 20-mL ethanol, 3-mL water, 20- μ L tetraethoxysilane (TEOS) and 400- μ L ammonia were added in a sequence into a 50-mL round-bottom flask. Finally, PVP-modified nanorubies in 4 mL ethanol were added into the flask. The mixture was left stirring at 400 rpm overnight at room temperature. The sample was washed with ethanol three times to remove an excess of the reaction agents. The silica-coated nanoruby sample was stored in ethanol.

μ -opioid receptor labelling (1) PEG functionalisation: 330 μ L of 210 μ g/mL silica-coated nanorubies were washed three times with MilliQ water. A solution containing 16-mM Silane-PEG and 4-mM Silane-PEG biotin was prepared in MilliQ water. These PEG-solutions were added to a nanoruby colloid, mixed and incubated at 40 °C overnight. The reaction product containing PEG-biotinylated nanorubies was washed three times with MilliQ water to remove unreacted reagents. (2) MOR-AtT-20 cells were plated on an 8-chambered slide and grown overnight in the presence of nanorubies in DMEM supplemented with 10% FBS, Penicillin/Streptomycin and 100 μ g.mL⁻¹ Hygromycin. The next day, the cells were serum-starved for 90 min in DMEM + 0.5% (w/v) BSA. The cells were fixed with 4% paraformaldehyde in PBS for 20 min and permeabilised with 0.25% TritonX-100 in PBS for 10 min. Before incubation of antibodies to tag MOR, the samples were blocked with 1% BSA solution prepared in PBS for 1 hour at room temperature. The cells were then incubated with 500 \times diluted monoclonal antibody (Covance) targeting the hemagglutinin epitope in PBS containing 1% BSA. Unbound antibodies were washed using 1% BSA solution in PBS three times. 1000 \times diluted Extravidin-FITC (Sigma) in 1% BSA in PBS was added to the cells and left for 1 hour. The samples were washed three times with 1% BSA in PBS. 4 μ g.mL⁻¹ of silica-coated nanorubies-PEG-biotin in 1 \times PBS with 1% BSA was added to the cells and incubated for

1 hour. The sample was washed one time with PBS, then quickly incubated with 10- μ M Hoechst in PBS. Finally, the samples were washed again one time with 1 \times PBS, and mounted in preparation for imaging. (3) For the imaging, an 70-mW 532-nm laser (pulse width, 10 ms) was used for optical microscopy. In the time-gated imaging mode, a gating time was set to 10 μ s. The camera exposure time was set to 10 ms, with an EM gain fixed at 100. 100 frames were accumulated to obtain one image.

RESULTS AND DISCUSSION

Size, zirconia contamination and yield. The milling process relies on collisions between milling balls and the inner wall of the bowl. Energy imparted to the sample during the collision process fractures particles, reducing their size¹⁷. At the same time, this process corrodes the surface of the balls/bowl, which leads to the sample contamination. In our case, the contaminant was primarily zirconia coming from the zirconia milling balls/bowl. Time evolution of the mean size of nanorubies and the contamination build up were monitored by collecting samples every one hour. DLS and EDX analyses were performed to measure the hydrodynamic diameter of the as-produced nanorubies and quantify the sample contamination, respectively. The results are presented in **Figure 1**. We observed a clear trend between the as-produced particle size and the milling duration. The particle mean-diameter reduced from 155 nm to 110 nm during 5 hours of milling. This decrease also correlated with an increase in the zirconia content from 16.8 % to 18.6 %.

Further, we assessed the production yield of this method, which was defined as the total mass of NPs produced with the size less than 100 nm. This was estimated from the colloidal size distribution obtained using DLS analysis. The percentage volume of particles < 100 nm was

estimated from a histogram of the colloidal nanoruby volume. By factoring in the total mass of the milled sample, the total mass of nanorubies (smaller than 100 nm in diameter) was calculated for each time point and shown in **Figure 1 (inset)**. Based on this calculation, 5 hours of milling yielded 0.8 grams of the nanoruby sample. Milling for the longer durations may result in an increase in the yield of NPs and perhaps reduce the particle size further, but also increase the contamination.

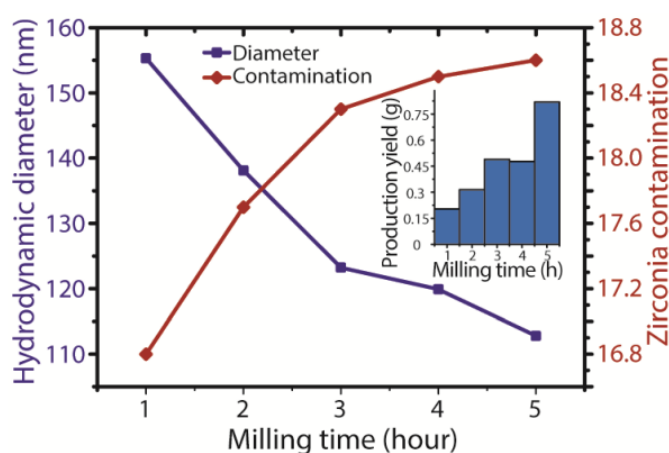


Figure 1. Plot of the hydrodynamic diameter of as-produced nanorubies and zirconia contamination as a function of the milling time. An inset shows a bar chart of the production yield of nanorubies as a function of the milling time.

Size fractionation. The as-produced aqueous nanoruby colloids exhibited a broad size distribution between 10 nm and 200 nm. Reduction of the size distribution and separation of nanorubies into different size-ranges were achieved by fractionation based on centrifugation. As a result, four different batches of nanoruby colloids were obtained, as shown in **Figure 2** (refer to Methods for details). These batches were labelled as samples S1, S2, S3 and S4. Note that DLS determined hydrodynamic diameters of colloidal particles, which represented an overestimate of

the physical diameter. Therefore, the mean physical diameter of the milled nanoruby sample was independently determined by TEM and found to be much smaller compared to DLS. This result offered an interpretation that the larger-size particles in S1 and S2 dominated the DLS readout, eclipsing the contribution of the smaller-sized particles, whereas the larger-size particle contribution was diminished in batches S3 and S4, revealing the presence of the small-size particles. Note that the aggregation observable in the TEM images was likely to be due to drying during the TEM sample preparation.

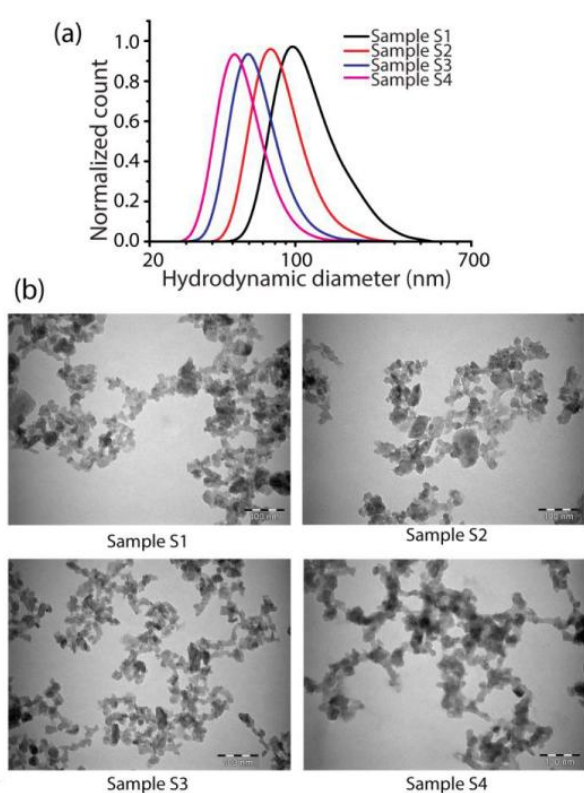


Figure 2. Nanoruby size fractionation: (a) A histogram plots of the hydrodynamic diameters based on the DLS analysis. (b) TEM images of as-produced nanorubies fractionated by centrifugation. Batches labelled as S1, S2, S3 and S4. Scale bar, 100 nm.

Selective acid etching. The purification process of the nanoruby samples was essential to remove unwanted contamination originated from the milling balls/bowl. The as-produced sample contained $\approx 18\%$ zirconia, as measured by EDX, following 5 hours of milling (see **Figure 1**). Although the contamination removal by acid treatment has been reported in literature^{18, 19}, these reports are scarce, most of the methods addressed the purification of iron, which originated from stainless steel bowls and milling balls. Walker *et. al.*²⁰ and other groups^{21, 22} have reported on the successful acid treatment to remove ceramic (zirconia) contaminants due to the corrosion rate of the ceramics. In my earlier work on the selective acid etching method for zirconia removal²³, a significant reduction of the zirconia contamination from 18% to 1% was demonstrated by etching the samples with 50% sulfuric acid, as shown in **Figure 3a**. This result was validated by the EDX analysis, which determined the ratio of zirconia and alumina, and also corroborated by the analysis of the results obtained using induction coupled plasma spectroscopy (ICPMS)²³.

Structural analysis. The crystal structure is a crucial factor that influences optical properties of PL NPs. The characteristic emission of ruby (see **Figure 4a**) originates from Cr^{3+} colour centres in a crystal matrix of Al_2O_3 in the alpha crystal phase (also known as corundum). Our research group and the others have reported marked changes in the photoluminescence characteristics upon the crystal phase change. For example, a spectrally broad photoluminescence of low quantum yield was observed in case of the gamma-phase crystal structure of Al_2O_3 doped with the amount of Cr^{3+} comparable to that of the ruby^{12, 24}. The recovery of the photoluminescence properties to these characteristic to ruby was demonstrated by annealing at 1200°C ²⁴. Therefore, we carried out analysis of the crystal phase of the as-produced nanoruby samples.

XRD spectroscopic analysis of the nanoruby sample before and after the purification was performed and benchmarked against that of as-received micro-ruby samples. The measured crystallography peaks of the samples were matched to the peaks to the PDF crystallography database, confirming the alpha phase of the as-produced NPs, with no peaks corresponding to the gamma-phase of alumina. The nanoruby photoluminescence spectra featured the characteristic ruby doublet at 692 nm identical to that of the micro-ruby sample, as shown in **Figure 3b**. This matched our expectation that the milling process would retain the crystals in its most stable alpha-phase, especially since the external bowl temperature was maintained $<100\text{ }^{\circ}\text{C}$, well below the temperatures required for the crystal phase transitions measured in hundreds of degree Celsius²⁵.

Two peaks emerged in the XRD spectra of as-produced nanorubies at the diffraction angles ($2\theta = 18^{\circ}$ and 20°) in comparison with the micro-ruby spectra, as can be seen in **Figure 3b**. These peaks were identified to be originating from bayerite $[\text{Al}(\text{OH})_3]$. The formation of $\text{Al}(\text{OH})_3$ during the milling process has been reported by Stenger *et al.*²⁶, where the authors hypothesised that $\text{Al}(\text{OH})_3$ was formed on the alumina surface due to the amorphisation and reaction with moisture, followed by crystallisation as aluminium hydroxide. Formation of nanometre-scale particles of bayerite partly doped with Cr^{3+} was another possible scenario. The acid etching procedure proved to be effective to eliminating the bayerite component in the sample, as can be seen by the complete suppression of the peaks in the XRD spectrum (**Figure 3b**). Note two peaks at 28.5° and 56.2° were identified originating from the sample holder made of silicon.

A closer observation at the peaks of the XRD spectra revealed broadening of the peaks in the milled ruby, which was indicative of the crystal size reduction²⁷. We applied Williamson-Hall (WH) analysis using Highscore Plus software version 3b (PANalytical, Netherlands) to

determine the average crystal size, and confirmed that it was reduced from 42.0 nm to 40.6 nm upon acid treatment. The WH plots are included in **Figure S2 (SI)**.

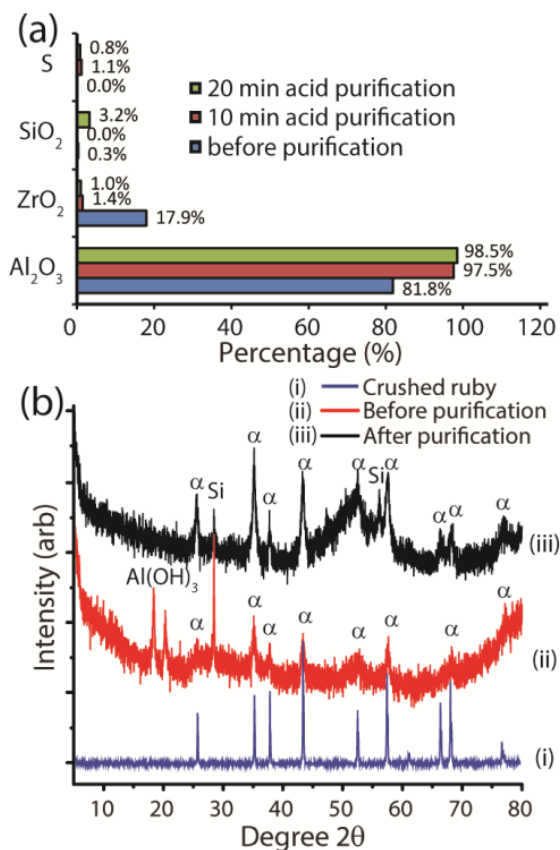


Figure 3. (a) Bar chart of the elemental analysis of nanorubies produced by the HEBM method based on the energy-dispersive X-ray (EDX) analysis: Nanorubies before purification, after acid treatment for 10 min, and after acid treatment for 20 min. (b) X-ray diffraction (XRD) spectra of (i) crushed ruby (micron-sized), (ii) nanorubies before acid treatment and (iii) after acid treatment.

Nanoruby photoluminescence characterisation. Photoluminescence excitation and emission spectra of the as-produced nanorubies are shown in **Figure 4a**. Two broad excitation peaks were observed at 402 nm and 557 nm, corresponding to the transitions from ground state 4A_2 to the

excited state 4F_1 and 4F_2 , respectively²⁸. Obviously, the greater absorption cross-section at 402 nm resulted in the greater observable emission intensity. A narrow emission doublet was observed, featuring two peaks at 690.6 nm and 692.1 nm, known as R_1 and R_2 lines, originated from the transitions $\bar{E} \rightarrow ^4A_2$ and $^2\bar{A} \rightarrow ^4A_2$ of the Cr^{3+} colour-centers in ruby^{29, 30}. The emission intensity versus nanoruby colloidal concentrations was measured, with the result presented in **Figure 4b**. This curve was used as a calibration for estimation of the nanoruby colloid concentration.

The normalised fluorescence intensity as a function of time at several excitation intensities are plotted in **Figure 4c** to demonstrate the nanoruby photostability. No reduction in the emission signal was observed for 1 h continuous laser illumination at the excitation intensity of 0.29 W/cm².

Nanoruby photoluminescence was verified to be unaffected by environmental conditions, with no observable quenching effects³¹, as compared to the other PL nanomaterials, such as fluorescent nanodiamonds³² and upconversion NPs³³. The photoluminescence lifetime of nanoruby was measured to be 4.2 ± 0.1 ms, as shown in **Figure 4d**. This value is comparable to the photoluminescence lifetime of bulk ruby, as reported elsewhere³⁴. Such long lifetime is advantageous for discrimination of nanoruby signals from short-lived optical background by using a time-gated detection scheme.

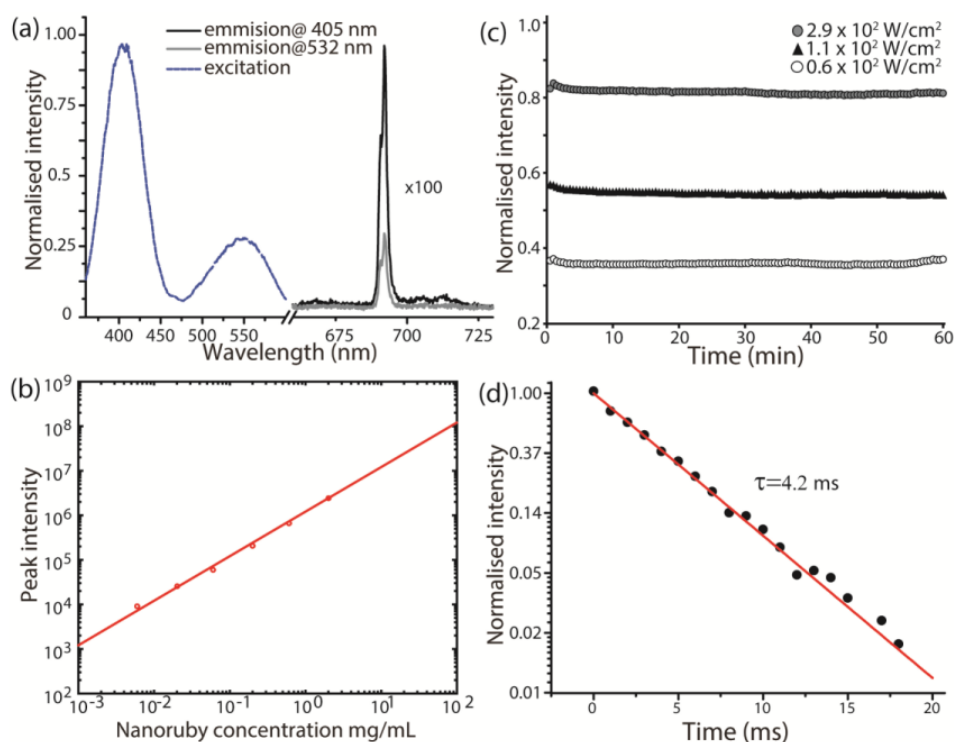


Figure 4. (a) Excitation, and emission spectra of the nanoruby sample under excitation with 405-nm and 532-nm lasers. (b) Nanoruby photoluminescence intensity at different concentrations of the colloidal nanoruby samples. (c) Nanoruby photoluminescence intensity as a function of time, excited with the laser intensities of $1.1 \times 10^2 \text{ mW/cm}^2$, $0.6 \times 10^2 \text{ mW/cm}^2$, and $2.9 \times 10^2 \text{ mW/cm}^2$ at 532 nm. (d) A semi-log plot of the nanoruby photoluminescence time trajectory. The solid line shows a single-exponential fit with the component of 4.2 ms.

Cytotoxicity. Figure 5 shows the results of an MTS assay designed to evaluate the cytotoxicity of nanorubies in a mouse pituitary tumour cell line (AtT-20). The results were obtained from two independent experiments using the nanoruby solution of known concentration. Cells plated at three densities (see Methods section) were used to evaluate the cell

viability. The fluorescence data was normalised to the viability of 100% for control samples with no nanorubies present. The cell viability was not decreased even at the highest colloidal nanoruby concentrations (100 $\mu\text{g/mL}$). This result shows that nanoruby provides very limited cytotoxicity, which is suitable to be applied as PL molecular probe.

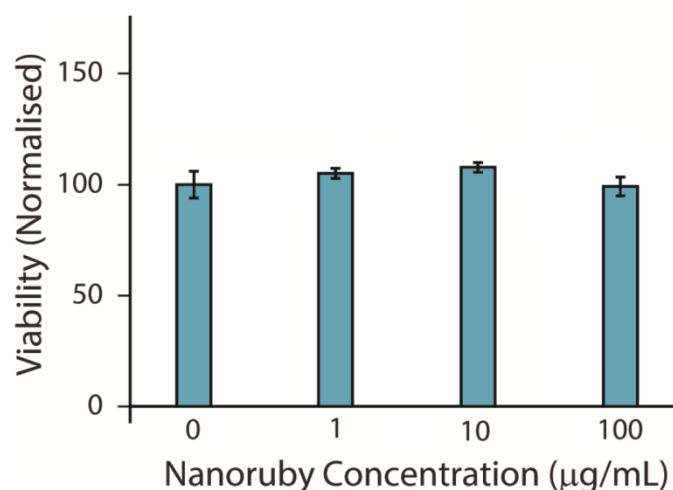


Figure 5. Bar chart of viability of cells treated with nanorubies at three different concentration: 1 $\mu\text{g/mL}$, 10 $\mu\text{g/mL}$ and 100 $\mu\text{g/mL}$. As a control, the viability of cells without nanorubies (0 $\mu\text{g/mL}$) also included.

Nonspecific super-resolution cell labelling. The performance of nanoruby as PL probe for the super-resolution imaging³⁵ was tested by imaging AtT-20 cells non-specifically labelled with nanorubies, as shown in **Figure 6**. The cell nuclei and membranes are coloured blue and green, respectively. Nanoruby signals are coloured red. In order to broaden the application scope of the developed nanorubies, surface-functionalisation procedures were developed to allow binding functional biomolecules, as discussed in the following section.

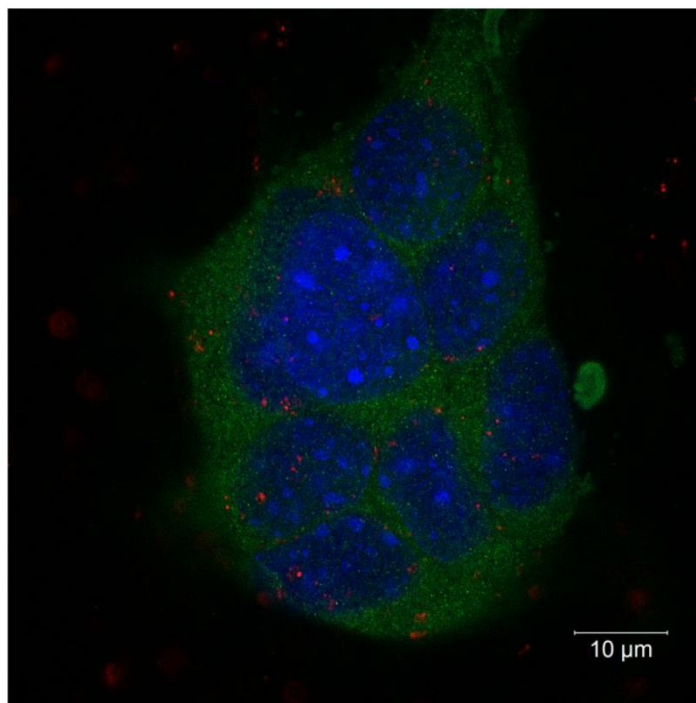


Figure 6. A super-resolution image of AtT-20 cells containing nanorubies. Three images spectrally-tuned to highlight the cell membrane immunostained with Alexa Fluor 594 (green), nuclei stained with Hoechst fluorescent dye (blue) and nanorubies (red) are superimposed.

Nanoruby surface-functionalisation. Functional chemical groups on the colloidal NP surface are required to control their chemical and biochemical properties. These functional groups serve as anchor points for biomolecules. We tested the amenability of the nanoruby surface for functionalisation with amine groups. Silane-functionalisation is known as a straightforward and efficient approach for surface functionalisation of metal oxides harbouring hydroxyl ($-OH$) moieties. Aminopropyl trimethoxy silane (APTES) was chosen as a coupling agent. NH_2 moiety

of the APTES enables nanorubies to anchor biomolecules and drugs by forming strong covalent bonds. The reaction of APTES with nanoruby is schematically presented in **Figure 7a**.

Several tests were performed to assay -NH_2 groups on the nanoruby surface. Firstly, we analysed the functionalised samples by FTIR spectroscopy. Five characteristic surface groups and their vibrational modes were identified from the FTIR spectrum (**Figure 7b**) and listed in **Table 1**. The band centred at 1026 cm^{-1} corresponded to the Al-O-Al bending vibration from the nanoruby core and it was present in both as-produced and surface-functionalised samples. The broad band between 3200 and 3600 cm^{-1} originated from the stretching vibration mode of O-H. After the nanoruby functionalisation with APTES, three new bands appeared, providing a strong evidence that the functionalisation reaction was successful. The bands at $1084\text{--}1172\text{ cm}^{-1}$, $1506\text{--}1560\text{ cm}^{-1}$, and $2820\text{--}3019\text{ cm}^{-1}$ were identified as C-N stretching, N-H bending, and C-H stretching respectively. We also tested the chemical availability of the amine groups detected by the FTIR by a reaction with anhydride. Succinic anhydride (SA) has been shown to spontaneously undergo covalent bonding with primary amine groups³⁶, resulting in the formation of a free carboxyl group, as schematised in **Figure 7a**. The FTIR spectra of these carboxyl modified nanorubies showed an additional band at $1560\text{--}1695\text{ cm}^{-1}$ corresponding to the C=O stretching, further confirming our interpretation of the nanoruby surface chemical groups.

We carried out a secondary analysis by measuring the surface charge of the nanoruby particles before and after the functionalisation with amine and carboxyl groups. In order to obtain statistically significant data, zeta-potential measurements were carried out in solutions of different pH (**Figure 7c**). The zero-crossing point, also known as the isoelectric point (IEP), of the as-produced bare nanorubies was measured as pH 9.5. The amine-modified sample exhibited a significant positive shift in the IEP ($\Delta\text{ IEP}= 1.4$) to pH 10.9, which was attributed to the

positive charge of the surface-coupled amine groups³⁶. The presence of amine groups was further confirmed by the pKa of non-cyclic primary amines to be in the range of pH from 10 to 11³⁷. As expected, the carboxyl-functionalised nanoruby sample showed a significant shift in the IEP from 10.9 to 6.0. This value was also in the range of pKa values reported for carboxylic acids³⁷.

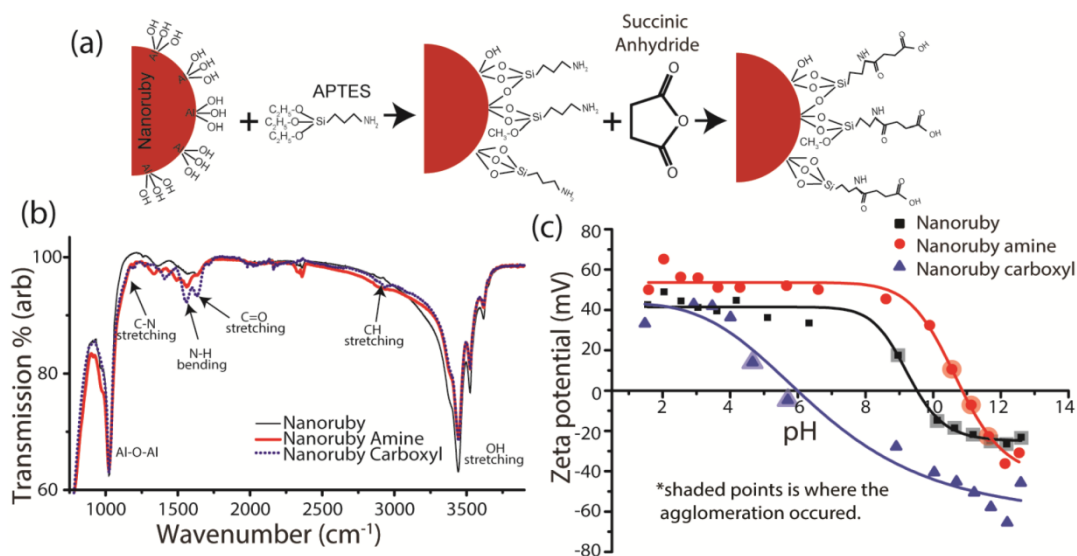


Figure 7. (a) Schematic diagram of the amine and carboxyl functionalisation of the nanoruby surface using aminopropyl triethoxysilane (APTES) and succinic anhydride (SA). (b) FTIR spectra of the bare nanorubies (black line), functionalised with amino groups (red line) and carboxyl groups (dotted blue line). (c) Zeta-potentials (left y axis) of three nanoruby samples in aqueous solutions of varying pH. Black closed squares, red closed circles, and blue triangles denote the zeta-potentials of bare, amine-functionalised, and carboxyl-functionalised nanoruby samples, respectively. The solid black, solid red, and solid blue lines represent sigmoidal fits to the respective data. Aggregation (defined as formation of particles of the mean-diameter >100 nm) was observed in the samples characterised by the zeta-potential in the range of -30 to +30 mV. These data points are demarcated by enlarged shaded shapes.

Table 1: Assignment of the infrared absorption bands of the amine-carboxyl-surface-functionalised nanoruby sample.

Characteristic band, cm^{-1}	Assignment	Refs
1026	Al–O–Al	³⁸
1084–1172	C–N stretching	³⁹
1506–1560	N–H bending	⁴⁰
1560–1695	C=O stretching	⁴⁰
2820–3019	CH stretching	⁴¹
3200–3600	OH stretching	⁴⁰

PEGylation and silica-coating. PEG (poly(ethylene) glycol) is an FDA-approved polymer, which is commonly used in in vivo applications, and widespread in colloidal chemistry due to its ability to render NP colloids stable even in saline solutions⁴². PEG has also been shown to prevent non-specific binding of NPs^{43–44}. NP surface-functionalisation with PEG, also known as PEGylation⁴⁵, was realised by using the silane chemistry approach, as schematically shown in **Figure 8a**. Silane PEG was employed to form covalent attachments with hydroxyl groups on the nanoruby surface⁴⁶.

FTIR analysis confirmed the presence of PEG groups on the surface of nanorubies. Unbound PEG was removed by thorough washing five times with MilliQ water. The PEG signature was identifiable as two peaks at 1105 cm^{-1} and 2876 cm^{-1} in the FTIR spectra (see **Figure 8b**), corresponding to the stretching of –C–O–C groups and –CH groups, respectively⁴⁷. The cross-comparison of the hydrodynamic diameters of the bare and PEGlated nanoruby samples (see

Table 2) clearly displayed the PEGylation effect. The hydrodynamic diameter of PEGylated nanorubies was not changed within the measurement error, when the sample was transferred from water to $1\times$ PBS solution, whereas the bare nanoruby diameter increased almost three times due to the aggregation. The PEGylated nanorubies gained more positive surface charge in comparison with the bare nanorubies due to an intrinsic positive charge of PEG.

Surface-coating with silica represents a radical surface-modification approach, which can further stabilise NPs in a broad range of solvents, increase the density of surface moieties, and make widespread silane chemistry applicable to silica-coated nanorubies⁴⁸⁻⁵⁰. We carried out silica surface-coating reactions. A layer of silica was observed in the TEM images of the silica-coated nanorubies, as shown in **Figure 8d**. The dispersibility of silica-coated nanorubies was improved dramatically, as compared to that of the bare nanorubies (**Figure 8c**). The silica coating resulted in the zeta-potential change from +40 mV to -22 mV in aqueous colloids (**Table 2**). At the same time, silica-coated nanorubies displayed a trend to aggregate in buffer solutions: their mean hydrodynamic diameter $\langle d \rangle = 160$ nm in water increased to $\langle d \rangle = 239$ nm in PBS. In order to mitigate this propensity for aggregation, silica-coated nanorubies were functionalised with PEG-biotin, where biotin served as the anchoring terminal for a bioconjugation reaction.

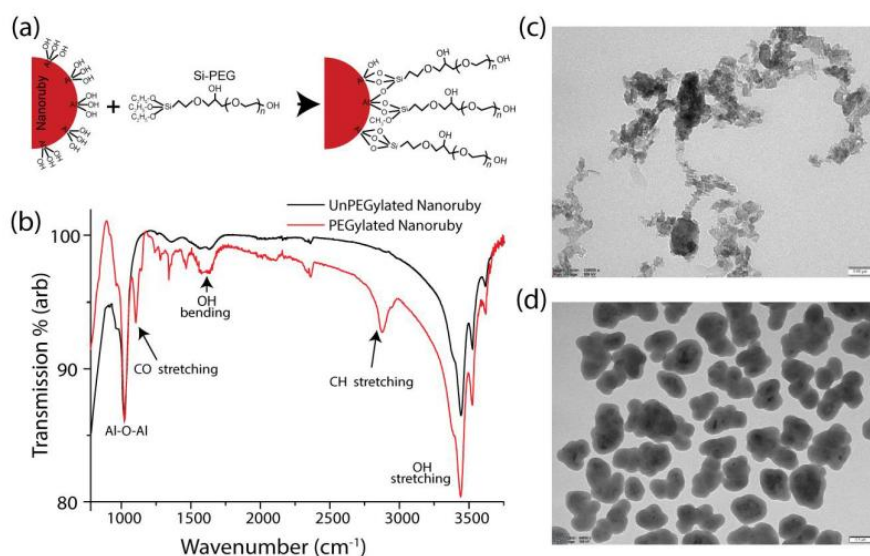


Figure 8. (a) Schematic diagram of PEG functionalisation of the nanoruby surface using silane PEG. (b) FTIR spectra of the nanoruby samples functionalised with PEG, 1 mM (black solid line) and 10 mM (red solid line). (c) and (d) TEM images of as-produced and silica-coated nanorubies, respectively. Scale bars for (c) and (d), 50 nm and 100 nm, respectively.

Table 2: The mean hydrodynamic diameters $\langle d \rangle$ and zeta-potentials ζ of PEG surface-functionalised and silica-coated nanoruby samples in water and 1× PBS. NR stands for nanoruby.

Sample	In water		In PBS 1×	
	$\langle d \rangle$ (nm)	ζ (mV)	$\langle d \rangle$ (nm)	ζ (mV)
Bare NR	100-150	30-40	300	-22
NR PEG	100-150	40-50	100-150	-10 to -4
NR PEG Biotin	100-140	30-45	100-160	-7 to -10

Silica-coated NR	160	-22	239	-24
Silica coated NR PEG Biotin	187	-12	187	-5

MOR specific-labelling. μ -opioid-receptors (MORs) are targets for the most effective pain-relieving drugs, as well as being a cellular substrate mediating the rewarding and dependence producing effects of many drugs of abuse⁵¹. Understanding the expression, function and regulation of these cellular receptors and interactions with ligands (e.g., drugs, neurotransmitters and hormones) is crucial for developing better drugs for analgesia and improvement of cancer diagnostics and therapy. In this study, nanorubies were used to specifically label MORs. To this aim, silica-coated nanorubies functionalised with PEG-biotin (NR-SiO₂-PEG-Biotin) groups were prepared (see Method for details). AtT-20 cells expressing MORs were tagged with biotinylated MOR antibody, followed by a streptavidin-FITC addition. Then the NR-SiO₂-PEG-Biotin was added to the cells to allow binding via the high-affinity streptavidin-biotin interaction. A schematic diagram of this process is illustrated in **Figure 9a**. **Figure 9b** shows an image of MORs labelled with nanorubies. The MOR labelling by the nanorubies was intense and highly reliable. The labelling was observable on the entire cell membrane, where the MOR was expressed in the basal conditions. The non-specific binding was remarkably small, as one can see in the photoluminescence image of the negative-control sample (see **Figure 9c**).

The dramatic reduction of the non-specific binding of the biotinylated nanorubies was attributed to PEG⁵². The MOR labelling with nanorubies was more profound in the case of using silica-coated colloidal nanorubies, as compared with bare nanorubies coupled with MOR antibody using silane surface-functionalisation protocol (**Figure 9e-f**). The higher density of the

functional groups (silane-PEG-biotin) on the silica-coated nanorubies was likely to account for the more efficient MOR labelling. Indeed, silica material is more reactive with silane groups than alumina material⁵³. The improved colloidal stability of the silica-coated nanoruby sample was another contributor to the cell labelling efficiency. The nanoruby colloidal sample untreated with silica displayed signs of degradation, manifested by a change in the zeta-potential in water over time. The successful MOR-labelling experiment paves way to application of the developed nanoruby-based technology to investigate the dynamics of ligand-receptor interactions at the single-molecule level, and provide a means of quantitating and localising opioid-receptors in endogenous tissues.

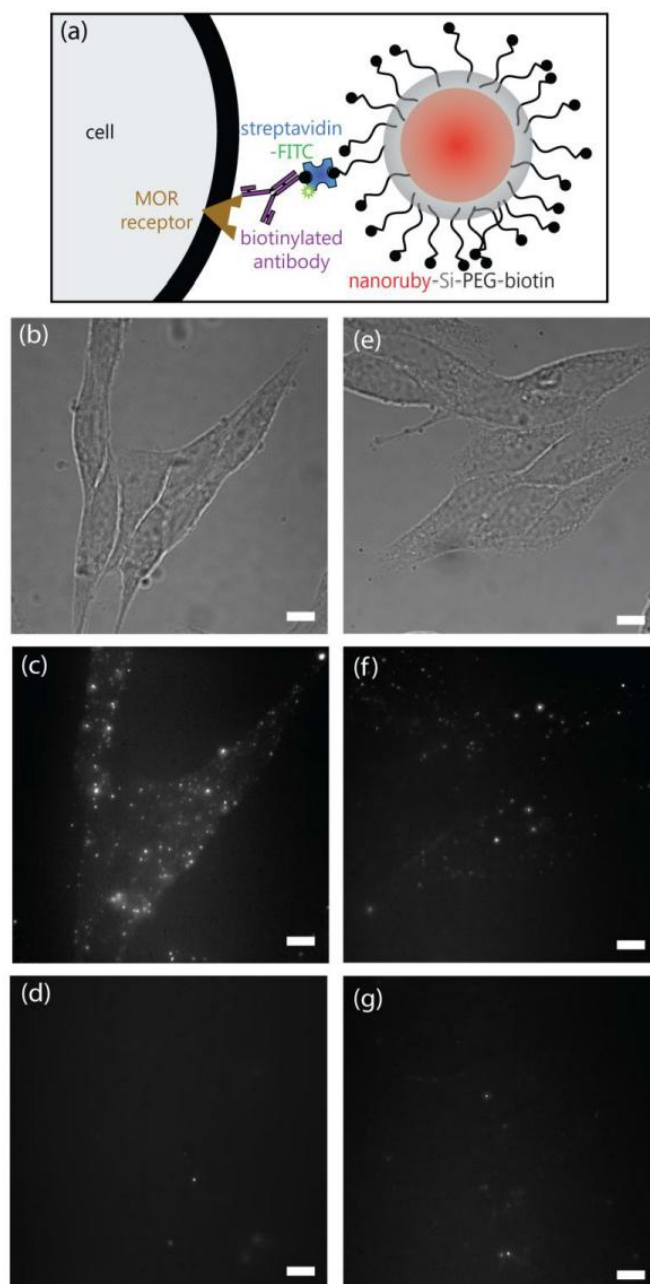


Figure 9. (a) Schematic diagram of the μ -opioid receptor labelling with nanorubies. Images of (b) bright-field, (c) time-gated photoluminescence microscopy showing specific labelling with silica-coated nanorubies. (d) The negative control is provided for comparison. (e) Bright field, (f)

time-gated photoluminescence images of uncoated-nanorubies specific labelling; (g) negative control. Scale bar, 10 μm .

CONCLUSION

We have demonstrated straightforward and high-yield production of nanorubies by using a HEBM method. As-produced nanorubies exhibited a narrow, zero-photon emission band at 692 nm, virtually unlimited photostability, ≈ 4 -ms-long photoluminescence lifetime, and negligible cytotoxicity. As-produced nanorubies were readily dispersible in water and were amenable for surface-functionalisation using facile silane wet chemistry protocols. Coating the nanoruby surface with a silica shell improved the colloidal properties and enabled the NP coupling with antibodies raised against μ -opioid receptors. As a result, efficient labelling of AtT20 cells expressing μ -opioid receptors was demonstrated using the developed biohybrid nanoruby complexes. A time-gated optical epi-luminescence microscopy system allowed ultrahigh-sensitivity observation of nanoruby-based PL probes in cells. We believe that the developed large-scale production, surface-functionalisation and bioconjugation of nanorubies in combination with the advanced time-gated optical microscopy will respond to challenges in the life sciences, such as single biomolecule imaging and tracking on the crowded optical background of cells and biological tissues.

ASSOCIATED CONTENT

Supporting Information. A home-built wide-field time-gated imaging system is depicted on **Figure S1**. **Figure S2** shows William-Hall analysis to determine the crystallite size and strain. This material is available free of charge via the Internet at <http://pubs.acs.org>.

AUTHOR INFORMATION

Corresponding Author

*Address correspondence to andrei.zvyagin@mq.edu.au.

Author Contributions

The manuscript was written through contributions of all authors. All authors have given approval to the final version of the manuscript. ‡These authors contributed equally.

Funding Sources

We acknowledge support of the Federal targeted program of the Russian Federation, Grant number RFMEFI57814X0030.

Acknowledgment

The authors thank Mr. Russell Field, Dept. of Environmental Sciences, Macquarie University for his assistance with DLS Mastersizer 2000 and hydraulic press equipment.

REFERENCES

1. Stephens, D. J.; Allan, V. J. Light microscopy techniques for live cell imaging. *Science* 2003, 300, 82-86.
2. Goldys, E.; Drozdowicz-Tomsia, K.; Zhu, G.; Yu, H.; Jinjun, S.; Motlan, M.; Godlewski, M. Fluorescence labelling. *Optica Applicata* 2006, 36, 217.
3. Santra, S.; Xu, J.; Wang, K.; Tand, W. Luminescent nanoparticle probes for bioimaging. *Journal of nanoscience and nanotechnology* 2004, 4, 590-599.
4. Sharma, P.; Brown, S.; Walter, G.; Santra, S.; Moudgil, B. Nanoparticles for bioimaging. *Advances in Colloid and Interface Science* 2006, 123–126, 471-485.
5. Ruedas-Rama, M. J.; Walters, J. D.; Orte, A.; Hall, E. A. Fluorescent nanoparticles for intracellular sensing: a review. *Analytica chimica acta* 2012, 751, 1-23.
6. Yuen Yung, H.; Chia-Liang, C.; Huan-Cheng, C. Nanodiamonds for optical bioimaging. *Journal of Physics D: Applied Physics* 2010, 43, 374021.
7. Duan, H.; Jiang, Y.; Zhang, Y.; Sun, D.; Liu, C.; Huang, J.; Lan, X.; Zhou, H.; Chen, L.; Zhong, H. High quantum-yield CdSexS1– x/ZnS core/shell quantum dots for warm white light-emitting diodes with good color rendering. *Nanotechnology* 2013, 24, 285201.

8. Mahler, B.; Spinicelli, P.; Buil, S.; Quelin, X.; Hermier, J.-P.; Dubertret, B. Towards non-blinking colloidal quantum dots. *Nature materials* 2008, 7, 659-664.
9. Alivisatos, A. P.; Gu, W.; Larabell, C. Quantum dots as cellular probes. *Annu. Rev. Biomed. Eng.* 2005, 7, 55-76.
10. Valizadeh, A.; Mikaeili, H.; Samiei, M.; Farkhani, S. M.; Zarghami, N.; Akbarzadeh, A.; Davaran, S. Quantum dots: synthesis, bioapplications, and toxicity. *Nanoscale research letters* 2012, 7, 1-14.
11. Nguyen, K. C.; Rippstein, P.; Tayabali, A. F.; Willmore, W. G. Mitochondrial toxicity of cadmium telluride quantum dot nanoparticles in mammalian hepatocytes. *Toxicological Sciences* 2015, kfv068.
12. Edmonds, A. M.; Sobhan, M. A.; Sreenivasan, V. K. A.; Grebenik, E. A.; Rabeau, J. R.; Goldys, E. M.; Zvyagin, A. V. Nano-Ruby: A Promising Fluorescent Probe for Background-Free Cellular Imaging. *Particle & Particle Systems Characterization* 2013, 1-8.
13. Bouzigues, C.; Gacoin, T.; Alexandrou, A. Biological applications of rare-earth based nanoparticles. *ACS nano* 2011, 5, 8488-8505.
14. Li, B.; Wang, H. Effect of Ball Milling on Powder Preparation by Mechanical Methods. *Applied Mechanics and Materials* 2012, 182-183, 1541-1544.
15. Matijašić, G.; Žižek, K.; Glasnović, A. Suspension rheology during wet comminution in planetary ball mill. *Chemical Engineering Research and Design* 2008, 86, 384-389.
16. Mio, H.; Kano, J.; Saito, F.; Kaneko, K. Optimum revolution and rotational directions and their speeds in planetary ball milling. *International Journal of Mineral Processing* 2004, 74, Supplement, S85-S92.
17. DeCastro, C. L.; Mitchell, B. S. Nanoparticles from mechanical attrition. *Synthesis, Functionalization, and Surface Treatment of Nanoparticles* 2002, 1-15.
18. Karagedov, G. R.; Lyakhov, N. Z. Preparation and sintering of nanosized α -Al₂O₃ powder. *Nanostructured Materials* 1999, 11, 559-572.
19. Reid, C. B.; Forrester, J. S.; Goodshaw, H. J.; Kisi, E. H.; Suaning, G. J. A study in the mechanical milling of alumina powder. *Ceramics International* 2008, 34, 1551-1556.
20. Walker, P.; Tarn, W. H. *CRC handbook of metal etchants*. CRC press: 1990.
21. Mikeska, K. R.; Bennison, S. J.; Grise, S. L. Corrosion of ceramics in aqueous hydrofluoric acid. *Journal of the American Ceramic Society* 2000, 83, 1160-1164.
22. Ćurković, L.; Jelača, M. F.; Kurajica, S. Corrosion behavior of alumina ceramics in aqueous HCl and H₂SO₄ solutions. *Corrosion Science* 2008, 50, 872-878.
23. Razali, W. A. W.; Sreenivasan, V. K. A.; Goldys, E. M.; Zvyagin, A. V. Large-Scale Production and Characterization of Biocompatible Colloidal Nanoalumina. *Langmuir* 2014, 30, 15091-15101.
24. Cheng, B.; Qu, S.; Zhou, H.; Wang, Z. Al₂O₃:Cr³⁺ Nanotubes Synthesized via Homogenization Precipitation Followed by Heat Treatment. *The Journal of Physical Chemistry B* 2006, 110, 15749-15754.
25. Jolly, B. M.; Divija, D.; Kumar, B. M.; Bhattacharya, S. S. In *Flame Spray synthesis of nanocrystalline alumina particles*, Advanced Nanomaterials and Emerging Engineering Technologies (ICANMEET), 2013 International Conference on, 24-26 July 2013; 2013; pp 557-559.
26. Stenger, F.; Mende, S.; Schwedes, J.; Peukert, W. The influence of suspension properties on the grinding behavior of alumina particles in the submicron size range in stirred media mills. *Powder Technology* 2005, 156, 103-110.

27. Ungár, T., The Meaning of Size Obtained from Broadened X-ray Diffraction Peaks. *Advanced Engineering Materials* **2003**, 5 (5), 323-329.
28. Walter Koechner, M. B., *Solid-State Lasers: A Graduate Text*. Springer: New York Berlin Heidelberg, 2002.
29. Pflitsch, C.; Siddiqui, R.; Atakan, B., Phosphorescence properties of sol–gel derived ruby measured as functions of temperature and Cr³⁺ content. *Appl. Phys. A* **2008**, 90 (3), 527-532.
30. Dobrovinskaya, E. R.; Lytvynov, L. A.; Pishchik, V., *Sapphire: material, manufacturing, applications*. Springer: 2009.
31. Zhang, W. Q.; Razali, W.; Sreenivasan, V.; Monro, T. M.; Taylor, D. In *Universal optical fibre fluorescence sensing platform for wine monitoring*, 40th Australian Conference on Optical Fibre Technology (In submission) Adelaide, Australia, Adelaide, Australia, 2015.
32. Inam, F. A.; Grogan, M. D.; Rollings, M.; Gaebel, T.; Say, J. M.; Bradac, C.; Birks, T. A.; Wadsworth, W. J.; Castelletto, S.; Rabeau, J. R., Emission and nonradiative decay of nanodiamond NV centers in a low refractive index environment. *ACS nano* **2013**, 7 (5), 3833-3843.
33. Zhao, J.; Jin, D.; Schartner, E. P.; Lu, Y.; Liu, Y.; Zvyagin, A. V.; Zhang, L.; Dawes, J. M.; Xi, P.; Piper, J. A., Single-nanocrystal sensitivity achieved by enhanced upconversion luminescence. *Nature nanotechnology* **2013**, 8 (10), 729-734.
34. Chandler, D. E.; Majumdar, Z. K.; Heiss, G. J.; Clegg, R. M., Ruby crystal for demonstrating time-and frequency-domain methods of fluorescence lifetime measurements. *Journal of fluorescence* **2006**, 16 (6), 793-807.
35. Fernández-Suárez, M.; Ting, A. Y., Fluorescent probes for super-resolution imaging in living cells. *Nature Reviews Molecular Cell Biology* **2008**, 9 (12), 929-943.
36. Kralj, S.; Drofenik, M.; Makovec, D., Controlled surface functionalization of silica-coated magnetic nanoparticles with terminal amino and carboxyl groups. *Journal of Nanoparticle Research* **2011**, 13 (7), 2829-2841.
37. Meder, F.; Daberkow, T.; Treccani, L.; Wilhelm, M.; Schowalter, M.; Rosenauer, A.; Mädler, L.; Rezwan, K., Protein adsorption on colloidal alumina particles functionalized with amino, carboxyl, sulfonate and phosphate groups. *Acta Biomaterialia* **2012**, 8 (3), 1221-1229.
38. Damayanti, N. P., Preparation of superhydrophobic PET fabric from Al₂O₃–SiO₂ hybrid: geometrical approach to create high contact angle surface from low contact angle materials. *J Sol-Gel Sci Technol* **2010**, 56 (1), 47-52.
39. Kim, J.; Seidler, P.; Wan, L. S.; Fill, C., Formation, structure, and reactivity of amino-terminated organic films on silicon substrates. *Journal of Colloid and Interface Science* **2009**, 329 (1), 114-119.
40. Stuart, B., *Infrared Spectroscopy: Fundamentals and Applications*. John Wiley & Sons, Ltd: 2004.
41. Ghezelbash, Z.; Ashouri, D.; Mousavian, S.; Ghandi, A.; Rahnama, Y., Surface modified Al₂O₃ in fluorinated polyimide/Al₂O₃ nanocomposites: Synthesis and characterization. *Bull Mater Sci* **2012**, 35 (6), 925-931.
42. Mishra, S.; Webster, P.; Davis, M. E., PEGylation significantly affects cellular uptake and intracellular trafficking of non-viral gene delivery particles. *European journal of cell biology* **2004**, 83 (3), 97-111.
43. Roy, R.; Hohng, S.; Ha, T., A practical guide to single-molecule FRET. *Nature methods* **2008**, 5 (6), 507-516.

44. Schwartz, M. P.; Cunin, F.; Cheung, R. W.; Sailor, M. J., Chemical modification of silicon surfaces for biological applications. *physica status solidi (a)* **2005**, *202* (8), 1380-1384.
45. Veronese, F. M.; Pasut, G., PEGylation, successful approach to drug delivery. *Drug discovery today* **2005**, *10* (21), 1451-1458.
46. Yang, Y.-C.; Jeong, S.-B.; Kim, B.-G.; Yoon, P.-R., Examination of dispersive properties of alumina treated with silane coupling agents, by using inverse gas chromatography. *Powder Technology* **2009**, *191* (1), 117-121.
47. Zheng, S.; Li, X.; Zhang, Y.; Xie, Q.; Wong, Y.-S.; Zheng, W.; Chen, T., PEG-nanolized ultrasmall selenium nanoparticles overcome drug resistance in hepatocellular carcinoma HepG2 cells through induction of mitochondria dysfunction. *Int. J. Nanomed* **2012**, *7*, 3939-3949.
48. Guerrero-Martínez, A.; Pérez-Juste, J.; Liz-Marzán, L. M., Recent progress on silica coating of nanoparticles and related nanomaterials. *Advanced materials* **2010**, *22* (11), 1182-1195.
49. Wang, S.-F.; Hsu, Y.-F.; Yang, T. C.; Chang, C.-M.; Chen, Y.; Huang, C.-Y.; Yen, F.-S., Silica coating on ultrafine α -alumina particles. *Materials Science and Engineering: A* **2005**, *395* (1), 148-152.
50. Graf, C.; Vossen, D. L.; Imhof, A.; van Blaaderen, A., A general method to coat colloidal particles with silica. *Langmuir* **2003**, *19* (17), 6693-6700.
51. Campa, D.; Gioia, A.; Tomei, A.; Poli, P.; Barale, R., Association of ABCB1/MDR1 and OPRM1 gene polymorphisms with morphine pain relief. *Clinical Pharmacology & Therapeutics* **2008**, *83* (4), 559-566.
52. Jokerst, J. V.; Lobovkina, T.; Zare, R. N.; Gambhir, S. S., Nanoparticle PEGylation for imaging and therapy. *Nanomedicine* **2011**, *6* (4), 715-728.
53. Szczepanski, V.; Vlassioux, I.; Smirnov, S., Stability of silane modifiers on alumina nanoporous membranes. *Journal of membrane science* **2006**, *281* (1), 587-591.

Supporting Information

Mass Production of Nanorubies Photoluminescent Probe for Bioimaging

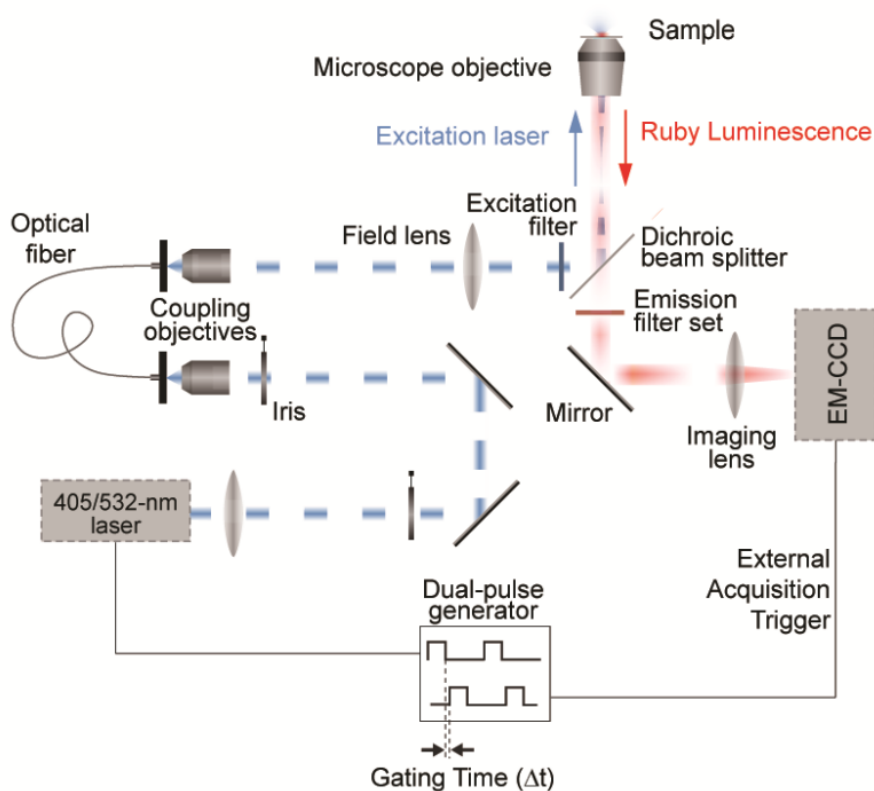


Figure S1: A schematic diagram of the optical microscopy system configured for the high-sensitivity imaging of nanoruby samples. A 405-nm or 532-nm laser beam is coupled to the microscope to provide a uniform illumination at the specimen plane. The PL emission from the sample is collected through optical filters by using an EMCCD. The laser output and camera exposure are synchronised by using a dual-pulse generator for time-gated imaging.

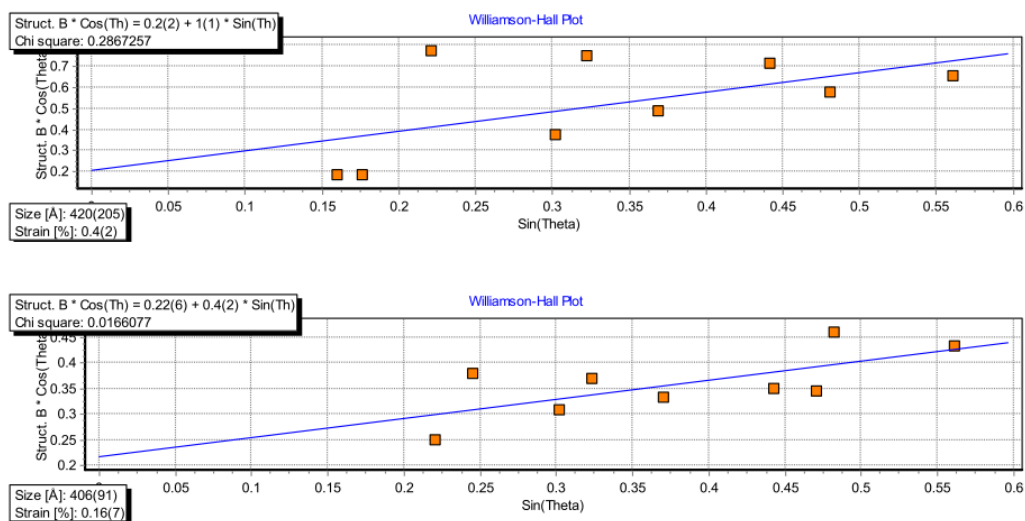


Figure S2: Williamson Plot of unpurified sample (above panel) and purified sample (below panel).

5.5 References

- [1] T. H. Maiman, "Stimulated Optical Radiation in Ruby," *Nature*, vol. 187, pp. 493-494, 1960.
- [2] C. Pflitsch, R. Siddiqui, and B. Atakan, "Phosphorescence properties of sol-gel derived ruby measured as functions of temperature and Cr^{3+} content," *Applied Physics A*, vol. 90, pp. 527-532, 2008.
- [3] H. Aizawa, N. Ohishi, S. Ogawa, T. Katsumata, S. Komuro, T. Morikawa, *et al.*, "Fabrication of ruby sensor probe for the fiber-optic thermometer using fluorescence decay," *Review of scientific instruments*, vol. 73, pp. 3656-3658, 2002.
- [4] K. Grattan, Z. Zhang, T. Sun, Y. Shen, L. Tong, and Z. Ding, "Sapphire-ruby single-crystal fibre for application in high temperature optical fibre thermometers: studies at temperatures up to 1500° C," *Measurement Science and Technology*, vol. 12, p. 981, 2001.
- [5] M. S. Bigelow, N. N. Lepeshkin, and R. W. Boyd, "Observation of ultraslow light propagation in a ruby crystal at room temperature," *Physical Review Letters*, vol. 90, p. 113903, 2003.
- [6] D. E. Chandler, Z. K. Majumdar, G. J. Heiss, and R. M. Clegg, "Ruby crystal for demonstrating time-and frequency-domain methods of fluorescence lifetime measurements," *Journal of fluorescence*, vol. 16, pp. 793-807, 2006.
- [7] T. Kobayashi, "Direct observation of large shock impedance jump upon shock-induced densification of powdered materials confirmed by in situ shock pressure and particle velocity measurements," *Chemical Physics Letters*, vol. 608, pp. 157-160, 2014.
- [8] E. Wisniewski-Barker, G. M. Gibson, S. Franke-Arnold, R. W. Boyd, and M. J. Padgett, "Mechanical Faraday effect for orbital angular momentum-carrying beams," *Optics express*, vol. 22, pp. 11690-11697, 2014.
- [9] E. Lanczi, "Amplification in a thick ruby lens," *Applied Optics*, vol. 5, pp. 255-257, 1965.
- [10] C. Pan, S.-Y. Chen, and P. Shen, "Photoluminescence and transformation of dense $\text{Al}_2\text{O}_3\text{:Cr}^{3+}$ condensates synthesized by laser-ablation route," *Journal of Crystal Growth*, vol. 310, pp. 699-705, 2008.

Wide-Field Time-Gated Photoluminescence Microscopy for Fast Ultrahigh-Sensitivity Imaging of Photoluminescent Probes

This chapter is adapted from Razali, *et al.*, “Wide-field time-gated photoluminescence microscopy for fast ultrahigh-sensitivity imaging of photoluminescence probes”, which was published in Journal of Biophotonics [1]. This chapter is structured as follows: The first section provides a short introduction to the paper, with the statement of the Ph.D. candidate’s contributions. The second section presents the full paper. The last section describes material related to this paper, including a description of its use in time-gated photoluminescence microscopy to provide single-molecule detection in biological application, and as well an introduction to avidin-biotin interaction, which was also used for the bioassay preparation described in this paper.

6.1 Introduction to the paper

This paper reports advancement in the time-gated photoluminescence (TGP) detection of long-photoluminescence lifetime nanomaterials (in this case nanorubies). We demonstrated a wide-field TGP imaging system, which enabled rapid, routine and ultrahigh-sensitivity imaging at the level of individual nanorubies. Correlative AFM and TGP imaging was carried out to demonstrate that our system had achieved sensitivity at

the single nanoparticle level. To assess the capability of the system, the nanorubies were submerged in a highly fluorescent yellow organic dye and then analysed. We also perform the imaging of cells containing nanorubies. In both cases, individual nanorubies can be visualised after elimination of the background signal. Furthermore, we demonstrated that live imaging of single-molecule binding kinetics is possible using a nanoruby-based bioassay. With these capabilities, we are able to record binding kinetics of nanorubies in biological solution. The new system described here offers new opportunities for the visualisation of single molecule intracellular molecular trafficking and the detection of rare biomolecular events in an optically crowded background containing cells and tissues.

6.2 Authors' contribution

The Ph.D. candidate (Mr. Wan Aizuddin W. Razali) is the first author of this paper. He contributed to the production and characterisation of nanorubies, which were then used to bind to targets in biological samples. He performed the sample preparation, which included spun coated nanorubies onto a coverslip and immersing nanorubies in yellow dye. He also completed the imaging work (epi-luminescent and TGP modes) and prepared the assay for live imaging of nanorubies' kinetic binding in blood serum. He did the majority of the data analysis, figure preparation, and manuscript writing.

Dr. Sreenivasan provided the important contribution to this paper of the development of time-gated imaging system, and carried out the correlative imaging between AFM and TGP imaging. He also prepared cell culture and performed live cell imaging. He was involved in data analysis, including Matlab programming. Dr. Bradac carried out the AFM imaging of nanoruby sample using his system. Prof Connor provided the biological model, gave advice and provided the facility for cell experiments. Dr. Sreenivasan, Prof. Goldys, and A/Prof. Zvyagin (corresponding author) coordinated this work, including experiments planning and results discussion. All authors contributed towards the preparation of the manuscript.

6.3 Full paper

**Wiley
Online
Library**

Early View publication on www.wileyonlinelibrary.com
(issue and page numbers not yet assigned;
citable using Digital Object Identifier – DOI)

J. Biophotonics 1–11 (2016) / DOI 10.1002/jbio.201600050

Journal of
BIOPHOTONICS

FULL ARTICLE

Wide-field time-gated photoluminescence microscopy for fast ultrahigh-sensitivity imaging of photoluminescent probes

Wan A. W. Razali^{1,2,3}, Varun K. A. Sreenivasan^{1,3}, Carlo Bradac⁴, Mark Connor⁵, Ewa M. Goldys^{1,3}, and Andrei V. Zvyagin^{*,1,3,6}

¹ MQ Photonics Research Centre, Faculty of Science, Macquarie University, Sydney, NSW 2109, Australia

² Department of Physics, Faculty of Applied Sciences, Universiti Teknologi MARA Pahang, 26400 Jengka, Pahang, Malaysia

³ ARC Centre of Excellence for Nanoscale BioPhotonics (CNBP), Macquarie University, Sydney, NSW 2109, Australia

⁴ ARC Centre of Excellence for Engineered Quantum Systems (EQuS), Department of Physics and Astronomy, Macquarie University, Sydney, NSW 2109, Australia

⁵ Department of Biomedical Sciences, Faculty of Medicine and Health Sciences, Macquarie University, Sydney, NSW 2109, Australia

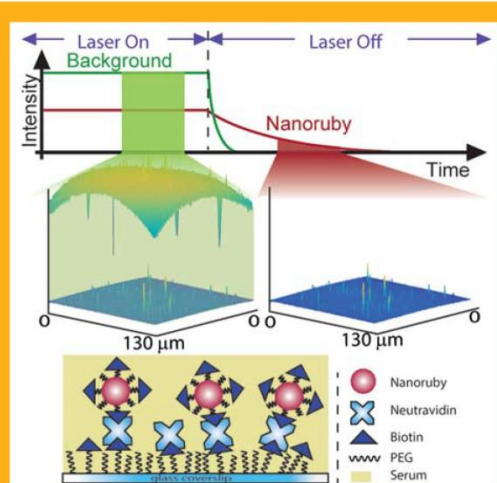
⁶ Laboratory of Optical Theranostics, N.I. Lobachevsky Nizhny Novgorod State University, 603950 Nizhny Novgorod, Russia

Received 22 February 2016, revised 12 May 2016, accepted 13 May 2016

Published online 7 June 2016

Key words: Imaging, nanoruby, time-gated detection, photoluminescence, sensitivity, autofluorescence, background suppression

Fluorescence microscopy is a fundamental technique for the life sciences, where biocompatible and photostable photoluminescence probes in combination with fast and sensitive imaging systems are continually transforming this field. A wide-field time-gated photoluminescence microscopy system customised for ultrasensitive imaging of unique nanoruby probes with long photoluminescence lifetime is described. The detection sensitivity derived from the long photoluminescence lifetime of the nanoruby makes it possible to discriminate signals from unwanted autofluorescence background and laser backscatter by employing a time-gated image acquisition mode. This mode enabled several-fold improvement of the photoluminescence imaging contrast of discrete nanorubies dispersed on a coverslip. It enabled recovery of the photoluminescence signal emanating from discrete nanorubies when covered by a layer of an organic fluorescent dye, which were otherwise invisible without the use of spectral filtering approaches. Time-gated imaging also facilitated high sensitivity detection of nanorubies in a biological environment of cultured cells. Finally, we monitor the binding kinetics of nanorubies to a functionalised substrate, which exemplified a real-time assay in biological fluids.



3D-pseudo colour images of nanorubies immersed in a highly fluorescent dye solution. Nanoruby photoluminescence is subdued by that of the dye in continuous excitation/imaging (left), however it can be recovered by time-gated imaging (right). At the bottom is schematic diagram of nanoruby assay in a biological fluid.

* Corresponding author: e-mail: andrei.zvyagin@mq.edu.au, Phone: +61-2-9850-7760, Fax: +61-2-9850-8115

1. Introduction

Labelling of biological molecules with fluorescence probes (more generally, photoluminescence probes) enables molecularly-specific, morphological and functional imaging. This has become an indispensable tool in modern biomedical research and practices [1–3]. Advances in optical imaging techniques and photoluminescence (PL) probes have enabled the development of fluorescence microscopy towards more rapid, sensitive and selective imaging.

Traditional PL probes based on organic dyes suffer from several drawbacks, such as photobleaching, broad emission spectrum, non-specific chemical reactivity and poor chemical stability [4–6], which limit the scope of their application towards ultrahigh-sensitivity and single-molecule imaging [7]. There is continuing interest in developing alternative PL probes. Fluorescent carbon dots [8], metal nanoclusters [9, 10] plasmonic nanoparticles, upconversion nanoparticles [11] and nanorubies [12] are some of the newly developed PL probes. They exhibit exceptional optical and physicochemical properties, such as virtually unlimited photostability, chemical stability and colloidal stability. Such PL probes have revolutionised fluorescence imaging by introducing modalities such as super-resolution microscopy using fluorescent nanodiamonds [13], in vivo optical imaging using upconversion nanoparticles [14], and time-gated microscopy using photoluminescent nanomaterials [12].

The time-gated detection makes use of photoluminescent millisecond-scale emission, and is realised by turning on a photoreceiver, following a short time delay after the excitation source is ended. The ability to discriminate probes with long PL lifetime from obscuring, but more rapidly decaying optical background gives time-gated microscopy a competitive edge over other methods. It is particularly advantageous when the optical background is such that spectral and other filtering methods are insufficient, as is the case for biological autofluorescence. The time-gated photoluminescence (TGP) detection concept is presented in Figure 1. The signal from a PL probe is acquired only after the intrinsic fluorescence of biological matter (autofluorescence) has decayed. The effectiveness of this technique generally improves when the PL lifetimes of the probe, τ_{PL} , greatly exceeds that of the autofluorescence, τ_{AF} . A gate time, Δt between the excitation pulse trailing edge and the onset of the emission signal acquisition is therefore set to satisfy the condition: $\tau_{AF} \ll \Delta t \ll \tau_{PL}$. Typical values of the emission lifetime range from tens of picoseconds [15] to several nanoseconds [16, 17] for τ_{AF} ; and from hundreds of microseconds [18] to milliseconds [12] for τ_{PL} . The TGP method (also termed “time-gated luminescence (TGL)” else-

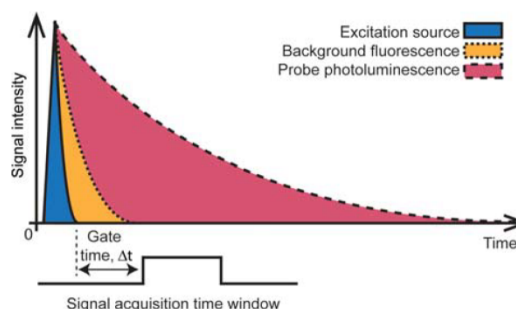


Figure 1 Conceptual illustration of normalised temporal profiles of three main optical signals (excitation, autofluorescence, probe photoluminescence) relevant to the time-gated photoluminescence imaging.

where) was applied extensively for high-sensitivity PL probe imaging [19] of cancer cells [20–22] and pathogens [23, 24]. In this paper, we used “photoluminescence” term because it is more accurately describes the phenomenon. The term “luminescence” is prone to misinterpretation with bioluminescence or chemiluminescence which is used in the field of biology [25].

In our earlier work [12], we used a home-built confocal fluorescence system to attain high sensitivity imaging of nanorubies. However, this system was inherently limited in the imaging acquisition rate. The long photoluminescence lifetime of nanoruby (τ_{NR}), demanded dwelling over each pixel for times longer than τ_{NR} . Therefore, it required approximately 30 min to acquire one image sized 1024×1024 pixels. Other reported TGP techniques can either be classified as sensitive or rapid, but not both. For example, Connally et al. demonstrated the suppression of the autofluorescent background to emphasise europium-chelate labelled prokaryotic parasites using time-resolved wide-field photoluminescence microscopy [26]. Even though their acquisition rate was very fast (25 frames per second), their sensitivity fell short from that required for studying single molecular events. Other TGP schemes featuring modest imaging sensitivities includes work by Bouccara et al., where the acquisition time of 0.15 s per image was demonstrated [27]. The fastest TGP scheme featuring single-particle sensitivity was reported by Zhang et al., and demonstrated the acquisition time of 30 s per frame [23]. Another way of increasing sensitivity without compromising on acquisition speed is by employing probes of high brightness. For example, tracking of single neurotransmitter receptors has been carried out with quantum dots as the labelling agent [28]. However, these advantages present drawbacks of cytotoxicity and blinking as well as poor contrast in a biological

environment with high levels of autofluorescence background.

Here, we report a time-gated photoluminescence system, which enables fast imaging (>0.3 Hz) of individual photoluminescent nanoparticles, suitable to visualise molecular trafficking in cells and biological fluids. We demonstrate the system performance by imaging nanoruby ($\alpha\text{-Al}_2\text{O}_3$ nanocrystals doped with Cr^{3+}). Cr^{3+} ions give rise to the nanoruby photoluminescence, which is characterised by long emission lifetime (3.7 ms). Complete recovery of discrete nanorubies from the background fluorescence of a substrate, a highly fluorescent dye and an autofluorescent biological environment is demonstrated, without any compromise on the imaging rate/sensitivity. Finally, we exemplify a single molecule kinetic binding assay by a avidin-biotin system, where the kinetics of nanoruby binding is monitored in a biological fluid.

2. Experimental

2.1 Nanoruby production

Synthetic ruby crystals with dimension approximately $7\text{ cm} \times 2\text{ cm} \times 1\text{ cm}$ (Henan Union Abrasive Corp, China) were crushed using a hydraulic press (Enerpac, US) and sieved through a $63\text{ }\mu\text{m}$ metal sieve. Dynamic light scattering (DLS, Mastersizer 2000, Malvern Instruments) measurements showed that the size of the produced microrubies varied from $1\text{--}100\text{ }\mu\text{m}$. This microruby powder was ball-milled to produce nanorubies by using an established protocol for producing nanoalumina [29].

2.2 Characterisation of nanoruby size and photoluminescence

15 mg of nanoruby powder was suspended in 1 mL Milli Q water and sonicated for 30 min followed by centrifugation for 5 min at $5000 \times g$. The supernatant devoid of large particles was collected and diluted 10 times in 1% (w/w) polyvinyl alcohol (PVA) for spin-coating. $20\text{ }\mu\text{L}$ of nanoruby in PVA was dropped on a copper grid adhered to a glass coverslip (borosilicate glass, BK7, Menzel Glaser) and spun for 100 s at 1500 rpm using a spin-coater (EC101D, Headway Research Inc.). The sample was imaged using a transmission electron microscope (TEM, Philips CM10) operating at an accelerating voltage of 100 keV .

Dilute nanoruby sample devoid of large particles was prepared in Milli Q water for colloidal size and

fluorescence characterisation. The mean hydrodynamic diameter and colloidal dispersion were determined using DLS (Zetasizer NS, Malvern Instruments). The excitation and emission spectra of sample placed in a quartz cuvette (Starna Pty. Ltd., 10 mm path length) were measured using a spectrofluorometer (Fluorolog Tau3, JY Horiba).

2.3 The time-gated photoluminescence (TGP) microscopy system

The system was developed based on an inverted microscope (Olympus IX71) platform, as shown schematically in Figure 2a. Either an external 405 nm laser (TG_405_1.1, Quantitative Ltd.) or 532 nm laser (FB-532-1000-FS-FS-1-1-ST, RGB Lase) source was coupled to an illumination port of the microscope using Köhler-type optical configuration to produce near-uniform illumination at the sample plane, as described elsewhere [30]. An oil-immersion objective lens ($100\times$, NA 1.3, Olympus) was used for acquiring high-resolution images in bright-field, epi-luminescence and time-gated modes. The microscope was equipped with three interchangeable filter-sets (Semrock), specified in Table 1. The filter sets contained a laser-line filter, dichroic beam-splitter and long-pass (and band-pass) filters. Spectral character-

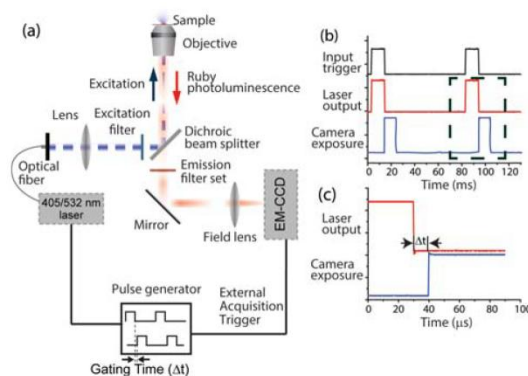


Figure 2 (a) A schematic diagram of the optical microscopy system configured for high-sensitivity imaging of nanoruby samples. A $405\text{ nm}/532\text{ nm}$ laser beam was coupled to the microscope to provide uniform illumination at the sample plane. The photoluminescence emission from the sample was collected through optical filters by using an EMCCD. The laser output and camera exposure were synchronised for TGP imaging. (b) Timing profiles of the input trigger signal, laser output and camera exposure during TGP imaging. (c) Magnified temporal sequence of the laser pulse and camera exposure (Δt stands for the gate time), for the region marked in (b) by a dashed rectangle.

Table 1 Optical filters used in this study.

Filter set #	Excitation filter	Dichroic mirror	Emission filter
1	650 nm SP*; FF01-650/SP-25	660 nm LP**; FF01-660/13-25	(a) 664 nm LP BLP01-664R-25 (b) 689 nm BP***; FF01-689/23-25
2	650 nm SP FF01-650/SP-25	660 nm LP FF01-660/13-25	(a) 664 nm LP BLP01-664R-25
3	–	511 nm LP FF511-Di01-25 × 36	450 nm LP

* SP = Short pass filter, ** LP = Long pass filter,

*** BP = Band pass filter.

istics of filter set #1 are presented in Figure S1 (Supporting Information, SI). An electron-multiplied CCD camera (EMCCD, iXon 885 DU, Andor Technology Ltd.) was attached to a detection port of the microscope. TGP imaging was realised by synchronous operation of the electrically-modulated lasers and the EMCCD, as shown in Figure 2.

In the case of 405 nm laser, its inbuilt circuitry was used to modulate its output and for synchronization. The pulse width was set at 11 ms, three times longer than the PL lifetime of nanoruby ($\tau_{\text{NR}} = 3.7$ ms), to allow steady-state excitation condition of Cr^{3+} . A short laser trailing edge time constant is crucial for TGP imaging. We ensured that this was much less than the gate time ($\Delta t \sim 10$ μs) to satisfy the condition $\tau_{\text{AF}} \ll \Delta t \ll \tau_{\text{PL}}$. A TTL output from the laser modulation circuit was used to trigger (input trigger in Figure 2b) a digital delay/dual pulse generator (DG535, Stanford Research System Inc, US). The DG535 generated a subsequent TTL pulse after a period of $\Delta t \approx 10$ μs following the trailing edge of the laser pulse, which was used to trigger the EMCCD image acquisition (Figure 2c). The laser pulses were separated by ≈ 70 ms to accommodate for the time required for image acquisition and pixel readout.

When 532 nm laser was used, a field programmable gate array (FPGA, NI PCIe-7841R Virtex-5, National Instruments) was used to synchronise the laser pulse and image acquisition. The FPGA was programmed to generate two TTL pulse trains, one to modulate the laser and another to trigger the EMCCD with flexible pulse durations, pulse separation and gating times (Δt).

The DG535 (via GPIB interface) and FPGA (via PCIe interface) were controlled via virtual instruments created using LabVIEW. The EMCCD camera was controlled by the Andor SOLIS software, version 4.22.

2.4 Characterisation of photoluminescence lifetime

65 μg of nanoruby was drop cast on a coverslip towards photoluminescence lifetime analysis with TGP using the 532 nm laser source (19 mW continuous optical power at sample plane, 10 ms pulse duration) and filter set #2. The gate time, Δt , was varied from 0.5 ms to 10 ms in 0.5 ms increments to cover the time scale of nanoruby photoluminescence. The exposure time was decremented by 0.5 ms between measurements to maintain the sum of exposure and gate times a constant, at 10 ms. An average pixel value was obtained for every measurement. The PL emission within every 0.5 ms time-window was defined as the difference between the pixel values of the subsequent measurements. τ_{NR} was estimated by fitting the time-dependent intensity to a single exponential function, $I(t) = I_0 \exp(-\Delta t/\tau_{\text{NR}})$ using Origin (OriginLab Corporation). Here, I_0 is the signal intensity at $\Delta t = 0$, which was used as a fitting parameter. Image analysis was performed using ImageJ (NIMH).

2.5 Correlative imaging

In order to correlate topography maps and photoluminescence images of discrete nanorubies, nanoruby aqueous colloid was drop-cast on a custom-made gridded coverslip and dried. Each $50 \mu\text{m} \times 50 \mu\text{m}$ grid was tagged for easy identification, as described elsewhere [31]. The topography maps and TGP images were acquired by using an atomic force microscopy system (AFM, NT-MDT) and our home-built TGP system respectively. The peak height of the nanoparticles were directly obtained from the AFM data. The TGP image presented here was acquired with filter set #1 and 405 nm laser excitation with 11 ms pulses and imaged with 10 μs gating time, 100 accumulations and an EM gain of 100.

2.6 Characterisation of TGP imaging sensitivity and contrast of discrete nanorubies

20 μL of nanoruby sample prepared in PVA (Section 2.2) was dropped on a square glass coverslip and spun for 100 s at 1500 rpm using a spin-coater. This coverslip was mounted on a glass slide and sealed with nail polish for PL (continuous excitation/detection and TGP) imaging. 405 nm laser was used at a power of 28 mW continuous power at the objective, with 11 ms pulse duration and 14% duty cycle. The electron-multiplication gain on the camera was

set to 100, and 40 frames, acquired at Δt varied from 0.3 μs to 1000 μs , were accumulated to obtain one image. The total time taken to generate an image was 3.2 s [$40 \times (11 \text{ ms laser pulse} + 10 \text{ ms camera acquisition} + 60 \text{ ms camera readout})$]. The autophotoluminescence background from empty glass- and quartz- slides and coverslips were also measured and analysed for evaluating background.

The imaging sensitivity of the microscope to detect individual nanorubies was determined by measuring the signal and background amplitudes expressed in terms of number of photons per second per pixel. In our experiments, the sensitivity was calculated using Weber contrast (C), which is defined as [32, 33]:

$$C = \frac{L_{\max} - L_{\min}}{L_{\min}} \quad (1)$$

where L_{\max} and L_{\min} are PL maximum and minimum, respectively. In our case the L_{\max} was equal to the sum of the signal and background, while L_{\min} was the background. Therefore Eq. (1) was re-written for convenience in our case as:

$$C_{\text{NR}} = \frac{(S + B) - B}{B} \quad (2)$$

where, S is signal and B is background. S and B were calculated by averaging the brightest 10% and dimmest 10% of all pixels associated with each detected nanoruby spot, after correcting for camera offset using images acquired in the dark. In the case of complete suppression of the background, Eq. (2) reduces to $C_{\text{NR}} = S/N$, where N represents the EMCCD noise. Automated particle identification, intensity level measurements and contrast evaluation were carried out using image processing toolbox version 8.2 in Matlab R2013a or higher versions.

2.7 Nanoruby submerged in fluorescent dye

Nanoruby, devoid of large particles, were prepared as described earlier and mounted face-down on an $\approx 1 \text{ mm}$ deep well on a glass slide made using nail polish. This well was pre-filled with 50 μL of a proprietary yellow fluorescent organic dye (L34959, Invitrogen), diluted 100 times using Milli Q water. Images of nanorubies excited by 405 nm laser were acquired in epi-luminescence and TGP modes with filter set #1. The laser power at the objective was set to 28 mW (continuous), with a pulse duration of 11 ms (14% duty cycle). The electron-multiplication gain on the camera was set to 50, accumulation to 40, and recursive average set to 5, and acquired at $\Delta t = 10 \mu\text{s}$.

2.8 Cell labelling and time-gated imaging

Mouse pituitary tumour cells (AtT-20) were cultured in DMEM (containing phenol red) supplemented with 10% FBS, 100 $\mu\text{g} \cdot \text{mL}^{-1}$ penicillin and 100 $\mu\text{g} \cdot \text{mL}^{-1}$ streptomycin. Cells were plated on coverslip-bottom 35 mm petri dishes (Cell E&G LLC), and grown for 1 day. On the day of the experiment, cells were serum starved in Lebovitz-15 (L-15) media (containing phenol red). Nanoruby colloid, devoid of large particles, was added to the cells at a final concentration of 25 $\mu\text{g} \cdot \text{mL}^{-1}$ in L-15, followed by incubation for 2 h. The cells were washed 3 \times with L-15 in preparation for TGP microscopy. Control cell samples not incubated with nanorubies were also prepared.

Images of the cells were acquired in brightfield to visualize the morphology and in PL mode to visualise bound nanorubies. 532 nm laser was used at a power of 132 mW (continuous wave) with a pulse width of 4 ms for epi-luminescence or 10 ms for TGP images. For TGP, Δt was fixed at 10 μs and a filter set #1 was used. The camera exposure time was set to 4 ms for epi-luminescence or 10 ms for TGP modes, with EM gain fixed at 100. Up to 25 images were collected for each cell at varying z -planes. These images were projected to form a single image by maximum pixel value in order to capture the best focal plane for individual nanorubies.

2.9 Nanoruby bioassay

Glass coverslips on glass-bottom-petri dishes (Cell E&G LLC) were biotinylated using a mixture of silane-PEG (20 mM, MW = 2 kDa, Laysan Bio Inc.) and silane-PEG-biotin (2 mM, MW = 3.4 kDa, Laysan Bio Inc.) prepared in Milli Q water. The coverslips were incubated for 2 hours at 40 $^{\circ}\text{C}$ to facilitate reliable biotinylation. Avidin (NeutrAvidin, Thermo Fisher Scientific) was added on the biotinylated coverslip. 1% (w/v) solution of BSA in PBS was used to block non-specific binding of nanorubies to the substrate/avidin. Biotinylated nanorubies were prepared at a concentration of 0.2 $\mu\text{g}/\text{mL}$ in fetal bovine serum (Gibco, Thermo Fisher Scientific) and added to initiate binding. Live imaging was carried out by obtaining an image in every 10 s. The excitation laser power was optimised to minimise photodamage of streptavidin while limiting the compromise on the acquisition frame rate. For control experiments, the binding sites were blocked by adding 1 mM biotin (Sigma Aldrich) to the avidin-immobilised coverslip prior to adding biotinylated nanorubies.

3. Results and discussion

3.1 Nanoruby characterisation

The morphology of nanoruby sample was characterised by TEM. Analysis of TEM images showed a mean particle diameter of 70 ± 40 nm (Figure 3a). This value was obtained based on individual particle area measured by the image analysis, followed by spherical approximation. The mean hydrodynamic diameter of nanorubies in an aqueous colloid was measured by DLS as 80 ± 20 nm, as shown in Figure 3b. These values were obtained based on non-linear curve fitting of the size histograms to the inbuilt 'Extreme' peak function of Microcal Origin. The slight overestimation of hydrodynamic size measured by DLS with respect to physical size measured by TEM has been observed previously in other types of nanoparticles [34]. Aggregation of nanoparticles can also contribute to the increased hydrodynamic size, but we mitigated this effect by sonicating the samples before every measurement.

The PL excitation and emission spectra of the colloidal nanoruby are shown in Figure 3c. Two broad excitation peaks centred at 402 nm and 557 nm were observed and found identical to the peaks observed in bulk ruby [35]. A very narrow emission doublet, featuring two peaks at 690.6 nm and 692.1 nm, referred to as the R_1 and R_2 lines, ori-

ginate from the transitions $\bar{E} \rightarrow {}^4A_2$ and ${}^2\bar{A} \rightarrow {}^4A_2$ of the Cr^{3+} colour-centres in ruby [36].

Using the time-gated photoluminescence microscopy (TGP), the PL lifetime of nanoruby, τ_{NR} , was estimated to be 3.7 ± 0.4 ms, as shown in Figure 3d. This value is comparable to the PL lifetime of bulk ruby reported elsewhere [37]. As mentioned earlier, such long lifetime makes nanorubies suitable for the time-gated imaging. Unlike the other promising PL nanomaterials, such as fluorescent nanodiamonds [38] and upconversion nanoparticles [39], nanoruby photoluminescence has been verified to be unaffected by environmental conditions, with no observed quenching effects [40].

3.2 Single particle sensitivity by correlative imaging

A sample of discrete nanorubies sparsely dispersed on a gridded glass coverslip was imaged with our TGP microscope. As shown in Figure 4 (bottom panel), TGP imaging revealed a number of discrete spots. The full wave half maximum (FWHM) of these spots, dictated by the point-spread function (PSF) of the microscope optics, was measured as 400 ± 20 nm (Figure 4 inset). In the diffraction-limited case, the FWHM of the Airy disk intensity profile would measure approximately 320 nm, whereas our system exhibited a larger PSF. We interpret this width broadening to the objective lens aberrations (probably, uncorrected for the cover slip thickness). It is possible that the non-zero size of the nanorubies

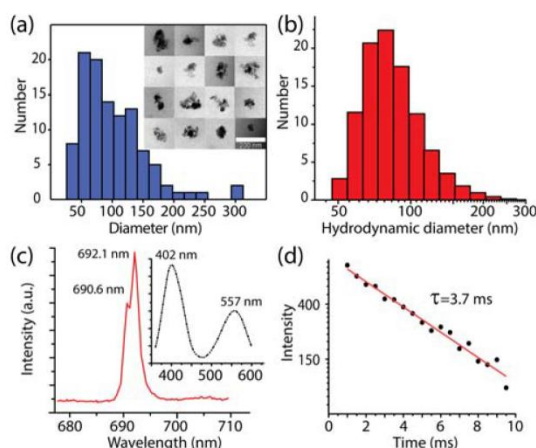


Figure 3 Histograms of nanoruby diameters measured by (a) TEM and (b) DLS. Inset in (a) presents images of 16 representative nanoruby particles. Scale bar, 200 nm. (c) Emission and excitation (inset) spectra of the as-produced nanoruby sample. (d) A semi-log plot of the photoluminescence intensity of nanoruby as a function of the time after the laser pulse. The solid line shows a single-exponential fit with $\tau_{\text{NR}} = 3.7$ ms.

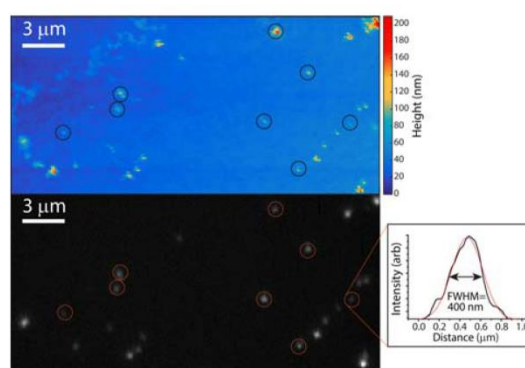


Figure 4 AFM (top) and TGP (bottom) images of discrete nanorubies deposited on a glass coverslip. The correlation between the AFM and TGP images is apparent, where circles indicate the corresponding particles matched between two images. (Inset) Intensity profile of one spot corresponding to a single 30 nm nanoruby (black), overlapped with a gaussian fit (red). The fit yielded an FWHM of 400 ± 20 nm.

might also explain the increased “apparent” point spread function of our imaging system. The asymmetric profile of the recorded lateral PSF pointed to coma aberrations, which was more profound for off-centre objects. In order to confirm that these spots corresponded to discrete nanorubies, we analysed the same sample area by AFM to measure their heights at the nanometer scale (Figure 4, top panel). The TGP and AFM images of the discrete spots closely matched one another, both with respect to the positions and signal intensities of the circled particles. Nanorubies with height as small as 30 nm measured by AFM were clearly observable in the TGP image, confirming that the EMCCD-detected optical signal levels corresponded to individual nanorubies. For example, a signal level of 280 photons per second per pixel corresponded to a single nanoruby particle of diameter 30 nm (circled), as measured by the AFM.

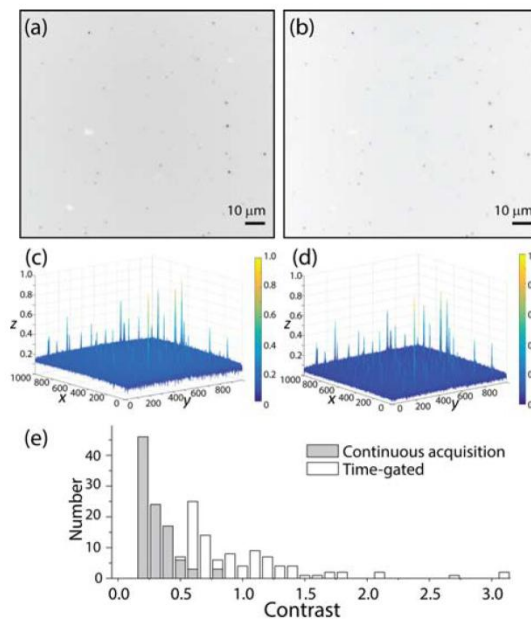


Figure 5 Optical images of nanorubies spin-coated on a glass coverslip acquired in (a) epi-luminescence and (b) TGP modes ($\Delta t = 1000 \mu\text{s}$) respectively using the filter set #1. Nanorubies appear as dark spots since the image is presented in an inverted brightness scale. (c) and (d) are the corresponding 3D-pseudo-colour plots after normalisation. The contrast enhancement in the TGP mode is especially evident in the 3D surface plots. (e) Histogram of the contrast values of discrete nanorubies imaged in epi-luminescence and TGP ($\Delta t = 1 \text{ ms}$) modes. Details of image processing and calculation of contrast are described in Experimental section.

3.3 Photoluminescence contrast of nanorubies and the background of glass substrate

Representative PL images of nanorubies spin-coated on a glass coverslip (Section 2.2), captured in epi-luminescence (continuous excitation/detection) and TGP modes ($\Delta t = 1000 \mu\text{s}$) are presented in Figures 5a, b. The contrast of discrete nanorubies (C_{NR}) in the epi-luminescence imaging mode was inferior ($\approx 25\%$) to that of the TGP mode (Figure 5e). Analysis of images acquired at smaller Δt values established that the photoluminescence of the BK7 glass substrate was a substantial contributor to the background observed in non-time gated images (B_s , where the subscript ‘s’ denotes substrate). Since imaging of biological specimens frequently occurs on a glass

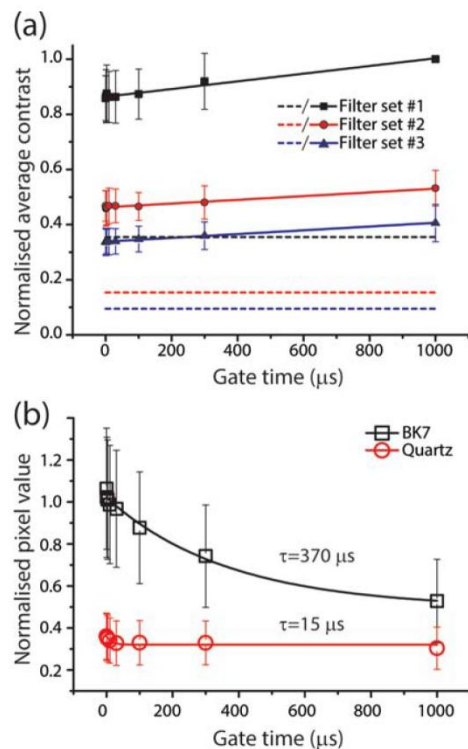


Figure 6 (a) A plot of the average contrast (C_{NR}) of discrete nanorubies placed on a BK7 glass coverslip, acquired in epi-luminescence (dashed lines) and TGP (data points fitted with solid lines) imaging modes, versus the gate time (not relevant for epi-luminescence imaging). Data sets represented by black squares, red circles and purple triangles were acquired using filter sets #1, #2 and #3 respectively. Lines are linear fits. (b) Temporal decay of optical signals from BK7 glass (open black squares) and quartz (open red circles) coverslips, expressed in terms of the pixel values. Solid lines represent single exponential fits.

slide or glass coverslip, it was worthwhile to investigate the glass substrate auto-photoluminescence and consider means of its suppression.

We compared spectral and time-gated methods to minimise B_s . Firstly, we attempted spectral discrimination. To this aim, three filter sets (Table 1), selected for suppression of a particular spectral range of B_s , were tested (Figure 6a). Secondly, we tested the time-gated discrimination. Here, the gate time, Δt was varied to analyse the effect of Δt on the contrast (Figure 6a). Lastly, we tested a non-auto-photoluminescent coverslip and slide made of fused quartz to reduce B_s (Figure 6b).

Figure 6a shows the C_{NR} of discrete nanorubies placed on a BK7 glass coverslip, as acquired in the epi-luminescence and TGP imaging modes plotted as a function of Δt . The filter set #1 demonstrated the best performance in terms of C_{NR} in both acquisition modes, while the set #3 displayed the worst performance. The filter set #1 transmitted the excitation and emission light with minimum losses; and it suppressed the auto-photoluminescence from the glass slide most efficiently, as shown in the transmission plot of the filter set #1 (Figure S1). The contrast enhancement in the TGP mode compared to the epi-luminescent mode was obvious for all three tested filter sets. The contrast increases with Δt , with values of 2.8, 3.5 and 4.4 fold for the filter sets #1, #2 and #3 respectively at $\Delta t = 1000 \mu s$ (Figure 6a). Even though the filter set #3 showed the highest enhancement upon the time gating, the absolute contrast was the highest when using the filter set #1.

The PL lifetimes of the empty BK7 glass and quartz substrates, spectrally filtered by the filter set #1, are shown in Figure 6b. The lifetime of the BK7 glass was measured to be $(3.7 \pm 0.6) \times 10^2 \mu s$. The time trajectory of the optical signal originating from quartz coverslips exhibited a fast decay with a time constant of $15 \pm 11 \mu s$, which likely originates from the trailing edge of the laser excitation.

From these analyses, two observations are noteworthy. Firstly, the excitation laser light bleeding through the spectral filter sets represented a non-zero component of the B_s , as inferred by comparing the C_{NR} in the TGP and epi-luminescence modes (Figure 6). The suppression of this background component by routine spectral filtering can be difficult even in a carefully optimised setting, and practically impossible in macro-scale optical imaging of highly-scattering biological tissue [41]. The time-gated imaging mode provides an effective and inexpensive approach to completely eliminate this component. Secondly, the intrinsic photoluminescence of the BK7 glass, presumably originating from impurities, also contributed to B_s . Since these impurities were characterised by a relatively long τ_{PL} (Figure 6b), suppressing this background was difficult by TGP imaging. At the same time, this contribution to the back-

ground was relatively low compared to that of biological autofluorescence (as seen below). Therefore, it is typically tolerable during optical imaging of biological samples, even when ultrahigh-sensitivity is desired. If this minimal background is intolerable, BK7 coverslips are to be replaced with quartz coverslips.

3.4 Time-gated imaging of single-nanorubies submerged in a fluorescent dye solution

In order to demonstrate the performance of the designed time-gated system, discrete nanorubies sparsely dispersed on a glass coverslip were submerged in a solution of a yellow-fluorescent organic dye. The results of the epi-luminescence and TGP imaging of this sample are shown in Figure 7. Despite the use of the filter set #1 (including a narrow, 23-nm wide, band-pass filter centred at 689 nm) optimised for the high-sensitivity detection of the nanoruby PL, the emission from the yellow dye subdued the nanoruby signal. However, in the TGP mode, the fluorescence signal from the yellow fluorescent dye was completely suppressed, which allowed for recovering the signal from discrete nanorubies. The background value of the signal from nanorubies in the dye solution is closely approached that of the EMCCD dark counts ($B_s = 5447 \pm 265$ count and Dark = 2972 ± 332 count)

3.5 Time-gated imaging of nanorubies in cells

The feasibility of using the TGP system to image nanorubies on a biological background of living cells was tested using cells (AtT-20, Section 2.8) incubated with nanorubies. Representative images of nanoruby-containing living cells, acquired in the bright

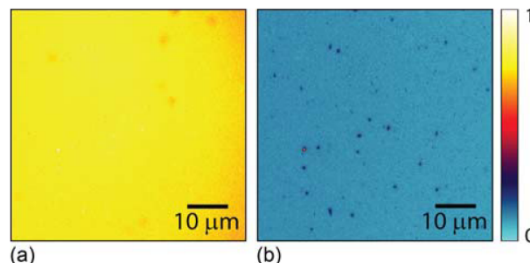


Figure 7 Images of nanorubies spin-coated on a glass coverslip and submerged in a solution of the yellow-fluorescent organic dye obtained by (a) epi-luminescence and (b) TGP imaging modes. Nanorubies are invisible in (a) whereas discrete nanorubies were clearly observed in (b).

field, epi-luminescence and TGP imaging modes are shown in Figure 8. In the TGP mode, the fluorescence originating from media and endogenous cell fluorophores (Figure 8b) is suppressed, resulting in background-free imaging of discrete nanorubies bound to the cell (Figure 8c).

This experimental configuration models a functional imaging scenario, where a fluorescent solution

probe assays the functional state of the cell (e.g., intracellular Ca^{2+}) modulated by ligands such as neurotransmitters, while molecular trafficking of the receptor-bound ligands labelled with photoluminescent nanoparticles are visualised using the TGP mode. The nanoruby signal is confirmed by the control sample without nanorubies as shown in Figure 8 (a–c, right panel).

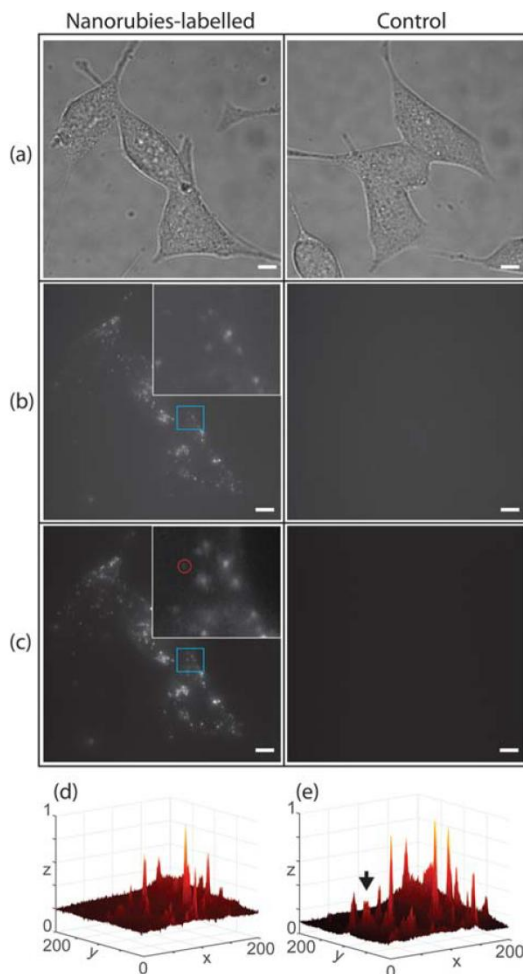


Figure 8 Microscopy images of AtT-20 cells. (a–c) Left and right columns: cells incubated with nanorubies and control, respectively. Rows: (a) Bright field, (b) epi-luminescence, and (c) TGP images. Insets in (b) and (c), blow-up images as framed by blue squares. A red circle marks the nanoruby indiscernible in (b). Scale bars in (a–c), 10 μm . (d) and (e) are normalised 3D-pseudo-colour plots of the epi-luminescence and TGP modes, respectively. The black arrow on (e) demarcates a representative peak which is only barely visible in (d).

3.6 Single-molecule kinetic binding assay

Detection of rare, but significant biomolecules or biological events in biological fluids, such as blood and urine, is known as “a needle in a haystack” prob-

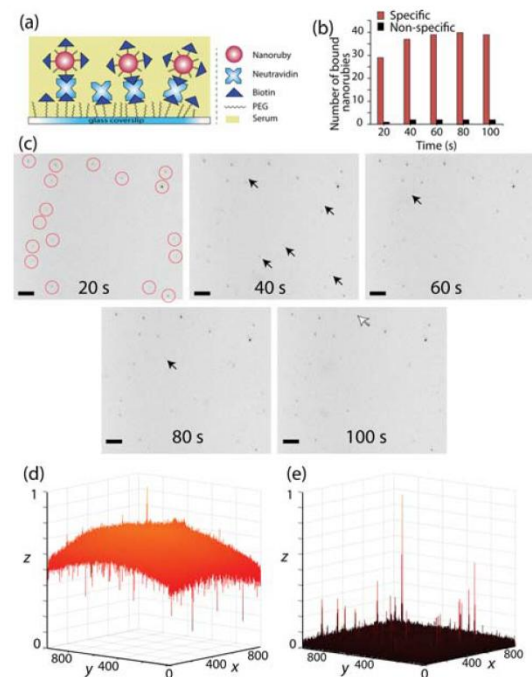


Figure 9 Schematic diagram of assaying antigens modelled by avidin with biotinylated nanorubies in serum. (b) A bar-chart of the number of nanorubies bound to the avidin-functionalised substrate, as a function of time, as observed in Video S2 and Video S3 (available in SI). Red and black bars represent specific and non-specific (negative control) binding. (c) Zoomed time-lapse images of the binding events (inverted color) captured from Videos S2 and S3. Red circles show nanorubies that had bound to the substrate before the start of video recording; black arrows show emerging bound nanorubies, a white arrow shows the detached nanoruby. Scale bar, 10 μm . (d) and (e) are normalised 3D-pseudo-colour plots of the epi-luminescence and TGP images, respectively.

lem, exacerbated by autofluorescence from endogenous flavins, nicotinamide adenine dinucleotides and porphyrins. Several assay formats and probes have been developed to detect clinically relevant proteins, nucleotides and other molecules (such as glucose) in biological fluids [42–44]. Here, we demonstrate our TGP method capability for a single-molecule kinetic assay, which is in our case modelled as an avidin-biotin pair in a biological fluid. We made use of nanorubies to label antigens modelled by avidin.

The binding of single biotinylated nanorubies to avidin in fetal bovine serum (serum) is schematised in Figure 9a. The binding was monitored over time and presented in Figure 9c, where black arrows mark newly bound nanorubies, while a white arrow shows the detachment of a weakly bound, presumably, adsorbed nanoruby from the coverslip. Video S2 (available in Supplementary Information file) shows the real time imaging of nanoruby kinetic binding, while Video S3 (see SI) shows the corresponding negative control assay, where few binding events registered.

The number of nanorubies bound to the immobilised avidin during the time series is presented in a bar chart in Figure 9b. Figure 9d and e, respectively, show epi-luminescence and TGP images of the specifically bound nanoruby distribution at the assay completion. In contrast with the epi-luminescent video microscopy, nanorubies were visualised clearly in the time-gated mode, thus showing the cutting-edge merit of the reported method. This demonstrates the feasibility of the method for assaying of molecular markers such as inflammatory markers or for bed-side monitoring of analytes in a clinical setting.

4. Conclusion

We demonstrate a time-gated photoluminescence microscopy system that enables fast and ultrahigh-sensitivity imaging of long-lifetime photoluminescent probes in optically crowded environments for extended periods of time. Time-gated imaging of nanoruby photoluminescence enabled its separation from short-lived laser scatter, autofluorescence of biological matter and organic fluorescent probes. By using time-gated imaging mode, we have been able to demonstrate the detection of single nanorubies dispersed on a coverslip, even when they were submerged in a solution of organic fluorescent dye, or bound to cells submerged in a fluorescent culture medium. The rapid imaging capability of the system enabled live monitoring of single particle binding events in autofluorescent biological fluids.

The presented results demonstrate the potential of nanorubies as molecular probes or labels for a

range of applications in the life sciences, such as real-time assaying of analytes in biological fluids. These developments will offer new opportunities for visualising intracellular molecular trafficking and detecting rare biomolecular events in an optically crowded background of cells and tissues.

Supporting Information

Additional supporting information may be found in the online version of this article at the publisher's website.

Acknowledgements We acknowledge support of the Federal targeted program of the Russian Federation, Grant number RFMEFI57814X0030. The authors thank Mr. Russell Field, Dept. of Environmental Sciences, Macquarie University for his assistance with DLS Mastersizer 2000 equipment.

Author biographies Please see Supporting Information online.

References

- [1] J. W. Lichtman and J.-A. Conchello, *Nat. Methods* **2**, 910–919 (2005).
- [2] M. P. Backlund, M. D. Lew, A. S. Backer, S. J. Sahl, and W. Moerner, *ChemPhysChem* **15**, 587–599 (2014).
- [3] J. R. Lakowicz, *Principles of Fluorescence Spectroscopy*, 3rd edition ed. (Springer, New York), (2006).
- [4] M. J. Ruedas-Rama, J. D. Walters, A. Orte, and E. A. Hall, *Anal. Chim. Acta* **751**, 1–23 (2012).
- [5] V. K. A. Sreenivasan, A. V. Zvyagin, and E. M. Goldys, *J Phys Condens Matter* **25**, 194101 (2013).
- [6] P. Sharma, S. Brown, G. Walter, S. Santra, and B. Moudgil, *Adv Colloid Interface Sci* **123–126**, 471–485 (2006).
- [7] W. E. Moerner, *Proc. Natl. Acad. Sci. U.S.A.* **104**, 12596–12602 (2007).
- [8] W. Kong, R. Liu, H. Li, J. Liu, H. Huang, Y. Liu, and Z. Kang, *J. Mater. Chem. B* **2**, 5077–5082 (2014).
- [9] L. Zhang and E. Wang, *Nano Today* **9**, 132–157 (2014).
- [10] P. Zhang, X. X. Yang, Y. Wang, N. W. Zhao, and C. Z. Huang, *Nanoscale* **6**, 2261–2269 (2014).
- [11] S. W. Wu, G. Han, D. J. Milliron, S. Aloni, V. Altoe, D. V. Talapin, B. E. Cohen, and P. J. Schuck, *Proc. Natl. Acad. Sci. U.S.A.* **106**, 10917–10921 (2009).
- [12] A. M. Edmonds, M. A. Sobhan, V. K. A. Sreenivasan, E. A. Grebenik, J. R. Rabeau, E. M. Goldys, and A. V. Zvyagin, *Part Part Syst Charact* **30**, 506–513 (2013).
- [13] K. Y. Han, K. I. Willig, E. Rittweger, F. Jelezko, C. Eggeling, and S. W. Hell, *Nano Lett.* **9**, 3323–3329 (2009).

- [14] Z. Yi, W. Lu, Y. Xu, J. Yang, L. Deng, C. Qian, T. Zeng, H. Wang, L. Rao, H. Liu, and S. Zeng, *Biomaterials* **35**, 9689–9697 (2014).
- [15] E. Dimitrow, I. Riemann, A. Ehlers, M. J. Koehler, J. Norgauer, P. Elsner, K. König, and M. Kaatz, *Exp. Dermatol.* **18**, 509–515 (2009).
- [16] M. S. Roberts, M. J. Roberts, T. A. Robertson, W. Sanchez, C. Thöring, Y. Zou, X. Zhao, W. Becker, and A. V. Zvyagin, *J Biophotonics*, **1**, 478–493 (2008).
- [17] M. Y. Berezin and S. Achilefu, *Chem. Rev.* **110**, 2641–2684 (2010).
- [18] D. J. Gargas, E. M. Chan, A. D. Ostrowski, S. Aloni, M. V. P. Altoe, E. S. Barnard, B. Sanii, J. J. Urban, D. J. Milliron, and B. E. Cohen, *Nat Nanotechnol* **9**, 300–305 (2014).
- [19] R. M. Rich, D. L. Stankowska, B. P. Maliwal, T. J. Sørensen, B. W. Laursen, R. R. Krishnamoorthy, Z. Gryczynski, J. Borejdo, I. Gryczynski, and R. Fudala, *Anal Bioanal Chem* **405**, 2065–2075 (2013).
- [20] E. A. Grebenik, A. Nadort, A. N. Generalova, A. V. Nechaev, V. K. Sreenivasan, E. V. Khaydukov, V. A. Semchishen, A. P. Popov, V. I. Sokolov, and A. S. Akhmanov, *J Biomed Opt* **18**, 076004 (2013).
- [21] Y. Y. Hui, L.-J. Su, O. Y. Chen, Y.-T. Chen, T.-M. Liu, and H.-C. Chang, *Sci Rep* **4**, 5574–1–5574-7 (2014).
- [22] G. Mandal, M. Darragh, Y. A. Wang, and C. D. Heyes, *Chem. Commun.* **49**, 624–626 (2013).
- [23] L. Zhang, X. Zheng, W. Deng, Y. Lu, S. Lechevallier, Z. Ye, E. M. Goldys, J. M. Dawes, J. A. Piper, and J. Yuan, *Sci Rep* **4**, 6597–1–6597-6 (2014).
- [24] L. Tian, Z. Dai, L. Zhang, R. Zhang, Z. Ye, J. Wu, D. Jin, and J. Yuan, *Nanoscale* **4**, 3551–3557 (2012).
- [25] B. Valeur, M. N. Berberan-Santos, *Molecular fluorescence: principles and applications* (John Wiley & Sons, 2012).
- [26] R. Connolly, D. Jin, and J. Piper, *Cytometry Part A* **69**, 1020–1027 (2006).
- [27] S. Bouccara, E. Giovanelli, G. Sitbon, N. Lequeux, T. Pons, V. Lorient, and A. Fragola, *Proc. SPIE Int. Soc. Opt. Eng.* **8947**, 89471B–1–89471B-8 (2014).
- [28] R. Frischknecht, M. Heine, D. Perrais, C. I. Seidenbecher, D. Choquet, and E. D. Gundelfinger, *Nat. Neurosci.* **12**, 897–904 (2009).
- [29] W. A. W. Razali, V. K. A. Sreenivasan, E. M. Goldys, and A. V. Zvyagin, *Langmuir* **30**, 15091–15101 (2014).
- [30] A. Nadort, V. K. Sreenivasan, Z. Song, E. A. Grebenik, A. V. Nechaev, V. A. Semchishen, V. Y. Panchenko, and A. V. Zvyagin, *PloS one* **8**, e63292 (2013).
- [31] C. Bradac, T. Gaebel, C. Pakes, J. M. Say, A. V. Zvyagin, and J. R. Rabeau, *Small* **9**, 132–139 (2013).
- [32] E. Peli, *J Opt Soc Am A Opt Image Sci Vis* **7**, 2032–2040 (1990).
- [33] P. Whittle, *Vision Res.* **26**, 1677–1691 (1986).
- [34] M. A. Dobrovolskaia, A. K. Patri, J. Zheng, J. D. Clogston, N. Ayub, P. Aggarwal, B. W. Neun, J. B. Hall, and S. E. McNeil, *Nanomedicine* **5**, 106–117 (2009).
- [35] M. B. Walter Koechner, *Solid-State Lasers: A Graduate Text* (Springer, New York Berlin Heidelberg, 2002).
- [36] C. Pflichtsch, R. Siddiqui, and B. Atakan, *Appl Phys A Mater Sci Process* **90**, 527–532 (2008).
- [37] D. E. Chandler, Z. K. Majumdar, G. J. Heiss, and R. M. Clegg, *J Fluoresc* **16**, 793–807 (2006).
- [38] F. A. Inam, M. D. Grogan, M. Rollings, T. Gaebel, J. M. Say, C. Bradac, T. A. Birks, W. J. Wadsworth, S. Castelletto, and J. R. Rabeau, *ACS nano* **7**, 3833–3843 (2013).
- [39] J. Zhao, D. Jin, E. P. Schartner, Y. Lu, Y. Liu, A. V. Zvyagin, L. Zhang, J. M. Dawes, P. Xi, and J. A. Piper, *Nat Nanotechnol* **8**, 729–734 (2013).
- [40] W. Q. Zhang, W. Razali, V. Sreenivasan, T. M. Monro, and D. Taylor, *Universal optical fibre fluorescence sensing platform for wine monitoring*, in: 40th Australian Conference on Optical Fibre Technology, Adelaide, Australia (2015).
- [41] F. Leblond, S. C. Davis, P. A. Valdés, and B. W. Pogue, *J. Photochem. Photobiol. B, Biol.* **98**, 77–94 (2010).
- [42] J. Li, W. Zhou, X. Ouyang, H. Yu, R. Yang, W. Tan, and J. Yuan, *Anal. Chem.* **83**, 1356–1362 (2011).
- [43] X. Meng, M. Xu, J. Zhu, H. Yin, and S. Ai, *Electrochim. Acta* **71**, 233–238 (2012).
- [44] Y. He, H.-F. Wang, and X.-P. Yan, *Anal. Chem.* **80**, 3832–3837 (2008).

Supporting Information

Wide-field time-gated photoluminescence microscopy for fast ultrahigh-sensitivity imaging of photoluminescent probes

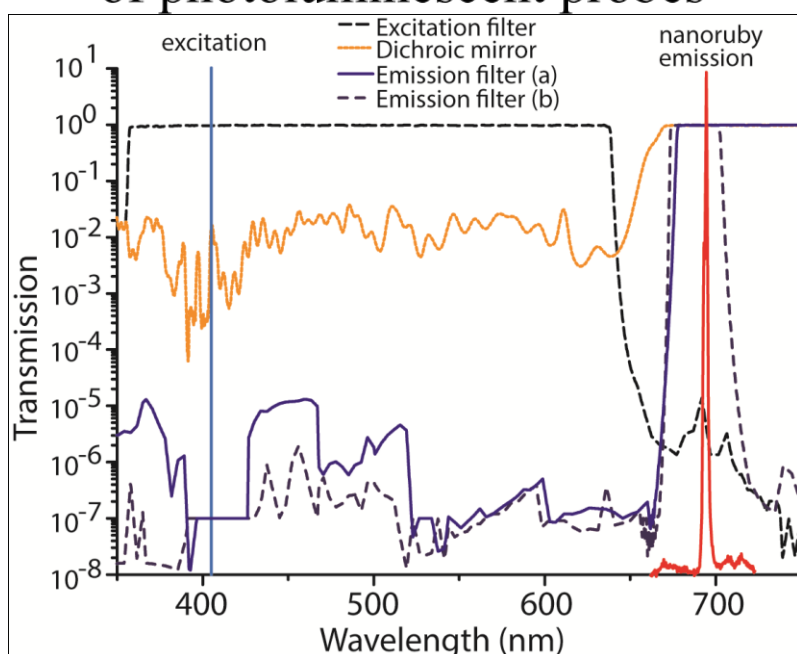


Figure S1 A semi-log plot of the transmission characteristics of the interference filters incorporated in the filter set #1 superimposed on the excitation laser and nanoruby emission spectra.

Video S2 Real time imaging of nanorubies' kinetic binding.

<https://www.dropbox.com/s/w6h8t9vdz6bmfw6/Video%20S2%20NR%20binding.avi?dl=0>

Video S3 Control sample of nanorubies' kinetic binding.

<https://www.dropbox.com/s/5jam31yzh73m5fy/Video%20S3%20NR%20binding%20control.avi?dl=0>

Author biographies



Wan Razali obtained his Master in Physics (Optoelectronic) from Universiti Teknologi Malaysia (UTM) and completed his first degree in Physics in 2004 from the same university. In 2008, he joined Universiti Teknologi MARA (UiTM) as a Physics Lecturer, where his research was focussed on the fabrication of rare earth-doped glasses for laser applications. Supported by the Malaysian Government Scholarship scheme, he is currently pursuing a Ph.D. degree at Macquarie University. His research is focussed on fabrication and characterization of novel nanomaterial with remarkable photostability and long photoluminescence lifetime suitable for ultrahigh-sensitivity background-free biological imaging at a single-molecule level.



Dr. Sreenivasan is a Postdoctoral Research Fellow at Macquarie University. He studied Photonics from Cochin University of Science and Technology in India, and later obtained a Ph.D. in physics at Maquarie University in Australia. He doctoral thesis focussed on the development and use of fluorescent nanoparticles to study molecular trafficking of somatostatin, a hormone that serves multitude of physiological functions in humans. He spent ten months as a postdoc associate at Baylor College of Medicine in USA. There, he studied the voltage-dependent capacitance of cochlear cells to identify fundamental parameters that may underlie variations in hearing between animals of different sex and skin colour. He also developed the algorithms with which the lab collects cytoskeletal force data using the optical tweezers. He returned to Maquarie University in 2013 after being awarded a Macquarie University Research Fellowship. His current research focuses on developing novel photoluminescent nanoparticles, especially on nanorubies. His goal is to construct a nano toolkit that will enable pharmacologists elucidate GPCR-based cellular signalling pathways in ways that are impossible today.



Dr Carlo Bradac is a Postdoctoral Research Fellow at Macquarie University. He studied physics and engineering at the Polytechnic of Milan (Italy) where he achieved his bachelor degree (B.S.) in Physical Engineering in 2004 and his master degree (M.S.) in Nanotechnologies and Physical Technologies in 2006. He worked as an Application Engineer at National Instruments (2006-2007) and as a Process Automation & Control Engineer at Maire Tecnimont S.p.a. (2007-2008). In August 2008 he was offered a Macquarie Research Excellence Scholarship (MQRES) from Macquarie University, Sydney (Australia), where he completed his Ph.D. in Physics in 2012. He worked as a Postdoctoral Research Fellow at Sydney University (2012-2013) and joined Macquarie University in July 2013. His research is focused on colour centres, specifically nitrogen-vacancy (NV) centres, in diamond and on their possible application in quantum information technologies, biomedical tracking and drug-delivery and high resolution single-spin sensing.



Mark Connor is Professor of Pharmacology in the Faculty of Medicine and Health Sciences at Macquarie University. He trained at Sydney University (BSc) and the University of Washington (Ph.D.) before working at Bristol University, Sydney University and the Vollum Institute. He is interested in the molecular mechanisms underlying the actions of opioids and cannabinoids, and in particular how diverse ligands differentially recruit signalling and regulatory pathways. His current focus is the use of fluorescent techniques to study the acute activation of naturally occurring polymorphisms of μ -opioid receptors and the modulation of diverse GPCR and ion channels by illicit synthetic cannabinoids and the constituents of cannabis.



Professor Ewa M. Goldys is Deputy Director of the Australian Research Council Centre of Excellence for Nanoscale Biophotonics at Macquarie University. (see www.cnbp.org.au).

Professor Goldys pioneered ultrasensitive analysis methods of non-invasive label-free characterisation for biology and health diagnostics. This characterisation is based upon the detection and quantification of various metabolites (free and bound NADH, flavins, A2E, lipofuscin, and cytochrome C). This approach provides a collective metabolic fingerprint which can be used to distinguish healthy from diseased cells in a variety of disease conditions.

Professor Goldys made major contributions to fluorescent labelling, a key optical technique to characterise cells and tissues by characterising and developing applications of specialised fluorescent nanoparticles including the first successful demonstration of fluorescence upconversion in nanoparticles and a sequence of works concerned with optical characterisation of lanthanide-doped nanoparticles. Professor Goldys is Fellow of Optical Society and she attracted over \$50M in external competitive research funding, also for interdisciplinary research.



Andrei V. Zvyagin received Diploma from the Moscow Engineering Physics Institute, Russia, and Ph.D. degree in Engineering from the Tokyo Institute of Technology in 1997. He spanned a range of positions from an Engineer to Senior Research Scientist in the Institute of Metrology for Time and Space, Moscow, Russia. From 1998 to 2004, he was an Australian Postdoctoral Fellow in the Optical & Biomedical Engineering Laboratory, The University of Western Australia. From 2004–2007, he joined The University of Queensland as a Lecturer/Senior Lecturer. Since 2007, Dr. Zvyagin is Associate Professor at the Macquarie University, Sydney, Australia. His current research interests include various areas of Biophotonics and Nanotechnology: nonlinear optical microscopy, luminescent nanomaterials, as molecular reporters for diagnosis and targeted delivery.

6.4 Time-gated photoluminescence microscopy

Fluorescence imaging is one of the most versatile and widely used methods in biomedical research. These methods are generally based on biomolecular-specific labelling of biological structures with photoluminescent (PL) nanomaterials, which offer direct and minimally invasive approaches to investigate the cellular morphology and processes in living cells and/or tissues, in their natural biological context. PL imaging in biological samples is often limited by the autofluorescence originating from the organelles, cellular structures and biomolecules within cells and tissues, for example NADH, flavins and porphyrins [2-4]. Autofluorescent background can be reduced by working in the near-infrared spectral region ranging from 650 nm to 900 nm [5]. However, this approach cannot fully eliminate the background signal. Another effective approach is by using time-gated photoluminescence (TGP) imaging system (also known as time-gated luminescence). TGP imaging is realised by turning on a detector, following a short time delay after the short-lived ($<1\ \mu\text{s}$) fluorescence is ended (detail discussion in attached paper) [6, 7]. Photoluminescence signal from a probe with longer photoluminescence lifetime is then captured in the absence of background, which greatly enhances signal to noise ratio [8]. It is possible to obtain high sensitivity, reaching the single molecule detection regime by using this approach.

The sensitivity of this approach relies on the properties of PL probe. The photoluminescence lifetime of the probe must longer than the background, to ensure complete elimination of background signal. Background normally originates from autofluorescence and excitation laser tail. Typical values of autofluorescence lifetime range from tens of picoseconds [15] to several nanoseconds [16, 17], whereas laser tail lifetime around few milliseconds depending to the laser quality. Probe with excellent photostability is also important to provide unlimited emission upon continuous excitation. This is to maintain the imaging sensitivity, which is highly desirable in single molecule tracking experiments. In terms of imaging system, confocal system has been used for TGP imaging to achieve single-molecule regime [9, 10]. However, this system requires to dwell on each pixel, which makes the image acquisition relatively slow. Therefore, wide-field epifluorescence microscope is preferable because it provides rapid acquisition and involves simple setup [11].

Gu *et al.* [12] demonstrated TGP imaging by using PL porous silicon nanoparticles as a PL probe. The nanoparticles were synthesised by electrochemical etching of the surface of single-crystal silicon in hydrofluoric acid. The sample was coated with polyethylene glycol by reacting with a PEG-silane. The photoluminescence lifetime of the nanoparticles was between 5 to 13 μs , which is long enough to eliminate short-lifetime background by applying TGP imaging. Using this probe, they achieved 50-fold reduction in background signal in vitro (Figure 6.1a, b) and greater than 20-fold in vivo (Figure 6.1c, d). Meanwhile, Sun *et al.* [13] reported the application of Eu15F (Europium complex)/PVK (poly(9-vinylcarbazole)) polymer dots (Pdots) as a probe for cell labelling. This probe has very narrow red fluorescence emission (612 nm) and excellent brightness. It also has long photoluminescence lifetime $\approx 500 \mu\text{s}$. For the cell labelling, the Eu15F/PVK Pdots were incubated with MCF-7 cells. Figure 6.2 a-e shows the time-gated and ungated microscopy images of MCF-7 cells with internalized Eu15F/PVK Pdots. Time-gated image (Figure 6.2c) shows great decrease of background signal compared to the ungated images (Figure 6.2a). Clear difference can be observed in 3D surface plots (Figure 6.2d,e). The signal to noise ratio improvement was reported around 3 folds [13].

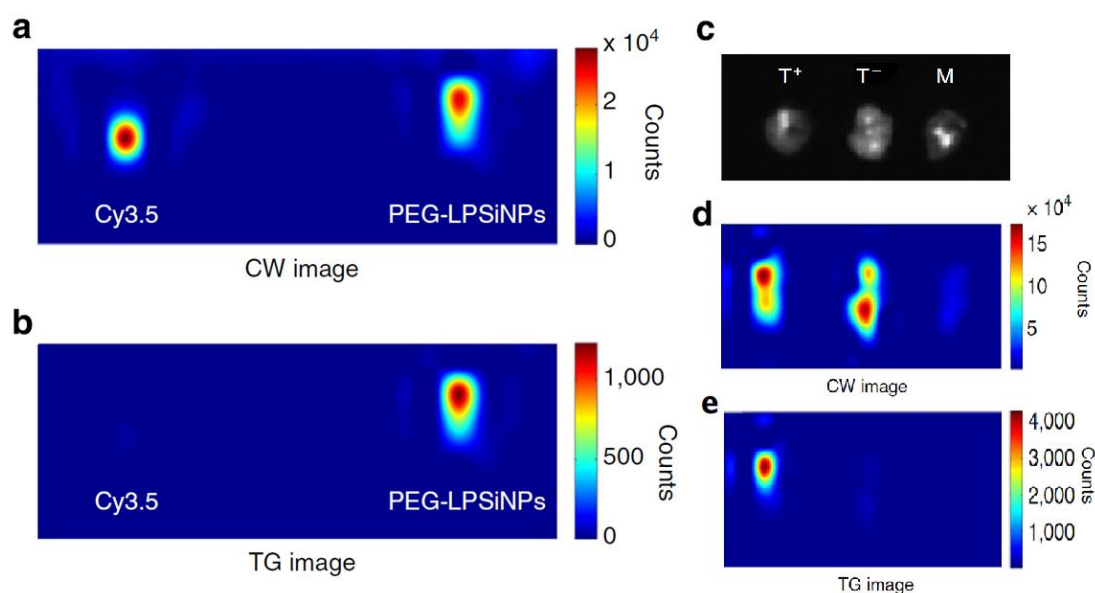


Figure 6.1: (a) CW PL images of Cy3.5 and PEG-LPSiNP. (b) TGP image of the same sample in (a). The image of the Cy3.5 sample almost completely disappears due to its short-lived emission. (c) Ex vivo bright field image of the PEG-LPSiNP-injected with

tumor (T^+), a control tumor (T^-) and muscle tissue excised from the animal post-injection (M). (d) CW PL image of the excised tissues in (c). (e) TGP image of the tissues in (c). Reproduced from Ref. [12].

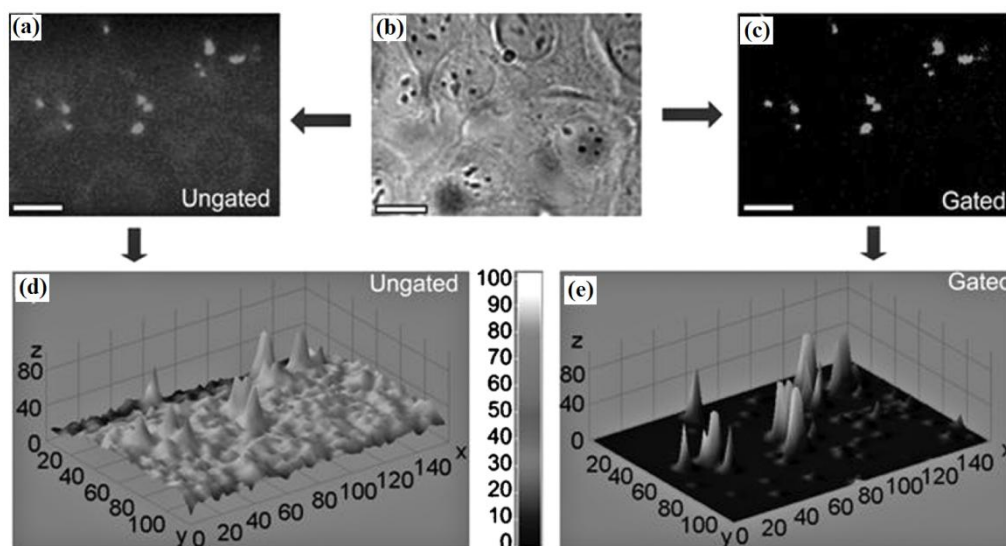


Figure 6.2: (a) Ungated (CW) PL microscopy image. (b) bright-field microscopy image, and (c) TGP microscopy image of unconjugated Eu15F/PVK Pdots inside MCF-7 cells; scale bar represents 50 mm. (d) and (e) are the interactive 3D surface plot of ungated image (a) and gated image (c) respectively. Reproduced from Ref. [13].

Single molecule detection has been used in cell receptors imaging and intracellular analytes detection [14]. Based on recent developments in nanobiophotonics, now single biomolecule imaging has been demonstrated for tracking molecular trafficking events in living cells [15, 16]. Vrljic *et al.* [17] demonstrated single-molecule epifluorescence microscopy for the motion of I-Ek protein molecules. Figure 6.3 shows the PL microscopy images of individual molecules of I-Ek protein that belongs to the major histocompatibility complex class II. The imaging was performed on the surface of living Chinese hamster ovary CHO cells by using a peptide that selectively binds to the I-Ek protein labelled with a fluorescent molecule, Cy5. Another example is the detection of a fluorescently labelled single virus, which enabled tracking the virus invasion of the cell and its diffusion towards the nucleus. This work provides an important insight in the area of immunology [18]. Chang *et al.*, demonstrated a single fluorescent nanodiamond (FND) particle tracking inside the cell in three

dimensions over a time span of more than 200 s under a wide-field microscope [19]. Figure 6.4a shows the bright-field and fluorescence images of a live HeLa cell after uptake of 35-nm FNDs. Figure 6.4b shows three-dimensional trajectory of a single FND inside the cell. This study suggests the feasibility of applying PL nanoparticle for long-term tracking application.

The above-mentioned applications show the importance of single-molecule detection and time-gated imaging. By combining these two modalities, ultrahigh sensitive imaging system can be achieved, which can be applied in complex bioimaging application.

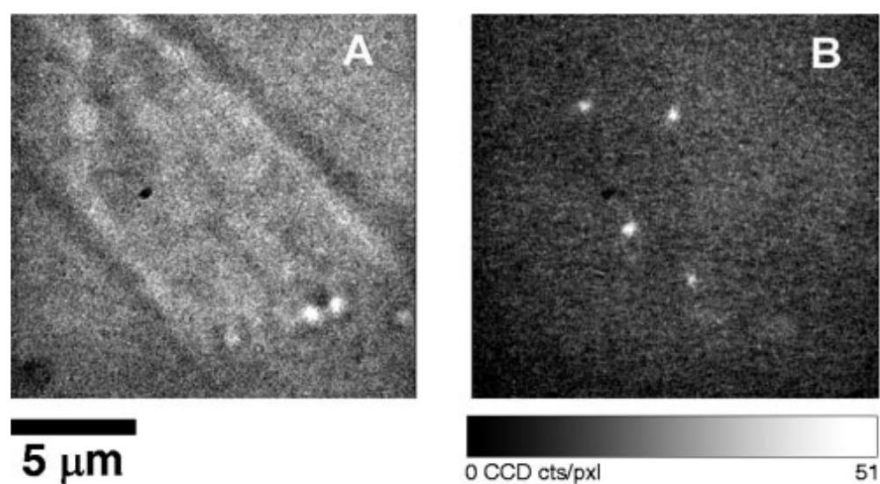


Figure 6.3: Visualisation of individual molecules of I-Ek protein in a CHO cell. **A.** Bright field image of a single CHO cell. **B.** PL image of the same cell showing spatial distribution of I-Ek protein molecules on the cell surface. Bright spots represent Cy5-labelled peptide bound to the protein. Reproduced from Ref. [17].

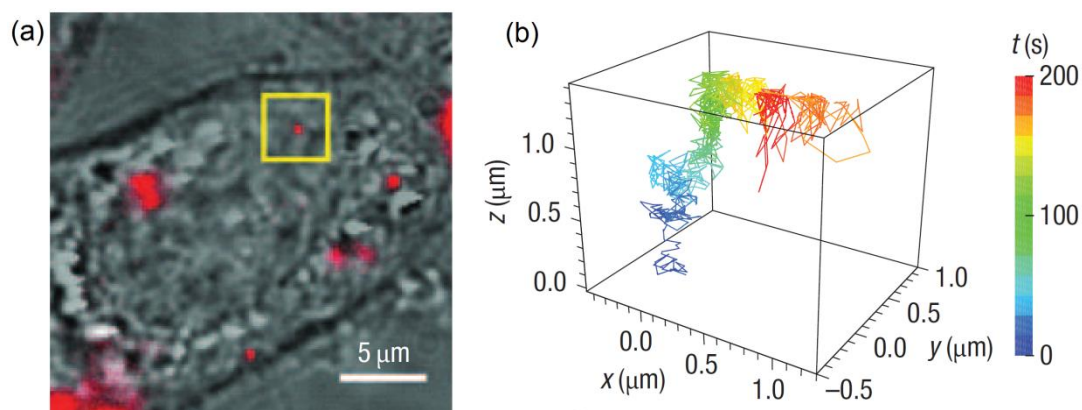


Figure 6.4: Three-dimensional tracking of a single 35-nm FND in a live HeLa cell. (a) Bright-field and epifluorescence merge images of the cell after FND uptake. (b) Three-dimensional trajectory of a single FND inside the cell over a time span of 200 s. Reproduced from Ref. [19].

6.5 Avidin-biotin interaction and its application.

Avidin is a common molecule used for PL immunoassaying. Avidin and biotin (vitamin H) interaction has high-affinity, where a biotinylated compound can strongly bind to an avidin molecule with strong noncovalent binding ($K_d \sim 10^{-15}$ M) [20]. Avidin composes of four identical subunits, and each subunit has a single binding site for biotin as illustrated in Figure 6.5. These proteins possess resistance to extreme temperatures (*i.e.*, midpoint temperature of denaturation, T_m of 73 °C for apo-streptavidin and 112 °C for biotin-streptavidin), pH conditions, denaturing agents, and enzymatic degradation [21].

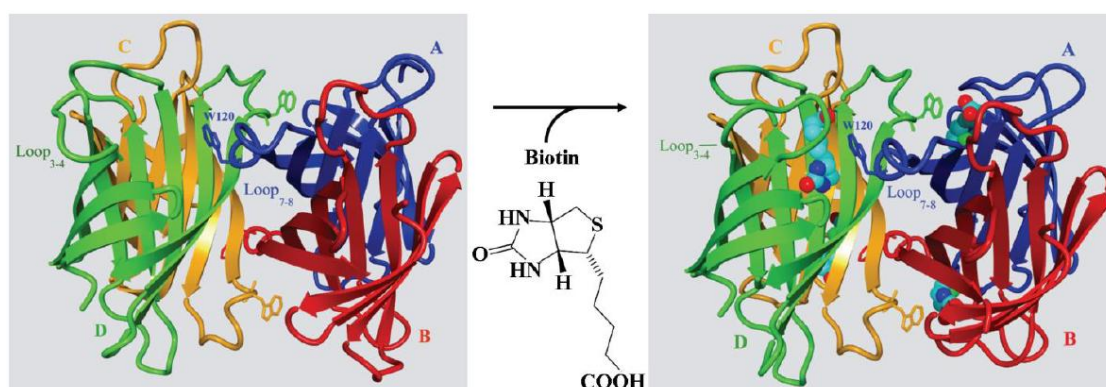


Figure 6.5. Biotin entry in streptavidin. Subunits **A**, **B**, **C**, and **D** are coloured in blue, red, yellow, and green respectively. Loop₃₋₄ between the third and fourth strands in each subunit functions as a lid for the entry and exit of biotin, loop₇₋₈ includes tryptophan that hydrophobically binds to biotin located in the neighbouring subunit. Reproduced from Ref. [22].

The [strept]avidin-biotin interaction has been applied in numerous laboratory methods especially in the areas of immunolabelling and molecular biology. For example, [strept]avidin-antibody conjugates are used for pre-targeting and sensing at the final step of immunoassay in the radiolabeled form. It also used as a clearing agent to remove circulating biotinylated antibodies [23]. Avidin-biotin interaction has been applied for sensitive antigen detection in biological sample. For this purpose, Huhtinen

et al. [24] developed an immunoassay for the prostate-specific antigen (PSA) detection in serum. The immunoassay configurations based on avidin-biotin of this work is shown in Figure 6.6. To test their assay, total PSA concentrations were determined from male serum samples. Their experiment results, shows good agreement with reference assay. However, the detection limit of this assay is 35 times lower compared to reference method [24]. Recently, Duijvesz *et al.* [25] developed sensitive time-resolved fluorescence immunoassay for prostate-cancer-derived exosomes capture/detection in urine. CD9 and CD63 are cell surface proteins which can be used as prostate cancer markers. In their work, antibodies against these proteins were biotinylated for optimal capture, and another batch labelled with a Europium (Eu)-chelate for time-resolved fluorescence detection. Sensitive exosomes detection in urine and cell medium was achieved by using this method [25]. In our work, avidin-biotin interaction was applied for immunoassay demonstration. Avidin immobilised on coverslip was used to capture biotinylated nanoruby in biological medium.

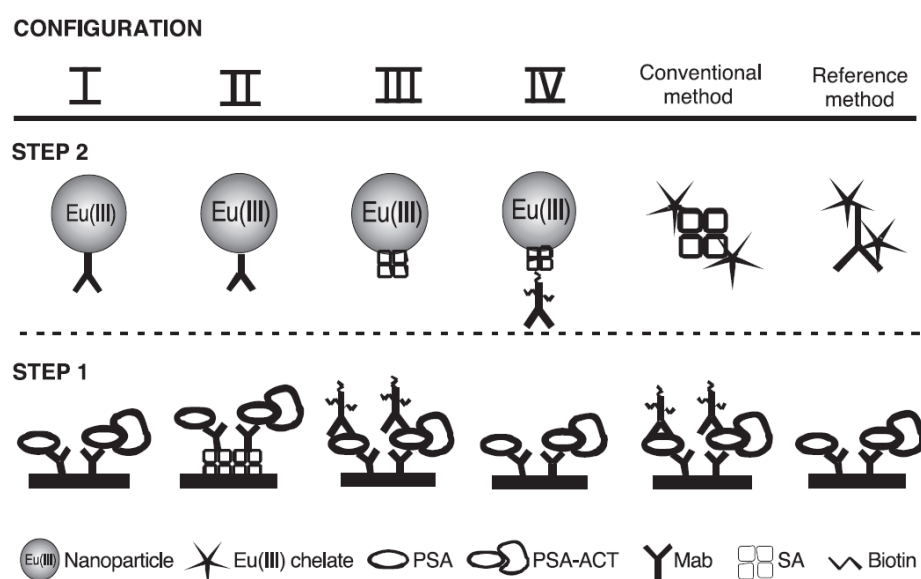


Figure 6.6: In configurations I and II, time-resolved fluorescence was detected with Mab-coated nanoparticles, while in configurations III and IV, SA-coated nanoparticles were utilised. The solid phase was passively coated with capture antibody in configurations I, III, and IV, whereas the capture antibody was biotinylated and attached on the solid phase via streptavidin in configuration II. Conventional and Reference methods are also presented, where either europium(III) chelate-labeled SA or Mab was used for signal generation. Reproduced from Ref. [24].

6.6 References

- [1] W. A. Razali, V. K. Sreenivasan, C. Bradac, M. Connor, E. M. Goldys, and A. V. Zvyagin, "Wide-field time-gated photoluminescence microscopy for fast ultrahigh-sensitivity imaging of photoluminescent probes," *Journal of biophotonics*, vol. 9, pp. 848-858, 2016.
- [2] M. Monici, "Cell and tissue autofluorescence research and diagnostic applications," *Biotechnology annual review*, vol. 11, pp. 227-256, 2005.
- [3] M. Neumann and D. Gabel, "Simple method for reduction of autofluorescence in fluorescence microscopy," *Journal of Histochemistry & Cytochemistry*, vol. 50, pp. 437-439, 2002.
- [4] H. Andersson, T. Baechi, M. Hoechl, and C. Richter, "Autofluorescence of living cells," *Journal of microscopy*, vol. 191, pp. 1-7, 1998.
- [5] P. Szuromi, "Beating Fluorescent Background," *Science*, vol. 341, pp. 1153-1153, 2013.
- [6] N. Sayyadi, R. E. Connally, and A. Try, "A novel biocompatible europium ligand for sensitive time-gated immunodetection," *Chemical Communications*, vol. 52, pp. 1154-1157, 2016.
- [7] L. Zhang, X. Zheng, W. Deng, Y. Lu, S. Lechevallier, Z. Ye, *et al.*, "Practical Implementation, Characterization and Applications of a Multi-Colour Time-Gated Luminescence Microscope," *Scientific reports*, vol. 4:6597, pp 1-7, 2014.
- [8] R. E. Connally and J. A. Piper, "Time-Gated Luminescence Microscopy," *Annals of the New York Academy of Sciences*, vol. 1130, pp. 106-116, 2008.
- [9] S. Wu, G. Han, D. J. Milliron, S. Aloni, V. Altoe, D. V. Talapin, *et al.*, "Non-blinking and photostable upconverted luminescence from single lanthanide-doped nanocrystals," *Proceedings of the National Academy of Sciences*, vol. 106, pp. 10917-10921, 2009.
- [10] A. M. Edmonds, M. A. Sobhan, V. K. A. Sreenivasan, E. A. Grebenik, J. R. Rabeau, E. M. Goldys, *et al.*, "Nano-Ruby: A Promising Fluorescent Probe for Background-Free Cellular Imaging," *Particle & Particle Systems Characterization*, vol. 30, pp. 1-8, 2013.
- [11] I. Sase, H. Miyata, J. Corrie, J. S. Craik, and K. Kinoshita Jr, "Real time imaging of single fluorophores on moving actin with an epifluorescence microscope," *Biophysical journal*, vol. 69, p. 323, 1995.
- [12] L. Gu, D. J. Hall, Z. Qin, E. Anglin, J. Joo, D. J. Mooney, *et al.*, "In vivo time-gated fluorescence imaging with biodegradable luminescent porous silicon nanoparticles," *Nature communications*, vol. 4: 2326, pp 1-7, 2013.
- [13] W. Sun, J. Yu, R. Deng, Y. Rong, B. Fujimoto, C. Wu, *et al.*, "Semiconducting Polymer Dots Doped with Europium Complexes Showing Ultranarrow Emission and Long Luminescence Lifetime for Time-Gated Cellular Imaging," *Angewandte Chemie International Edition*, vol. 52, pp. 11294-11297, 2013.
- [14] J.-C. G. Bünzli and S. V. Eliseeva, "Intriguing aspects of lanthanide luminescence," *Chemical Science*, vol. 4, pp. 1939-1949, 2013.
- [15] W. Moerner, "New directions in single-molecule imaging and analysis," *Proceedings of the National Academy of Sciences*, vol. 104, pp. 12596-12602, 2007.
- [16] T. Xia, N. Li, and X. Fang, "Single-molecule fluorescence imaging in living cells," *Annual review of physical chemistry*, vol. 64, pp. 459-480, 2013.

- [17] M. Vrljic, S. Y. Nishimura, S. Brasselet, W. Moerner, and H. M. McConnell, "Translational Diffusion of Individual Class II MHC Membrane Proteins in Cells," *Biophysical Journal*, vol. 83, pp. 2681-2692, 2002.
- [18] G. Seisenberger, M. U. Ried, T. Endress, H. Büning, M. Hallek, and C. Bräuchle, "Real-time single-molecule imaging of the infection pathway of an adeno-associated virus," *Science*, vol. 294, pp. 1929-1932, 2001.
- [19] Y.-R. Chang, H.-Y. Lee, K. Chen, C.-C. Chang, D.-S. Tsai, C.-C. Fu, *et al.*, "Mass production and dynamic imaging of fluorescent nanodiamonds," *Nature nanotechnology*, vol. 3, pp. 284-288, 2008.
- [20] V. S. Malik and E. P. Lillehoj, *Antibody techniques*: Academic Press, 1994.
- [21] C. M. Dundas, D. Demonte, and S. Park, "Streptavidin-biotin technology: improvements and innovations in chemical and biological applications," *Applied microbiology and biotechnology*, vol. 97, pp. 9343-9353, 2013.
- [22] V. J. O'Sullivan, I. Barrette-Ng, E. Hommema, G. T. Hermanson, M. Schofield, S.-C. Wu, *et al.*, "Development of a tetrameric streptavidin mutein with reversible biotin binding capability: engineering a mobile loop as an exit door for biotin," *PloS one*, vol. 7, p. e35203, 2012.
- [23] H. Sakahara and T. Saga, "Avidin-biotin system for delivery of diagnostic agents," *Advanced drug delivery reviews*, vol. 37, pp. 89-101, 1999.
- [24] P. Huhtinen, T. Soukka, T. Lövgren, and H. Härmä, "Immunoassay of total prostate-specific antigen using europium (III) nanoparticle labels and streptavidin-biotin technology," *Journal of immunological methods*, vol. 294, pp. 111-122, 2004.
- [25] D. Duijvesz, C. Y. L. Versluis, C. A. van der Fels, M. S. Vredenburg-van den Berg, J. Leivo, M. T. Peltola, *et al.*, "Immuno-based detection of extracellular vesicles in urine as diagnostic marker for prostate cancer," *International Journal of Cancer*, vol. 137, pp. 2869-2878, 2015.

Summary and Future Scope

7.1 Summary

Fluorescence microscopy has become a powerful tool for visualising tissues, cells and biomolecules. It is utilised for investigation of complex biological interactions in biology. The integration of the fluorescence microscopy with molecular probes based on photoluminescent (PL) nanoparticles (NPs) is rapidly emerging due to its several advantages over widespread fluorescent molecules, with the photostability, large surface and biocompatibility being the most important. Fluorescent carbon dots [1], metal nanoclusters [2, 3], plasmonic NPs, upconversion NPs [4] and nanorubies [5] are some of the newly developed PL NPs. This trend shows that PL NPs with unique properties are highly demanded.

In this work, nanoruby is chosen due to its remarkable properties that are suitable for ultrahigh-sensitivity bioimaging applications and long-term biomolecule tracking in the broad context of cell morphology and functionality. These properties are, as follows. Firstly, nanoruby is extremely photostable, displaying unfading emission under continuous excitation, which extends to the excitation intensities of MW/cm^2 and beyond. This allows uninterrupted monitoring of biological processes over prolonged periods at the level of single molecules, and has been successfully demonstrated in this project. Secondly, nanoruby emission is characterised by the exceptionally long-photoluminescence lifetime measured in milliseconds. This allows the effective separation of nanoruby-emitted photoluminescence from the background fluorescence

by using the time-gated imaging system, which has been introduced in this thesis. As a result, ultrahigh-sensitive imaging can be realised due to the dramatic improvement of the image contrast. Thirdly, nanoruby has been proven to be non-cytotoxic, which suggests its biocompatibility, and hence enables a range of imaging and therapeutic applications in the life sciences, where toxicity of the molecular probe and/or drug delivery nanovehicle is a concern. In addition, nanoruby is characterised by a narrow photoluminescence emission band, large Stokes shift, and its good colloidal stability is achievable, as we have demonstrated. This work addressed the large-scale, straightforward and affordable nanoruby production methods, aiming to meet potential demands of mass-production of nanorubies and other PL materials derived from the existing bulk materials for applications in the life science. We have demonstrated the feasibility of applying nanorubies in ultrahigh-sensitive bioimaging, including cells and receptors labelling, and the real-time monitoring of the single nanoruby binding assay in biological fluid.

Most of the existing methods for PL NPs production have several limitations. These include complexity, substantial time consumption, high cost, and low-scale production. In order to overcome these limitations, we explored the feasibility of the high-energy ball milling (HEBM) method for the large-scale nanoruby production. To this aim, we have demonstrated the proposed top-down production approach by transforming alpha-alumina micronised powder to nanoalumina. Alumina was used as a prototype, since it is the host material of ruby crystal. The optimised HEBM method, which included particle fractionation and chemical etching procedures, enabled the production of stable nanoalumina colloid, with the average size of 25 nm, excellent production yield ($\approx 30\%$) and purity (98 %). The cell viability MTT test has demonstrated non-cytotoxicity of nanoalumina, which represents an important initial step towards proving its biocompatibility. We demonstrated that the nanoalumina surface was readily amenable to surface-functionalisation, such as biologically-amiable amine groups, by using facile silane chemistry.

The developed HEBM protocol was utilised to produce nanoruby powder from as-procured micronised ruby powder. This yielded grams of nanorubies per batch, with the size range of 10 - 200 nm. The narrower size distributions were obtained by centrifugal fractionation, whereas the acid-based purification procedure yielded nanoruby powder of

the 98 % purity. XRD analysis revealed α -crystal structure of the milled sample. As-produced nanorubies were exceptionally photostable, featuring the expected narrow emission band at 692 nm. In addition, they exhibited long photoluminescence lifetime ≈ 3.7 ms, enabling ultrasensitive time-gated photoluminescence imaging. The ease of the nanoruby functionalisation was demonstrated by using the silane chemistry method, resulting the surface-functionalisation with amine groups and surface-redressing with carboxyl groups. As-produced nanorubies colloids were stable in water, but their stability in buffers was marginal. In order to counter this, nanorubies were functionalised with silane-terminated poly-ethylene glycol reagents, resulting in stable colloids in buffers. Furthermore, silica-coating of the nanoruby surface was carried out to increase the surface functional groups density, and demonstrated improved colloidal stability.

The long-photoluminescence lifetime of nanoruby was utilised for the time-gated photoluminescence (TGP) imaging, which enabled the visualisation of discrete nanorubies submersed in the highly fluorescent dye and fluorescent cellular environment by fully suppressing the laser-scatter and fluorescence background. The rapid imaging capability of the TGP system combined with the excellent photostability of nanoruby enabled live monitoring of single particle binding events in scattering and autofluorescent biological fluids. These results pave way for ultrafast, optical imaging and tracking at the single-nanoparticle sensitivity.

7.2 Future Scope

This study placed significant contribution in theranostics area, which is a new approach for diagnostic and therapeutics. Nanoalumina and nanorubies have been produced in large scale for this purpose. Nanoalumina is known as a promising drug carrier, which has been used for cancer treatment [6]. Meanwhile, nanorubies will enable drug delivery and deposition at single-molecule level in cells. This new type of PL nanomaterial will hopefully allow safe ways of drug delivery, manipulation and visualisation. In this project, my colleagues and I have demonstrated the real-time monitoring of nanoruby binding assay in serum. This assay can be extended to the other biological fluids, such as blood and urine. Nanorubies coupled to antibodies can be employed to recognise and bind to antigens for diagnostics of pathological conditions.

For example, a prostate cancer biomarker, CD9 antigen, can be detected using nanoruby-based assay, leading to early cancer diagnostic [7]. The demonstrated potential of nanoruby-enabled single biomolecule tracking is applicable to μ -opioid receptor labelling towards investigation of the molecular mechanisms behind pain-relief. This understanding is crucial for developing better analgesic drugs with reduced side-effects.

HEBM has been shown to provide a powerful approach for production of a variety of nanomaterials from their bulk form. These nanomaterials exhibit excellent properties in terms of size, biocompatibility, and colloidal stability. HEBM can be applied to transform existing bulk material with properties desirable for theranostics application into new PL NPs. Now, there is a wide range of bulk materials in particular laser material, featuring a variety of photoluminescence properties. The laser materials are chosen based on the absorption and emission range, and efficiency. One of the potential laser crystal is Yb:KGW. This crystal has simple two-level electronic structure, which prevents undesired loss processes including upconversion, excited state absorption, and concentration quenching [8]. In addition, it requires 980-nm excitation source. This property is very important for deep tissue imaging, where the absorption of this crystal is in the biological tissue transparency window ranging from 700 nm to 1300 nm.

Several improvements will have to be implemented before high-quality nanomaterials become available routinely and at a large-scale. Adjustment of pH during the milling process is an important control parameter, which can improve minimally achievable size and surface quality of as-produced nanocrystallites. It has been reported the smaller-size alumina NPs were obtained by adjusting pH to the lower value [9]. This indicates that the milling efficiency can be improved by controlling the sample stability. It can be interpreted in terms of the aggregation propensity of colliding particles at the submicron-size range, which is minimised by controlling pH. Replacement of water with purpose-selected media is expected to improve the milling outcomes in terms of the colloidal stability. For example, Polyethylene glycol (PEG) solution can be applied in order to increase colloidal stability of NPs in buffer solutions.

The photoluminescence action cross-section of as-produced nanoruby can be increased by increasing the chromium content in the ruby crystal. However, only few

types of synthetic ruby crystal with different chromium doping is available commercially. The combustion synthesis [10] represents a promising solution for the high chromium -doping ratio nanorubies, where the doping ratio can be controlled. It is interesting to note, nanoruby lifetime depends on the chromium content due to the intersystem crossing effects [11]. This can be exploited in lifetime-based spectral multiplexing, which can be applied for multiple analytes detection in biological samples as reported elsewhere [12, 13].

7.3 References

- [1] W. Kong, R. Liu, H. Li, J. Liu, H. Huang, Y. Liu, *et al.*, "High-bright fluorescent carbon dots and their application in selective nucleoli staining," *J. Mater. Chem. B*, vol. 2, pp. 5077-5082, 2014.
- [2] L. Zhang and E. Wang, "Metal nanoclusters: new fluorescent probes for sensors and bioimaging," *Nano Today*, vol. 9, pp. 132-157, 2014.
- [3] P. Zhang, X. X. Yang, Y. Wang, N. W. Zhao, and C. Z. Huang, "Rapid synthesis of highly luminescent and stable Au 20 nanoclusters for active tumor-targeted imaging in vitro and in vivo," *Nanoscale*, vol. 6, pp. 2261-2269, 2014.
- [4] S. W. Wu, G. Han, D. J. Milliron, S. Aloni, V. Altoe, D. V. Talapin, *et al.*, "Non-blinking and photostable upconverted luminescence from single lanthanide-doped nanocrystals," *Proceedings of the National Academy of Sciences of the United States of America*, vol. 106, pp. 10917-10921, 2009.
- [5] A. M. Edmonds, M. A. Sobhan, V. K. A. Sreenivasan, E. A. Grebenik, J. R. Rabeau, E. M. Goldys, *et al.*, "Nano-Ruby: A Promising Fluorescent Probe for Background-Free Cellular Imaging," *Particle & Particle Systems Characterization*, vol. 30, pp. 1-8, 2013.
- [6] H. Li, Y. Li, J. Jiao, and H.-M. Hu, "Alpha-alumina nanoparticles induce efficient autophagy-dependent cross-presentation and potent antitumour response," *Nat Nano*, vol. 6, pp. 645-650, 2011.
- [7] D. Duijvesz, C. Y. L. Versluis, C. A. van der Fels, M. S. Vredenburg-van den Berg, J. Leivo, M. T. Peltola, *et al.*, "Immuno-based detection of extracellular vesicles in urine as diagnostic marker for prostate cancer," *International Journal of Cancer*, vol. 137, pp. 2869-2878, 2015.
- [8] A. Brenier and G. Boulon, "Overview of the best Yb³⁺-doped laser crystals," *Journal of alloys and compounds*, vol. 323, pp. 210-213, 2001.
- [9] F. Stenger, S. Mende, J. Schwedes, and W. Peukert, "The influence of suspension properties on the grinding behavior of alumina particles in the submicron size range in stirred media mills," *Powder Technology*, vol. 156, pp. 103-110, 2005.
- [10] X. Mi, X. Zhang, X. Ba, Z. Bai, L. Lu, X. Wang, *et al.*, "Preparation and luminescent properties of Cr³⁺:Al₂O₃ nano-powders by low-temperature combustion synthesis," *Advanced Powder Technology*, vol. 20, pp. 164-168, 2009.

- [11] D. G. Liu, "Effects of Cr content and morphology on the luminescence properties of the Cr-doped α - Al_2O_3 powders," *Ceramics International*, vol. 39, pp. 4765-4769, 2013.
- [12] Y. Lu, J. Lu, J. Zhao, J. Cusido, F. M. Raymo, J. Yuan, *et al.*, "On-the-fly decoding luminescence lifetimes in the microsecond region for lanthanide-encoded suspension arrays," *Nature communications*, vol. 5, 2014.
- [13] M. Grabolle, P. Kapusta, T. Nann, X. Shu, J. Ziegler, and U. Resch-Genger, "Fluorescence lifetime multiplexing with nanocrystals and organic labels," *Analytical chemistry*, vol. 81, pp. 7807-7813, 2009.

APPENDIX A

The addendum shows the results of the initial milling experiments, which were milled with a different parameters to what were reported in the paper. The milling parameters are given in Table A.1. This work established a foundation to design better milling protocols. In this experiment, multi-steps milling was applied. 5-mm zirconia milling balls was chosen for the first stage of micro alumina powder milling (mean size 1.5 μm). The milling was done in 1 hour, which was aimed at breaking large particles present in the alumina sample. Then, the milled sample was extracted by using 0.08-mm sieve and loaded again in the milling bowl for second milling step. For the second stage, 1-mm zirconia milling ball was used for breaking smaller agglomerated particle. This milling process was performed for 1 hour. Then, the milled sample was extracted again, and used for final milling step by using 0.2-mm zirconia milling ball. This process was performed for 3 hours, which functioned to reduce the particle size until nanometer range. Distilled water was used as a milling aid throughout the milling process, which help to disperse the particle as well as increase the milling efficiency by reducing the agglomeration phenomena. The milled sample was analysed in terms of their size and composition.

Table A.1: Multi-steps milling parameter

Milling duration	Ball size	Ball number/mass	speed	Ball/powder mass ratio (Charge ratio)
1 hour	5 mm	80 pcs	1000 rpm	25
1 hour	1 mm	25 g	1100 rpm	
3 hours	0.2 mm	25 g	1100 rpm	

SEM image of milled alumina is shown in Figure A.1. It can be observed that the alumina particle size decreases with longer milling time. In order to determine the morphology of the alumina nanoparticles, TEM analysis was carried out. From TEM image shown in Figure A.2, the mean size of the alumina particle was determined as 66 nm. The shape of the particle is irregular with quasi-spherical shape. XRD analysis was carried out to examine the contamination in the sample. From the XRD spectra depicted in Figure A.3, strong zirconia peak was observed (shown by the arrow). This indicates a

huge amount of zirconia contamination in the sample. The contamination was estimated around 52 %, based on EDX analysis. In order to reduce the contamination, milling parameters were modified, including using only small milling balls, and set lower charge ratio.

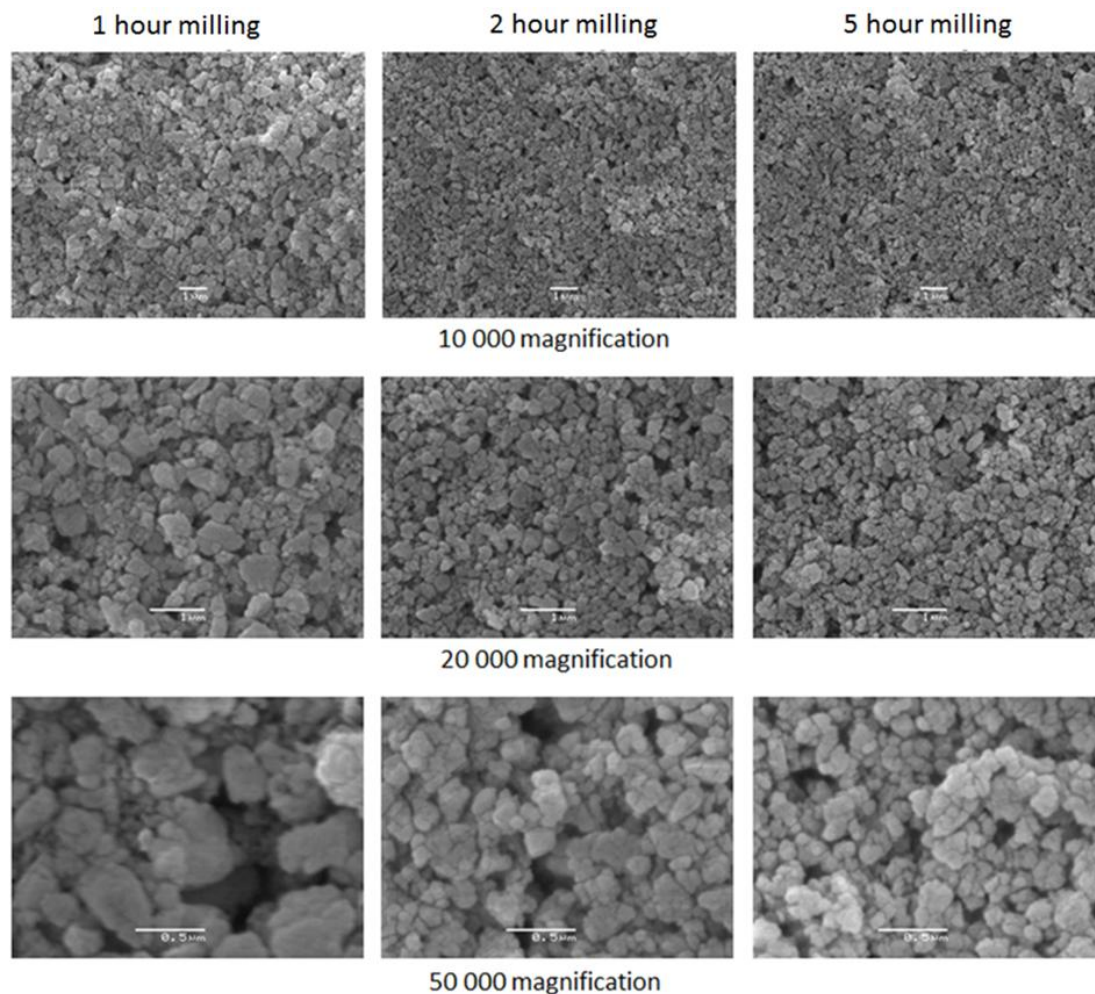


Figure A.1: SEM micrographs of milled alumina. Columns: 1 hour, 2 hours and, 5 hours milling time in 10 000, 20 000 and 50 000 magnification respectively. Scale bar for 10 000 and 20 000 magnifications is 1 μm .

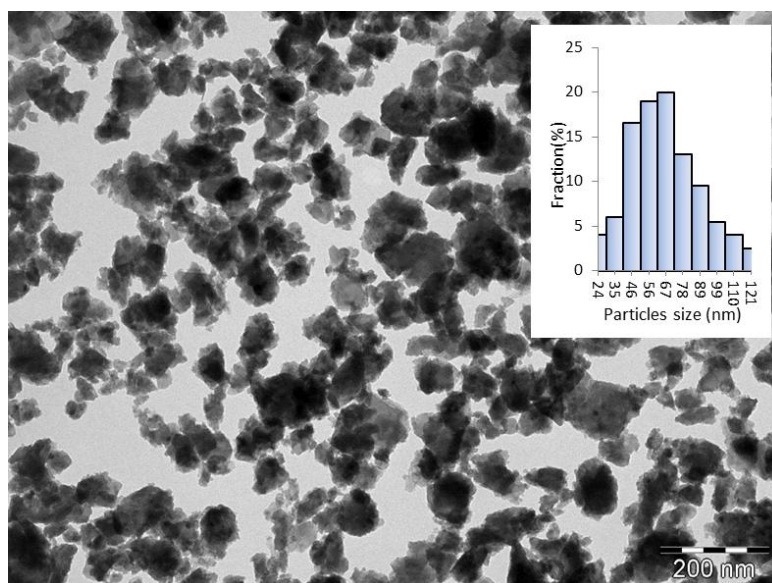


Figure A.2: TEM image of milled alumina

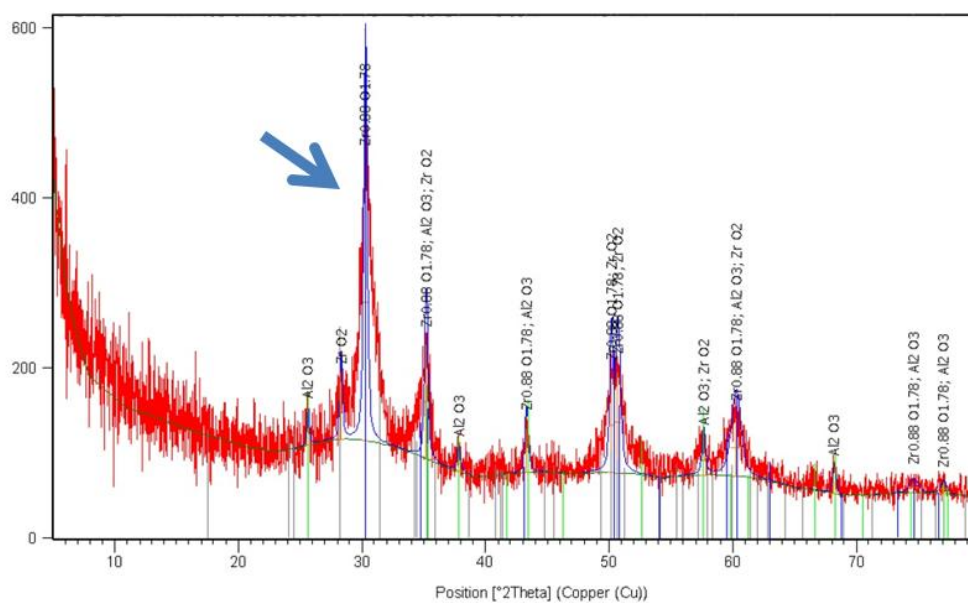


Figure A.3: XRD pattern of 5 hour milling alumina sample. The arrow shows the zirconia peak.

APPENDIX B

PROTOCOL FOR AMINE AND CARBOXYL FUNCTIONALISATION

1. 30 mg of nanoalumina/nanoruby powder was thoroughly washed 3 times with MilliQ water by centrifugation and resuspended in 1 mL of 95% ethanol (5% MilliQ water) in a clear vial, followed by sonication for 5 minutes to prepare a stable colloid.
2. For surface-functionalisation with amino-groups, 100 μ L of (3-Aminopropyl) triethoxysilane (APTES) (Sigma-Aldrich, Australia) was added to the colloid, and the mixture was sonicated in a bath-sonicator for 1 hour.
3. The sample was then washed 5 times with ethanol to ensure complete removal of unreacted APTES, and dried in an oven at 60°C for 1 hour.
4. For the carboxyl functionalisation, 20 mg of Succinic anhydride (SA) was dissolved in 120 μ L Dimethyl sulfoxide (DMSO).
5. 10 mg of amine-functionalised nanoalumina/nanoruby was dispersed in 300 μ L 100% ethanol. These two solutions were mixed together and left on the shaker overnight. The sample was then washed 5 times with ethanol, and dried in an oven.

PROTOCOL FOR NANORUBY PEGYLATION

1. 1 mg.mL⁻¹ Nanoruby solution was rinsed 3 times in water by centrifugation for 5 min at 5000×g, followed by replacing the supernatant with MilliQ water and redispersion by sonication and vortex.
2. The rinsing step was repeated once more, but ethanol was added to the pellet instead of water. 10 mM Silane-PEG (Mw=2000 Da; Laysan Bio, Inc, US) solutions were prepared in ethanol.
3. This PEG solution was used to replace the ethanol in the nanoruby solution.
4. The samples were vortex thoroughly and sonicated for 1 hour.
5. The samples were washed 5 times with ethanol at 10,000×g for 5 min and dried overnight in a convection oven.

PROTOCOL FOR NANORUBY SILICA COATING

1. 5 mg of poly(vinylpyrrolidone) (Sigma-Aldrich, Australia) with molecular weight of 360000 Da (PVP-360) was dissolved into 4 mL MilliQ water followed by sonication for 5 mins.
2. This solution was added into 25-mL round-bottom flask containing 4 mL of nanoruby suspension.
3. The mixture was stirred at 400 rpm for overnight.
4. To remove the excess PVP, the PVP-modified nanoruby was washed with MilliQ water, followed by washing with a mixture of MilliQ water and ethanol (1:1 in volume).

5. For the silica coating, 20 mL ethanol, 3 mL water, 20 μ L tetraethoxysilane (TEOS) and 400 μ L ammonia were added in sequence into a 50-mL round-bottom flask.
6. Then, washed PVP-modified nanoruby in 4 mL ethanol was added.
7. The mixture was left stirring at 400 rpm for overnight at room temperature.
8. The sample was washed with ethanol 3 times to remove the excess reaction agents.
9. The silica coated nanorubies was stored in ethanol.